A LATTICE-BASED EQUIVALENT CIRCUIT MODEL FOR FREQUENCY SELECTIVE SURFACES

A Dissertation

by

DAVID LEE ROLANDO

Submitted to the Office of Graduate and Professional Studies of
Texas A&M University
in partial fulfillment of the requirements for the degree of

DOCTOR OF PHILOSOPHY

Chair of Committee,	Gregory H. Huff
Committee Members,	Robert D. Nevels
	Jean-Francois Chamberland-Tremblay
	Stephen A. Fulling
Head of Department,	Chanan Singh

December 2014

Major Subject: Electrical Engineering

ABSTRACT

This work introduces a novel analytical framework for designing and synthesizing frequency selective surfaces (FSSs). In this framework, referred to as the “lattice model”, a periodic FSS is represented as an infinite lattice of interconnected admittances arranged in a multiport network. The model provides a compromise between traditional full-wave numerical analyses and simplistic aggregated circuit models, effectively dividing the analysis into two parts: a "circuit domain", in which the periodicity of the FSS is accounted for using a discrete lattice of admittances; and an "electromagnetic domain", in which the admittances of the lattice are calculated using classic full-wave techniques.

The bulk of this dissertation provides the mathematical theory underlying the lattice model. The details of the model are initially developed for single-element, single-layer FSSs under uniform normal plane wave incidence. The theory is then extended to several additional cases: multi-element and multilayer topologies; non-uniform incidence, with particular emphasis on oblique plane wave incidence; and impedance analysis of integrated structures combining FSSs with antennas. Next, the model is applied to the task of FSS synthesis - specifically in the form of constrained optimization problems. For illustration, the lattice model is applied to a variety of specific FSS designs comprising rectangular aperture resonators. Several of these designs are fabricated, and the measured performance is compared to lattice model and simulation results.

The most general result of the various avenues of investigation in this work is the verification of the lattice model as a legitimate and accurate tool for FSS analysis. Beyond this, two important features of the model are established that set it apart from other analysis techniques. First, changes in an incident field can be accounted for entirely in the circuit domain by changing the input currents to the multiport network; the admittances of the lattice remained unchanged, allowing for versatility under different scenarios of FSS illumination. Second, decomposition of an FSS into such a lattice provides an opportunity to approximate the lattice admittances as multidimensional polynomial functions of the FSS dimensions. A novel class of computationally-tractable optimization problems for FSS synthesis can be formulated using this polynomial-based scheme.

TABLE OF CONTENTS

Page

LIST OF FIGURES

Page

LIST OF TABLES

Page

CHAPTER I

INTRODUCTION

The term frequency selective surface (FSS) designates a wide range of electromagnetic structures that are designed to interact with and modulate unguided electromagnetic (EM) energy [1]. FSS can be thought of as “spatial filters” [2] – that is, they filter spatially-distributed EM waves by causing energy at certain frequencies to be transmitted, reflected or absorbed. In this sense, FSS are analogous to traditional circuit filters. However, instead of filtering a signal confined to a wire or a transmission line (a guided wave), FSS filter freely propagating electromagnetic energy.

Physically, FSS comprise a periodic arrangement of a large number of electromagnetically-functionalized until cells [3]. The unit cells are usually constructed of metal and dielectric materials patterned such that currents and fields are excited on the unit cell by certain desired frequencies (hence the term “frequency selective”). Typically, the periodicity of these unit cells is two-dimensional, and the unit cells themselves are planar, being relatively thin in the third dimension (hence the term "surface"). FSSs come in a wide variety of topologies and geometries; an overview of such topologies is given in Chapter II.

FSSs are employed in an wide array of applications that involve spatial electromagnetic windowing or beamforming. In the former category, the spectrum of frequencies allowed into a specific spatial region is controlled, while in the latter category, the spatial distribution of freely propagating energy is controlled (much like an optical lens may focus light). Many of these FSS applications directly involve antennas or antenna arrays, such that the spectrum or spatial distribution of radiation from an antenna is deliberately controlled. Although this is the most common use of FSSs, they can be applied to many other applications in which spatial management of EM energy is necessary.

A straightforward FSS application is to integrate it into a radome, a surface enclosing an antenna which essentially provides physical protection and electromagnetic transparency (e.g. [4], [5]). A radome can be outfitted with an FSS layer to only allow certain desired frequencies to interact with the enclosed antenna (i.e. EM windowing). Other applications involve a more direct integration of an FSS with an antenna. In particular, the antenna and FSS may be deliberately placed in close proximity, such that their mutual behavior is strongly coupled. In [6], a "filtenna" is proposed that integrates an FSS directly into the aperture of a horn antenna. The FSS restricts the transmission and reception of the horn to a particular bandwidth within its otherwise larger operating range. In [7], a high-order FSS filter is placed directly over an array of patch antennas as a proposed alternative to bulky integrated radio frequency (RF) circuit filters for a digital beamforming (DBF) system. The possibility of using FSSs to enhance the performance of antennas has also been investigated. In [8], a FSS is placed as a superstrate over a patch antenna, providing an increase in the bandwidth and directivity of the patch.

As stated above, not all FSS applications directly involve antenna systems. For example, FSSs can be used to shield rooms in a building from unwanted frequency bands (or alternatively, to confine the propagation of a local wireless network inside a building). FSS are also employed to reduce the radar cross section (RCS) of various structures. Additionally, FSS can be designed as RF beamsplitters (much like optical beamsplitters), in which various frequencies of quasi-optical incident waves can be separated and directed to different spatial locations. This kind of design can find application in radiometers for remote sensing, particularly in space-borne systems [9]. In general, FSSs can find a multitude of uses as spatial filters for various sensors and instrumentation.

Given such a variety of applications, the accurate electromagnetic analysis of FSS behavior is critical for the purpose of making practical designs. FSS analysis can present many unique challenges related to the periodicity, the complexity of the unit cells, and the electrically large size of the overall structure. Two distinct methodologies typically employed for analysis are full-wave numerical methods based on Maxwell's equations and aggregated circuit model approximations. While it is clear that there is not a one-size-fits-all approach for different FSS topologies, these varied approaches offer unique trade-offs between accuracy, computational cost, and physical insight. Computational costs aside, computer aided drafting (CAD) capabilities can generate intricately parameterized models, and the use of powerful full-wave EM solvers can generate highly accurate solutions using traditional Floquet analysis of periodic structures [10]. Depending on the complexity of an FSS, this computational framework can remove some of the physical insight from the design process, providing only a limited amount of intuition for the purpose of tuning a design to meet desired performance criteria. Alternatively, a variety of equivalent circuit models can be invoked to simplify analysis (e.g. [11], [12], [13]). These methods may provide convenient insight into the fundamental behavior of an FSS by way of analogy to circuit resonators, but aggregating all unit cells into a few circuit elements is often only applicable on a case-by-case basis, and the accuracy of this abstraction can be limited.

The goal of this work is to propose a new, canonical, lattice-based analytical model for FSSs and to demonstrate the potential utility of such an analytical framework for their practical design. This new "lattice model" treats an FSS as an infinite lattice of interconnected circuit components, providing a compromise between full-wave numerical techniques and simplistic aggregated circuit models. Rather than aggregating the behavior of all unit cells into a few circuit components, each individual FSS element is treated as its own port in a multiport network that has been extended to infinity. Within this network, each FSS element is represented by a self admittance, and mutual admittances represent the interaction between elements. Instead of accounting for periodicity by imposing periodic boundary conditions on Maxwell's equations, an infinite circuit lattice is solved. The model essentially divides FSS analysis into an "electromagnetic (EM) domain" problem and a "circuit domain" problem. In the EM domain, the lattice admittances are computed using classic electromagnetic techniques; in the circuit domain, the periodicity is accounted for. Also, unlike many aggregated circuit models, the lattice model is canonical in the sense that it is not limited to specific unit cell geometries.

The lattice model allows FSS analysis to be abstracted into the circuit domain in two unique ways. First, changes in an incident field impinging on an FSS can be computed entirely in the circuit domain by simply changing the input currents to the multiport network and re-analyzing the lattice. The lattice admittances are the same regardless of the incident field. This is in contrast to some full-wave techniques, in which the entire problem may have to be re-solved for different incident fields. This is especially true when using commercial simulation tools, where, in general new simulations must be run when different EM sources are assumed. Second, the model provides a unique opportunity to approximate FSS performance as a function of geometric dimensions. The lattice admittances are generally well-behaved functions of the dimensions and can be represented using multidimensional polynomials. Thus, the FSS performance over an entire geometric design space can be represented as a circuit domain problem with polynomial-based admittances. This allows the lattice model to be used for computationally-tractable FSS optimization routines that do not require full-wave solutions at every iteration. Instead, the optimization is performed entirely in the circuit domain.

This dissertation is organized as follows. In Chapter II, a selection of FSS background material is presented to provide context for the rest of the paper. This material includes an overview of different FSS geometries and topologies, a discussion of reconfigurable FSSs, and a summary of commonly employed FSS analysis techniques. Chapter III introduces the new lattice model. The motivation behind the model is developed in more detail, and a conceptual model is presented to help visualize the general framework behind the method. Chapters IV and V are devoted to developing the mathematical details required to implement the lattice model. For simplicity, these chapters only consider single-element, single-layer FSSs under uniform normal plane wave incidence. Specifically, Chapter IV looks at the circuit domain portion of the analysis; this includes the structure of the multiport lattice network and the calculation of the lattice port voltages. Chapter V explores the EM domain analysis, which consists of computing the self and mutual admittance elements within the lattice. Also included in this chapter is the specific application of the model (both circuit and EM domains) to rectangular aperture FSS designs for the purpose of illustration. In Chapter VI, the mathematical basis of the model is extended to include more complex cases: multi-element unit cells, multilayer FSSs, and reconfigurable FSSs. Computational examples of these various cases are provided, again using rectangular aperture resonant elements. Next, in Chapter VII, cases of non-uniform incidence are considered. To this end, an alternative formulation of the lattice model in the spectral domain using a two-dimensional (2D) discrete Fourier transform (DFT) is introduced. The specific case of oblique plane wave incidence is explored in detail. Examples comprising rectangular aperture elements are again provided. In Chapter VIII, the model is extended even further to analyze structures that integrate FSSs with antennas or antenna arrays. The antenna elements are treated as additional ports in the multiport lattice network. The chapter explores several example cases of waveguide aperture antennas radiating through FSSs (again, rectangular aperture FSSs are employed for illustration). In Chapter IX, the utility of the model for the purpose of FSS synthesis through constrained optimization is explored. Specifically, polynomial approximations of the lattice admittances are computed which dictate FSS performance over a multidimensional geometric design space. Simple optimization problems are formulated and solved using this circuit domain polynomial model. Several design examples are provided for both pure FSS topologies and combined antenna-FSS structures. Finally, Chapter X concludes the dissertation, summarizes the main contributions of this work, and briefly discusses the possibilities for future work.

CHAPTER II

BACKGROUND

The purpose of this chapter is to provide a brief overview of FSSs: how they are designed physically, how they operate, and how they are analyzed. This task is primarily accomplished through examples and a general survey of FSS-related literature. It is by no means meant to be a comprehensive treatment of the subject, but rather is intended to provide a reasonable intellectual foundation on which primary focus of this dissertation - the lattice model - can be built.

The chapter begins by relating some basic concepts behind FSSs: their physical structure and an assessment of their EM performance. Then, a summary of some common FSS unit cell topologies is provided. This includes different unit cell geometries as well as multi-element and multilayer FSSs. Next, a brief discussion of reconfigurable FSSs is provided along with some examples of reconfiguration mechanisms. This is followed by a discussion of periodic EM structures closely related to FSS: artificial magnetic conductors, metamaterials, etc. Finally, the mathematical analysis of FSSs is considered. The most common technique, full-wave numerical analysis based on periodic Floquet theory, is reviewed first. This is followed by a short consideration of some examples of equivalent circuit models, as well as a brief discussion of finite FSS analysis.

FSS Basics

Physically, FSSs comprise a periodic arrangement of identical until cells that are composed of specific geometric patterns of metal and dielectric materials. These unit cells are typically planar with two-dimensional periodicity. This physical structure is best illustrated by an example. Fig. 1 shows a very simple FSS comprising thin metallic crosses arranged periodically over two dimensions in a rectangular grid pattern. The crosses are supported by a dielectric substrate (gray). The substrate primarily provides mechanical support, but its EM material properties (e.g. relative permittivity) can nonetheless significantly alter the FSS performance. Each cross represents a single unit cell (Fig. 1 (b)). This structure is referred to as a cross-dipole FSS [14] because it essentially consists of two perpendicular resonant dipoles. The horizontal and vertical portions of the crosses are excited by incident electromagnetic energy polarized in the horizontal and vertical directions, respectively. Thus, the FSS can respond to plane waves of arbitrary polarization. The FSS resonates at frequencies with corresponding wavelengths that are twice the length of the dipoles.

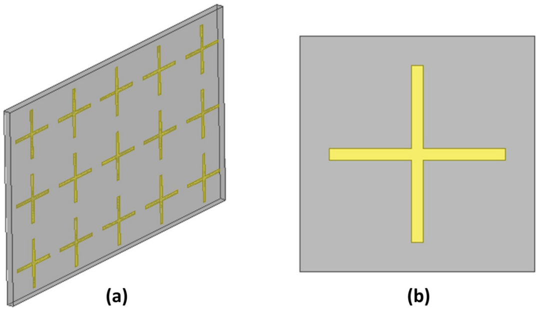

Fig. 1. Cross dipole FSS. (a) Periodic arrangement of metallic crosses supported by a dielectric substrate. (b) Unit cell geometry.

Fig. 2 illustrates how the performance of a simple FSS such as that in Fig. 1 may be assessed. In Fig. 2 (a), the FSS screen, viewed from the side, separates two regions of free space (A and B). It is assumed that an electromagnetic field, $\mathbf{E}_i$, exists in Region A and impinges upon the FSS (note that the bold-faced variable $\mathbf{E}_i$ represents a vector-valued quantity; this notation is used throughout this dissertation). As a result, there will be a scattered field, $\mathbf{E}_s$, in Region A and a transmitted field, $\mathbf{E}_t$, in Region B. The total field in Region A is the superposition of the incident and reflected fields, $\mathbf{E}_A = \mathbf{E}_i + \mathbf{E}_s$, and the total field in Region B is equal to the transmitted field, $\mathbf{E}_B = \mathbf{E}_t$. It is possible to discuss the performance of the FSS directly in terms of these vector-valued fields. However, it is more common to discuss the performance in terms of equivalent scalar circuit values. Specifically, in (b), the FSS is viewed as a "black box" two-port network, with the ports corresponding to Regions A and B. An incoming voltage wave from Region A, V_A^+, corresponds to the vector-valued incident field $\mathbf{E}_A$. The outgoing voltage waves, V_A^- and V_B^-, correspond to the reflected and transmitted fields, respectively. Using these voltages, the standard two-port scattering parameters (S-parameters, [15]) can be defined; specifically, S_{11} is the reflection coefficient of the FSS, and S_{21} is the transmission coefficient. The squared magnitudes of these quantities are the reflectivity R and the transmissivity T, which essentially give the percentage of incident power that is reflected or transmitted (when scaled by a factor of 100). It is common to report these values in a logarithmic decibel (dB) scale.

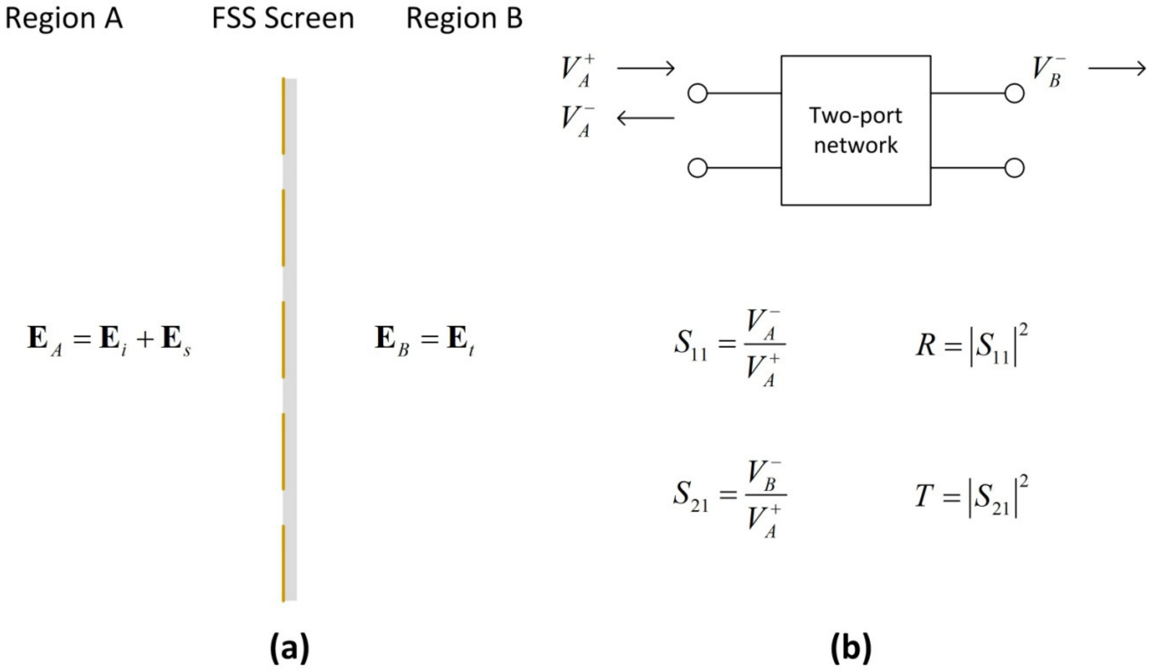

Fig. 2. Analysis of FSS performance.

In order to demonstrate the performance of the cross dipole FSS, it is assigned dimensions and simulated for its S-parameters. The simulation is performed in [16], a commercial program that solves Maxwell's equations for three dimensional structures using the finite element method. The metallic cross is given a length of 8.2 mm, a width of 0.5 mm, and a unit cell size of 12x12 mm. The dielectric substrate is assumed to have a relative dielectric constant of $\varepsilon_r = 2.2$ and a thickness of 62 mil. The resulting reflectivity and transmissivity (in dB) are plotted as a function of frequency in Fig. 3. The FSS achieves near 100% power reflection (R = 0 dB) and virtually no transmission (T < -40 dB) near 14 GHz. Reflection of at least 90% (T < -10 dB) occurs over a narrow bandwidth of about 13.7-14.3 GHz. Thus, the cross dipole is considered to be a narrowband bandstop filter: that is, it causes frequencies in a specific narrow “stopband” to be mostly reflected, while allowing most other frequencies to transmit through the FSS.

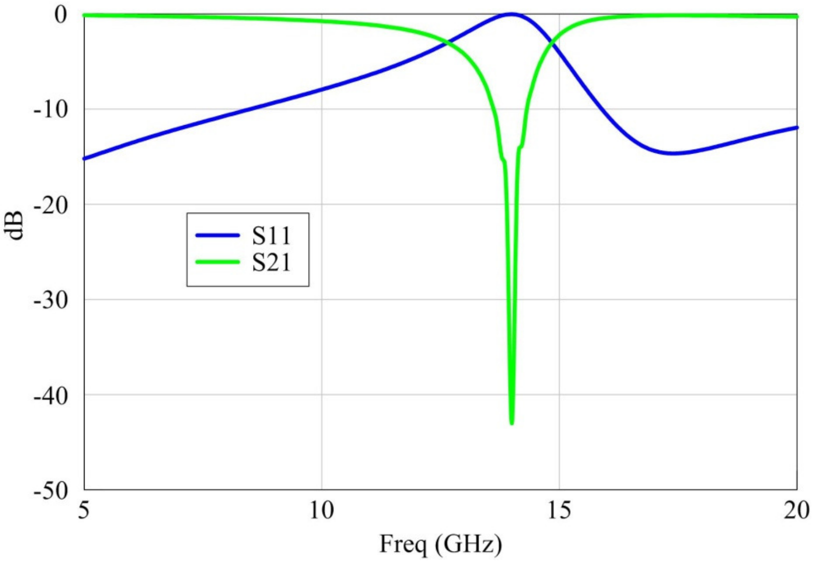

Fig. 3. Magnitude of S-parameters for a rectangular strip FSS.

FSS Topologies

FSS Unit Cell Geometries

There are an endless number of possible FSS unit cell geometries, and the metallic cross of Fig. 1 is only one of many common geometries. Fig. 4 gives a summary of some of the simplest but most commonly employed unit cells. Included are (a) a metallic strip [17], (b) a square patch [18], (c) a circular patch [19], (d) an annular ring [20], (e) a square ring [21], and (f) a Jerusalem cross [22]. Each of these structures is resonant at frequencies determined by the geometric dimensions of the designs.

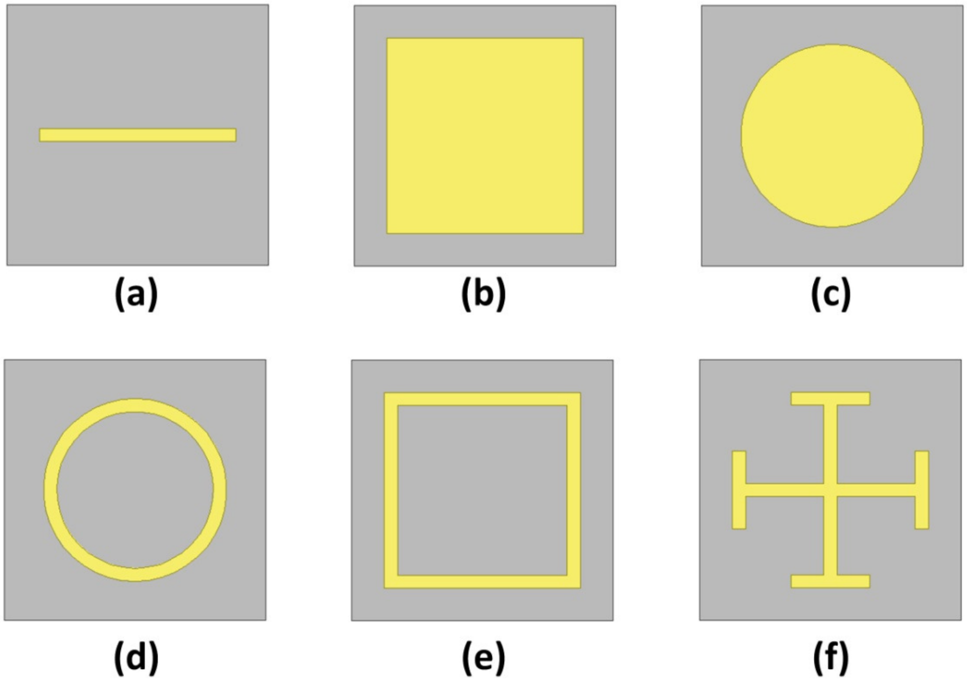
(a) (b) (c) (d) (e) (f)

Fig. 4. Basic FSS unit cell geometries. (a) Rectangular strip, (b) square patch, (c) circular patch, (d) annular ring, (e) square ring, and (f) Jerusalem cross.

Besides the variations in unit cell geometries discussed above, another significant category of FSSs are complementary unit cells. A complementary unit cell is achieved by retaining the same geometry but interchanging the regions of metallization with the areas free of metallization. Fig. 5 shows the complementary versions of the Jerusalem cross FSS. The unit cells in Fig. 4 are considered “capacitive”-type FSSs. Their complements are considered “inductive”-type FSSs. At frequencies near resonance, capacitive-type FSSs exhibit a bandstop filter response (like the cross-dipole of Fig. 1). Inductive-type FSSs exhibit a bandpass filter response, meaning that a narrow band of frequencies are transmitted while all other frequencies are reflected. If no supporting dielectric is present and a perfect two-dimensional metallic screen is assumed, then two complementary FSSs will resonate at the same frequency, according to Babinet's principle [23]. If a dielectric is present on one side of the conducting screen, the perfect complementary nature of the two designs will be slightly perturbed, although the resonant frequency will still be similar.

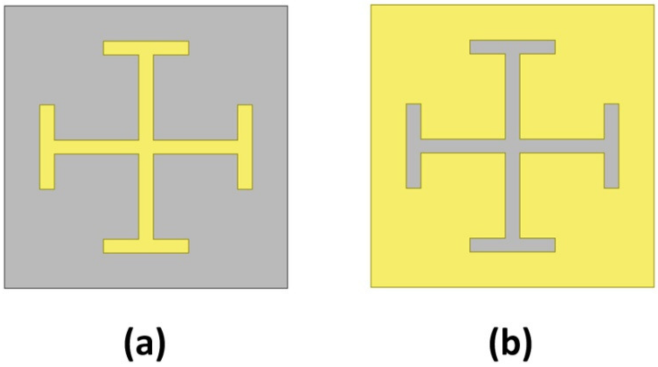

Fig. 5. Complementary Jerusalem cross FSS. (a) Capacitive-type and (b) inductive-type.

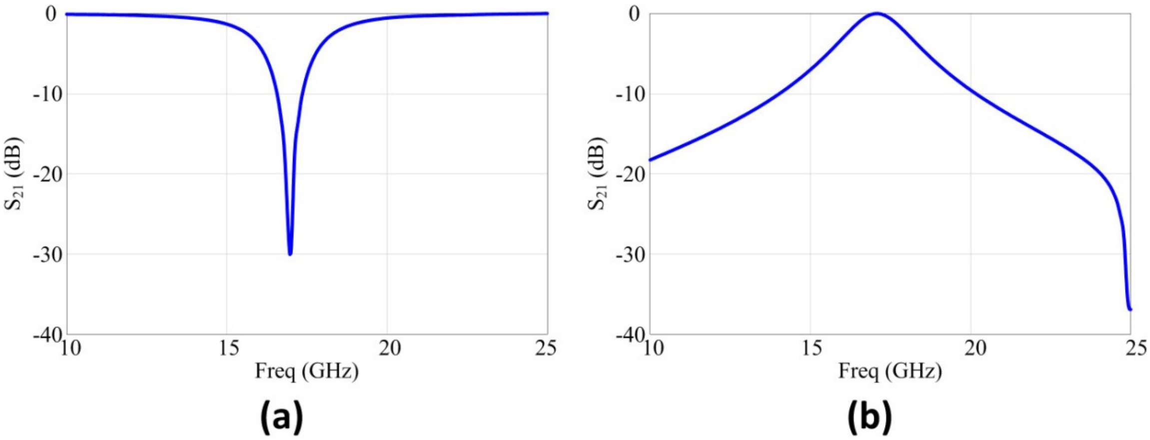

Fig. 6. Transmission properties of complementary FSSs. (a) Bandstop response of capacitive-type FSS and (b) bandpass response of inductive-type FSS.

Multilayer FSS

The FSSs described above reside on a single two-dimensional layer, and the filter response is first-order. However, it is common to cascade several such layers together to achieve a higher-order filter response. This is analogous to adding more lumped elements to a circuit filter in order to achieve higher-order responses. Higher-order filters result in wider bandwidths of operation and sharper transitions between frequencies of reflection and transmission. Fig. 7 provides a generic illustration of the multilayer concept. Specifically, four inductive-type FSS screens with arbitrarily-shaped apertures are cascaded together with a finite spacing between layers.

Fig. 8 provides some examples of multilayer FSSs from literature. In (a), two FSS layers are sandwiched between three separate dielectric layers [24]. In (b), metallic dipoles (strips) are arranged into two layers (essentially the unit cell geometry of Fig. 4 (a)). Note that no dielectric support is defined and the dipoles are suspended in air; this particular work is more theoretical in nature and not intended for an actual physical realization [25].

Fig. 9 shows a more practical multi-order filter design [26]. In (a) and (b), alternating layers of inductive- and capacitive-type FSS are sandwiched between dielectric slabs. The dimensions are designed so that a seventh-order bandpass response is achieved from roughly 60-64 GHz, as shown in (c). Note that the passband is relatively wide and flat. At the edges of the passband, the FSS response drops sharply into areas of strong reflection. Such a multi-order response is usually more desirable than a first-order filter because it can accommodate wideband applications while achieving a strong contrast in behavior between frequencies in the desired bandwidth and those frequencies just outside the band.

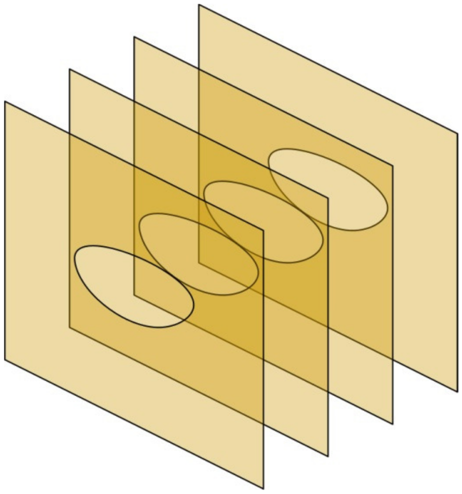

Fig. 7. Generic four-layer inductive-type FSS.

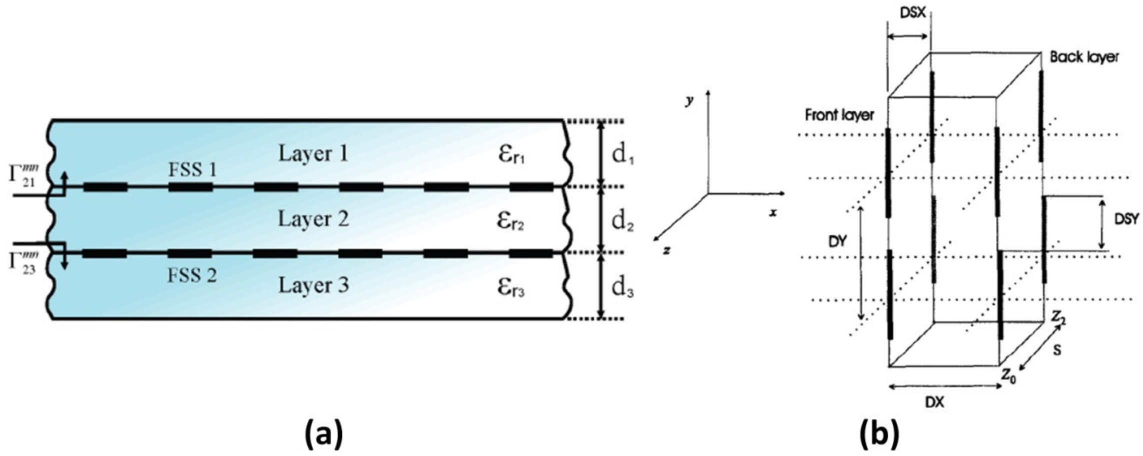

Fig. 8. Multilayer FSS designs. (a) Two FSS screens sandwiched between three dielectric layers. (b) Two-layer dipole FSS.

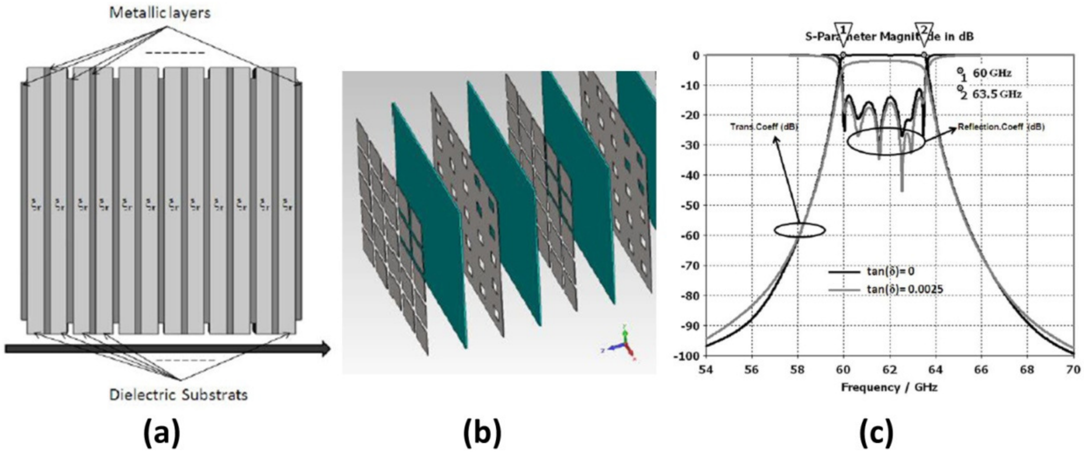

Fig. 9. Multilayer seventh-order bandpass FSS. (a) Side view. (b) Alternating capacitive-type and inductive-type screens separated by dielectric layers. (c) Filter response.

Multi-Element FSS

It is also possible to design FSSs with periodic unit cells that contain more than one resonant element. This is typically done to either achieve multiple resonant frequencies or to add additional degrees of freedom to the design. Fig. 10 shows examples of both of these cases, as described in [17]. In (a), two metallic strips of differing lengths (and thus differing resonances) are placed in the same rectangular unit cell. The reflectance (a quantity that is interchangeable with reflectivity for the purposes of this work), plotted on a linear scale, achieves two distinct frequency bands of strong reflection. These dual stopbands are separated by a region of low reflectance. In (b), the two metallic strips are made to be the same size. In this case, since there is only one kind of resonant element present, only a single stopband exists (much like Fig. 6 (a)). However, the dimension *h* introduces an additional degree of freedom compared to the case of a single metallic strip repeated periodically. It was shown in [17] that the dual-strip design can achieve a small widening of the FSS bandwidth.

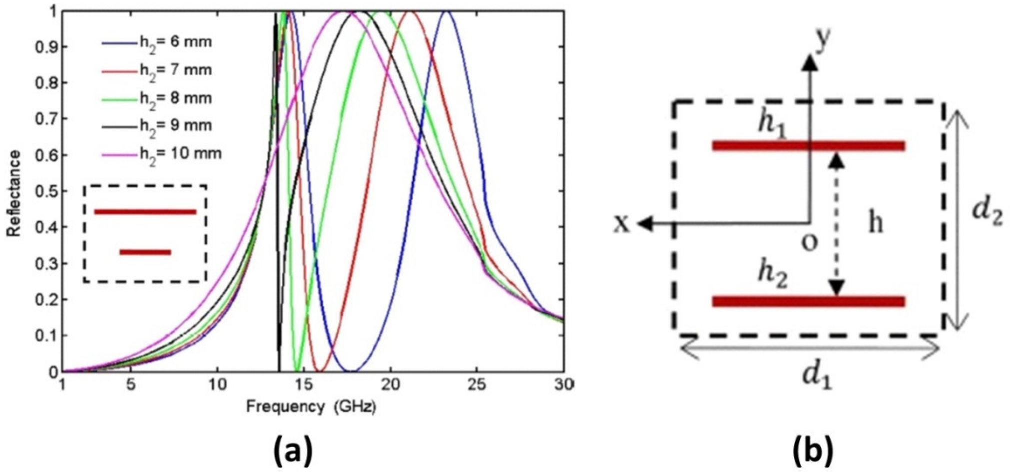

Fig. 10. Two metallic strips per unit cell. (a) Dual-band and (b) single-band design.

Fig. 11 shows two additional examples of multi-element FSS designs. In (a), multiple rectangular apertures of different sizes and orientations are placed in a single unit cell [27]. In (b), cross dipoles are arranged in a “multi-periodic” fashion [28]. Specifically, three different sizes of cross dipoles are each arranged in their own periodic rectangular grid, or “stage”. The periodicity of the three stages are multiples of each other such that they can be superimposed. In this arrangement, the unit cell of the largest cross dipole actually contains multiple cross dipoles from the two smaller stages. The net result is an FSS with three resonant bands.

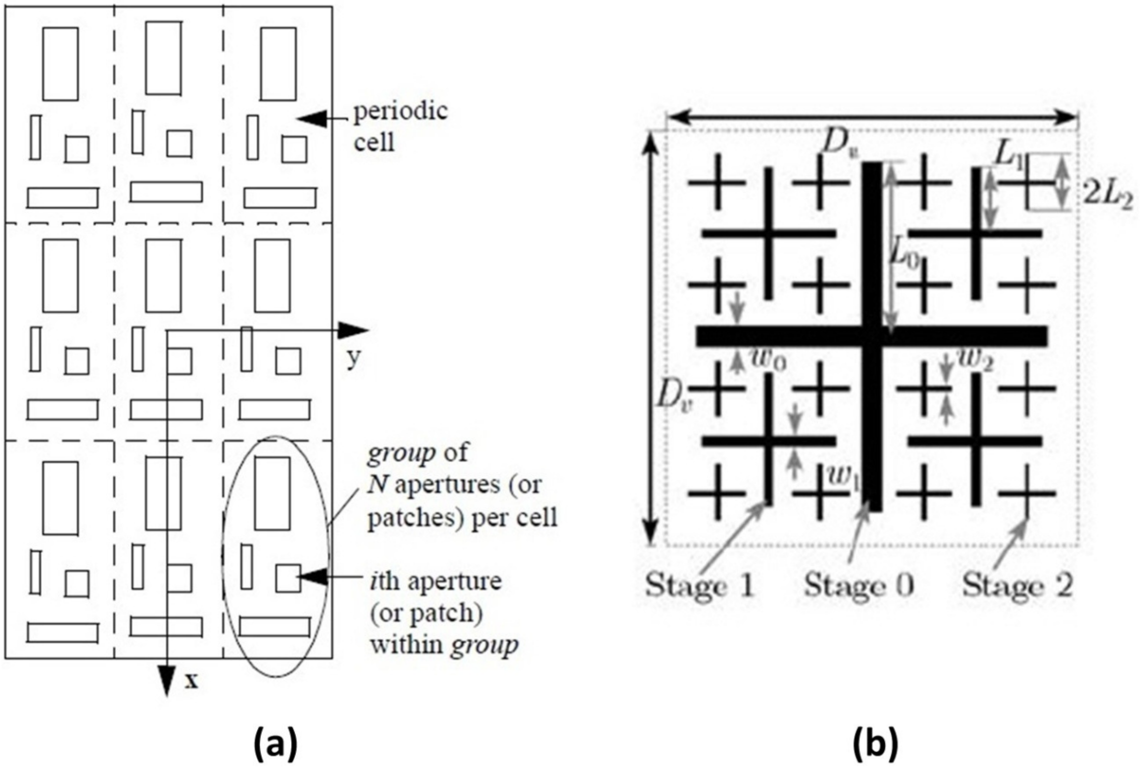

Fig. 11. Examples of multi-element FSS. (a) Multiple rectangular apertures and (b) multi-periodic cross dipoles.

Reconfigurable FSSs

An additional variation on FSSs is to make reconfigurable designs. This means that some kind of functionality is built into an FSS so that its resonant behavior and frequency response can be quickly changed, or reconfigured. Such designs are very attractive for practical applications that require some kind of dynamic adaptability. A simple example would be an FSS that can tune its resonant frequency up or down across a certain bandwidth. Reconfigurable FSSs are directly analogous to reconfigurable designs of antennas, filters, and other devices in microwave engineering (e.g. [29]), and they employ similar types of reconfiguration mechanisms. The reconfiguration is typically achieved through electrical or mechanical means.

A simple example of an electrically reconfigurable FSS is shown in Fig. 12 (a) [30]. Here, rectangular apertures cut into a ground plane are loaded with varactors (capacitors whose capacitance can be varied within a continuous range by an applied DC bias). The varactors add a capacitive effect to the resonance of the aperture. As the varactor capacitance is increased or decreased by a controlled DC bias voltage, the resonant frequency of the aperture can be shifted down or up, respectively. Fig. 12 (b) shows such frequency tuning for a three layer design (each layer is tuned separately). It is important to note that this FSS requires a DC biasing network (shown in (a)) in order to operate. This will generally be true for most electrically reconfigurable FSSs, since the devices used for reconfiguration (in this case a varactor) typically require DC voltages to operate. The DC biasing network can add a significant amount of complexity to the fabrication of reconfigurable FSSs. Additionally, for more complex biasing schemes, the biasing network itself can potentially interfere with the RF performance of an FSS. Thus, electrically-reconfigurable FSSs often come with a tradeoff between biasing complexity and the convenience and speed of electrical tunability.

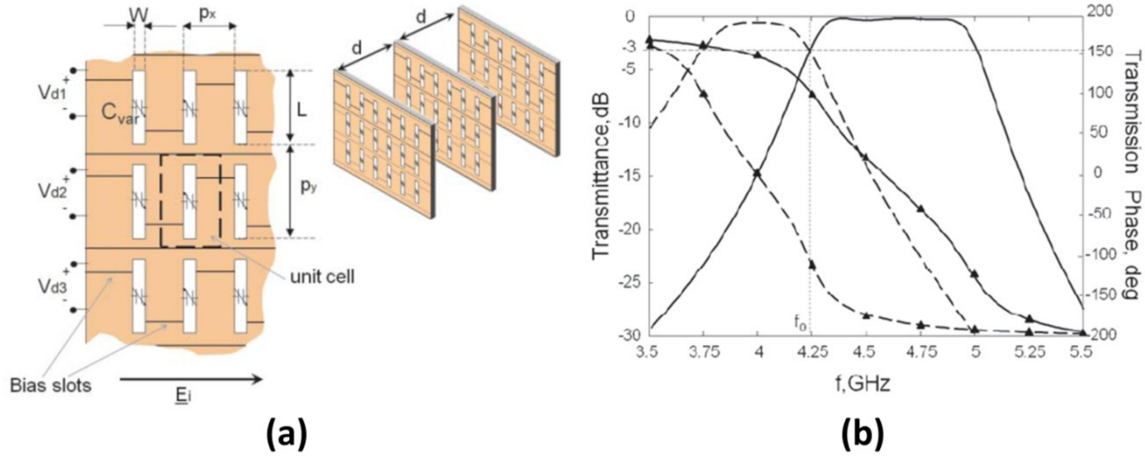

Fig. 12. Reconfigurable FSS with varactor-loaded rectangular slots. (a) FSS topology with DC biasing. (b) Reconfigurable filter response.

Fig. 13 shows an example of another class of reconfigurable FSSs employing microelectromechanical systems (MEMS) [31]. RF MEMS have become popular in recent years for high-frequency switching and tuning applications, especially in RF integrated circuits (RFIC) for devices such as filters and phase shifters. As an alternative to purely electrical semiconductor switches, RF MEMS switches offer low losses, good power-handling capabilities, and fast switching speeds at high frequencies. The details of RF MEMS will not be explored here, but they essentially comprise micro-scale mechanical switches that are activated through electrical biasing. In (a), a rectangular slot loop unit cell (similar to Fig. 4 (e)) is loaded with two MEMS switches on opposite sides of the loop. A detailed view of a single MEMS switch is shown in (b). When the switches are in the OFF state, the slot sloop behaves as a typical inductive-type FSS, achieving a passband at 60 GHz, as shown in (c). When the switches are in the ON state, the resonance of the loop is broken, and the FSS does not transmit (T < -25 dB) from 55 to 65 GHz. Thus, the FSS can be switched between a passband state and a completely opaque state. As with the FSS in Fig. 12 , this FSS requires a DC biasing network.

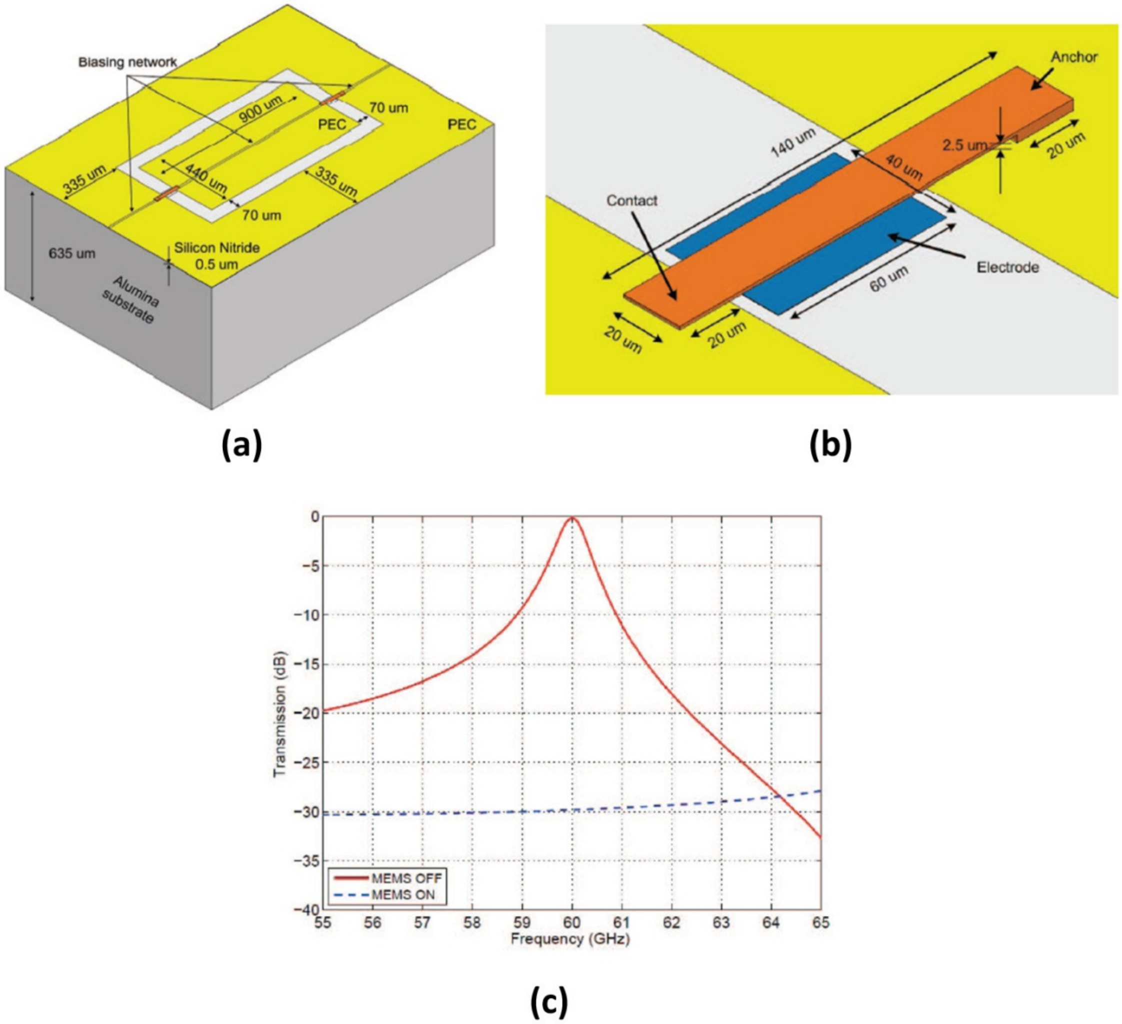

Fig. 13. Reconfigurable rectangular slot loop FSS employing MEMS. (a) Unit cell topology. (b) Close-up view of RF MEMS. (c) Frequency response.

Fig. 14 shows an example of an FSS that is frequency-tunable via completely mechanical means. This straightforward design uses coiled metallic springs as unit cell resonators in the FSS [32]. As resonators, the springs share some similarities with the annular ring of Fig. 4 (d), but the multiple coils and resultant depth add additional complexity. The shape of the springs, and thus their resonance, is changed by simply expanding and contracting them mechanically. In fact, the springs can be used as both bandpass and bandstop resonators. When strongly compressed, as in the middle image of Fig. 14 (a), the springs create a bandstop response, as shown in (c). When sufficiently expanded, as in the right-most image of (a), the springs create a bandpass response, shown in (d). Physically, the spring size is changed by sandwiching them between two foam layers, as shown in (b), and applying an appropriate amount of pressure. Clearly, one advantage of such a design over electrically tunable FSSs is the lack of a complex biasing network. Thus, although simplistic, such a spring-based FSS demonstrates the potential of purely mechanically-controlled designs.

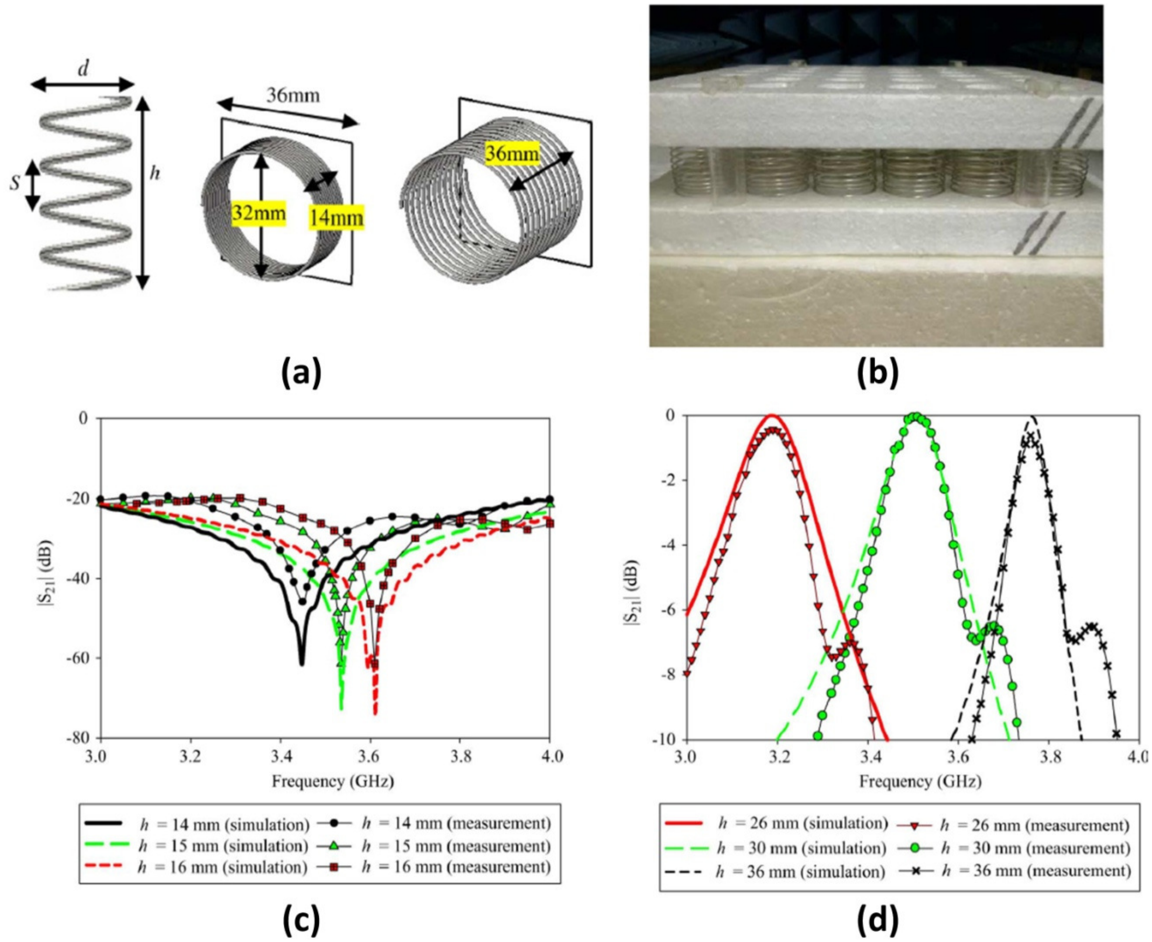

Fig. 14. Mechanically-reconfigurable FSS employing coiled spring unit cells. (a) Unit cell. (b) Fabricated prototype. (c) Bandstop response under strong mechanical compression. (d) Bandpass response under low mechanical compression.

Related Structures

A number of other electromagnetic structures are closely related to FSSs. These include metamaterials, electromagnetic bandgap materials, artificial magnetic conductors, and high impedance surfaces. The common feature among all of these structures is the use of periodically repeated unit cells.

Metamaterials (MM) is a broad term that has been applied liberally to a variety of structures. In the most general sense, it denotes any artificially engineered structure that exhibits bulk material properties that otherwise cannot be found in naturally occurring materials. In electromagnetics, the term is commonly applied to so-called double-negative materials (DNG), which can exhibit negative values of relative permittivity and permeability. Wilson et al. introduced the first such structure in 1995 comprising a periodic arrangement of metallic wires and split ring resonators, which together resonate at certain frequencies to achieve effectively negative permittivity [33]. All DNG MM, like FSSs, in some way make use of periodically arranged unit cells. However, the design focus for DNG structures is on the effective electromagnetic material properties, rather than the reflected and transmitted power, as is the case for FSSs. Also, MM tend to use sub-wavelength unit cells, meaning that the size of the unit cells are smaller than roughly one-tenth of the wavelength at the operating frequency. Traditional FSSs, in contrast, typically have resonant-sized elements (on the order of half a wavelength). There are a class of MM-inspired FSSs which use sub-wavelength cells to achieve desired reflection and transmission properties [34]. Application of the term "metamaterial" to such structures varies.

Other kinds of structures related to FSSs are electromagnetic bandgap materials (EBG), high impedance surfaces (HIS), and artificial magnetic conductors (AMC) [35]. To some extent, these terms have overlapping meanings and can refer to the same structure, depending on the context. Again, all of these structures use periodicity to achieve certain EM properties. EBG materials typically suppress the propagation of EM energy in a certain bandwidth (hence "bandgap"). High impedance surfaces are designed to achieve a certain surface impedance over a target bandwidth. AMC are essentially artificial approximations to a perfect magnetic conductor (PMC). A PMC ground plane may be beneficial, for instance, when a radiating element needs to be placed parallel to the ground plane. In this case, reflections from the PMC add constructively with the radiation from the element, whereas with a standard perfect electric conductor (PEC) ground plane, the reflections interfere destructively with the element's radiation. A commonly employed AMC is Sieveniper's mushroom geometry, shown in Fig. 15 [36]. It comprises periodically arranged hexagonal metallic patches above a metallic ground plane; metallic posts connect the patches to the ground plane. The vertical posts act to suppress surface waves from developing. The design uses a very thin substrate and approximates a PMC over a narrow bandwidth determined by its dimensions.

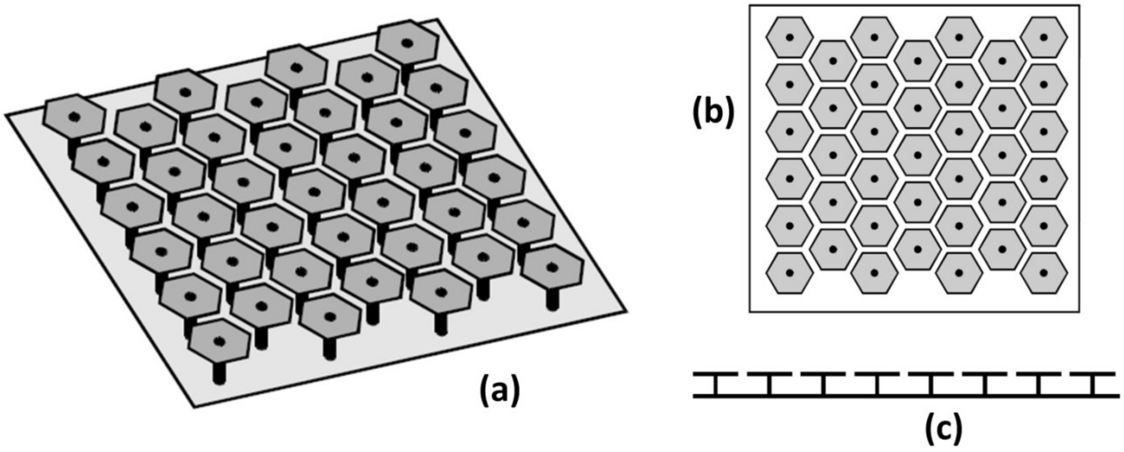

Fig. 15. Sievenpiper's mushroom AMC. (a) Hexagonal unit cells over a ground plane. (b) Top view. (c) Side view.

FSS Analysis

Floquet Analysis

The most accurate way to compute the performance of an FSS is to fully solve Maxwell's equations for particular unit cell geometries. Usually, it is easiest to do this by assuming that the FSS is infinite in extent; that is, the periodicity is assumed to extend indefinitely in all directions. Practical FSSs, of course, must be finite in extent, but as long as a large number of unit cells are present, the infinite approximation gives good results and significantly simplifies the full-wave analysis.

The most common way of solving the infinite FSS problem is by applying Floquet theory for periodic structures. This approach works by only solving Maxwell's equations over a single unit cell; the entire FSS is accounted for by applying periodic conditions to the boundaries of the unit cell. The method is based on Floquet's theorem, which, in words, states that a differential equation with periodic coefficients and periodic boundary conditions will have a solution that is also periodic [37]. The details of applying this idea to specific FSS geometries can vary widely. The following is a brief discussion of the basic mathematics underlying this approach.

For illustrative purposes, a simple FSS is proposed in Fig. 16. A single-layer aperture-type FSS is illuminated by an incident plane wave propagating in the upper half-space. The FSS has a rectangular periodicity with dimensions D_x and D_y. The apertures are arbitrarily shaped to emphasize the generality of the approach. The plane wave is incident at an angle defined by the standard spherical coordinates θ and ϕ. The incident field, of course, causes both a reflected field in the region $z > 0$ and a transmitted field in region $z < 0$.

Using Floquet’s theorem, solutions to Maxwell's equations for the FSS can be found in terms of a so-called scalar mode potential [10]:

$$\psi_{pq} = \exp\left[-j\left(u_{pq}x + v_{pq}y + \gamma_{pq}z\right)\right] \tag{1}$$

The indexes p and q are integers that represent a countably infinite set of modes. Note that the modes, being a complex exponential, are periodic in the x, y, and z direction, and satisfy the periodicity required by the geometry of a specific problem. The coefficients inside the exponential are given by:

$$u_{pq} = k\sin\theta\cos\phi + \frac{2\pi p}{D_x} \qquad p,q = 0,\pm1,\pm2,... \tag{2}$$

$$v_{pq} = k\sin\theta\sin\phi + \frac{2\pi q}{D_y} \qquad p,q = 0,\pm1,\pm2,... \tag{3}$$

$$\begin{aligned} \gamma_{pq} &= \sqrt{k^2 - t_{pq}^2}, \qquad k^2 > t_{pq}^2 \\ \gamma_{pq} &= -j\sqrt{t_{pq}^2 - k^2}, \qquad k^2 < t_{pq}^2 \end{aligned} \tag{4}$$

The following identity is also satisfied:

$$t_{pq}^2 = u_{pq}^2 + v_{pq}^2$$

The mode potential (1) can be used to construct a set of "Floquet modes" as follows:

$$\boldsymbol{\phi}_{pq}^{TE} = \frac{1}{\sqrt{D_x D_y}}\left(\frac{v_{pq}}{t_{pq}}\hat{\mathbf{x}} - \frac{v_{pq}}{t_{pq}}\hat{\mathbf{y}}\right)\psi_{pq} \tag{5}$$

$$\boldsymbol{\phi}_{pq}^{TM} = \frac{1}{\sqrt{D_x D_y}} \left(\frac{u_{pq}}{t_{pq}} \hat{\mathbf{x}} + \frac{v_{pq}}{t_{pq}} \hat{\mathbf{y}} \right) \psi_{pq} \tag{6}$$

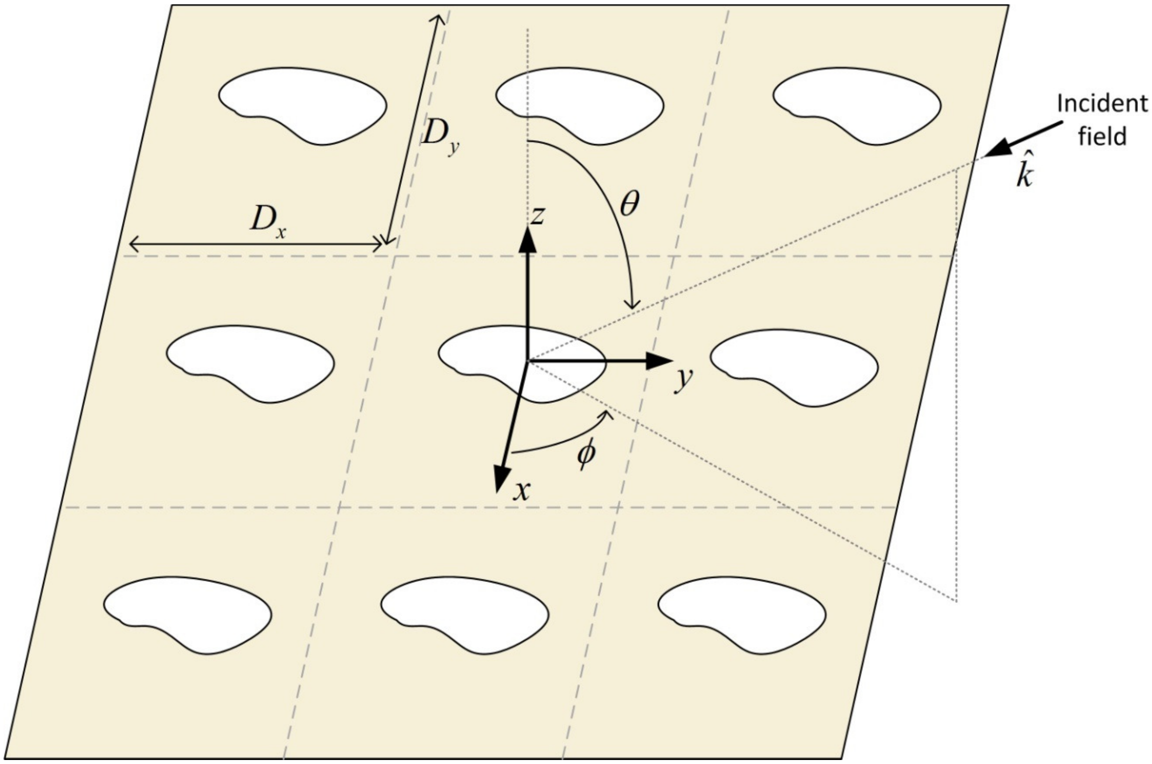

Fig. 16. Generic single-layer aperture-type FSS with incident plane wave.

The modes are divided into two sets: transverse electric (TE) and transverse magnetic (TM). This infinite collection of Floquet modes, based on the definitions (2)-(3) with integer indexes p and q, form an orthonormal set. These vector-valued modes can be thought of as the field components of arbitrary plane waves whose electric or magnetic field is transverse to the plane of incidence. The plane of incidence is defined by the propagation vector $\mathbf{k}$ (which points in the direction of incidence) and its projection on the xy plane. In particular, the TE modes refer to plane waves whose electric field is transverse to the plane of incidence, whereas the TM modes refer to plane waves whose magnetic field is transverse to the plane of incidence. Any field in the upper or lower halfspace can be written as a linear combination of these Floquet modes, and the field will necessarily satisfy the periodicity of the FSS. Specifically, any arbitrary incident plane wave can be written as a weighted sum of the lowest order TE and TM modes. The resulting reflected and transmitted fields can be written as an infinite weighted sum of all of the modes. Determination of these weightings (coefficients) of these linear combinations can be accomplished through a variety of methods, but the general Floquet mode expansion discussed above is common to all FSSs.

In practical problems, computation of the Floquet mode coefficients must be done numerically. One of the most common techniques for accomplishing this is the method of moments (MOM). The MOM in electromagnetics is essentially identical to the boundary element method used to solve general partial differential equations. In the MOM formulation, the fields on the aperture of a single unit cell (for inductive FSSs such as that in Fig. 16) are expanded using a set of orthonormal basis functions that span the aperture (different from the Floquet modes). The basis functions are usually chosen such that they coincide with the natural geometry of the aperture and allow the problem to be cast as a linear system that can be solved through matrix inversion. Chen introduced a straightforward application of the method of moments to aperture-type FSSs in [10]. It is also popular to use the so-called "spectral domain" version of the

MOM (e.g. [38]). In this version, the MOM is combined with a two-dimensional Fourier transform over the spatial dimensions of the aperture. The spectral domain refers to the transform domain when spatial variables are transformed (as opposed to when the time variable is transformed using a Fourier transform).

The computations involved in MOM formulations are extensive enough, even for relatively simple FSS geometries, to require the use of a computer. The method can be implemented using custom code or commercial simulation tools. Other methods besides MOM are also possible for implementing general Floquet theory; for instance, among commercial simulators, [16] uses the finite element method (FEM), and [39] employs the Finite Integral Technique (FIT). A variety of other hybrid schemes have been suggested in literature, none of which will be discussed here. No matter what technique is employed, a numerical solution is required; Floquet theory can typically not be used to arrive at strict closed-form representations of the fields scattered from an FSS.

Equivalent Circuit Models

Numerical application of Floquet theory, whether by commercial simulation software or customized code routines, is by far the most common form of FSS analysis. As an alternative, a variety of circuit models, transmission line modes, and lumped element formulations have been suggested to represent FSS behavior in a simpler and more intuitive way.

The simplest possible circuit model of an FSS is a two-port network comprising an inductor and capacitor (LC resonator). Fig. 17 shows such a model for a capacitive-type FSS (bandstop). Clearly, such a network will exhibit a single band of resonance, depending upon the values of L and C. For some simple FSS geometries, closed-form algebraic expressions for these values as a function of the geometric parameters have been derived using quasi-static approximations, including for the square loop [40] and the Jerusalem cross [41]. This basic model can be extended to multi-element designs, such as the double square loop shown in Fig. 18 [42]. Here, two parallel LC resonant tanks are employed, again using closed-form expressions from quasi-static approximations.

Another example from literature takes the basic LC model and attempts to achieve a best-fit solution for the values of L and C using full-wave simulated data for an annular ring FSS [11]. The values of L and C are extracted for several parametric variations of the FSS dimensions. Then, the FSS behavior at arbitrary dimensions can be estimated by interpolating the values of the lumped element values, without having to perform additional full-wave calculations. Thus, the LC resonant model is used in a systematic design process whereby FSS dimensions are determined by an iterative process.

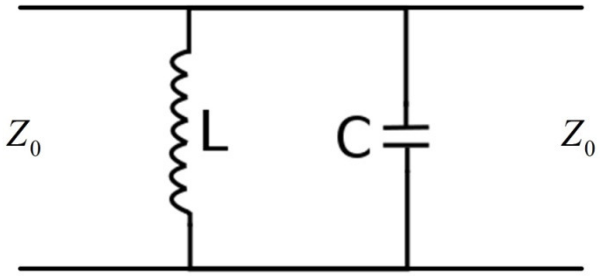

Fig. 17. Basic LC resonator model for bandstop capacitive-type FSS.

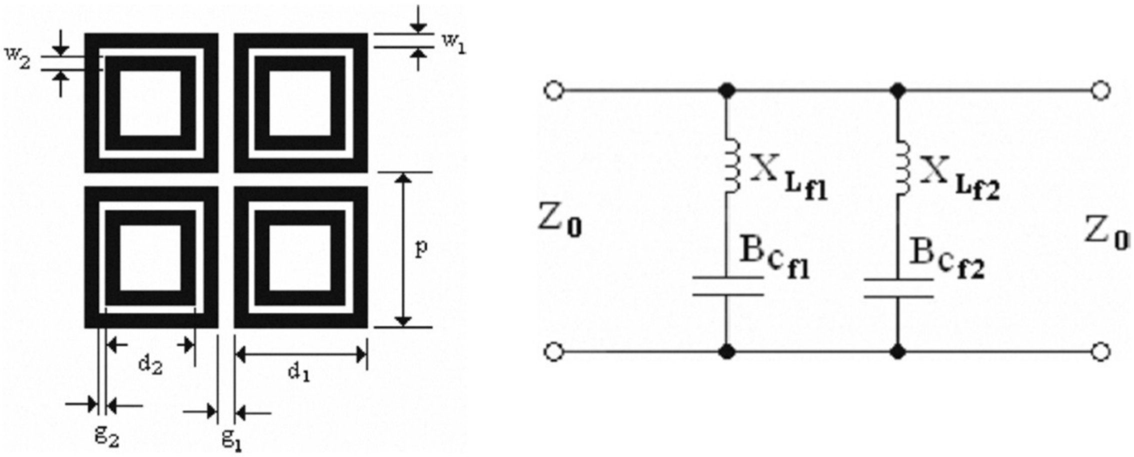

Fig. 18. Equivalent circuit model for a double square loop FSS.

The representation of FSS using LC resonant networks can be extended to multilayer designs as well. This is often accomplished by cascading several such resonant networks together using transmission lines. The transmission lines represent the propagation of fields in the space between the FSS screens, which, in a physical design, would usually be some kind of dielectric layer. Fig. 19 shows an example of such a model employing transmission lines for a two-layer annular ring FSS [13]. It is also possible to start with a more traditional multi-order filter circuit topology.

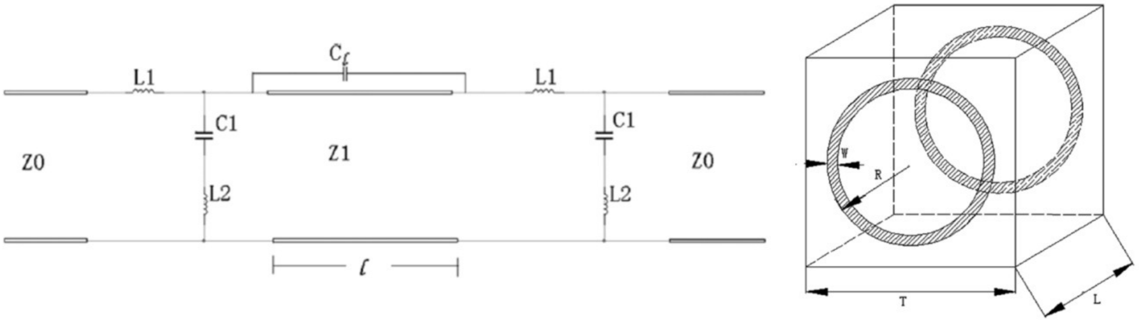

Fig. 19. Circuit model for two-layer annular ring FSS.

Fig. 20 shows the equivalent circuit model of the seventh-order bandpass FSS that was already introduced in Fig. 9. Initially, the FSS is represented using a generic bandpass filter topology with only inductors and capacitors (a). Then, using a series of transformations via classic filter theory (specifically, involving admittance inverters), the circuit can be recast as shown in (b), where alternating capacitors and inductors are separated by short segments of transmission lines. Physically, this topology can be realized by alternating inductive and capacitive-type FSS screens spaced by thin dielectric layers (i.e. the structure shown in Fig. 9).

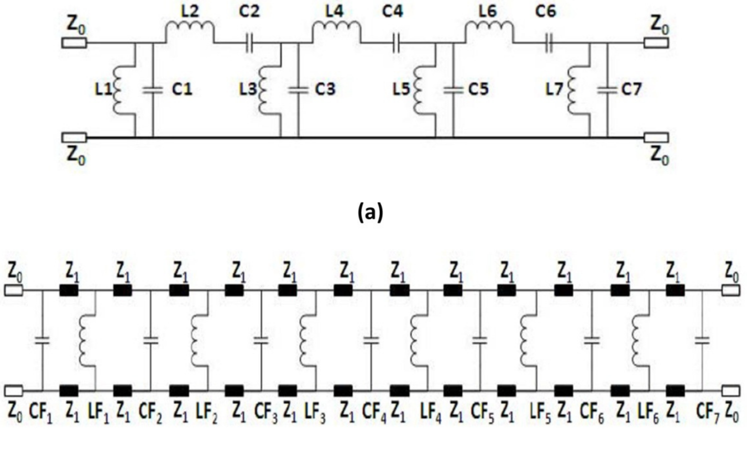

(a)

(b)

Fig. 20. Circuit model for seventh-order bandpass FSS. (a) Generic bandpass filter representation using inductors and capacitors. (b) Transformed filter topology using transmission lines and shunt inductors and capacitors.

The circuit models above are relatively simplistic, essentially amounting to traditional circuit filters. Fig. 21 shows an example of a somewhat more involved circuit model that is actually based on Floquet theory and thus takes into account much more of the full-wave behavior of an FSS [12]. In (a), the FSS is represented as an admittance coupled by transformers to the TE and TM Floquet modes in the halfspaces on either side of the FSS. The admittance itself is expanded in (b), and essentially amounts to a combination of the various Floquet modes, each with its own coupling coefficient represented by a transformer. The details of this model will not be elaborated on here, but it is clear that it remains much more faithful to the Floquet theory of periodic structures and thus represents a form of compromise between full-wave techniques and the simplistic LC-resonator circuit models.

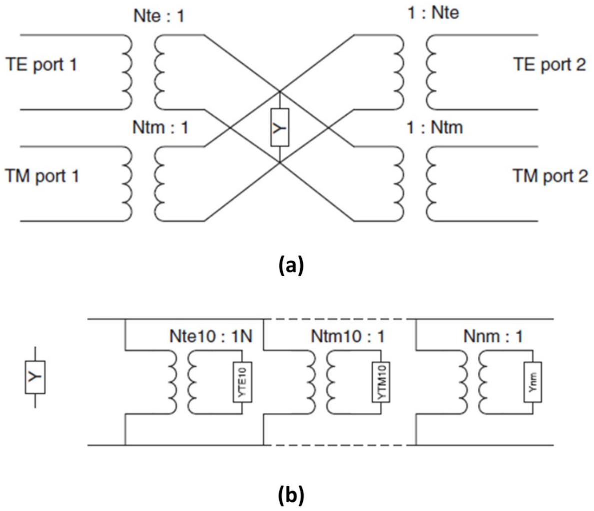

Fig. 21. FSS circuit model based on decomposition of Floquet modes. (a) FSS admittance coupled to TE and TM Floquet modes via transformers. (b) Expanded admittance comprising various TE and TM modes.

Finite FSS

The Floquet analysis discussed above assumes an infinitely periodic FSS. In practice, of course, a fabricated FSS will have a finite number of unit cells. The infinite approximation is accurate enough for many applications. Nonetheless, it is still often of interest to examine the effects of a finite array of FSS unit cells, and, by extension, the "edge effects" that occur at the boundary of such finite arrays. A variety of approaches to the finite FSS problem have been proposed.

In [43], two of the most widely used approaches to finite FSS are summarized. The first is essentially a brute-force application of full-wave electromagnetics that includes all unit cells in the finite FSS. Specifically, a spectral domain MoM procedure is employed. This approach is only practical for FSSs with a relatively small number of unit cells, since the computational cost increases with the size of the finite array. The second approach is summarized in Fig. 22. The basic idea is to approximate the finite FSS with an infinite FSS that is locally illuminated (i.e. only a finite number of unit cells are excited by an incident field). In this particular instance, the locally illuminated infinite FSS is analyzed using a plane wave spectral decomposition method (PWSD), but other formulations would conceptually be appropriate. In general, the infinite approximation becomes better as the number of unit cells increases. This is because less unit cells lie on the boundary of the finite array, where edge effects can dominate. Simultaneously, the computational time saved by using the infinite approximation becomes more dramatic as the number of unit cells increases.

Besides the general approaches outlined above, a variety of other work has been performed on finite FSSs. In [44], the so-called scale changing technique (SCT) is applied to finite FSSs. The SCT results in a less computationally expensive implementation than full-wave treatment of an entire finite FSS using commercial simulation tools. In [45], the surface waves of finite FSSs are investigated. In general, surface waves can exist on infinite FSSs, but different kinds of surface waves appear on finite FSSs.

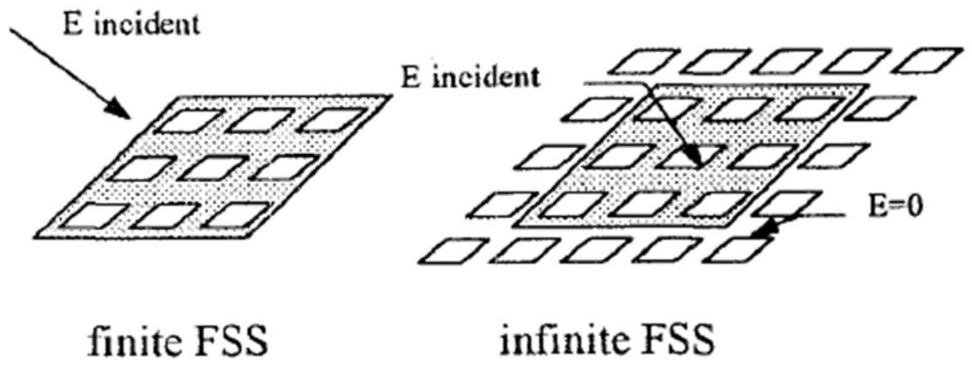

Fig. 22. Approximation of a finite FSS using an infinite, locally illuminated FSS.

CHAPTER III

A LATTICE-BASED EQUIVALENT CIRCUIT MODEL FOR FSS

Motivation

The discussion of FSS analysis in Chapter II demonstrated that most techniques can be lumped into one of two categories: Floquet-based full-wave analysis or equivalent circuit models. Methods involving full-wave Floquet theory (including commercial simulation packages) are generally very accurate. However, these methods are typically entirely numerical, and computational time can be significant, particularly in the context of optimization, where multiple iterations of the problem have to be solved. Furthermore, these full-wave approaches tend to leave little room for a systematic design process. Typically, an engineer must rely on experience, intuition, and parametric studies using commercial software to determine an “optimum” FSS design for a given set of performance constraints. This is true for even the simplest of FSS geometries. For more complicated structures that involve multiple layers or a multiplicity of resonant element types, designing through intuition quickly becomes more difficult, and simulation times increase exponentially, making parametric studies cumbersome.

Circuit models, on the other hand, can greatly simplify computation of FSS performance. However, they tend to be applicable to only specific FSS geometries, and their accuracy may be limited. Another common feature common to FSS circuit models is that they treat the FSS as a bulk structure. Specifically, the behavior of all of the individual unit cells is aggregated into a few lumped elements. Thus, the electromagnetic interactions between unit cells are not accounted for individually, but only on aggregate.

The subject of this dissertation - the lattice model - is meant to be a kind of hybrid framework that draws on some of the positive aspects of both full-wave techniques and equivalent circuit approximations. The goal is to arrive at a new kind of circuit model - specifically, an "element-level" model - that treats each individual element in a periodic FSS structure as its own circuit element, rather than aggregating all elements together. Additionally, the mutual interaction between any two unit cells is also accounted for by separate circuit elements. More specifically, this "element-level" concept is achieved, using the terminology of microwave engineering, by treating an FSS as a multiport network (or lattice) in which the number of ports has been extended to infinity; each element in the FSS array acts as its own port in the network. By incorporating the individual EM coupling interactions between FSS elements (i.e. the coupling between ports in the network), the overall accuracy of the technique should be more comparable to full-wave methods than typical aggregate circuit models.

It is also desirable that this element-level, multiport lattice model be canonical. This means that it must be applicable to a wide variety of FSS geometries and topologies. Furthermore, the model should be general enough so as to be extendable to the cases of multi-element, multilayer, and reconfigurable FSS designs. The concept of a multiport network representation should be equally applicable to any of these cases.

There are a number of overarching motivations for developing such a model. The immediate rationale is to provide an intuitive analytical framework for FSSs that is applicable to very general and arbitrary topologies while maintaining reasonable levels of EM accuracy. Fig. 23 shows a conceptualized FSS design to demonstrate what is meant by more "arbitrary topologies". Note that this FSS is purely illustrative in nature, and is not meant to represent an actual functional FSS topology. This conceptual FSS consists of multiple layers, each of which comprises unit cells with hexagonal symmetry. The unit cells themselves contain multiple resonant elements of different sizes and shapes; in other words, each unit cell acts as a kind of "sub-array" within the larger FSS array. It is also possible that the individual elements of the FSS are reconfigurable in nature, adding to the complexity of the structure. In general, such a conceptual topology could serve as a robust and adaptable EM structure that could reconfigure to achieve multiple passbands and stopbands across different frequency regimes, as well as numerous spatial filter responses of varying degree. Analyzing such a structure using full-wave techniques could prove to be quite time-consuming, particularly in the reconfigurable case where multiple states must be considered. The lattice model, conceptually, could provide a much more convenient and tractable modeling tool by abstracting the analysis of the structure to that of a multiport network.

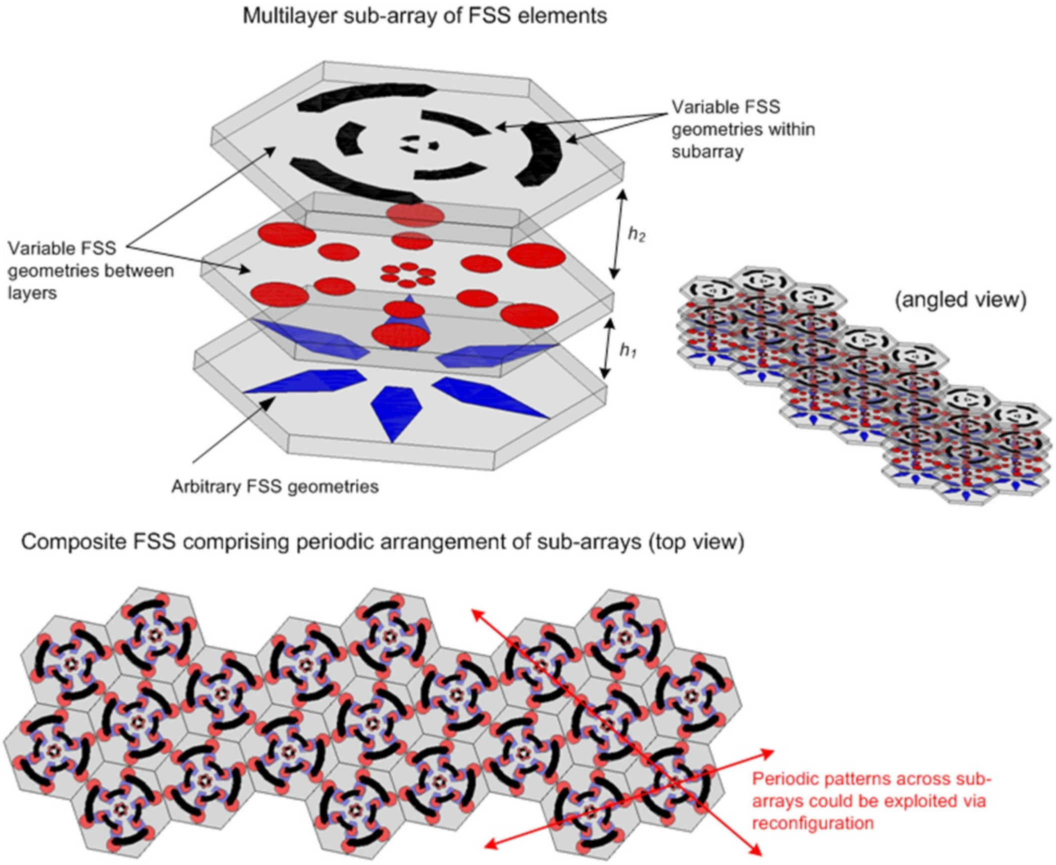

Fig. 23. Conceptual multi-element, multilayer FSS with hexagonal symmetry.

The lattice model is also meant to provide a novel and perhaps more intuitive framework for thinking about FSS design in an equivalent circuit context, as opposed to always resorting to full-wave analysis. In particular, it would be desirable, once a multiport lattice model is established for an FSS, to account for changes in the analysis - whether changes in the geometric dimensions, changes in a reconfiguration mechanism, or changes in the incident fields impinging on the FSS - by corresponding changes in the equivalent multiport network. Computations involving the voltages and currents of multiport networks promise to be significantly less costly than computations using three-dimensional vector-valued fields based on Maxwell's equations. In fact, as will be shown in Chapter VI, the lattice model allows changes in an incident field impinging on an FSS to be accounted for entirely by simply changing the input currents to the multiport network. In summary, then, one of the goals of developing the lattice model is to provide a means by which FSS can be conveniently but accurately analyzed in a circuit domain (network) context.

Beyond these analytical purposes for the lattice model, it is also of interest to explore the inverse problem of FSS optimization. Most FSS optimization routines amount to a brute-force approach via full-wave numerical computations. The lattice model is intended to provide an opportunity to develop more simplified formulations of optimization problems. As will be shown in Chapter IX, the decomposition of an FSS into a lattice of circuit elements provides a unique opportunity to develop a polynomial-based model for the FSS, and, by extension, to perform optimization through this simplified model.

Conceptual Model

Fig. 24 illustrates the basic concept underlying a lattice representation of an FSS. For simplicity, a standard circular aperture FSS (circles cut into a metallic ground plane) is assumed as a representative structure, as shown in (a). The basic idea is to represent each individual circular aperture as a single admittance element, as illustrated in (b). Then, all of the self admittance elements are interconnected using additional admittance elements in order to account for the mutual coupling between apertures (c). In the case of Fig. 24, these interconnecting mutual admittance elements are arranged in T-networks between unit cells, but other configurations are possible. Also, note that the illustration in (c) only shows interconnection between immediately adjacent unit cells; in general, coupling admittances can be included between any two unit cells in the FSS, no matter how far apart. Finally, in (d), the original circular aperture screen is removed from the picture, leaving only a lattice of interconnected admittances. In the ideal case (infinite FSS), this lattice extends to infinity in two dimensions. The equivalent admittance of this lattice, in theory, should represent the performance of the FSS in a circuit context.

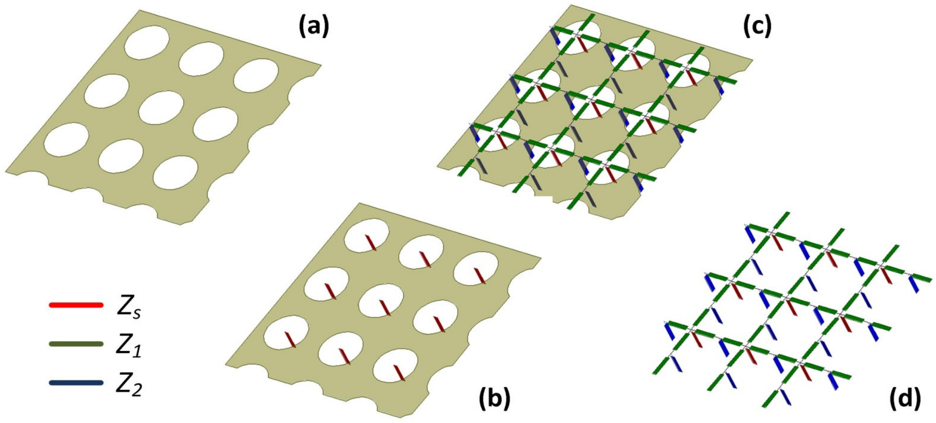

Fig. 24. Conceptual model of a lattice-based representation of an FSS. (a) Circular aperture FSS. (b) Self admittances assigned to each aperture. (c) Apertures connected together using mutual admittances. (d) FSS removed, leaving lattice of admittances.

The lattice model, as illustrated conceptually in Fig. 24, effectively divides the analysis of an FSS into two distinct parts: an "electromagnetic domain" analysis and a "circuit domain" analysis. In the EM domain, individual FSS elements are isolated from the rest of the FSS and analyzed to determine self and mutual admittance values. In the case of Fig. 24, a single circular aperture is analyzed in isolation using classic EM techniques to determine an equivalent aperture self admittance parameter. Likewise, any two circular apertures can be analyzed using classic EM techniques to determine an equivalent mutual admittance parameter. In the circuit domain, all of the self and mutual admittances are used to populate a lattice structure. The lattice, in turn, is analyzed as an infinite multiport network in order to take into account the periodicity of the structure.

Given this twofold breakdown of the analysis problem, the lattice model can be thought of as a compromise between full-wave numerical analysis of FSS using Floquet theory on one hand, and simplified bulk circuit models on the other hand. The EM domain is based on full-wave analysis of isolated FSS elements, whereas the entire periodic structure is obviously accounted for by a circuit model (albeit with an infinite number of ports). This compromise is illustrated conceptually in Fig. 25, which suggests a "spectrum" of possible analysis techniques: full-wave techniques on one end, and simple circuit models on the other end. The lattice model fits somewhere in between and incorporates favorable elements of techniques from both ends of the spectrum: namely, both the accuracy of full-wave techniques and the convenience of circuit models.

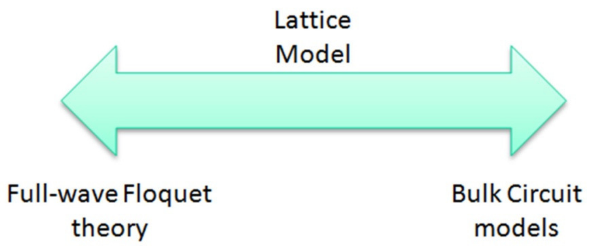

Fig. 25. Conceptual spectrum of FSS analysis techniques.

CHAPTER IV

LATTICE MODEL ANALYSIS: CIRCUIT DOMAIN

The conceptual version of the lattice model described in Chapter III must be translated into a precisely defined lattice structure. The goal of this chapter is to define this specific lattice structure and discuss how it is analyzed from a circuit (or network) perspective. First, the basic components of the lattice, the self and mutual admittances, are introduced, and the construction of one-dimensional and two-dimensional lattices using these components is discussed. Then, the analysis of a two-dimensional FSS lattice is presented. This analysis includes the representation of the lattice as an infinite N-port network; the determination of an equivalent input impedance using lattice Green's functions; the simplification of the lattice under uniform normal plane wave incidence; and the mathematical treatment of infinite two-dimensional series that arise naturally from the lattice.

Building Blocks of the Lattice Structure

The backbone of the lattice model is formed by an array of self admittance elements, which represent individual resonant elements in the FSS (as suggested by Fig. 24 (b)). The self admittances essentially treat each resonant element as a one-port network with a single admittance element placed across its terminals. Conceptually, the real power dissipated by the conductance (real part) of a self admittance component represents the EM power transferred through the FSS plane at a given frequency. The susceptance (imaginary part) of a self admittance component represents the reactive energy associated with the FSS at that frequency. In general, the determination of these self admittances must be done through a carefully formulated EM problem; this is the primary subject of Chapter V. For the purposes of this chapter, it is assumed that such an equivalent self admittance can indeed be found for any given FSS element.

The other key part of the lattice model of Fig. 24 is the mutual admittances that connect the self admittances together. The EM coupling between any two elements in an FSS array can be represented by a two-port network, as shown in Fig. 26. Specifically, any two self admittances (Y_s)representing FSS elements are connected using either a Pi-network (a) or T-network (b) of coupling admittances. The admittances comprising these Pi- and T- networks, Y_1 and Y_2, can be found by comparison to the canonical Pi- and T-network representations of a reciprocal two-port Y-matrix [15], shown in (c) and (d), respectively. The Y-matrix is given by:

$$Y = \begin{bmatrix} Y_{11} & Y_{12} \\ Y_{12} & Y_{22} \end{bmatrix} \tag{7}$$

Thus, if equivalent Y-parameters describing the two FSS elements are found, then the lattice elements can be determined. By extension, if the two-port Y-parameters for any pair of elements in an FSS are known, an entire lattice can be constructed by interconnecting many such two port networks.

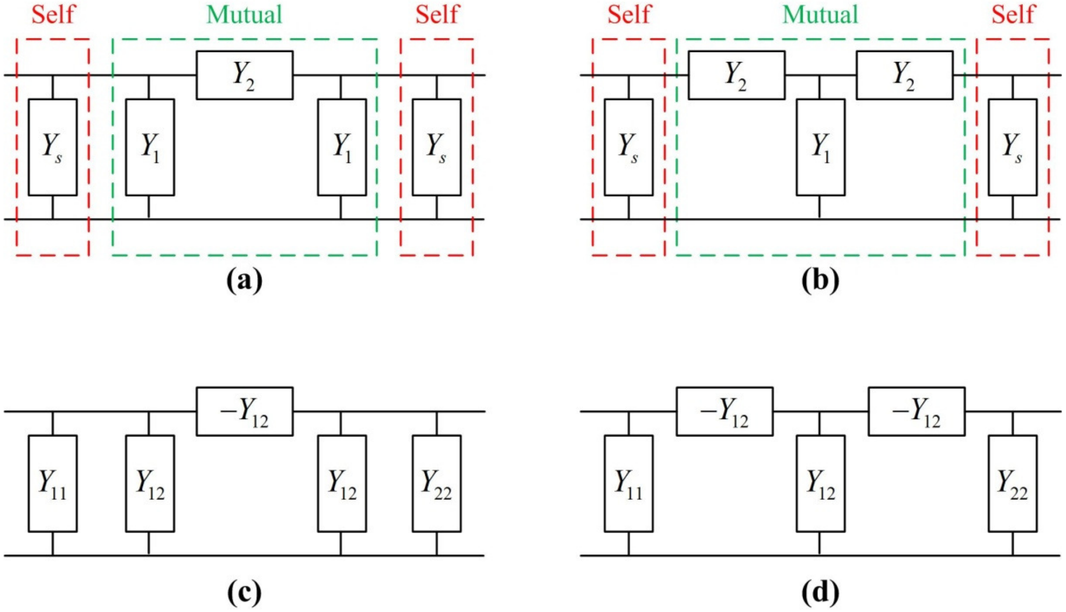

Fig. 26. Two-port network representation of FSS coupling. The self admittance elements are connected with either (a) a Pi-network or (b) a T-network of admittances. The admittances of these networks are determined via the canonical (c) Pi-network or (d) T-network representations of a Y-matrix.

Together, the self admittance elements and the coupling Pi- or T-networks form the basic building blocks of the lattice model. Using these components, an entire FSS can be constructed with an arbitrary number of elements. Furthermore, the coupling between any two elements in the FSS can be accounted for, as desired, no matter their location within the periodic structure. In the next section, a one-dimensional lattice example is provided to demonstrate how these building blocks are put together. Then, in the following section, an analogous two-dimensional FSS is constructed.

One-Dimensional Lattice Example

To see how an entire lattice can be constructed from two-port networks of the self and mutual admittances introduced in the previous section, it is instructive to start with a lattice of one-dimensional periodicity. Although one-dimensional periodicity does not correspond to any practically realizable FSS design, the extension to two dimensions is relatively straightforward.

Fig. 27 illustrates how such a one-dimensional lattice may be constructed using the two-port building blocks of Fig. 26. In (a), self admittances (outlined in red) are arranged in periodic fashion from left to right, and the periodicity is assumed to extend infinitely in either direction. Any two immediately adjacent self admittances are coupled together using a Pi-network of mutual admittances. This coupling between immediately adjacent elements is referred to as the "first level" of coupling. Also, note that network ports, with positive and negative terminals, are assigned across each one of the self admittances. Thus, the one-dimensional lattice is assumed to be an N-port network with the number of ports tending to infinity. Voltages can be excited at the ports by exciting the lattice with input currents.

Fig. 27 (b) demonstrates how a "second level" of coupling can be added. Specifically, this refers to coupling between elements that are spaced two ports apart. The coupling network is again a Pi-network, and it overlaps the already-defined first-level coupling networks. Additional second-level coupling networks can also be defined between other similarly spaced ports. Also, it is not difficult to extend this idea to third-level coupling, fourth-level coupling, etc, in which the coupled elements are spaced three and four ports apart, respectively. Such coupling networks can be defined between any two ports for which non-trivial, finite coupling is assumed to exist. Thus, the one-dimensional lattice of Fig. 27 is infinite in two senses: first, an infinite number of ports extend to the left and right; second, an infinite number of mutual coupling networks and coupling levels can be defined between all of these ports.

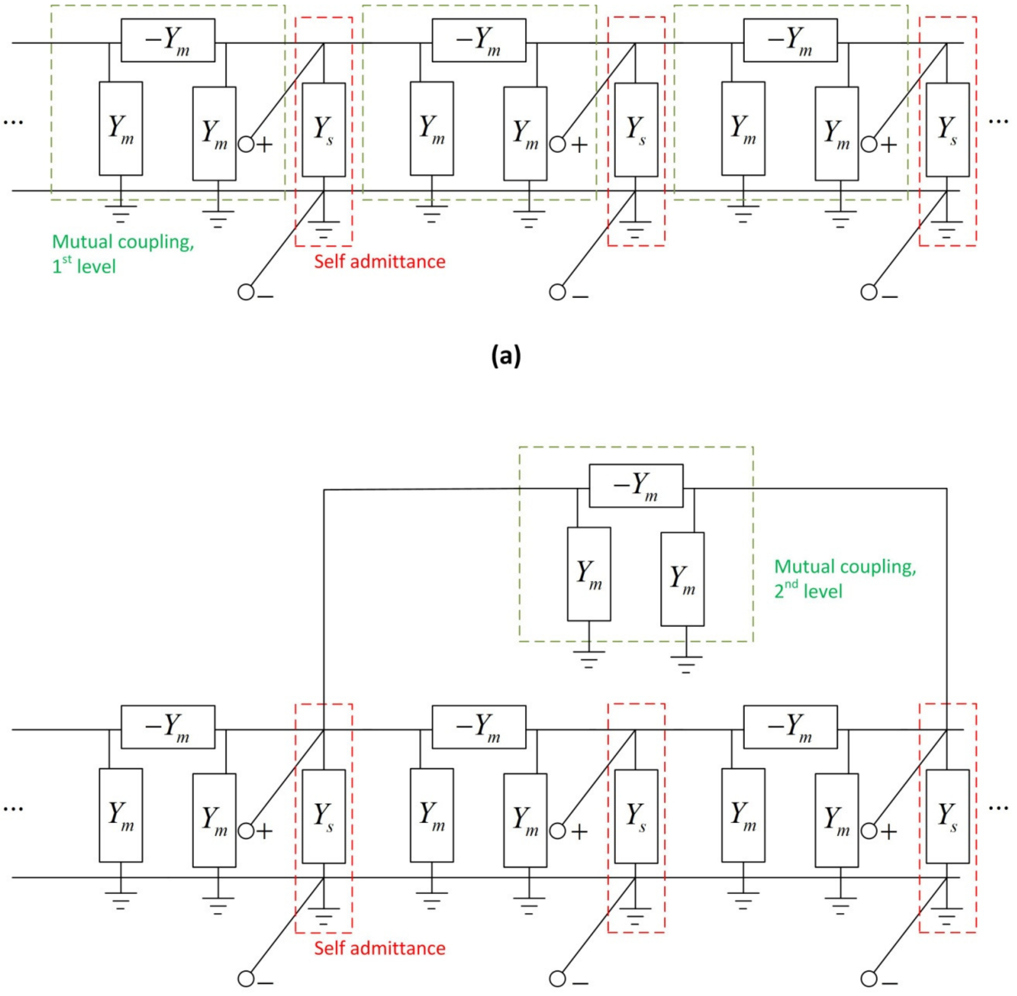

(a)

(b)

Fig. 27. One-dimensional lattice. (a) one level of coupling and (b) two levels of coupling.

Multiport Network Representation

The construction of a one-dimensional lattice above can easily be extended to two dimensions, which is applicable to physically realizable FSSs. The lattice representation of a single-layer FSS comprising a single resonant element repeated periodically is presented in Fig. 28. Specifically, in (a), a basic aperture-type (or equivalently, inductive-type) FSS is assumed that consists of arbitrarily shaped apertures cut into a metallic ground plane. For simplicity, such an aperture-type FSS is assumed throughout the scope of this dissertation. Nonetheless, a similar model can, in principle, be developed for the complementary case of a capacitive-type FSS.

In Fig. 28 (b), each aperture is assigned a port as if it were part of an multiport network [15]. Each aperture thus has a corresponding port voltage V_i. Physically, this scalar port voltage corresponds to the magnitude of the electric field distribution excited on the aperture surface. As discussed before, each unit cell in the FSS is represented by a self-admittance Y_s, which is identical for each aperture and is placed across the terminals of each port. The coupling between any two ports is represented as a *pi*-network of elements Y_{mi} and $-Y_{mi}$, shown explicitly in (c). Note that the lattice of (b) only accounts for one level coupling; in other words, only immediately adjacent unit cells are assumed to be coupled. It is not difficult, though, to add additional pi-networks to account for coupling between unit cells spaced further apart (as was done in Fig. 27). However, these additional levels of coupling are not included in the figure because the visualization of so many overlapping networks quickly becomes cumbersome.

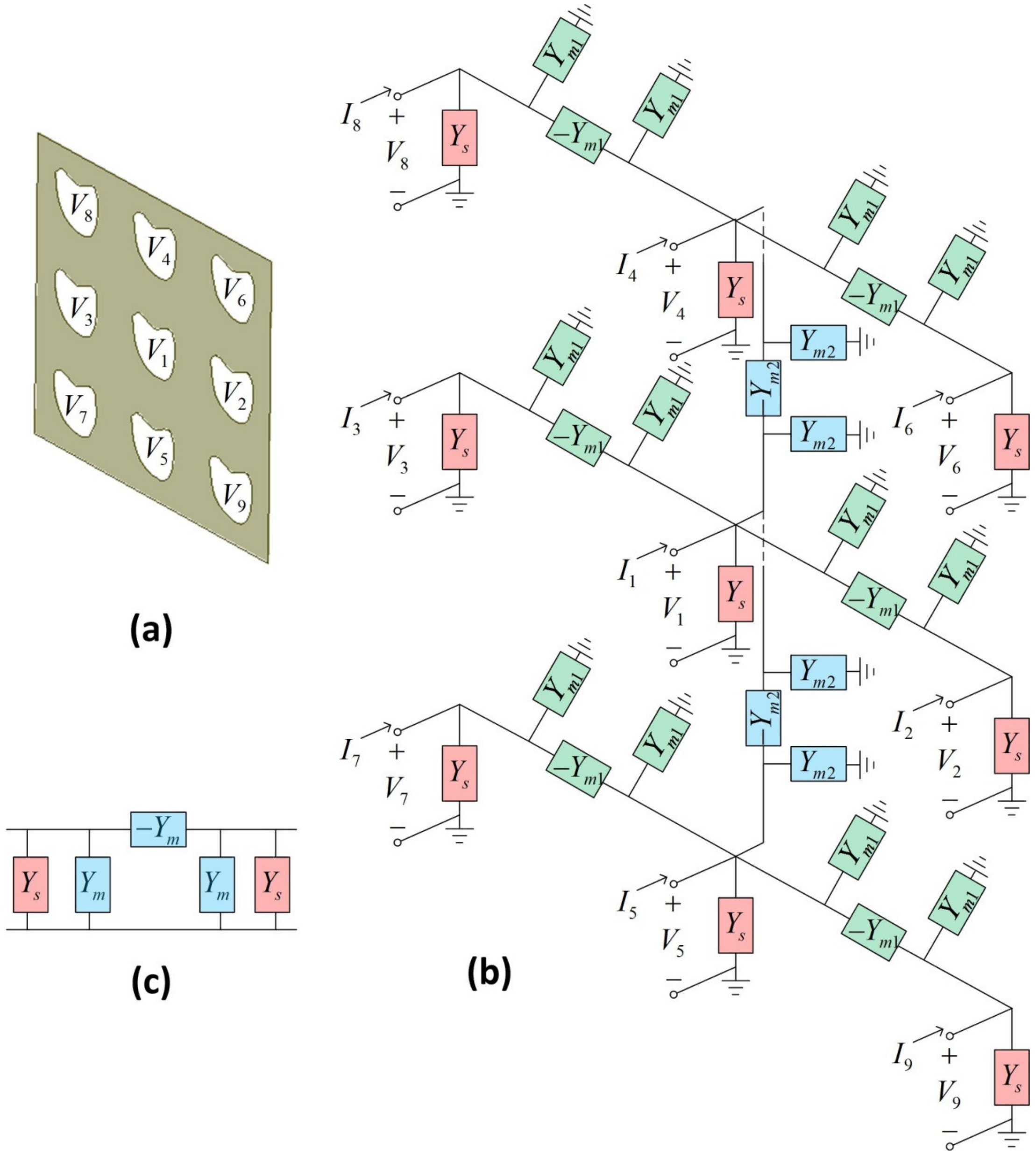

Fig. 28. N-port network representation of an FSS. (a) A generic aperture-type FSS with scalar voltages assigned to each unit cell. (b) Two-dimensional lattice of impedances with ports assigned to each aperture. (c) Canonical representation of two-port admittance matrix that accounts for the coupling between any two unit cells.

The port voltages V_i are excited by currents I_i that flow into each port. Physically, the currents represent incident electromagnetic energy impinging upon the

FSS screen. In the most general case of arbitrary, non-uniform incidence, the incident field on each unit cell – and, by extension, the current at each port of the lattice – is different. The following section discusses how a lattice can be analyzed to determine the voltages and currents at the lattice ports.

Lattice Equivalent Impedance

The problem of solving for the equivalent impedance of an infinite lattice of circuit components is not new. It has been pursued extensively in various contexts of theoretical physics [46]. Perhaps the most classic formulation of the problem is that of finding the equivalent resistance of an infinite grid of resistors [47]. This section aims to outline the analysis of such lattice problems in the context of an FSS model.

Mathematically, a lattice, such as that in Fig. 28, can be described in terms of a finite difference equation. The solution to this difference equation yields the lattice port voltages and currents. One way to solve the difference equation is to construct a lattice Green's function from the eigenfunctions and eigenvalues of the difference equation. Another possibility is to transform the difference equation into an algebraic equation using any number of discrete transform techniques. The former technique will be outlined briefly here, whereas the latter technique will be developed in detail in Chapter VII.

For the lattice structure in Fig. 28, a finite difference equation can be written by applying Kirchhoff's current law at the positive terminal of any port in the lattice:

$$Y_s V\left[n_x, n_y\right] + \sum_k Y_{m,k} V\left[n_x - a_k, n_y - b_k\right] = I\left[n_x, n_y\right] \tag{8}$$

Here, the port voltages $V\left[n_x, n_y\right]$ are a function of the discrete variables n_x and n_y, which indicate the position of the port within the two-dimensional lattice. The bracket notation $[\ ]$ is used to denote a function dependent on discrete rather than continuous variables. The input currents $I\left[n_x, n_y\right]$ are also a function of their discrete position in the lattice. The self admittance Y_s is assumed, in this case, to be identical at each port. The mutual admittance $Y_{m,k}$ accounts for the mutual coupling between the port at $\left[n_x, n_y\right]$ and the port at $\left[n_x - a_k, n_y - b_k\right]$ (a_k and b_k are integers). The summation over the indexing integer k accounts for all ports for which non-negligible coupling is assumed to exist. Equation (8) can be summarized in operator notation:

$$LV\left[n_x, n_y\right] = I\left[n_x, n_y\right] \tag{9}$$

Here, L is a linear difference operator operating on the port voltages.

When the input currents $I\left[n_x, n_y\right]$ are completely arbitrary, the solution to (8) can be written in terms of a lattice Green's function [48]:

$$V\left[n_x, n_y\right] = \sum_{n'_x, n'_y} G\left[n_x, n_y; n'_x, n'_y\right] I\left[n'_x, n'_y\right] \tag{10}$$

The Green’s function $G\left[n_x, n_y; n'_x, n'_y\right]$ accounts for the voltage response at port $\left[n_x, n_y\right]$ due to a current excitation at port $\left[n'_x, n'_y\right]$. The Green’s function itself can be written in terms of an eigenfunction expansion [49]:

$$G\left[n_x, n_y; n'_x, n'_y\right] = \sum_{m=0}^{\infty} V_m^*\left[n_x, n_y\right] V_m\left[n'_x, n'_y\right] \big/ \lambda_m \tag{11}$$

Here, $V_m\left[n_x,n_y\right]$ and λ_m are the eigenfunctions and eigenvalues, respectively, of the difference operator L. They are found by applying the appropriate periodic boundary conditions to the following eigenvalue problem:

$$LV_m\left[n_x,n_y\right]=\lambda_m V_m\left[n_x,n_y\right] \tag{12}$$

It can be shown that the Green's function is, in fact, equal to an element of the impedance matrix (Z-matrix) of the multiport network:

$$Z_{ij}=G\left[n_x,n_y;n'_x,n'_y\right] \tag{13}$$

Equations (9)-(12) summarize the most general possible analysis of the circuit domain of the lattice model. In practice, other techniques are more likely to be employed. In the following section, it will be shown how the analysis simplifies greatly under uniform normal plane wave incidence. Later, in Chapter VII, non-uniform incidence will be addressed using a two-dimensional discrete Fourier transform.

Uniform Normal Plane Wave Incidence

In most cases, FSS analysis is concerned with the specific scenario of uniform normal plane wave incidence. This means that a plane wave impinges with equal amplitude on all unit cells in an infinitely periodic FSS (uniform incidence). Also, the plane wave propagates in a direction perpendicular to the surface (normal incidence). In the circuit domain, this corresponds to exciting each port in the network with a current of equal magnitude and equal phase. By extension, the voltages excited at each port (and thus the physical fields excited on each aperture) will also be identical. The assumption of uniform normal plane wave incidence allows the general treatment of the model using lattice Green's functions to be greatly simplified. Specifically, if the lattice in Fig. 28 is assumed to be have identical currents and voltages at each port, then, by symmetry arguments, the entire lattice can actually be collapsed down into a single equivalent admittance Y^{Σ}, as shown in Fig. 29. This reduction of the lattice to a finite network is possible because the equal voltages at all ports dictates that no currents flow through the mutual admittances between the ports. Rather, all of the current flows through the admittances that are placed parallel across the port terminals. At each port, these admittances are precisely the sum of the self admittance and all of the mutual admittances connecting that port to surrounding ports. The equivalent admittance Y^{Σ}, then, is actually a sum of admittances: specifically, an infinite sum of the self admittance element and all mutual admittances which are included in the lattice:

$$Y^{\Sigma} = Y_s + \sum_k Y_{m,k} \tag{14}$$

Clearly, the lattice cannot practically include an infinite number of mutual coupling connections between all FSS elements. Additionally, it makes sense that the coupling between any two elements will eventually become negligible as their distance of separation becomes arbitrarily large. Thus, the summation in (14) must be handled by either a reasonable truncation or by estimating the value of the infinite series. The details of handling this summation are discussed in the following section.

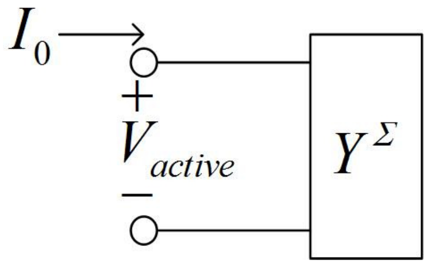

Fig. 29. Equivalent single-element network under uniform normal incidence.

Mathematical Treatment of Infinite Series

For a typical FSS with a two-dimensional periodic arrangement of elements, the infinite sum (14) can be rewritten more explicitly as a two-dimensional series:

$$Y^{\Sigma} = Y_s + \sum_{k=1}^{\infty} Y_{mk} = \sum_{n=0}^{\infty}\sum_{m=0}^{\infty} Y_{mn} \tag{15}$$

Here, the admittance term Y_{mn} equals Y_s when $m = n = 0$. Otherwise, Y_{mn} is equal to $Y_{m,k}$, where the single index k has been replaced by the two-dimensional indexes mn. The indexes m and n correspond to the two physical dimensions of the FSS array. A partial sum corresponding to (15) can also be defined:

$$Y_{MN}^{\Sigma} = \sum_{n=0}^{N}\sum_{m=0}^{M} Y_{mn} \tag{16}$$

The population of terms in such a partial sum is illustrated in Fig. 30. Here, a rectangular grid array of arbitrarily-shaped FSS apertures is assumed. A "central" aperture, shown in blue in (a), is chosen as a reference. This aperture, by itself, only has a self admittance value; this corresponds to the case of $M = N = 0$. In (b), the mutual coupling to eight additional apertures immediately surrounding the central aperture is included; this corresponds to the case of $M = N = 1$ and is referred to as level 1 coupling. Similarly, in (c) and (d), additional levels of coupling are added, corresponding to $M = N = 2$ (level 2 coupling) and $M = N = 3$ (level 3 coupling). This idea can be extended to produce a partial sum Y_{MN}^{Σ} with an arbitrary number of coupling terms included.

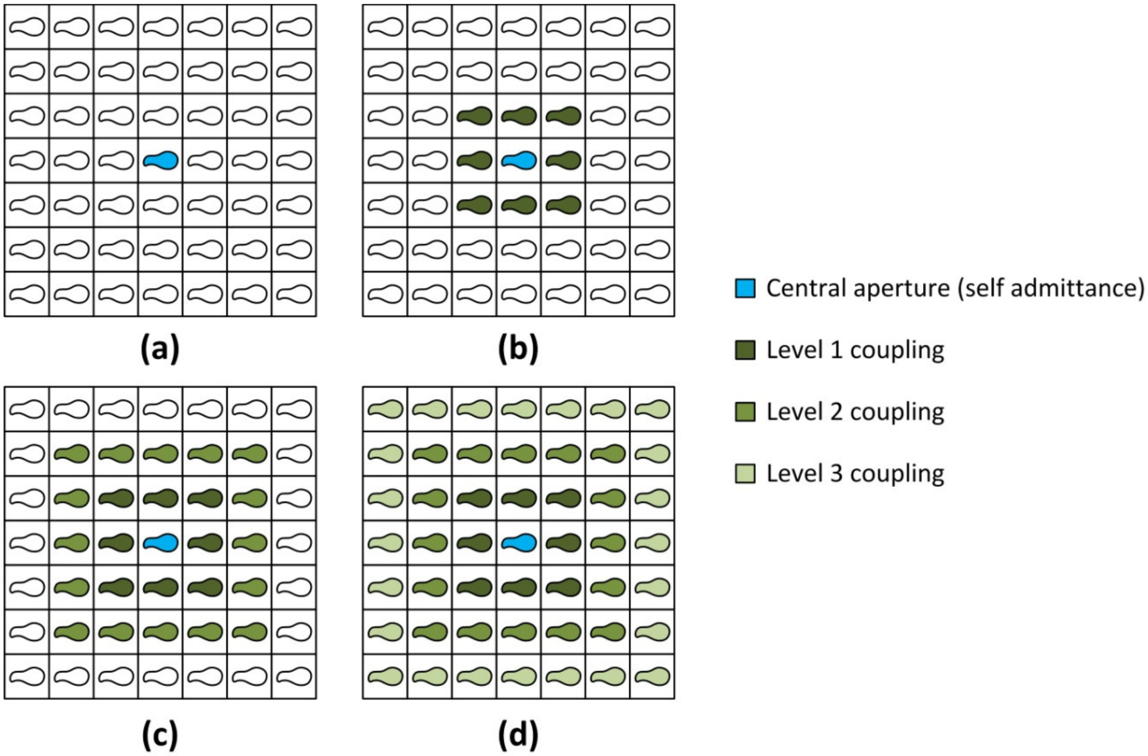

Fig. 30. Illustration of coupling levels in a two-dimensional array of FSS elements.

In practice, computing the partial sums (16) for any FSS results in a very slowly converging series (15). Although the mutual coupling between any two individual FSS elements becomes very small as the distance between them increases, the additional coupling caused by successive two-dimensional layers of elements, as suggested in Fig.

30, is non-trivial, even for layers that are far removed from the central reference aperture. This behavior is very similar to what has been observed in two-dimensional antenna arrays [50]. An example of such a slowly converging series of admittances is given in Fig. 31. The plotted values are the normalized real part of the admittances from the analysis of an actual FSS. The specific FSS geometry is not important, as the behavior of the series observed is typical for any FSS and is only shown here for the purpose of illustration. Note that even for $M = 6$ and $N = 16$, the series of partial sums has not converged, and their variation is highly oscillatory.

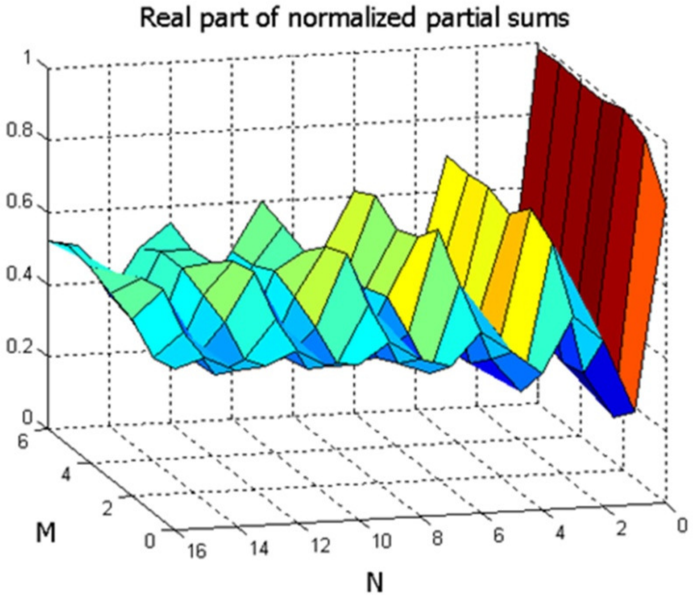

Fig. 31. Slowly converging two-dimensional series.

The slowly converging series illustrated by Fig. 31 presents a practical challenge for any implementation of the lattice model. It is computationally intractable to estimate the converged value of Y^{Σ} by simply summing a finite number of terms. In the most general case, there may be no useful knowledge of the analytical form of the series beyond that shown in (16). Specifically, the terms Y_{mn}, which can be computed using any number of EM techniques (discussed more thoroughly in the next section), are only known as individual numerical values. This severely limits the number of techniques that could possibly be used to analyze and estimate the convergence of the series. In the formulation of the lattice model for a specific FSS, it may be possible to find a convenient analytical formulation for Y_{mn}, in which case other applicable series estimation techniques could be employed.

For the purposes of this work, it is assumed that there is no *a priori* knowledge of the analytical form of the terms Y_{mn} , and the converged value of the series (16) is estimated using a two-dimensional version of the Shanks transformation [51]. The Shanks transformation is a common series acceleration technique that has found numerous applications in computational electromagnetics [52]. Using successive applications of the Shanks transformation in two dimensions, the converged value of the series can be estimated as:

$$Y^{\Sigma} \cong \left.\begin{vmatrix} A_{11} & \cdots & A_{1,k+1} \\ \Delta A_{11} & \cdots & \Delta A_{1,k+1} \\ \vdots & \cdots & \vdots \\ \Delta A_{k,1} & \cdots & \Delta A_{k,k+1} \end{vmatrix} \middle/ \begin{vmatrix} 1 & \cdots & 1 \\ \Delta A_{11} & \cdots & \Delta A_{1,k+1} \\ \vdots & \cdots & \vdots \\ \Delta A_{k,1} & \cdots & \Delta A_{k,k+1} \end{vmatrix}\right. \qquad (17)$$

The following definitions relate (17) to the partial sums Y_{MN}^{Σ}:

$$\begin{aligned} A_{ij} &= Y^{\Sigma}_{\phi_1(i)+\phi_1(j),\phi_2(i)+\phi_2(j)} \\ i = j &= 1,2,\ldots,\left(\frac{M+1}{2}\right)\left(\frac{N+1}{2}\right) \\ \Delta A_{ij} &= A_{i+1,j} - A_{ij} \end{aligned} \tag{18}$$

$$\begin{aligned} &\left(\phi_1(i),\phi_2(i)\right) = (p,q) \in D \\ &p = 1,2,\ldots,\frac{M+1}{2} \\ &q = 1,2,\ldots,\frac{N+1}{2} \end{aligned} \tag{19}$$

It can be seen, then, that the Shanks transformation consists of a ratio of determinants, where the determinants are systematically populated using the partial sums of the series in question.

The Shanks transform defined above is used throughout the scope of this dissertation to estimate infinite admittance summations from a finite series of admittances. No claim is made here that this transform is the most efficient or accurate technique that could be possibly employed. It provides sufficiently accurate results for the purpose of this work, but the investigation of other possible techniques is an area that should be strongly considered in future work.

CHAPTER V

LATTICE MODEL ANALYSIS: ELECTROMAGNETIC DOMAIN

Chapter IV was an overview of the circuit domain portion of the lattice model and focused on how the multiport network is analyzed to obtain performance parameters of an FSS. However, it did not address how the individual self and mutual admittances of the lattice are calculated – specifically, how the terms of the infinite summation (15) are populated. These admittances must be determined by solving an appropriate electromagnetic problem based on Maxwell's equations, and they must provide a well-defined relationship between the EM fields interacting with the physical FSS structure and the voltages and currents of the lattice. Computing these admittances and establishing the relationship between field and circuit quantities is the focus of the EM domain of the lattice analysis.

This chapter begins by developing the mathematical framework for computing the lattice admittances. For simplicity, the discussion is restricted to aperture-type FSS elements. In principle, similar techniques should be applicable to capacitive-type FSS. Next, the idea of multiport FSS elements is introduced; this involves assigning multiple ports (i.e. multiple lattice voltages) to each FSS element such that it is now represented by a multiport network rather than by a single self admittance. Finally, the theory of both the circuit domain and EM domain of the lattice model are put together and applied to the specific case of a rectangular aperture FSS. Examples are provided and compared to simulated results.

Computation of Lattice Admittance Elements

The lattice admittances, in general, are either self admittances or mutual admittances. In order to calculate a self admittance, a single aperture element in the FSS must be isolated from all other apertures. Then, the resulting aperture problem – that is, an incident plane wave illuminating a single aperture - must be solved to determine the fields on the aperture and a corresponding port voltage and equivalent admittance for the circuit domain. For a mutual admittance calculation, any two apertures must be isolated from the others, and the resulting problem must be solved for the fields on both apertures simultaneously. Thus, the determination of the lattice admittances consists of isolating individual resonators (apertures) within the FSS array and analyzing their electromagnetic behavior.

In principle, any valid electromagnetic technique can be employed to solve the problem of isolated apertures. The technique will depend on the specific geometry of the aperture and the desired level of accuracy. In the most general case, full-wave numerical techniques can be employed, which will typically be accurate but computationally expensive. However, if a closed-form approximation exists with sufficient accuracy, it can certainly be used instead of the full-wave solution. The range of possible techniques for solving these electromagnetic aperture problems is too diverse to be explored in full detail here. For the purposes of this work, the problems are formulated using the equivalence principle and solved using what amounts to a MOM technique.

Self Admittance Calculation

The self admittance a single aperture, as stated above, is determined by isolating that aperture from all other apertures in the FSS and solving the associated electromagnetic problem. Fig. 32 below shows the classic equivalence principle formulation of a one-aperture scattering problem [35]. In (a), an aperture in an ideal infinite ground plane divides the problem into regions A and B (semi-infinite half-spaces). Note that the ground plane is infinite; this corresponds to an infinite FSS screen where all other apertures have been removed. An incident EM field in region A is defined by electric and magnetic fields $\mathbf{E}^i$ and $\mathbf{H}^i$, respectively. In (b) and (c), the equivalence principle is used to define the equivalent problems in regions A and B, respectively, by closing the aperture and introducing an equivalent magnetic surface current $\mathbf{M}$.

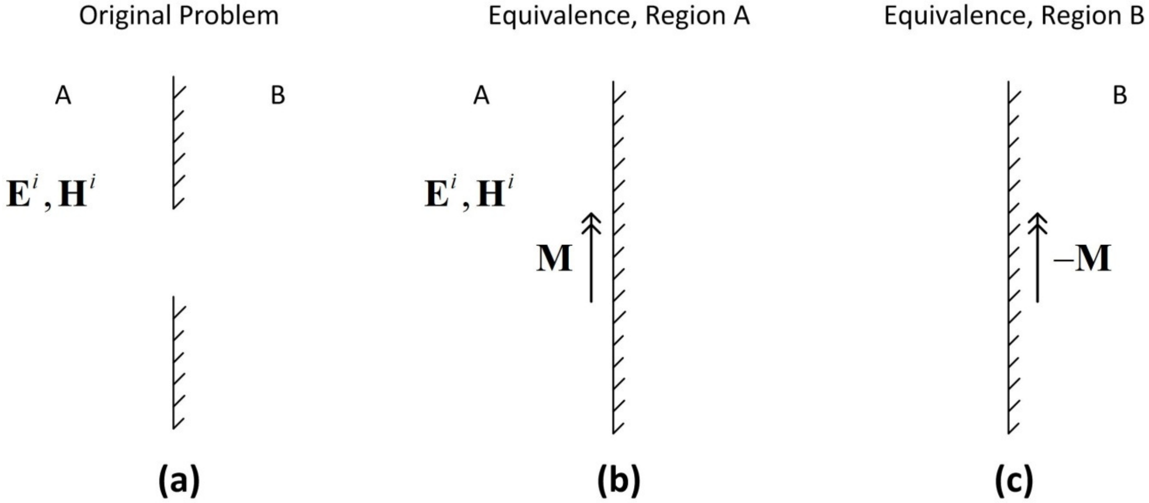

Fig. 32. Electromagnetic problem of one aperture in a ground plane. (a) Original aperture problem. (b) Equivalent problem in region A. (b) Equivalent problem in region B.

The problem summarized in Fig. 32 can be conveniently represented in terms of an equivalent circuit, as demonstrated by Harrington in 1991 [53]. In the simplest case, the variation of the field across the aperture is assumed to be known, except for an unknown scalar amplitude; this allows the magnetic current to be written as:

$$\mathbf{M} = V\mathbf{M}_0 \tag{20}$$

Here, the amplitude V will correspond to the port "voltage" employed in the lattice model. In this simple case, an equivalent circuit can be constructed as shown in Fig. 33. The term Y_s^{hs}, called the half-space self admittance, is given by:

$$Y_s^{hs} = -\left\langle \mathbf{M}_0, \mathbf{H}\left(\mathbf{M}_0\right)\right\rangle \tag{21}$$

Here, $\mathbf{H}\left(\mathbf{M}_0\right)$ is the magnetic field produced by the magnetic current $\mathbf{M}_0$, and $\langle\ \rangle$ denotes an inner product defined as a surface integral over the aperture area S:

$$\left\langle \mathbf{A}, \mathbf{B}\right\rangle = \iint_S \mathbf{A} \cdot \mathbf{B} dS \tag{22}$$

The current source term I_0 of Fig. 33 is also defined as an inner product:

$$I_0 = \left\langle \mathbf{M}_0, \mathbf{H}_t^i \right\rangle \tag{23}$$

Here, $\mathbf{H}_t^i$ is the tangential (to the ground plane) component of the incident magnetic field.

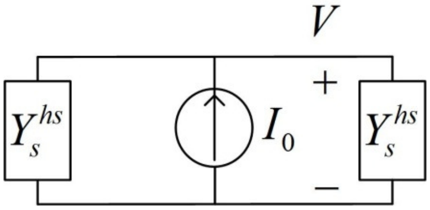

Fig. 33. Harrington's equivalent network for a single-aperture scattering problem.

Mutual Admittance Calculation

Fig. 34 shows the electromagnetic problem for a two-aperture mutual admittance calculation. For full generality, the apertures are at first assumed to be dissimilar. As before, the equivalence principle is used to separate the problem into two regions, and to introduce, in this case, two different equivalent magnetic currents, $\mathbf{M}_1$ and $\mathbf{M}_2$. Also, for simplicity, the magnetic currents are assumed to take the form:

$$\mathbf{M}_1 = V_1 \mathbf{M}_{0,1} \tag{24}$$

$$\mathbf{M}_2 = V_2 \mathbf{M}_{0,2} \tag{25}$$

In this simplified case, Harrington's network representation of a single-aperture problem (Fig. 33) is easily extended to the two-aperture problem, as shown in Fig. 35. Each half-space region is now represented by a two-port network. Note that the terms Y_{s1}^{hs} and Y_{s2}^{hs} are the self admittances of the two apertures, in precisely the same sense as (21) in the single-aperture problem. The additional term Y_m^{hs} is the mutual half-space admittance between the apertures and is defined as follows:

$$Y_m^{hs} = -\left\langle \mathbf{M}_1, \mathbf{H}\left(\mathbf{M}_2\right)\right\rangle_1 = -\left\langle \mathbf{M}_2, \mathbf{H}\left(\mathbf{M}_1\right)\right\rangle_2 \tag{26}$$

Note that the indexes of the apertures are interchangeable in this definition; thus, the mutual admittance satisfies electromagnetic reciprocity. The surface integral of the inner product is computed over the area of the first aperture listed inside the brackets; this fact is emphasized by adding subscripts to the inner product operators to denote which aperture the integral is performed over. The two amplitudes V_1 and V_2 associated with the aperture fields are the voltages present at the ports of the admittance network in Fig. 35. Also, there are now two current sources, one for each aperture, which are both functions of the same incident magnetic field:

$$I_1 = \left\langle \mathbf{M}_{0,1}, \mathbf{H}_t^i \right\rangle_1 \tag{27}$$

$$I_2 = \left\langle \mathbf{M}_{0,2}, \mathbf{H}_t^i \right\rangle_2 \tag{28}$$

When all of the apertures in the FSS are identical, it is straightforward to see that the two magnetic currents $\mathbf{M}_{0,1}$ and $\mathbf{M}_{0,2}$ are identical. It follows that the voltages V_1 and V_2, as well as the current sources I_1 and I_2, are equal as well. In fact, comparing (27)-(28) to (23), both current sources are equal to I_0 of the single aperture problem.

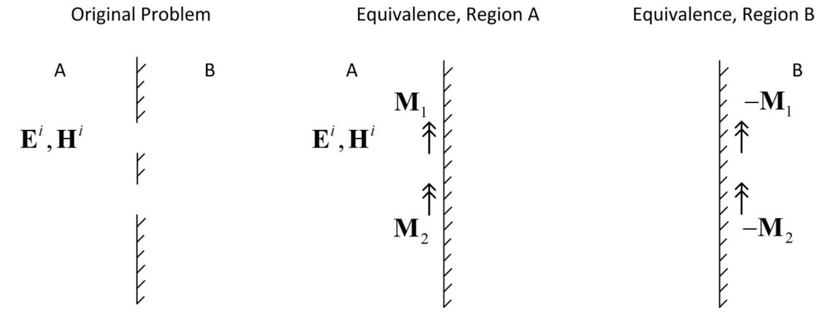

Fig. 34. Equivalence principle for a two-aperture problem. (a) Original dual-aperture problem. (b) Equivalent problem in region A. (c). Equivalent problem in region B.

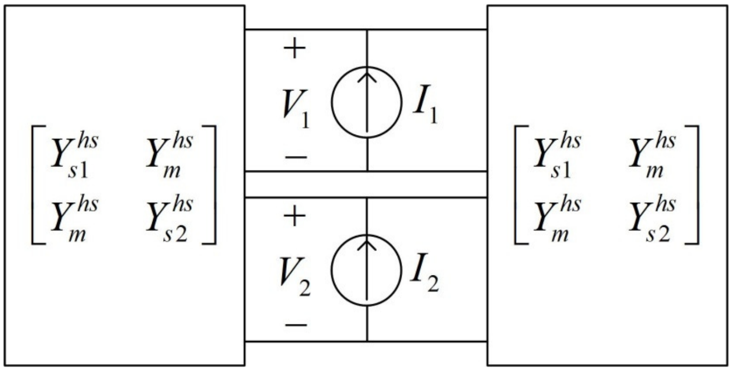

Fig. 35. Equivalent circuit representation of a two-aperture problem.

Relationship between Circuit Domain and Electromagnetic Domain

In order to implement the lattice model, a correct relationship must be established between, on one hand, the equivalent networks used to compute admittances in the EM domain, and on the other hand, the lattice structure defined in the circuit domain. The following sections detail this relationship between the two domains of analysis. First, the circuit domain lattice is populated with admittance values from the EM domain. Then, the performance of the FSS is ascertained by considering the circuit domain and EM domain simultaneously.

Populating the Lattice with Admittances

Harrington's circuit representation of a single aperture problem (Fig. 33), along with the extension of this idea to a two-aperture problem (Fig. 35), can together be used to populate the admittance terms of the canonical lattice structure shown in Fig. 28 for any aperture-type FSS. Any two apertures in the FSS are represented by the π-network in Fig. 28 (b), and the terms Y_s and Y_m in that network are equal to exactly twice the self admittance (21) and mutual admittance (26) of the corresponding aperture problem. In other words, mathematically:

$$Y_s = 2Y_s^{hs} \tag{29}$$

$$Y_m = 2Y_m^{hs} \tag{30}$$

In this way, the admittances associated with isolated aperture problems in the EM domain can be translated directly into the periodic lattice of the circuit domain. That the factor of two is necessary in (29)-(30) becomes apparent when comparing the network in Fig. 33 to the collapsed one-port circuit domain network of Fig. 29 under uniform normal plane wave incidence. Specifically, in Harrington's formulation, the input current is split between two identical halfspace admittances, whereas in Fig. 29, there is only a single admittance driven by the input current.

The formulation discussed above – using the equivalence principle and Harrington's network representation – is one particular approach to bridging the EM domain of the analysis with the circuit domain. Other alternative approaches could be equally valid. In particular, other approaches could employ more approximations in the EM domain in order to achieve faster computation times at the expense of accuracy. In this sense, the EM and circuit domains of the lattice model are truly separate portions of the analysis problem. The method by which the self and mutual admittances of the lattice are calculated in the EM domain does not affect how the lattice structure itself is analyzed from a network perspective; it is only important that a well-defined relationship between the EM and circuit domains be established such that the lattice can be correctly populated with admittance terms. The lattice model, then, is quite flexible in terms of its implementation.

FSS Performance from Circuit Domain

The final step in implementing the lattice model analysis is to use the voltages and currents of the equivalent multiport network in the circuit domain to find meaningful performance characteristics of the FSS. In this work, determining the magnitude response of a spatial filter (i.e. transmitted versus reflected power) is of primary interest. In other FSS applications, different quantities may be of interest: for example, the radiated field pattern through a transmitarray, or the phase characteristics of a beam-steering surface. In principle, any of these should be obtainable from the computed network parameters, as the model itself is built off a well-formulated link between the fields of the EM domain and the voltages and currents of the circuit domain. However, consideration of all of these special cases is beyond the scope of the current work.

To find the magnitude of the filter response of an FSS under uniform normal plane wave incidence, the input power to the network of Fig. 2 (d) must be known. Physically, in this scenario, EM energy impinges on the FSS with uniform power density S_i (in watts per square meter) across the entire incident half-space. Within each unit cell, an absolute incident power P_i (in watts) can then be found as:

$$P_i = S_i A \tag{31}$$

Here, A is the cross-sectional area of a unit cell. If the incident electric field intensity is $\mathbf{E}_i$, then the associated incident magnetic field intensity can be written as:

$$\mathbf{H}_i = \frac{1}{\eta} \times \mathbf{E}_i \tag{32}$$

Here, η is the free space wave impedance. Also:

$$\left|\mathbf{H}_i\right| = \frac{\left|\mathbf{E}_i\right|}{\eta} \tag{33}$$

The Poynting vector of this incident plane wave is given by:

$$\mathbf{S}_i = \frac{1}{2} \mathbf{E}_i \times \mathbf{H}_i \tag{34}$$

The incident power density is simply the magnitude of the Poynting vector:

$$S_i = \left|\mathbf{S}_i\right| = \frac{1}{2} \frac{\left|\mathbf{E}_i\right|\left|\mathbf{H}_i\right|}{\eta} \tag{35}$$

If the magnitude of the incident electric field is assumed to be equal to 1, then the absolute incident power per unit cell, per (31), can be written as:

$$P_i = \frac{1}{2} \eta \left|\mathbf{H}_i\right|^2 A \tag{36}$$

In Harrington’s network formulation of an aperture problem, it can be shown that the power transmitted through the aperture is equal to the power dissipated in a single halfspace admittance. In terms of Fig. 33:

$$P_t = \frac{1}{2} V \left(\frac{I_0}{2} \right)^* = \frac{1}{4} V I_0^* \tag{37}$$

The “t” subscript here denotes the power transmitted through the aperture. Note that the current I_0 in Fig. 33 is split evenly between the two halfspaces (hence the factor $I_0/2$). In terms of the multiport lattice network of the circuit domain, the absolute power transmitted through a single aperture in the FSS array can likewise be found by simply using the voltage and current at single port, or, equivalently, by using the voltage and current of the equivalent single-port collapsed network of Fig. 29. There is one important caveat, however. In Fig. 29, the admittance element Y^{Σ} contains (implicitly) both halfspace admittances of Fig. 33 (per (29)-(30)). Thus, only half of the power dissipated in Y^{Σ} actually corresponds to the power transmitted through the aperture:

$$P_t = \frac{1}{2}\left(\frac{1}{2}VI^*\right) = \frac{1}{4}VI^* \tag{38}$$

Comparing with (37), the total power transmitted per unit cell in the FSS is given by (38) when $I = I_0$ (I_0 as defined in Fig. 33).

Using P_i and P_d, the amount of power transmitted and reflected from the FSS can be determined. The transmissivity T is defined as the ratio of the transmitted power to the incident power:

$$T = \frac{P_d}{P_{in}} \tag{39}$$

The reflectivity R is defined as the ratio of the reflected power to the transmitted power:

$$R = \frac{P_{in} - P_d}{P_{in}} \tag{40}$$

Note that, by definition, $T + R = 1$.

More General Representations of Aperture Voltage

The self and mutual admittance calculations above assume that the aperture fields - specifically, the form of the equivalent magnetic current posited in (20) - can accurately be represented by a single scalar port voltage in the circuit. It amounts to a single-mode approximation and thus assumes that the current is known *a priori*, except for an unknown magnitude (voltage) V . For simple FSS topologies over a relatively small frequency band, such an approximation is feasible. For more complex geometries, the current cannot be written adequately in closed form. Moreover, even for simple geometries, the form of the current can change significantly if a wide enough frequency range is considered. Several possibilities exist for incorporating a more accurate magnetic current into the lattice model. These possibilities are discussed briefly below but are not pursued in extensive detail in this work.

Multiport FSS Elements

The first possibility for a more accurate aperture field is to use multiple voltages to represent the field. Specifically, the aperture field – and by extension, its associated equivalent magnetic current – may be represented as a linear combination of N vector-valued functions:

$$\mathbf{M} = \sum_{n=1}^{N} V_n \mathbf{M}_n \tag{41}$$

This could apply to either a finite set of known full-domain basis functions, or to a numerical scheme, wherein each current $\mathbf{M}_n$ only has limited support within a discretized aperture. In either case, (41) dictates that each FSS element now has multiple network ports (i.e. multiple voltages). Under this scenario, Harrington's equivalent circuit representation of Fig. 33 must be generalized to that in Fig. 36, as demonstrated in [54]. The behavior of a single aperture is now governed by a half-space admittance matrix Y^{hs}, rather than a single scalar self admittance. The elements of this matrix are defined by :

$$Y_{mn}^{hs} = -\iint_A \mathbf{M}_m \cdot \mathbf{H}_t\left(\mathbf{M}_n\right) dA \tag{42}$$

Furthermore, there are now N current sources corresponding to the N basis functions of the magnetic current. The values of these current sources are computed as:

$$I_m = \iint_A \mathbf{M}_m \cdot \mathbf{H}_i dA \tag{43}$$

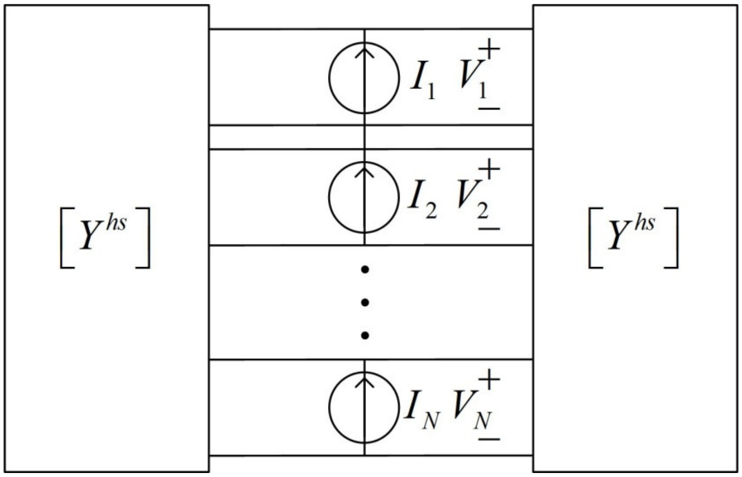

Fig. 36. Multiport representation of a single FSS element.

Numerically-Computed Single-Mode FSS Elements

It is clear that the multiport FSS elements suggested by (41) could quickly increase the complexity of the lattice itself by introducing a large number of additional ports. The intuitive nature of the model may be somewhat compromised in this case. Also, the number of admittance values for which an infinite series approximation must be computed increases as the size of the matrix Y^{hs} increases. Thus, the computational cost increases significantly. Furthermore, it is unclear whether handling the convergence of all these infinite series is possible through the Shanks transform. Overall, the multiport element method does not seem to be particularly desirable if it can in any way be avoided.

An alternative approach is to obtain a suitably accurate numerical solution to the single aperture problem (using a technique such as MOM) and then approximate the current analytically as a single mode using a spline or some other suitable piecewise representation. The resulting current envelope can then be used in the lattice model computations (21), (23), and (26) as in the single-mode case. In this way, an analytical form of the magnetic current is not necessary *a priori*, but the lattice model still benefits from having only one network port for each FSS element. Note that with this approach, a numerical solution need only be obtained for the single aperture problem (i.e. self admittance calculation); after this, the single-mode current envelope approximation can be used for all mutual admittance calculations.

If the desired frequency range of analysis is small enough, the current can be approximated as being constant over that whole range, and the numerical aperture solution need only be performed once at a single frequency in the middle of the band. However, if the frequency range is large enough, the current envelope over the aperture may change significantly in form as additional higher-order modes are introduced. In this case, the frequency band can be divided into smaller sub-bands. The numerical aperture solution is then performed at single frequency points within these sub-bands, and the aperture field is assumed to be constant within these sub-bands.

For the most accurate analysis versus frequency, however, the numerical aperture solution should be repeated at every frequency point of interest. Even in this case however, it should be stressed that the numerical aperture solution need only be performed once for each frequency point. The same current envelope can be used in the computation of all self and mutual admittance values at that frequency. Overall, this numerical approach to achieve a single-mode field representation over an aperture seems much more computationally desirable than the multi-mode, multiport option, since it keeps the lattice structure itself simple, using only a single port for each FSS element.

Application to Rectangular Aperture FSS

The circuit domain analysis of Chapter IV and the EM domain analysis of this chapter provide the basic tools for a lattice model analysis of a single-layer, single-element FSS. However, the actual implementation of the lattice model is best illustrated through an example. In order to demonstrate the basic utility of the lattice theory developed so far, it is applied here to the specific case of a rectangular aperture FSS. In fact, rectangular aperture geometries ared used throughout this dissertation as representative FSSs for example calculations. Rectangular apertures have been chosen as illustrative resonant elements in this work because their behavior under plane wave incidence is well studied, and the admittance calculations are relatively straightforward.

In this section, a rectangular aperture design is first analyzed using the single-mode formulation of the lattice model. Then, the analysis is extended to a multiport case in which a one-dimensional MOM discretization of the aperture is employed. Finally, the effect of the number of levels of coupling on the lattice model solution is studied.

Single-Mode Formulation

The unit cell geometry of a rectangular aperture FSS is defined in Fig. 37. A single rectangular-shaped slot with length L and width W is cut into a rectangular-shaped unit cell of dimensions D_x and D_y. The FSS plane is assumed to be an infinitely thin, perfectly conducting plane. The transmission passband center frequency of such an FSS roughly corresponds to the wavelength at which L is about a half-wavelength.

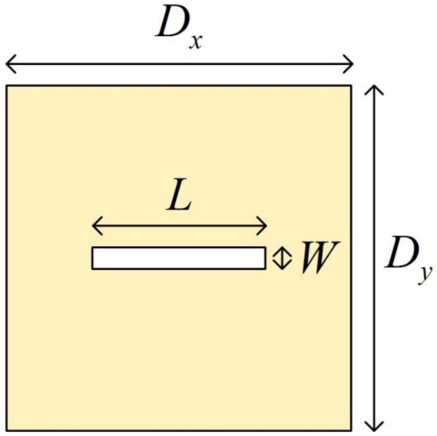

Fig. 37. Rectangular aperture FSS unit cell geometry.

For simplicity, the length of the rectangular aperture is assumed to be large compared to the width. In this case, the electric field distribution across the length aperture can be approximated with a fair amount of accuracy as a half-sinusoid [53]; the field is assumed to be constant across the narrow width of the aperture. In the context of the lattice EM domain analysis, this means that the single-mode, single-port formulation can be used, and the equivalent magnetic current of the aperture will take the form of (20). Specifically, the magnetic current can be written, following the convention of [53], as:

$$\mathbf{M} = \frac{1}{W}\sin\left(\frac{\pi x}{L}\right)\hat{\mathbf{x}} \tag{44}$$

The electric field associated with this magnetic current is illustrated visually, with the appropriate coordinate axes, in Fig. 38 (the relationship between the magnetic current and the electric field, dictated by equivalence principle, is $\mathbf{M} = \hat{\mathbf{n}} \times \mathbf{E}$, where $\hat{\mathbf{n}}$ is a unit vector normal to the aperture). Note that the field goes to zero at the two ends of the aperture and reaches its maximum at the center of the aperture.

The computation of the self admittance (21) and mutual admittances (26) for a the rectangular apertures in FSS assuming the magnetic current (44) is detailed in Appendix A. The integrals are evaluated using a mixture of analytical and numerical techniques. The input current (23) is a much more straightforward integral over the area of the rectangular aperture. It employs the magnetic current (44), but it also requires knowledge of the input current to the lattice, which in turn requires knowledge of the incident field impinging on the FSS. Following [53], the incident magnetic field at the plane of the FSS is defined as $\mathbf{H}_t^i = \hat{\mathbf{x}}/\eta$, where η is the wave impedance of free space; the resulting input current from the integral is $I = 4L/\pi\eta$.

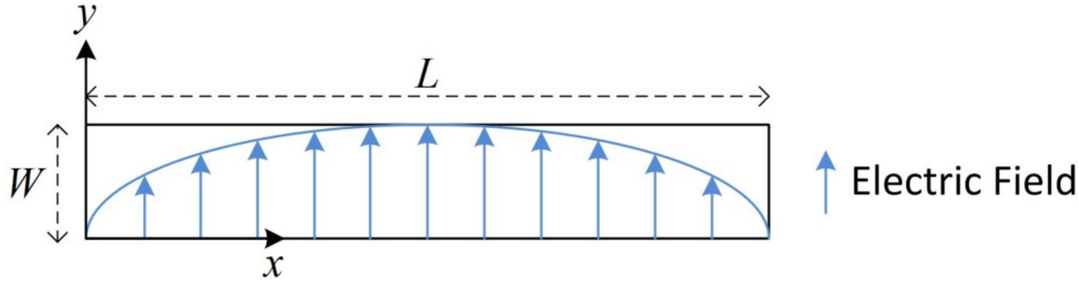

Fig. 38. Rectangular aperture with single-mode sinusoidal field distribution.

In Fig. 39, the performance of a rectangular aperture FSS is plotted for dimensions of $L = 7.5\text{ mm}$, $W = 0.75\text{ mm}$, and $D_x = D_y = 12\text{ mm}$. The performance is calculated using the lattice model - under the single mode approximation (44) - and compared to the results using commercial simulation software [16]. Clearly, for the particular case of Fig. 39, there is very good correspondence between the lattice model and simulation, even at frequencies away from the transmission passband.

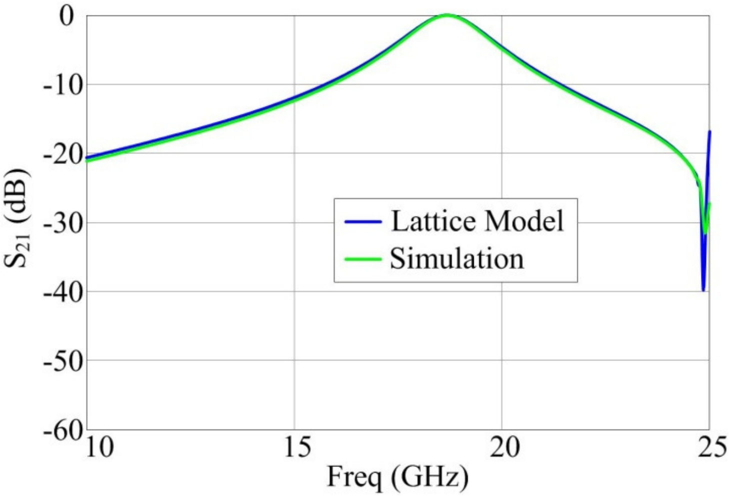

Fig. 39. Lattice model vs. simulation for a basic rectangular aperture FSS.

Multiport Formulation: Zero-Width MOM

The rectangular aperture FSS of Fig. 37 can also be analyzed using a multiport MOM approach. There are various ways that the MOM problem can be formulated, but one of the simplest approaches is summarized in Fig. 40. Here, the length of the aperture is divided into N even segments over which triangular basis functions $T_n(x)$ are defined with unknown amplitudes a_n [55]. The equivalent magnetic current - and, by extension, the electric field across the aperture - is assumed to be constant across the width of the aperture, so the discretization is only in one dimension. This is sometimes referred to as the zero-width approximation [56]. Note that this approximation is only good when the width of the aperture is relatively small compared to its length (and compared to the wavelength at a particular frequency of interest). The triangular basis functions of the one-dimensional discretization are defined as:

$$T_n(x) = \begin{bmatrix} \dfrac{x-(n-1)\Delta x}{\Delta x} & (n-1)\Delta x \le x \le \Delta x \\ \dfrac{(n+1)\Delta x - x}{\Delta x} & \Delta x \le x \le (n+1)\Delta x \end{bmatrix} \tag{45}$$

Each basis function is defined across the span of two consecutive segments of the aperture. These basis functions, when scaled by the appropriate amplitudes a_n, represent the equivalent magnetic current distribution across the aperture as per (41); specifically, the triangular basis functions correspond to the functions $\mathbf{M}_n$ of (41). Only $N-2$ triangle functions are defined, such that the total magnetic current is zero at the endpoints of the aperture (thus satisfying the PEC boundary conditions). For brevity, no example calculations are provided for this particular formulation of the rectangular aperture problem; the detailed implementation would follow the multiport aperture formulation established by (41)-(43).

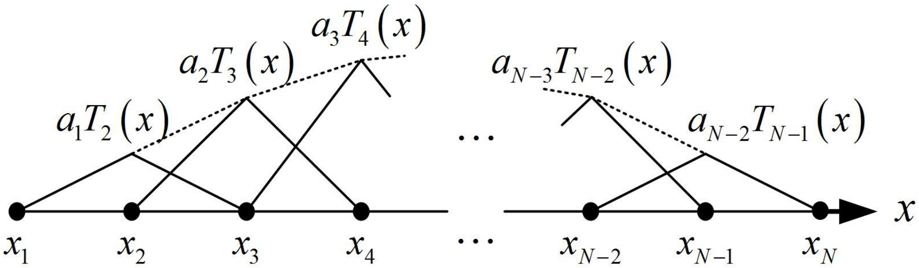

Fig. 40. MoM discretization using triangular basis functions.

Effect of Coupling Levels

One important consideration in the practical implementation of the lattice model is the number of levels of mutual coupling used for the computation of the infinite admittance (15) (these levels of coupling were previously illustrated in Fig. 30). Clearly, it is desirable to use the least number of mutual admittance terms that are necessary for a fairly accurate Shanks transformation approximation of the infinite admittance. Of course, it is difficult to assess the accuracy of the Shanks transform itself without having the true solution available; the only reasonable evaluation of its accuracy is to test it using different numbers of terms. A formal study of the effect of the number of coupling levels is beyond the scope of this work. Such a study is admittedly of interest, though, since the computational efficiency of the lattice method – particularly for more complicated FSS topologies – is significantly dependent on the number of mutual admittance terms that must be calculated.

For the purposes of this dissertation, a brief empirical study is performed using the single rectangular aperture FSS of Fig. 37 in order to show how the lattice model results are affected by changing the number of levels of coupling. For this study, the dimensions of the rectangular aperture FSS are fixed using the same values as the design in Fig. 39, and only the number of terms used in the finite two-dimensional series (16) are varied. Specifically, the integers M and N are varied independently (M and N correspond to the number of unit cells used in the x direction and y directions, respectively, where the coordinate axes are relative to Fig. 38). Fig. 41 shows the results of the lattice model as these integers are varied (for comparison, the lattice model results in Fig. 39 are obtained using $M = 6$ and $N = 10$).

In part (a) of Fig. 41, $M = N$ for all cases. The number of levels of coupling is varied from 2 to 10 in increments of 2. Clearly, near the center frequency of the transmission passband, the results are almost identical; only $M = N = 2$ has any discernible difference from the other curves (and only a slight variation at that). The most noticeable difference between the various solutions occurs between 20-25 GHz, where the transmission profile experiences a local minimum. Compared to the simulated results using commercial software, as shown in Fig. 39, it is clear that a larger number of coupling levels achieves better agreement with the expected results; in particular, for larger levels of coupling, the local minimum is sharper and located closer to 25 GHz, as is observed in simulation.

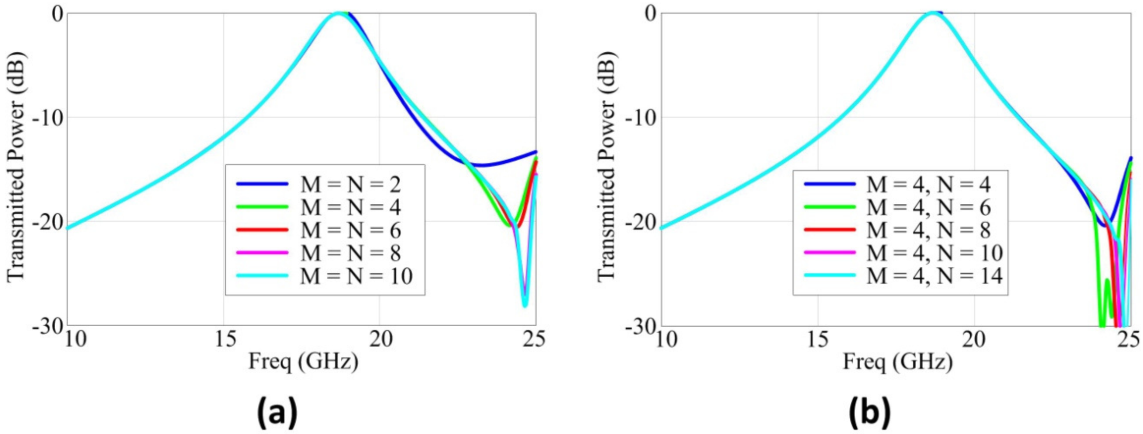

Fig. 41. Effect of the number of levels of mutual coupling in the lattice model. The geometry is a single-layer, single-element rectangular aperture FSS. (a) The number of terms in the two-dimensional admittance series is the same in both dimensions. (b) The number of terms is fixed in one dimension.

In part (b) of Fig. 41, M is kept constant at 4, while N is varied between 4 and 14. The reasoning behind this choice of variation comes from intuition regarding the EM coupling expected with the rectangular aperture FSS elements. Specifically, the coupling between two rectangular apertures is expected to be much stronger in the broadside direction (i.e. along the width, or y direction) than in the longitudinal direction (i.e. along the length, or x direction). Thus, the inclusion of terms in the broadside direction is expected to affect the final solution more significantly than those terms in the longitudinal direction. The solutions due to varying N while keeping M constant support this expectation. As in part (a), the only noticeable difference between the various solutions in part (b) is between 20-25 GHz where the local transmission minimum occurs, and the solutions become more "accurate" (i.e. compared to the simulation in Fig. 39) as N is increased. It is noteworthy to compare the solution for $M = N = 10$ in part (a) to that of $M = 4$, $N = 10$ in part (b). Both solutions are very close to the simulated results, suggesting that increasing M from 4 to 10 is largely an unnecessary addition of mutual coupling terms in the longitudinal direction.

The conclusions that can be drawn from the empirical study summarized in Fig. 41 are limited at best. The results only apply directly to the rectangular aperture geometry and cannot necessarily be expected to hold for other FSS geometries. Nonetheless, two observations are worth making. First, it seems that the number of coupling levels necessary for an accurate solution certainly depends on the frequency in question. It may be valid, then, to use a relatively small number of admittance terms at certain frequencies, thus saving computational time. Second, it is not necessary to use the same number of terms along both dimensions of the lattice; the rectangular aperture design, for instance, demonstrates that fewer terms are needed in the longitudinal coupling direction to obtain accurate results. Overall, then, it is clear that when using the lattice model, a careful balance must be made between using too few terms (thus losing accuracy) and using too many terms (thus wasting computational effort) in the infinite admittance series. Determining an “optimal” number of coupling terms to use for any given FSS design is certainly a topic of interest, but exploring this rigorously is beyond the scope of this work.

CHAPTER VI

IMPORTANT EXTENSIONS OF THE LATTICE MODEL

As suggested by the conceptual FSS in Fig. 23, the lattice model was originally intended to provide a methodology for exploring composite FSS structures that combine features such as multiple types of resonant elements, sub-array structures, multiple layers that may or may not be similar, and various reconfiguration mechanisms. It is important, then, to extend the formulations of Chapters IV and V – which only focused on single-layer, single-aperture designs - to cases of increasing complexity. This chapter demonstrates how the lattice analysis of the previous two chapters can be extended to three specific cases: multi-element, multilayer, and reconfigurable FSS designs. The lattice structures for these cases are developed in very general form and then specialized for the purpose of computational examples. For simplicity, the excitations of the lattices in these examples are restricted to uniform normal plane waves; consideration of non-uniform incidence is deferred until Chapter VII.

The chapter is organized as follows. First, the lattice theory for multi-element designs is considered, with specific focus on two-element unit cells for the purpose of illustration. Then, the theory is extended to multilayer designs, with simple two-layer designs serving as the primary illustration. For both multi-element and multilayer designs, examples are provided of rectangular aperture FSSs. Finally, the reconfigurable FSSs are discussed in general, with specific focus on varactor-tuned rectangular aperture designs.

Extension to Multi-Element Designs

The lattice model can easily be extended to multi-element FSS designs in which several different resonant elements reside within a single unit cell. For the purposes of illustration, a simple two-element design will be considered here in detail. These details can, in principle, be generalized to unit cells with more than two elements.

Fig. 42 (a) shows an example of a two-element FSS comprising two arbitrarily-shaped apertures contained within a unit cell with dimensions $D_x \times D_y$. In terms of a lattice representation, each individual aperture is assigned a port and a corresponding voltage, so that each unit cell now has two ports. For now, only the case of uniform normal plane wave incidence will be considered. Thus, by symmetry, the fields excited, although different for each aperture within a unit cell, are repeated across multiple unit cells. This means that only two voltages are required to describe the whole infinite lattice: V_1 and V_2 for apertures 1 and 2, respectively. As is the case in Fig. 29, where the single-element lattice reduces to a one-port network, the entire two-element lattice (not shown) can be collapsed to an equivalent two-port network, shown in Fig. 42 (b).

In Fig. 42 (b), the terms $Y^{\Sigma_1}, Y^{\Sigma_2}$, and Y^{Σ_3} are infinite summations of admittances defined by:

$$Y^{\Sigma_1} = Y_{s1} + \sum_k Y_{m1,k} \tag{46}$$

$$Y^{\Sigma_2} = Y_{s2} + \sum_k Y_{m2,k} \tag{47}$$

$$Y^{\Sigma_3} = \sum_k Y_{m3,k} \tag{48}$$

Here, Y_{s1} and Y_{s2} are the self admittances of apertures 1 and 2, respectively. $Y_{m1,k}$ is the mutual admittance between aperture 1 and any surrounding occurrence of aperture 1 in the FSS. The index k accounts for an unspecified number of such mutual admittances (the number will depend on the number of levels of coupling accounted for, similar to Fig. 30). Likewise, $Y_{m2,k}$ is the mutual admittance between aperture 2 and any surrounding occurrences of aperture 2. Finally, $Y_{m3,k}$ is the mutual admittance between aperture 1 and any surrounding occurrence of aperture 2 (or equivalently, the mutual admittance between aperture 2 and any surrounding occurrence of aperture 1; reciprocity dictates that the admittance will be identical using either definition).

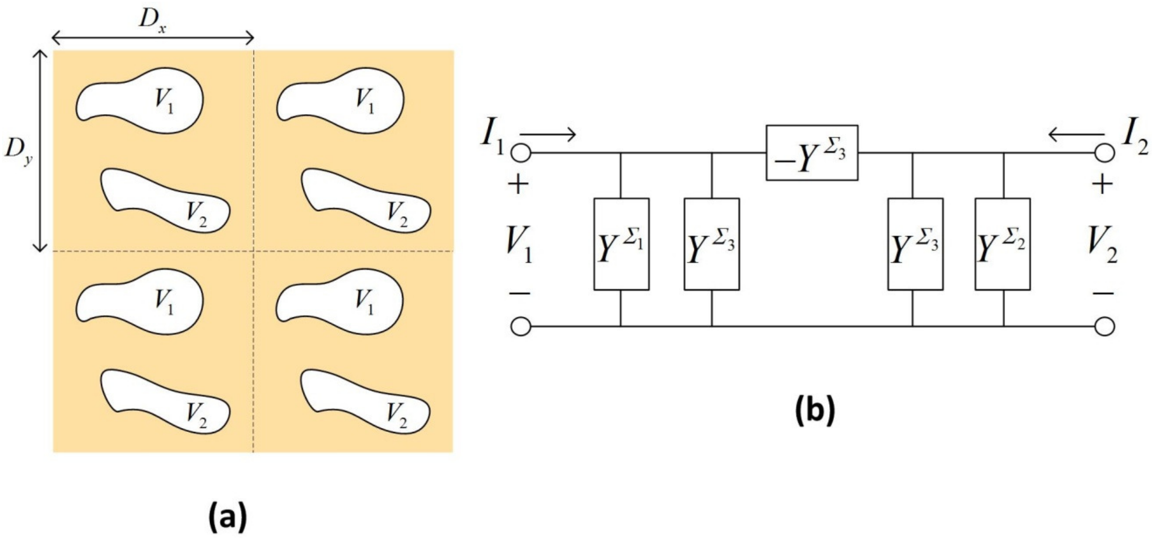

Fig. 42. Dual-aperture FSS. (a) Two arbitrary aperture geometries per unit cell. (b) Equivalent circuit model when lattice is collapsed due to symmetry under uniform incidence.

The three infinite summations are handled by applying two-dimensional Shanks transformations to each one, as is done for Y^{Σ} (15) in case of the single-element FSS of Fig. 29. Once the three Shanks transformations are performed, the port voltages of Fig. 42 (b) can be calculated using two-port network theory:

$$\begin{bmatrix} V_1 \\ V_2 \end{bmatrix} = \begin{bmatrix} Y^{\Sigma_1} & Y^{\Sigma_3} \\ Y^{\Sigma_3} & Y^{\Sigma_2} \end{bmatrix}^{-1} \begin{bmatrix} I_1 \\ I_2 \end{bmatrix} \tag{49}$$

To demonstrate the application of the lattice model to a multi-element FSS, a dual rectangular aperture design is proposed in Fig. 43. The unit cell geometry, shown in (a), consists of two rectangular apertures of equal width (W) but different lengths (L_1 and L_2) oriented parallel to each other and separated by a distance of h. The apertures are assumed to be centered within the unit cell with respect to the unit cell dimensions D_x and D_y. For computation, the FSS is given dimensions of $L_1 = 7\text{ mm}$, $L_2 = 10\text{ mm}$, $D_x = D_y = 11.8\text{ mm}$, $W = 0.5\text{ mm}$, and $h = 4\text{ mm}$. The performance is computed from 10-25 GHz using the lattice model and is compared to simulation results in (b). The design achieves a dual-passband filter response with passbands near 15 GHz and 20 GHz. Good correspondence between the two computation methods demonstrates the validity of the multiple-element lattice model approach.

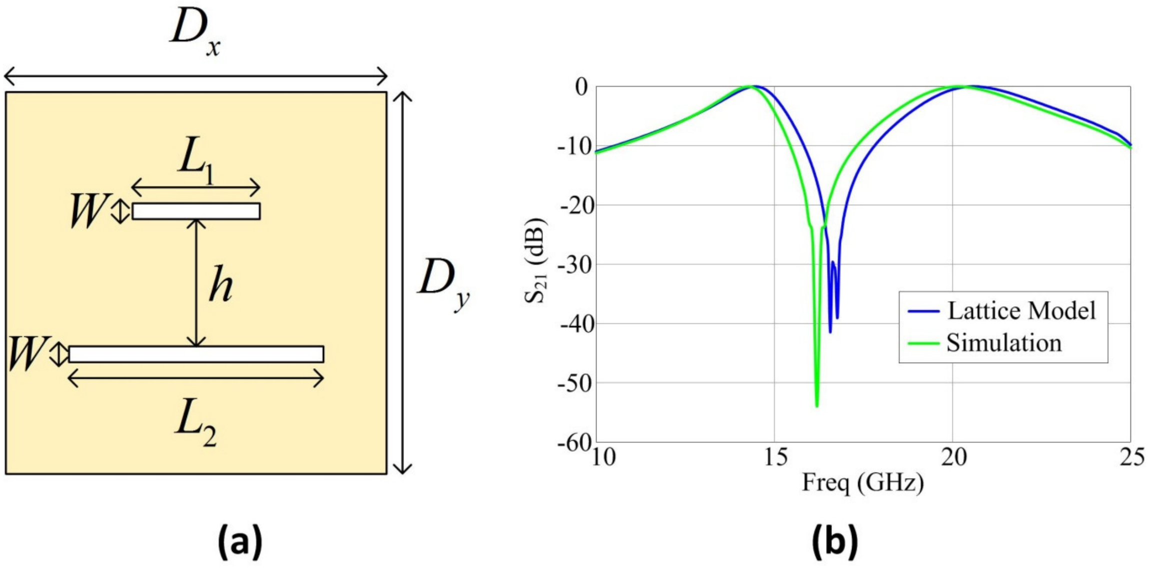

Fig. 43. Lattice model vs. simulation for a dual rectangular aperture FSS.

Extension to Multilayer Designs

It is also straightforward to extend the lattice model to multilayer FSSs. However, the classic aperture problems (as represented in Fig. 32 and Fig. 34) used thus far to determine the lattice admittances in the EM domain must themselves be extended to multilayer cases. Specifically, two-layer aperture problems can be used as the basis for computing the admittances of lattices with any arbitrary number of layers.

Dual-Layer Aperture Problem #1

The first problem that must be considered, shown in Fig. 44, is a two-layer problem with one aperture in each layer. Using the equivalence principle, the problem is divided into three regions: region A, where the incident plane wave is present; region B, between the two FSS layers; and region C, where the transmitted field resides. Two equivalent magnetic currents are defined on the two apertures, and parts (b), (c), and (d) of the figure show the equivalent problems in the three regions.

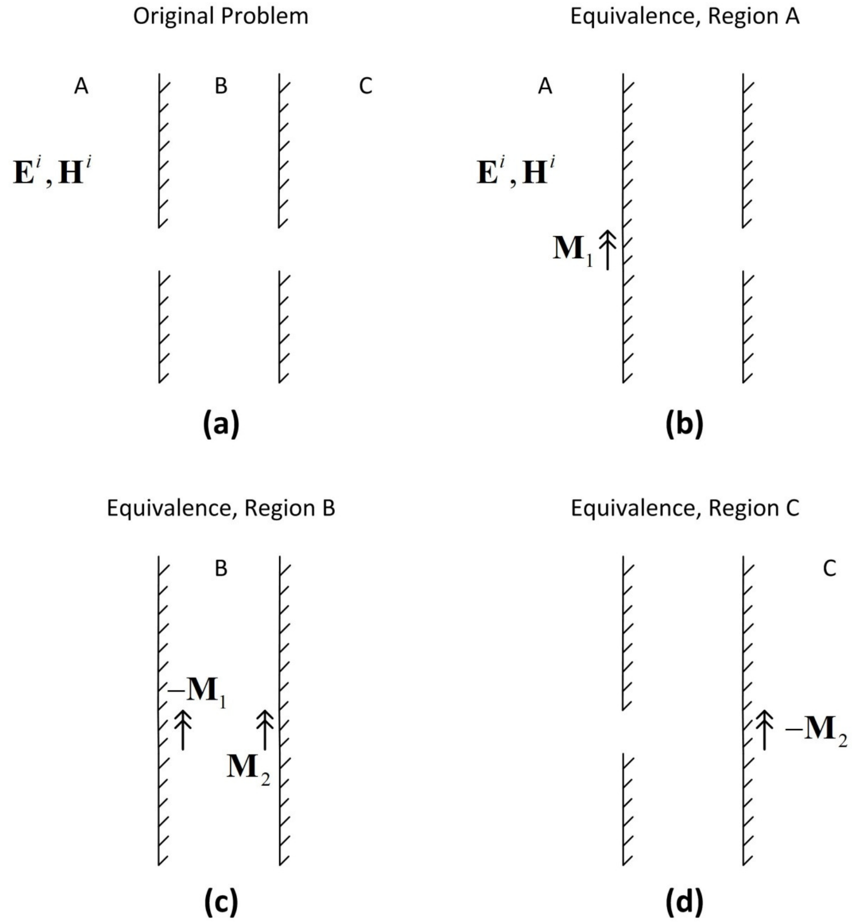

Fig. 44. Dual-layer aperture problem with one aperture on each layer. (a) Original problem and equivalent problems in (b) region A, (c) region B, and (d) region C.

While the equivalent problems in regions A and C are identical to those that have been encountered in the single layer FSS analysis (i.e. halfspace admittance problems), the equivalent problem in region B requires closer inspection. Specifically, the two ground planes dictate that in order to use image theory to remove the ground planes, the equivalent magnetic currents must be imaged an infinite number of times (e.g., as in [57]).

Fig. 45 illustrates the principle of an infinite set of images. In (a)-(d), the two ground planes are removed by imaging magnetic currents $\mathbf{M}_1$ and $\mathbf{M}_2$. Specifically, in (a), $\mathbf{M}_1$ is imaged an infinite number of times along the horizontal axis, starting with an image across the first ground plane; the successive images alternate the ground plane with respect to which they are calculated. In (b), $\mathbf{M}_1$ is again imaged an infinite number of times, this time starting with an image with respect to the second ground plane. Thus, there are two infinite sets of images associated with $\mathbf{M}_1$. Likewise, there are two infinite sets of images associated with $\mathbf{M}_2$. In (c), $\mathbf{M}_2$ is imaged stating with respect to the second ground plane; in (d) it is imaged starting with respect to the first ground plane (alternating ground planes with each successive image). The contributions of all images in (a)-(d) must be included when calculating the fields in region B. The computational handing of these infinite sets will be discussed shortly.

With the equivalent two-layer regional problems defined in Fig. 44 and Fig. 45, standard EM boundary conditions can be used to write equations relating the fields in each region. Specifically, the magnetic fields are forced to be continuous across each aperture. Equating the field on aperture 1 in region A to field on aperture 1 in region B yields:

$$\begin{aligned}&\mathbf{H}_{imp}+2\mathbf{H}_1^A\left(\mathbf{M}_1,0\right)=\\&-2\mathbf{H}_1^B\left(\mathbf{M}_1,0\right)-4\sum_{n=1}^{\infty}\mathbf{H}_1^B\left(\mathbf{M}_1,2nd\right)-4\sum_{n=1}^{\infty}\mathbf{H}_1^B\left(\mathbf{M}_2,(2n-1)d\right)\end{aligned} \tag{50}$$

Here, $\mathbf{H}_{imp}$ is the impressed magnetic field due to the incident plane wave (in the presence of the first layer ground plane). $\mathbf{H}_m^{\alpha}(\mathbf{M}_n, z)$ is the magnetic field over aperture m in region α caused by radiation from the magnetic current over aperture n located at distance of z. Note that this distance z is only the component of the distance in the direction normal to the FSS layers (i.e. the horizontal direction in Fig. 44). Also, d here is defined as the separation distance between the two FSS layers.

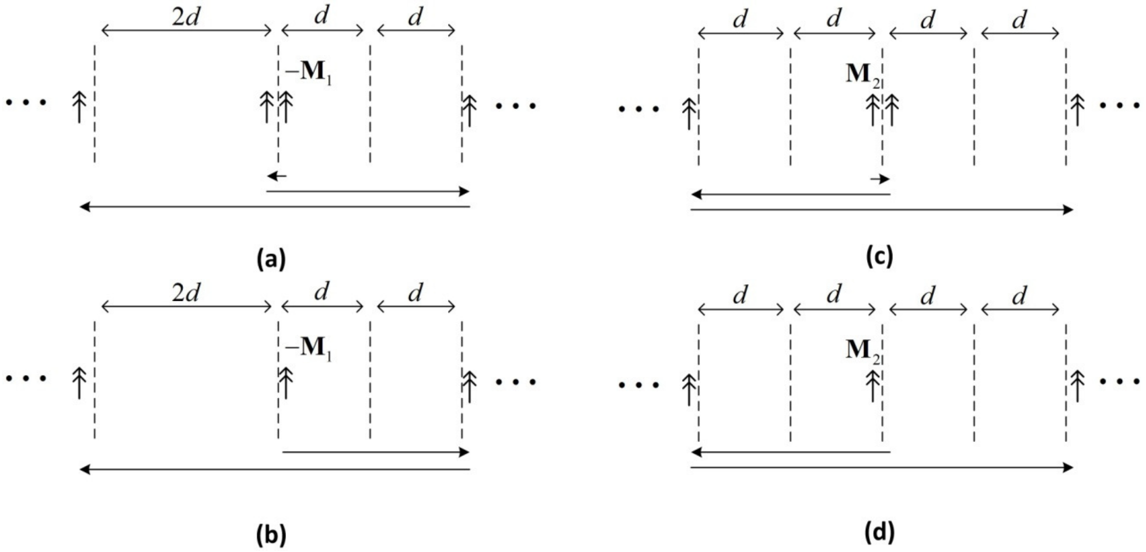

Fig. 45. Infinite image treatment of dual-layer aperture problem. Set of images (a) of the first magnetic current, starting with respect to the first ground plane, (b) of the first magnetic current, starting with respect to the second ground plane, (c) of the second magnetic current, starting with respect to the second ground plane, and (d) of the second magnetic current, starting with respect to the first ground plane.

The terms on the left hand side of (50) (fields in region A) are based on the equivalent problem of Fig. 44 (b). The contributions to the total field are from the incident plane wave and the magnetic current $\mathbf{M}_1$. Similarly, the terms on the right hand side (fields in region B) are based on the equivalent problem of Fig. 44 (c). The contributions to the total field over aperture 1 are from $\mathbf{M}_1$, $\mathbf{M}_2$, and the infinite number of images associated with those currents. The contribution of $\mathbf{M}_1$ and its image with respect to the first ground plane is accounted for by the term $2\mathbf{H}_1^B\left(\mathbf{M}_1,0\right)$; the remaining images associated with $\mathbf{M}_1$ are collected into an infinite series with index n. Note that the distance of separation between the images in this series increases as an even multiple of the layer separation distance ($2dn,\ n=1,2,3,\ldots$). The total contribution of $\mathbf{M}_2$ and all of its images are likewise collected into a second infinite series; the distance of separation between these images increases as an odd multiple of layer separation distance ($2d\left(n-1\right),\ n=1,2,3,\ldots$).

It is also important to discuss the factors of two and four appearing in front of the terms in (50). On the left hand side, $\mathbf{H}_1^A\left(\mathbf{M}_1,0\right)$ is multiplied by two to account for the image of this current due to the first layer ground plane; on the right hand side, $\mathbf{H}_1^B\left(\mathbf{M}_1,0\right)$ is similarly multiplied by two. The factors of four appearing on the right hand side before the two infinite series arise naturally when mathematically collecting all of the infinite images after enforcing the boundary conditions. Specifically, this occurs for two reasons: first, there are two sets of images associated with $\mathbf{M}_1$ and two sets of images associated with $\mathbf{M}_2$; second, reciprocity dictates that images at the same distance on either side of the original magnetic current are equal (i.e. $\mathbf{H}_m^\alpha\left(\mathbf{M}_n,z\right)=\mathbf{H}_m^\alpha\left(\mathbf{M}_n,-z\right)$). The first set of images associated with $\mathbf{M}_1$ (Fig. 45 (b)) contributes an infinite number of identical pairs of images (due to reciprocity), as does the second set of images associated with $\mathbf{M}_1$ (Fig. 45 (c)). This leads to an infinite collection of images in sets of four. Likewise, the two sets of images associated with $\mathbf{M}_2$ (Fig. 45 (d) and (e), respectively) produce identical images in sets of four. Finally, it should be noted that the impressed magnetic field $\mathbf{H}_{imp}$ is assumed to be calculated in the presence of the first layer ground plane (i.e. without applying image theory), so no factor of two appears explicitly here; it is understood that $\mathbf{H}_{imp} = 2\mathbf{H}_i$, where $\mathbf{H}_i$ is the magnetic field of the actual incident plane wave. The choice to write (50) using $\mathbf{H}_{imp}$ rather than $\mathbf{H}_i$ is an arbitrary convention adopted here for the multilayer problem.

A similar equation to (50) can be written to enforce the continuity of the field between regions B and C:

$$2\mathbf{H}_2^B\left(\mathbf{M}_2,0\right)+4\sum_{n=1}^{\infty}\mathbf{H}_2^B\left(\mathbf{M}_2,2nd\right)+4\sum_{n=1}^{\infty}\mathbf{H}_2^B\left(\mathbf{M}_1,(2n-1)d\right)=-2\mathbf{H}_2^C\left(\mathbf{M}_2,0\right) \qquad (51)$$

The left hand side terms correspond to the fields in region B and include all of the images due to the dual ground planes. The right hand side terms correspond to the fields in region C due to $\mathbf{M}_2$ and its image (factor of two).

Equations (50)-(51) form a system describing the two-layer aperture problem of Fig. 44. In the next step of the analysis, (50) is multiplied by $\mathbf{M}_1$, and an inner product is applied (i.e. a surface integral over aperture 1). Likewise, (51) is multiplied by $\mathbf{M}_2$, and a different inner product is defined (i.e. a surface integral over aperture 2). These operations yield:

$$\begin{aligned}&\left\langle \mathbf{M}_1,\mathbf{H}_{imp}\right\rangle+2\left\langle \mathbf{M}_1,\mathbf{H}_1^A\left(\mathbf{M}_1,0\right)\right\rangle=\\&-2\left\langle \mathbf{M}_1,\mathbf{H}_1^B\left(\mathbf{M}_1,0\right)\right\rangle-4\left\langle \mathbf{M}_1,\sum_{n=0}^{\infty}\mathbf{H}_1^B\left(\mathbf{M}_1,2dn\right)\right\rangle-4\left\langle \mathbf{M}_1,\sum_{n=1}^{\infty}\mathbf{H}_1^B\left(\mathbf{M}_2,2d\left(n-1\right)\right)\right\rangle\end{aligned}\tag{52}$$

$$\begin{aligned}&2\left\langle \mathbf{M}_2,\mathbf{H}_2^B\left(\mathbf{M}_2,0\right)\right\rangle+4\left\langle \mathbf{M}_2,\sum_{n=1}^{\infty}\mathbf{H}_2^B\left(\mathbf{M}_2,2dn\right)\right\rangle+\\&4\left\langle \mathbf{M}_2,\sum_{n=1}^{\infty}\mathbf{H}_2^B\left(\mathbf{M}_1,2d\left(n-1\right)\right)\right\rangle=-2\left\langle \mathbf{M}_2,\mathbf{H}_2^C\left(\mathbf{M}_2,0\right)\right\rangle\end{aligned}\tag{53}$$

Using the fact that $\mathbf{H}_1^A\left(\mathbf{M}_1,0\right)=\mathbf{H}_1^B\left(\mathbf{M}_1,0\right)$ and $\mathbf{H}_2^B\left(\mathbf{M}_2,0\right)=\mathbf{H}_2^C\left(\mathbf{M}_2,0\right)$, and employing the linearity of the inner products and summations, (52)-(53) can be rewritten as:

$$\begin{aligned}&\left\langle \mathbf{M}_1,\mathbf{H}_{imp}\right\rangle+4\left\langle \mathbf{M}_1,\mathbf{H}_1\left(\mathbf{M}_1,0\right)\right\rangle=\\&-4\sum_{n=1}^{\infty}\left\langle \mathbf{M}_1,\mathbf{H}_1\left(\mathbf{M}_1,2dn\right)\right\rangle-4\sum_{n=1}^{\infty}\left\langle \mathbf{M}_1,\mathbf{H}_1\left(\mathbf{M}_2,(2n-1)d\right)\right\rangle\end{aligned}\tag{54}$$

$$\begin{aligned}&4\sum_{n=1}^{\infty}\left\langle \mathbf{M}_2,\mathbf{H}_2\left(\mathbf{M}_2,2dn\right)\right\rangle+4\sum_{n=1}^{\infty}\left\langle \mathbf{M}_2,\mathbf{H}_2\left(\mathbf{M}_1,(2n-1)d\right)\right\rangle-\\&4\left\langle \mathbf{M}_2,\mathbf{H}_2\left(\mathbf{M}_2,0\right)\right\rangle=0\end{aligned}\tag{55}$$

Note that the A, B, and C superscripts have been dropped from the magnetic field terms $\mathbf{H}_1$ and $\mathbf{H}_2$ in both equations; this is because after applying image theory, these radiated magnetic fields are calculated with respect to free space and do not depend on the various regions.

Harrington's equivalent circuit formulation of a single-layer, single-aperture problem (Fig. 33) can now be extended to this two-layer problem The following scalar circuit quantities are defined from (54)-(55):

$$I_1=\left\langle \mathbf{M}_1,\mathbf{H}_{imp}\right\rangle_1\tag{56}$$

$$Y_{s1}^{hs} = \left\langle \mathbf{M}_1, \mathbf{H}_1\left(\mathbf{M}_1, 0\right)\right\rangle_1 \tag{57}$$

$$Y_{s1}^{i} = \sum_{n=1}^{\infty} \left\langle \mathbf{M}_1, \mathbf{H}_1\left(\mathbf{M}_1, 2dn\right)\right\rangle_1 \tag{58}$$

$$Y_{mz}^{i} = \sum_{n=1}^{\infty} \left\langle \mathbf{M}_1, \mathbf{H}_1\left(\mathbf{M}_2, (2n-1)d\right)\right\rangle_1 = \sum_{n=1}^{\infty} \left\langle \mathbf{M}_2, \mathbf{H}_2\left(\mathbf{M}_1, (2n-1)d\right)\right\rangle_2 \tag{59}$$

$$Y_{s2}^{hs} = \left\langle \mathbf{M}_2, \mathbf{H}_2\left(\mathbf{M}_2, 0\right)\right\rangle_2 \tag{60}$$

$$Y_{s2}^{i} = \sum_{n=1}^{\infty} \left\langle \mathbf{M}_2, \mathbf{H}_2\left(\mathbf{M}_2, 2dn\right)\right\rangle_2 \tag{61}$$

Here, the inner product subscripts denote surface integrals over either aperture 1 or 2. More explicitly, if S_1 and S_2 are the areas of the two apertures, respectively, then:

$$\begin{aligned} \left\langle \mathbf{A}, \mathbf{B}\right\rangle_1 &= \iint_{S_1} \mathbf{A} \cdot \mathbf{B} dS_1 \\ \left\langle \mathbf{A}, \mathbf{B}\right\rangle_2 &= \iint_{S_2} \mathbf{A} \cdot \mathbf{B} dS_2 \end{aligned} \tag{62}$$

The scalar quantities (56)-(61) and the system of equations (54)-(55) can be used to form an equivalent network for the two-layer aperture problem, shown in Fig. 46. The equivalent network comprises two single-port networks (corresponding to regions A and C of the aperture problem) and a two-port network (corresponding to region B).

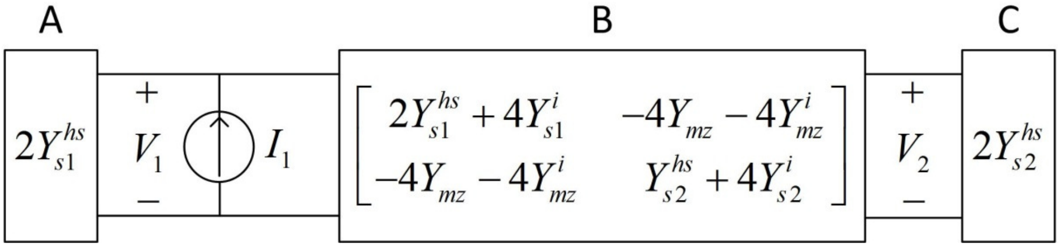

Fig. 46. Equivalent network of dual-layer problem with one aperture on each layer.

For this network, “port 1” is defined as the port between networks A and B, and “port 2” is defined to the port between regions B and C. I_1 is an input current source at port 1 that accounts for the incident plane wave in region A. Note that no current source exists at port 2 since there is no incident field from region C. The one-port network for region A comprises the aperture 1 halfspace self admittance Y_{s1}^{hs} (57). Similarly, the one-port network for region C comprises the aperture 2 halfspace self admittance Y_{s2}^{hs} (60). The two-port network of region B consists of several admittance terms, including the same halfspace self admittances as in regions A and C. Two “self image” terms, Y_{s1}^{i} (58) and Y_{s2}^{i} (61), account for all of the images of the two magnetic currents due to the dual ground planes. Y_{mz}^{i} (59) is a “mutual image” term that contains the mutual coupling between the two layers, along with the mutual coupling due to the infinite images. Note that because of reciprocity, (59) can be calculated as an inner product over either aperture.

The three "image" terms - Y_{s1}^{i}, Y_{s2}^{i}, and Y_{mz}^{i} - comprise one-dimensional infinite summations of inner products involving the magnetic current images. It turns out that these one-dimensional summations are slowly converging series (much like the slowly converging two-dimensional series of (15) and Fig. 31). In fact, the sum of the sum of these images can be readily handled by a one-dimensional version of the Shanks transformation. The specific formulation is similar the two-dimensional version and, for brevity, will not be repeated here. In summary, these three admittance terms are computed by determining a finite number of the images and then applying the Shanks transformation to (58), (59), and (61).

The network of Fig. 46 can be summarized in matrix form by rewriting (54)-(55) using the circuit quantities (56)-(61):

$$\begin{bmatrix} I_1 \\ 0 \end{bmatrix} = \begin{bmatrix} 4Y_{s1}^{hs} + 4Y_{s1}^{i} & -4Y_{mz} - 4Y_{mz}^{i} \\ -4Y_{mz} - 4Y_{mz}^{i} & 4Y_{s2}^{hs} + 4Y_{s2}^{i} \end{bmatrix} \begin{bmatrix} V_1 \\ V_2 \end{bmatrix} \tag{63}$$

The port voltages V_1 and V_2 represent the magnitudes of the fields on the apertures. Obviously, these voltages can be solved for by simple matrix inversion. As mentioned earlier, the three infinite image terms are calculated by taking a finite number of images and applying a one-dimensional version of the Shanks transformation.

Dual-Layer Aperture Problem #2

The aperture problem of Fig. 44 accounts for the coupling between apertures on two different layers. It is also important to consider another related multilayer aperture problem: the case of two apertures residing on the same layer backed by a second layer. This problem is illustrated in Fig. 47 and accounts for the coupling between apertures on a single layer in the presence of a second layer. Again, the problem is divided into regions A, B, and C, and the equivalence principle is used to close off the apertures and derive equivalent problems in reach region. Note that the equivalent problem in region C is trivial because no equivalent magnetic current exists there.

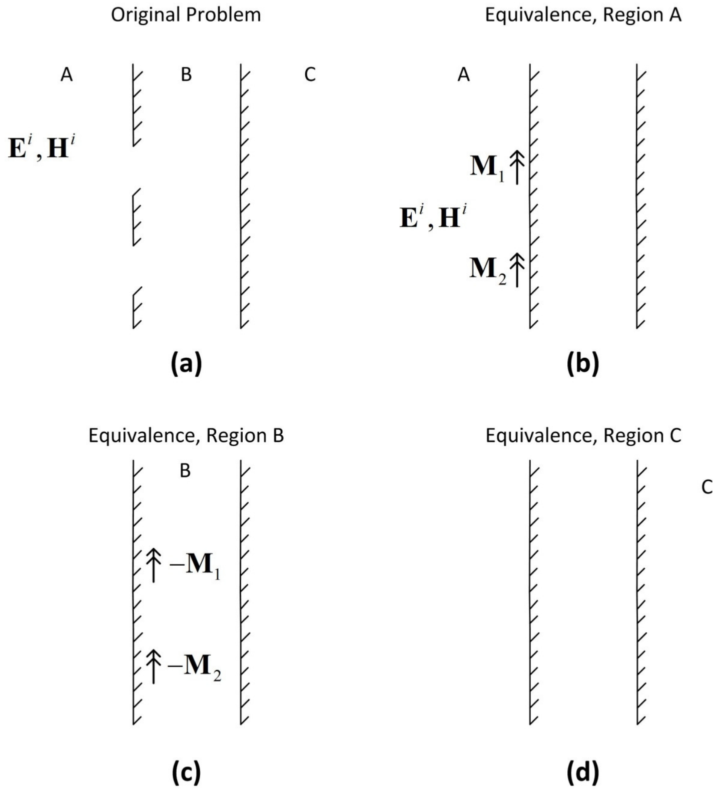

Fig. 47. Dual-layer aperture problem with two apertures on one first layer. (a) Original problem and equivalent problems in (b) region A, (c) region B, and (d) region C.

As is done in (50)-(51) for the problem of Fig. 44, a system of two equations can be written to enforce the boundary conditions at the two apertures of Fig. 47:

$$\begin{gathered}\mathbf{H}_{imp}+2\mathbf{H}_1^A\left(\mathbf{M}_1,0\right)+2\mathbf{H}_1^A\left(\mathbf{M}_2,0\right)= \\ -2\mathbf{H}_1^B\left(\mathbf{M}_1,0\right)-2\mathbf{H}_1^B\left(\mathbf{M}_2,0\right)-4\sum_{n=1}^{\infty}\mathbf{H}_1^B\left(\mathbf{M}_1,2dn\right)-4\sum_{n=1}^{\infty}\mathbf{H}_1^B\left(\mathbf{M}_2,2dn\right)\end{gathered} \tag{64}$$

$$\begin{gathered}\mathbf{H}_{imp}+2\mathbf{H}_2^A\left(\mathbf{M}_2,0\right)+2\mathbf{H}_2^A\left(\mathbf{M}_1,0\right)= \\ -2\mathbf{H}_2^B\left(\mathbf{M}_2,0\right)-2\mathbf{H}_2^B\left(\mathbf{M}_1,0\right)-4\sum_{n=1}^{\infty}\mathbf{H}_2^B\left(\mathbf{M}_2,2dn\right)-4\sum_{n=1}^{\infty}\mathbf{H}_2^B\left(\mathbf{M}_1,2dn\right)\end{gathered} \tag{65}$$

Equation (64) is written with respect to aperture 1 and (65) with respect to aperture 2. Again, the left hand side of the equations corresponds to the fields in region A, whereas the right hand side of the equations corresponds to region B.

Next, the inner product of (64) with $\mathbf{M}_1$ (i.e. a surface integral over aperture 1) is computed. The equivalence relations $\mathbf{H}_1^A(\mathbf{M}_1,0)=\mathbf{H}_1^B(\mathbf{M}_1,0)=\mathbf{H}_1(\mathbf{M}_1,0)$ and $\mathbf{H}_1^A(\mathbf{M}_2,0)=\mathbf{H}_1^B(\mathbf{M}_2,0)=\mathbf{H}_1(\mathbf{M}_2,0)$ are employed, as well as the linearity of the inner product and summation operators. The result is:

$$\begin{gathered}\left\langle \mathbf{M}_1,\mathbf{H}_{imp}\right\rangle_1+4\left\langle \mathbf{M}_1,\mathbf{H}_1(\mathbf{M}_1,0)\right\rangle_1+4\left\langle \mathbf{M}_1,\mathbf{H}_1(\mathbf{M}_2,0)\right\rangle_1=\\-4\sum_{n=1}^{\infty}\left\langle \mathbf{M}_1,\mathbf{H}_1(\mathbf{M}_1,2dn)\right\rangle_1-4\sum_{n=1}^{\infty}\left\langle \mathbf{M}_1,\mathbf{H}_1(\mathbf{M}_2,2dn)\right\rangle_1\end{gathered}\tag{66}$$

A similar inner product with $\mathbf{M}_2$ is applied to (65), yielding:

$$\begin{gathered}\left\langle \mathbf{M}_2,\mathbf{H}_{imp}\right\rangle_2+4\left\langle \mathbf{M}_2,\mathbf{H}_2(\mathbf{M}_2,0)\right\rangle_2+4\left\langle \mathbf{M}_2,\mathbf{H}_2(\mathbf{M}_1,0)\right\rangle_2=\\-4\sum_{n=1}^{\infty}\left\langle \mathbf{M}_2,\mathbf{H}_2(\mathbf{M}_2,2dn)\right\rangle_2-4\sum_{n=1}^{\infty}\left\langle \mathbf{M}_2,\mathbf{H}_2(\mathbf{M}_1,2dn)\right\rangle_2\end{gathered}\tag{67}$$

The following scalar circuit quantities can be defined using terms from (66)-(67):

$$I_1=\left\langle \mathbf{M}_1,\mathbf{H}_{imp}\right\rangle_1\tag{68}$$

$$Y_{s1}^{hs}=\left\langle \mathbf{M}_1,\mathbf{H}_1(\mathbf{M}_1,0)\right\rangle_1\tag{69}$$

$$Y_{s1}^{i}=\sum_{n=1}^{\infty}\left\langle \mathbf{M}_1,\mathbf{H}_1(\mathbf{M}_1,2dn)\right\rangle_1\tag{70}$$

$$Y_{m}^{hs}=\left\langle \mathbf{M}_1,\mathbf{H}_1(\mathbf{M}_2,0)\right\rangle_1=\left\langle \mathbf{M}_2,\mathbf{H}_2(\mathbf{M}_1,0)\right\rangle_2\tag{71}$$

$$Y_{m}^{i}=\sum_{n=1}^{\infty}\left\langle \mathbf{M}_1,\mathbf{H}_1(\mathbf{M}_2,2dn)\right\rangle_1=\sum_{n=1}^{\infty}\left\langle \mathbf{M}_2,\mathbf{H}_2(\mathbf{M}_1,2dn)\right\rangle_2\tag{72}$$

$$I_2 = \left\langle \mathbf{M}_2, \mathbf{H}_{imp} \right\rangle_2 \tag{73}$$

$$Y_{s2}^{hs} = \left\langle \mathbf{M}_2, \mathbf{H}_2\left(\mathbf{M}_2, 0\right) \right\rangle_2 \tag{74}$$

$$Y_{s2}^{i} = \sum_{n=1}^{\infty} \left\langle \mathbf{M}_2, \mathbf{H}_2\left(\mathbf{M}_2, 2dn\right) \right\rangle_2 \tag{75}$$

These circuit quantities can be used to construct an equivalent network. I_1 and I_2 are the input currents to this network that depend on the incident field. Y_{s1}^{hs} and Y_{s2}^{hs} are the halfspace self admittances of the two apertures, while Y_{s1}^{i} and Y_{s2}^{i} are the corresponding "self image" terms comprising infinite series of images associated with region B. Y_{m}^{hs} is the halfspace mutual admittance between the two apertures, and Y_{m}^{i} is the corresponding "mutual image" term for region B (which is also an infinite series of images). Note that Y_{m}^{hs} and Y_{m}^{i} can be calculated, due to reciprocity, by employing either an inner product over aperture 1 or an inner product over aperture 2.

The network representation for this dual-layer problem - extend from Harrington's original single aperture equivalent network - is shown in Fig. 48 (again, corresponding to the physical problem in Fig. 47). Note that two one-port networks represent region A (one for each aperture), while a single two-port network represents region B; there is no network for region C, as it is electromagnetically isolated from the incident field by the second ground plane.

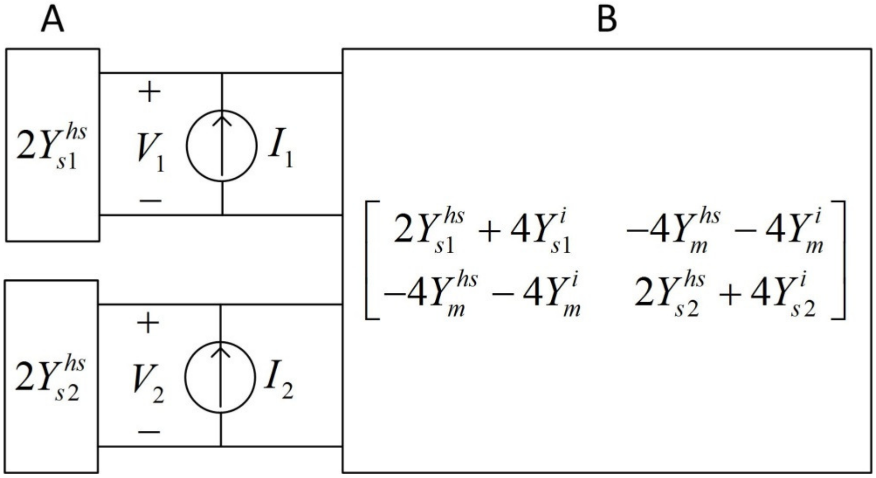

Fig. 48. Equivalent network of dual-layer problem with two apertures on one layer.

Dual-Layer Lattice Model

The equivalent networks of Fig. 46 and Fig. 48 form the building blocks of the infinite multiport lattice network for any multilayer FSS. Any FSS of more than two layers can always be broken down, using the equivalence principle, into equivalent problems involving only two ground planes (as in Fig. 46 and Fig. 48), from which the whole lattice can be constructed. As the number of apertures and layers increases, the lattice may become increasingly difficult to visualize conceptually. However, Fig. 49 illustrates, from a three-dimensional perspective, what the lattice may look like in the case of a two-layer design. For simplicity, two arbitrarily-shaped apertures are cut into the first ground plane, and a third arbitrarily-shaped aperture is cut into the second ground plane. It is understood that additional apertures could extend this FSS to infinity; likewise, the lattice structure shown is understood to only be a finite section (specifically, only three network ports) of an otherwise infinite lattice. As before, the two FSS screens of this dual-layer case separate the problem into three regions: A, B, and C. An incident field is assumed in region A, leading to input currents I_1 and I_2 to the first two aperture ports.

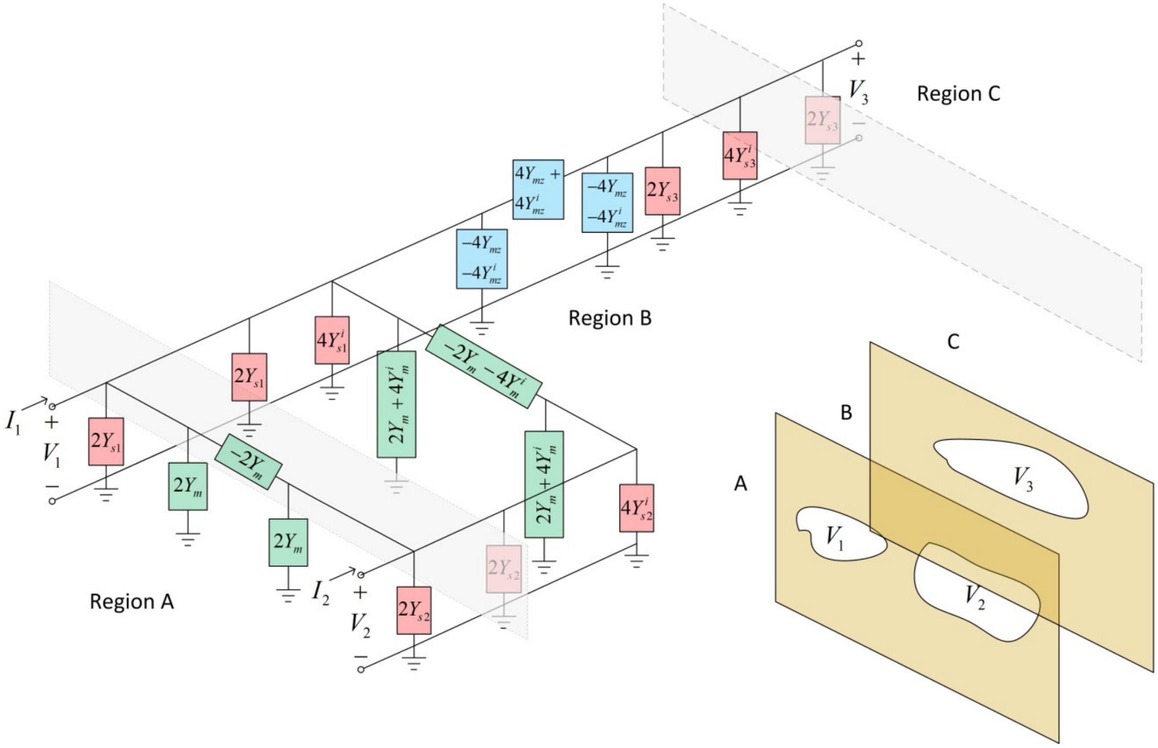

Fig. 49. Extension of lattice model to two-layer FSS design.

The lattice in region A looks identical to that of Fig. 28: a pi-network connects two self admittance elements. In region B, there is still a pi-network connection (green) between apertures on the same FSS layer, but the elements of the pi-network contain the additional "image terms" (58), (59), (61), (70), (72), and (74) that account for the infinite series of images due to the dual ground planes. Note that the self image terms (70) and

(74) are essentially the same kinds of terms as (58) and (61); they are simply derived from two different dual-layer problems. There is also an additional pi-network (blue) in region B that accounts for the coupling between apertures on different layers. This coupling network contains the additional image term (59). In all, there are six unique types of admittance terms that can be identified in the multilayer lattice: standard self admittances, standard mutual admittances between apertures on the same layer, standard mutual admittances between apertures on different layers, "self image" terms, "mutual image" terms between apertures on the same layer, and "mutual image" terms between apertures on different layers. These basic categories of multilayer admittances will not change if additional layers are added to the FSS.

As for the single-element and multi-element formulations of the lattice model, the multilayer lattice under uniform normal plane wave incidence can be collapsed to a much simpler network based on symmetry arguments. The collapsed network of a two-layer, single-element design is shown in Fig. 50. It is a two-port network, with the voltages on each port corresponding to the field amplitudes on each of the two FSS layers. Like the two-port network of Fig. 42 (b), this network involves three infinite admittance terms. The specific definitions of these admittances will not be elaborated on here. These admittances, as before, can be handled using a Shanks transform.

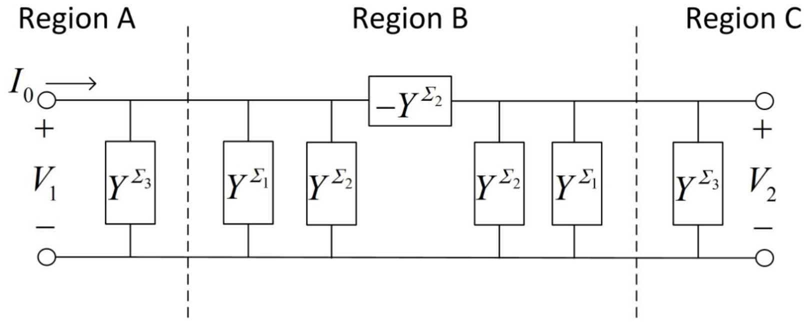

Fig. 50. Collapsed two-layer network under uniform plane wave incidence.

To illustrate the multilayer extension of the lattice model, a dual-layer, single-element rectangular aperture FSS is designed. The unit cell geometry on both layers is assumed to be identical to that of Fig. 37 (with the same dimensions on both layers). The assigned dimensions are $L = 4$ mm, $W = 0.2$ mm, $D_x = 5$ mm, and $D_y = 2$ mm. The two FSS layers are separated by duroid (relative permittivity $\varepsilon_r = 2.2$) with a thickness of 62 mil. The computed performance of this FSS using the lattice model are shown in Fig. 51 and compared to simulated results with very good agreement. The design achieves second-order passband response that covers much of the Ku-band (26.5-40 GHz).

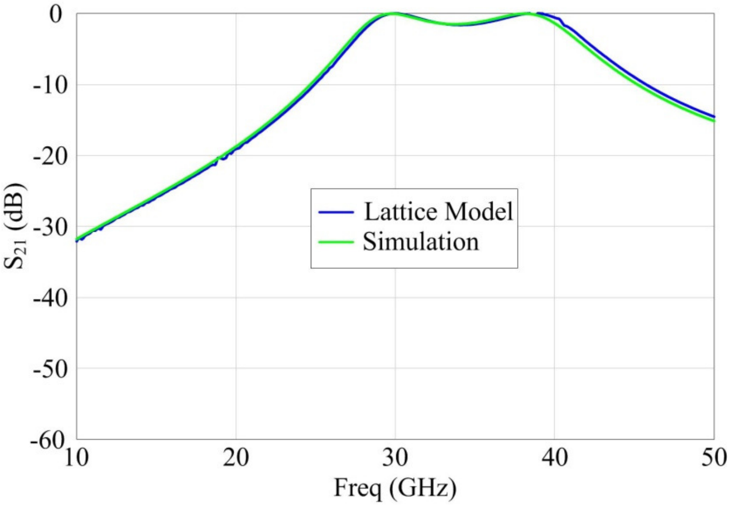

Fig. 51. Performance of a dual-layer, single-element rectangular aperture FSS.

Extension to Reconfigurable Designs

As discussed in Chapter II, FSSs can be functionalized by a wide variety of reconfiguration mechanisms, ranging from electrical components controlled by DC biasing to purely mechanical methodologies. The lattice model, in principle, is general enough in its formulation that any number of these reconfiguration mechanisms can be readily incorporated into it. The details of how to incorporate any one reconfiguration mechanism into the model will be different for each mechanism.

Broadly speaking, most approaches to constructing a lattice model for a reconfigurable FSS can be lumped into one of two categories: the reconfiguration method is accounted for in the EM domain or in the circuit domain. The most direct way to account for the reconfiguration mechanism is to do so entirely in the EM domain. In other words, all of the self and mutual admittance calculations using isolated resonant elements are performed with the reconfiguration mechanism included. In this case, the circuit domain problem remains unchanged. This method should be applicable to almost any type of reconfiguration mechanism. The second approach involves accounting for the reconfiguration entirely in the circuit domain. In this approach, the lattice is first constructed assuming no reconfiguration mechanism; then, additional admittances are added that account for the reconfiguration. This approach assumes that appropriate equivalent admittances can be computed for the reconfiguration mechanism that are independent of the admittances of the FSS itself without the reconfiguration mechanism. Consequently, this approach may not be feasible for every type of FSS.

For the purposes of this work, only a single type of reconfigurable FSS will be considered: varactor-tuned rectangular apertures. This type of tunable FSS was introduced in Fig. 12 of Chapter II. The varactor reconfiguration can be accounted for entirely in the circuit domain, as will be shown. This particular reconfigurable FSS is intended to serve as a simple illustration of the model's applicability to reconfigurable designs; it is by no means meant to elucidate how other reconfiguration mechanisms might be handled. An exhaustive treatment of various reconfiguration mechanisms using the lattice model is beyond the scope of the current work.

Fig. 52 shows the unit cell geometry of a rectangular aperture FSS tuned by a varactor to be used in this work. The geometry is identical to that of Fig. 37, except that the varactor (in red) is added at the middle of the aperture. The varactor spans the width of the rectangular aperture, and its two terminals are assumed to contact the ground plane on either side of the aperture. A DC voltage drop applied across the terminals of the varactor will cause a capacitance C to appear between these terminals. For simplicity, the DC biasing scheme necessary for such a design will not be considered here (see [30] for an example of how a biasing scheme might be implemented).

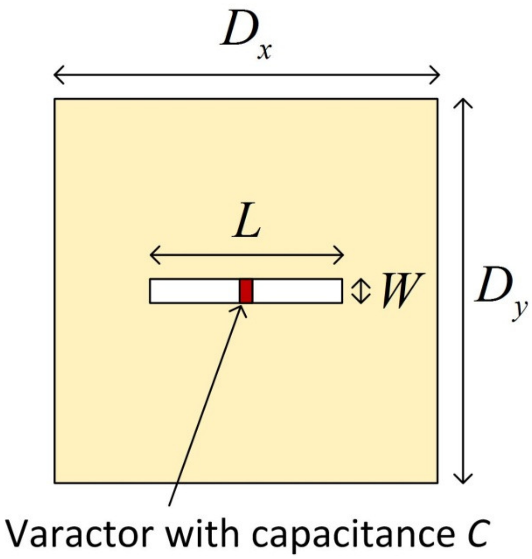

Fig. 52. Unit cell geometry of varactor-tuned rectangular aperture FSS.

The capacitive admittance Y_c associated with the varactor capacitance C can be directly incorporated into the circuit domain of the lattice model. Specifically, the lattice structure is initially identical to that discussed for the single-element, single-layer FSS of Chapter IV, and the self and mutual admittances are identical to those calculated for the same structure in Chapter V. In this case, Y_c is added in parallel to the self admittance term at each port in the lattice. The reasoning behind this modification can be argued heuristically as follows. The lattice port voltages correspond to electric potential drop across the width of the apertures caused by the y-directed electric field on the apertures. Placing the capacitive admittance of the varactors across the apertures causes the electric field excited on the apertures to be modified; the port voltage are consequently modified in proportion to this. It follows, then, that Y_c can be added across the terminals of the lattice ports - that is, in parallel to the self admittance elements. In terms of the finite collapsed one-port network of Fig. 29, Y_c is simply added to the infinite admittance summation (14). In other words:

$$Y^{\Sigma} = Y_s + \sum_k Y_{m,k} + Y_c \tag{76}$$

Thus, the performance of the FSS for different capacitive values of the varactor can be determined by simply modifying the circuit domain analysis of the model; the lattice admittances do not have to be recalculated for each reconfiguration state.

The performance of such a reconfigurable aperture FSS, as computed by both the lattice model and simulation, is shown in Fig. 53. The simulated results are obtained by simulating the rectangular aperture FSS in [39] without the varactor. In addition to the two typical waveports used to excite the FSS with plane waves from either direction, the simulation includes a third "lumped port" spanning the aperture. This third port measures the voltage between the points where the terminals of the varactor would otherwise be located. Thus, the simulation is effectively performed with the varactor terminals open-circuited. The results are exported in the form of equivalent three-port parameters; this three-port network is then post-processed in [58]. The third port of the network is terminated in a capacitive admittance to simulate the varactor being tuned to different capacitances. After termination, the resulting network is analyzed for its equivalent two-port parameters; these parameters represent the performance of the FSS tuned by the varactor. The details of this simulation procedure are provided in Appendix B.

The dimensions for this particular design are $L = 10$ mm, $W = 0.5$ mm, $D_x = 15$ mm, and $D_y = 7$ mm. The varactor is assigned capacitance values of 0.05 pF, 0.1 pF, and 0.1 pF. Good agreement is achieved between the lattice model and simulation. The design achieves frequency reconfiguration between 9 and 13 GHz.

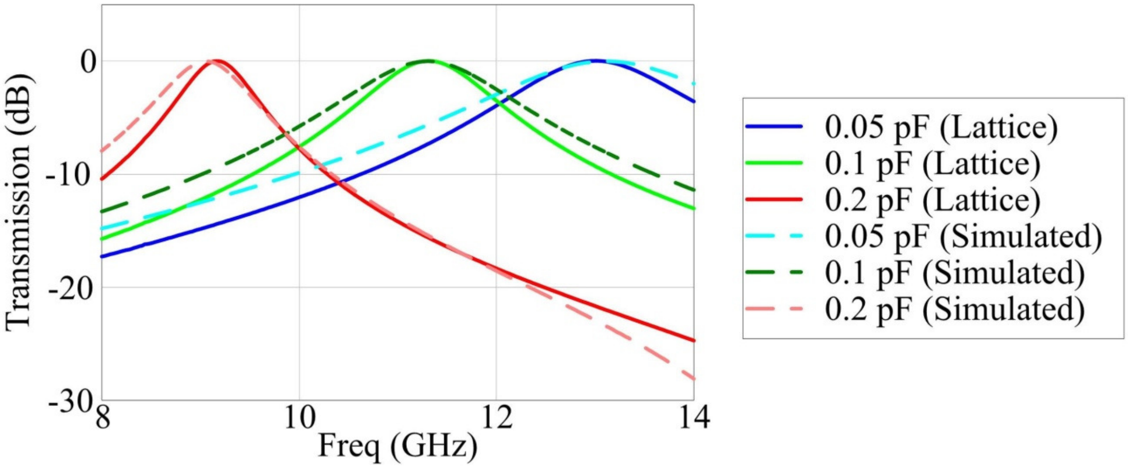

Fig. 53. Performance of a varactor-tuned FSS.

CHAPTER VII

NON-UNIFORM INCIDENCE

Chapters IV, V, and VI all developed the lattice model under the assumption of uniform normal plane wave incidence. This assumption leads to symmetry in the input currents and excited port voltages on the lattice, allowing the infinite multiport network to be collapsed into an equivalent network with a finite number of ports. The reduction of an infinite FSS lattice to a finite network is a convenient result, but it does not apply to cases of non-uniform incidence. This is of much practical importance for cases such as oblique incidence, spot beam illumination, etc. Most practical FSS applications must account for some type of non-uniform incidence. It can also be applicable in the analysis of finite FSSs with a large number of elements: a decent approximation is to consider an infinite FSS that is locally illuminated.

As discussed in Chapter IV, the multiport lattice network of Fig. 28 can be analyzed under any arbitrary set of inputs current using in terms of a general lattice Green's function. However, the practical implementation of this analysis using (10)-(12) for any specific situation may be quite cumbersome. In order to facilitate the practical study of non-uniform incidence, then, a “spectral domain” version of the lattice model is developed using a two-dimensional (2D) discrete Fourier transform (DFT). As will be shown, the lattice model under this formulation provides a unique way of approaching different cases of non-uniform incidence: changes in the incident field can be accounted for entirely in the circuit domain, with no need to recalculate the admittances of the EM domain. For the purposes of this paper, only the case of oblique incidence will be considered explicitly, but application to other cases would follow a similar procedure.

This chapter begins with a short discussion about some of the features and benefits of the lattice model regarding non-uniform incidence. Then, the 2D DFT formulation of the lattice model is developed. The analysis is first outlined for the single-element, single-mode case; it is then extended to a multimode case (or, equivalently, a multi-element case). The multilayer version of the DFT analysis is also discussed. Next, the specific case of oblique plane wave incidence is considered. Computational examples are provided comprising rectangular aperture resonant elements.

General Considerations for Non-Uniform Incidence

An important feature of the lattice model under non-uniform incidence is that the lattice admittances are identical to those calculated for the case of uniform normal incidence. Thus, once these admittances are calculated for the normal incidence case, they can be used for other arbitrary incident fields, and no further calculations in the EM domain are necessary. Changing the incident field is accounted for entirely in the circuit domain by modifying the magnitude and phase of the lattice current excitations.

A rigorous treatment of this claim - that the same lattice admittances can be used for both normal and non-uniform incidence - is beyond the scope of this paper. However, in lieu of this, a simple heuristic argument can be submitted. As an example, it is easy to revisit the aperture problem of Fig. 3 and reformulate it for an oblique incidence. The same can be done for the two-aperture mutual admittance problem. In either case, one can show that the extracted admittance values (self or mutual) are the same as in the normal incidence case. This result is, in fact, fairly intuitive, since the admittances essentially determine a scaling ratio between the incident field and the corresponding fields excited on the apertures. The scaling ratio will be the same for an incident field of any angle, even though the actual magnitude of the fields will be different at different angles.

DFT Analysis of Lattice

For any case of non-uniform incidence, the general case of arbitrary input currents to the lattice must be solved. However, rather than dealing with the lattice Green's function directly, an alternative approach is to solve the difference equation (8) using a 2D DFT. The DFT is applied to the difference equation to transform the problem into the "spectral domain". Here, "spectral domain" refers to the fact that the transform is performed with respect to spatial variables, rather than with respect to a time variable (for which the transform domain is typically referred to as the "frequency domain").

This approach is exactly analogous to any number of spectral domain solutions commonly employed in EM problems, in which a continuous Fourier transform is applied (e.g. [19], [38]). The primary difference is that in this case, a discrete transform is applied to a discrete-valued difference equation, whereas in classic spectral domain analysis, a continuous transform is applied to a continuous-valued differential equation.

Discrete Fourier Transform Theory

Conceptually, the DFT yields a discrete "frequency spectrum" representation of a discrete periodic signal. The basic one dimensional version of the transform is considered first before being extended to two dimensions. Several variable definitions of the DFT exist; for the purposes of this work, the DFT is defined by the following transform pair:

$$f\left[n\right]\Leftrightarrow\tilde{f}\left[k\right] \tag{77}$$

$$\tilde{f}\left[k\right]=\sum_{x=1}^{N}f\left[x\right]e^{-j2\pi(k-1)(n-1)/N} \tag{78}$$

$$f\left[n\right]=\frac{1}{N}\sum_{k=1}^{N}\tilde{f}\left[k\right]e^{j2\pi(k-1)(n-1)/N} \tag{79}$$

Here, the function $f\left[n\right]$ - which is a function of the discrete variable n - is assumed to have a period of N. The transform, computed via (78), is referred to as an N-point DFT. The transformed function $\tilde{f}\left[k\right]$ is a function of the discrete transform variable k. The original function $f\left[n\right]$ can be recovered from $\tilde{f}\left[k\right]$ using the inverse transform (79). An important property of this transform, relevant to its application to difference equations, is the so-called shift property:

$$f\left[n-a\right]\Leftrightarrow\tilde{V}\left[k\right]e^{-j2\pi(k-1)a/N} \tag{80}$$

In words, this property dictates that if the original function $f\left[n\right]$ is shifted by an integer n_a, the DFT of the shifted function $f\left[n-n_a\right]$ is equal to the DFT of the original function, $\tilde{f}\left[k\right]$, multiplied by a complex exponential factor.

The DFT can easily be extended to a two-dimensional formulation. Given discrete variables n_x and n_y and a two-dimensional function $f\left[n_x,n_y\right]$, the transform pair becomes:

$$f\left[n_x,n_y\right] \Leftrightarrow \tilde{f}\left[k_x,k_y\right] \tag{81}$$

$$\tilde{f}\left[k_x,k_y\right] = \sum_{x=1}^{N_x}\sum_{y=1}^{N_y} f\left[n_x,n_y\right] e^{-j2\pi\left[(k_x-1)(n_x-1)/N_x+(k_y-1)(n_y-1)/N_y\right]} \tag{82}$$

$$f\left[n_x,n_y\right] = \frac{1}{N}\sum_{k_x=1}^{N_x}\sum_{k_y=1}^{N_y} \tilde{f}\left[k_x,k_y\right] e^{j2\pi\left[(k_x-1)(n_x-1)/N_x+(k_y-1)(n_y-1)/N_y\right]} \tag{83}$$

The transform is now referred to as an $N_x \times N_y$-point DFT. Also, the shift property can be extended to two dimensions:

$$f\left[n_x-a,n_y-b\right] \Leftrightarrow \tilde{f}\left[k_x,k_y\right] e^{-j2\pi\left[(k_x-1)a/N_x+(k_y-1)b/N_y\right]} \tag{84}$$

In this work, the transform variables k_x and k_y are referred to as spectral domain variables, since the transform is applied to the discrete spatial variables n_x and n_y. This maintains analogy to classic spectral domain analysis using continuous variables.

Single-Element, Single-Mode FSS

The two-dimensional version of the transform is now used to solve the difference equation governing the lattice of a single-element, single-mode FSS shown in Fig. 28. First, the original lattice difference equation (8) is rewritten as follows:

$$\left(Y^s + \sum_n Y_n^m\right) V\left[n_x, n_y\right] - \sum_n Y_n^m \left(V\left[n_x, n_y\right] - V\left[n_x + a_n, y + b_n\right]\right) = I\left[n_x, n_y\right] \tag{85}$$

Here, a_n and b_n are integers corresponding to spatial shifts in the x and y dimensions of the lattice, respectively. Applying the transform (82) and the shift property (84) to (85) yields:

$$\begin{aligned} &\left(Y^s + \sum_n Y_n^m\right) \tilde{V}\left[k_x, k_y\right] - \\ &\sum_n Y_n^m \left(\tilde{V}\left[k_x, k_y\right] - \tilde{V}\left[k_x, k_y\right] e^{-j2\pi\left[(k_x-1)a_n/N_x + \left(k_y-1\right)b_n/N_y\right]}\right) = \tilde{I}\left[k_x, k_y\right] \end{aligned} \tag{86}$$

The transform effectively changes the difference equation in terms of $V\left[n_x, n_y\right]$ to a purely algebraic equation in terms of a spectral domain voltage $\tilde{V}\left[k_x, k_y\right]$. Solving (86) algebraically for $\tilde{V}\left[k_x, k_y\right]$ yields:

$$\tilde{V}\left[k_x, k_y\right] = \frac{\tilde{I}\left[k_x, k_y\right]}{Y^s + \sum_n Y_n^m e^{-j2\pi\left[(k_x-1)a_n/N_x + \left(k_y-1\right)b_n/N_y\right]}} \tag{87}$$

Note that this solution is valid for any arbitrary input current $I\left[n_x, n_y\right]$. Given a specific input current, the port voltages can be obtained by transforming $I\left[n_x, n_y\right]$ and calculating the lattice admittances as usual; then, (87) is computed, and the inverse transform (83) is applied to recover $V\left[n_x,n_y\right]$ from $\tilde{V}\left[k_x,k_y\right]$.

The necessary size of the two-dimensional DFT, $N_x \times N_y$, depends on the nature of the input current $I\left[n_x,n_y\right]$. Three general cases can be identified. The simplest case, which has already been extensively discussed, is that of uniform normal plane wave incidence. In this case, the port voltages and currents are known, *a priori*, to be identical across the entire lattice; in other words, the solution is "periodic" in two dimensions with a period of one in both directions. Thus, any choice of $N_x \geq 1$, $N_y \geq 1$ would suffice to give the correct solution, with $N_x = N_y = 1$ obviously being the easiest choice. Furthermore, when $N_x = N_y = 1$, the transform variables $k_x = k_y = 1$, and (87) reduces to:

$$\tilde{V}\left[k_x,k_y\right] = \frac{\tilde{I}\left[k_x,k_y\right]}{Y^s + \sum_n Y_n^m + \sum_n Y_n^m \left(1-1\right)} = \frac{\tilde{I}\left[k_x,k_y\right]}{Y^s + \sum_n Y_n^m} \tag{88}$$

Note that the denominator is now independent of the transform variables k_x and k_y. Thus, the inverse transform of (88) can be found explicitly as:

$$V\left[x,y\right] == \frac{I\left[x,y\right]}{Y^s + \sum_n Y_n^m} \tag{89}$$

Observe that this is identical to the solution obtained when symmetry was used to collapse the lattice network down into a single port network, as in Fig. 29; the denominator of (89) is equivalent to the infinite summation of impedances (14). Thus, under uniform normal plane wave incidence, the DFT lattice solution is identical to that already obtained.

The second general case of arbitrary input currents to the lattice is when $I\left[n_x, n_y\right]$ is periodic with an integer period greater than one. Specifically, if the periodicity is $N_x \times N_y$, it is quite clear, from the definition of the transform, that the size of the corresponding DFT must be chosen as $N_x \times N_y$. This DFT will result in an exact solution to the lattice problem via (87), and the port voltages will also be two-dimensionally periodic with period $N_x \times N_y$.

The third and final case of arbitrary input currents is when $I\left[n_x, n_y\right]$ has a non-integer periodicity or is completely aperiodic. In this case, computation of the exact solution from (87) is not possible, since the DFT transform itself assumes a periodic solution with integer periodicity. In other words, the solution will only be approximate, and the DFT is used here as a finite approximation to the exact infinite solution. This is done for computational and practical reasons. The size of the DFT necessary for an acceptably accurate solution will depend on the specific case of non-uniform incidence under consideration. The larger the number of terms in the DFT, the more accurate the final solution will be.

An observation regarding the general DFT solution (87) is that the denominator is essentially an infinite summation of admittances in the spectral domain, analogous to the infinite summation (14) in the spatial domain for normal incidence. The summation only differs by the presence of a complex exponential factor, which is a function of the spectral domain variables k_x and k_y. In the spatial domain, the summation encountered was very slowly converging. Even in the spectral domain, however, the analogous summation is still a slowly converging series. In practice, no discernible advantage in convergence is obtained in either the spatial or spectral domain. The infinite spectral domain sum can be approximated using the Shanks transformation, as was done in the spatial domain. However, this summation must be computed separately at all values of k_x and k_y. In this sense, the DFT solution for arbitrary input currents will be more expensive than the spatial domain solution for uniform inputs. It is also clear that minimizing the size of the DFT is desirable for computational efficiency.

DFT Formulation of Multiport Unit Cells

The multi-mode representation of a single-element FSS can also be analyzed using the DFT formulation of lattice theory. Multi-element designs can be analyzed in the same manner. The analysis is identical because both classes of FSS comprise multiple lattice ports per unit cell. For a single aperture with N lattice ports, a system of N finite difference equations can be written:

$$\begin{gathered}
\left(Y_1^s+\sum_j\sum_{\substack{i=1\\ i\neq 1}}^{N}Y_{1,i,j}^m\right)V_1\left[n_x,n_y\right]-\sum_j\sum_{\substack{i=1\\ i\neq 1}}^{N}Y_{1,i,j}^m\begin{pmatrix}V_1\left[n_x,n_y\right]-\\ V_{i,j}\left[n_x+a_j,n_y+b_j\right]\end{pmatrix}=I_1\left[n_x,n_y\right]\\
\left(Y_2^s+\sum_j\sum_{\substack{i=1\\ i\neq 2}}^{N}Y_{2,i,j}^m\right)V_2\left[n_x,n_y\right]-\sum_j\sum_{\substack{i=1\\ i\neq 2}}^{N}Y_{2,i,j}^m\begin{pmatrix}V_2\left[n_x,n_y\right]-\\ V_{i,j}\left[n_x+a_j,n_y+b_j\right]\end{pmatrix}=I_2\left[n_x,n_y\right]\\
\vdots\\
\left(Y_N^s+\sum_j\sum_{\substack{i=1\\ i\neq N}}^{N}Y_{N,i,j}^m\right)V_N\left[n_x,n_y\right]-\sum_j\sum_{\substack{i=1\\ i\neq N}}^{N}Y_{N,i,j}^m\begin{pmatrix}V_N\left[n_x,n_y\right]-\\ V_{i,j}\left[n_x+a_j,n_y+b_j\right]\end{pmatrix}=I_N\left[n_x,n_y\right]
\end{gathered}\tag{90}$$

These equations are written by applying Kirchhoff's current law to the N ports of a single reference aperture in the FSS; all of the integer indexes are defined with respect to this reference aperture. The index m refers to the multiple ports of the reference aperture itself. Specifically, $V_m\left[n_x,n_y\right]$ is the voltage of the m^{th} port of the reference aperture, $I_m\left[n_x,n_y\right]$ is the input current to that port, and Y_m^s is the self admittance associated with that port. The index j accounts for the other apertures surrounding the reference aperture to which coupling is assumed to exist; the index i accounts for the N ports associated with any specific one of these surrounding apertures. In particular, $Y_{m,i,j}^m$ is the mutual admittance between the m^{th} port of the reference aperture and the i^{th} port of the j^{th} surrounding aperture.

The forward DFT (82) can be applied separately to each equation of (90). The result is a system of N algebraic equations in the spectral domain:

$$\left(Y_1^s + \sum_j \sum_{\substack{i=1 \\ i\neq 1}}^{N} Y_{1,i,j}^m \right) \tilde{V}_1\left[k_x,k_y\right] - \sum_j \sum_{\substack{i=1 \\ i\neq 1}}^{N} Y_{1,i,j}^m \begin{pmatrix} \tilde{V}_1\left[k_x,k_y\right] - \\ \tilde{V}_i\left[k_x,k_y\right] \times \\ e^{-j2\pi\left[(k_x-1)a_j/N_x+(k_y-1)b_j/N_y\right]} \end{pmatrix} = \tilde{I}_1\left[k_x,k_y\right]$$

$$\left(Y_2^s + \sum_j \sum_{\substack{i=1 \\ i\neq 1}}^{N} Y_{2,i,j}^m \right) \tilde{V}_2\left[k_x,k_y\right] - \sum_j \sum_{\substack{i=1 \\ i\neq 2}}^{N} Y_{2,i,j}^m \begin{pmatrix} \tilde{V}_2\left[k_x,k_y\right] - \\ \tilde{V}_i\left[k_x,k_y\right] \times \\ e^{-j2\pi\left[(k_x-1)a_j/N_x+(k_y-1)b_j/N_y\right]} \end{pmatrix} = \tilde{I}_2\left[k_x,k_y\right]$$

$$\vdots$$

$$\left(Y_N^s + \sum_j \sum_{\substack{i=1 \\ i\neq 1}}^{N} Y_{N,i,j}^m \right) \tilde{V}_N\left[k_x,k_y\right] - \sum_j \sum_{\substack{i=1 \\ i\neq N}}^{N} Y_{N,i,j}^m \begin{pmatrix} \tilde{V}_N\left[k_x,k_y\right] - \\ \tilde{V}_i\left[k_x,k_y\right] \times \\ e^{-j2\pi\left[(k_x-1)a_j/N_x+(k_y-1)b_j/N_y\right]} \end{pmatrix} = \tilde{I}_N\left[k_x,k_y\right]$$

(91)

This system of equations can be somewhat simplified:

$$\begin{gathered} Y_1^s\tilde{V}_1\left[k_x,k_y\right] + \sum_j \sum_{\substack{i=1 \\ i\neq 1}}^{N} Y_{1,i,j}^m \tilde{V}_i\left[k_x,k_y\right] e^{-j2\pi\left[(k_x-1)a_j/N_x+(k_y-1)b_j/N_y\right]} = \tilde{I}_1\left[k_x,k_y\right] \\ Y_2^s\tilde{V}_2\left[k_x,k_y\right] + \sum_j \sum_{\substack{i=1 \\ i\neq 2}}^{N} Y_{2,i,j}^m \tilde{V}_i\left[k_x,k_y\right] e^{-j2\pi\left[(k_x-1)a_j/N_x+(k_y-1)b_j/N_y\right]} = \tilde{I}_2\left[k_x,k_y\right] \\ \vdots \\ Y_N^s\tilde{V}_N\left[k_x,k_y\right] + \sum_j \sum_{\substack{i=1 \\ i\neq N}}^{N} Y_{N,i,j}^m \tilde{V}_i\left[k_x,k_y\right] e^{-j2\pi\left[(k_x-1)a_j/N_x+(k_y-1)b_j/N_y\right]} = \tilde{I}_N\left[k_x,k_y\right] \end{gathered} \tag{92}$$

Next, the following summation definition is introduced:

$$Y_{n,i}^{m,k} = \sum_j Y_{n,i,j}^m e^{-j2\pi\left[(k_x-1)a_j/N_x+(k_y-1)b_j/N_y\right]} \tag{93}$$

Specifically, (93) defines a spectral domain summation of mutual admittances between the m^{th} port of the reference aperture and the i^{th} port of all surrounding apertures. In general, this is an infinite summation if an infinite number of surrounding apertures are assumed.

Using (93) in (92) and expanding the remaining summations allows the system of equations to be written in the following form:

$$\begin{gathered}
Y_1^s\tilde{V}_1\left[k_x,k_y\right]+\tilde{V}_2\left[k_x,k_y\right]Y_{1,2}^{m,k}+\cdots+\tilde{V}_N\left[k_x,k_y\right]Y_{1,N}^{m,k}=\tilde{I}_1\left[k_x,k_y\right]\\
Y_2^s\tilde{V}_2\left[k_x,k_y\right]+\tilde{V}_1\left[k_x,k_y\right]Y_{2,1}^{m,k}+\cdots+\tilde{V}_N\left[k_x,k_y\right]Y_{2,N}^{m,k}=\tilde{I}_2\left[k_x,k_y\right]\\
\vdots\\
Y_N^s\tilde{V}_N\left[k_x,k_y\right]+\tilde{V}_1\left[k_x,k_y\right]Y_{N,1}^{m,k}+\cdots+\tilde{V}_{N-1}\left[k_x,k_y\right]Y_{N,N-1}^{m,k}=\tilde{I}_N\left[k_x,k_y\right]
\end{gathered} \tag{94}$$

Finally, the algebraic system of equations (94) can be reorganized into matrix form:

$$\begin{bmatrix} Y_1^s & Y_{1,2}^{m,k} & \cdots & Y_{1,N}^{m,k} \\ Y_{2,1}^{m,k} & Y_2^s & \cdots & Y_{2,N}^{m,k} \\ \vdots & \vdots & \ddots & \vdots \\ Y_{N,1}^{m,k} & Y_{N,2}^{m,k} & \cdots & Y_N^{sh} \end{bmatrix} \begin{bmatrix} \tilde{V}_1\left[k_x,k_y\right] \\ \tilde{V}_2\left[k_x,k_y\right] \\ \vdots \\ \tilde{V}_N\left[k_x,k_y\right] \end{bmatrix} = \begin{bmatrix} \tilde{I}_1\left[k_x,k_y\right] \\ \tilde{I}_2\left[k_x,k_y\right] \\ \vdots \\ \tilde{I}_N\left[k_x,k_y\right] \end{bmatrix} \tag{95}$$

Here, the $N \times N$ matrix is an admittance matrix. Specifically, the diagonal terms are all single self admittances, whereas the off-diagonal terms are infinite summations of mutual admittances defined by (93). Each of these spectral domain summations of admittances must be handled by calculating a finite number of terms and then applying the two-dimensional Shanks transformation to estimate the converged values. The column vector of spectral domain currents can be determined by taking the known spatial input currents and transforming them using the forward DFT. Once the admittance matrix terms and spectral domain currents are known, the matrix system (95) can be solved for the unknown column vector of spectral domain voltages. These are the voltages associated with the N ports of the original unit cell. The spatial domain version of these voltages can be found by employing the inverse two-dimensional DFT (83) individually to each component of the vector.

Extension to Oblique Incidence

Oblique plane wave incidence of arbitrary polarization and angle of incidence is of practical significance to any FSS design, since normal incidence cannot be guaranteed and a variety of incidence angles may be encountered. Oblique incidence is a specific case of non-uniform incidence that involves the phase of the incident field experiencing a linear gradient along the spatial extent of the FSS; the magnitude of the incident field is constant. This case is treated here using the DFT formulation introduced above. For simplicity, only a single-element, single-mode formulation will be considered explicitly.

Oblique incidence can be incorporated into the lattice model through changes in the circuit domain analysis. In particular, only the input currents to the lattice must be modified, while the lattice admittances themselves are identical to the case of uniform normal incidence. The phase of the input currents must account for the phase gradient across the spatial dimensions of the FSS. This gradient, of course, is caused by any given incident phase front reaching different spatial parts of the FSS at different times. Furthermore, the magnitude of the input currents must also be modified to reflect the polarization of the incident field relative to the apertures. This magnitude, however, will be constant across all apertures (ports).

Since the lattice input currents under oblique incidence are no longer constant, it is necessary to employ the two-dimensional DFT solution (87). Physically, the phase of the incident field on the surface of the FSS will be spatially periodic for any angle of incidence. However, in general, this periodicity will not be commensurate with the discrete integer periodicity of the lattice ports. Thus, as explained earlier, an exact solution to the problem is not possible using a DFT of finite dimension $N_x \times N_y$. Nevertheless, it will be shown that an approximate solution through the will suffice as long as the size of the DFT chosen is large enough.

To demonstrate oblique incidence in the lattice model, the specific problem of a single-layer, single rectangular aperture FSS is solved. The unit cell geometry is identical to that depicted in Fig. 37. Also, for simplicity, the single-mode, half-wave sinusoid approximation for the equivalent aperture magnetic currents is employed.

For a TM incident plane wave, the wave vector can be defined in terms of two incident angles [35]:

$$\mathbf{k} = -\sin\theta\cos\phi\hat{\mathbf{x}} - \sin\theta\sin\phi\hat{\mathbf{y}} - \cos\theta\hat{\mathbf{z}} \tag{96}$$

Here, the angles of incidence θ and ϕ are the standard angles from spherical coordinates. In this case, the xy-plane coincides with the plane of the FSS (with the aperture length coincident with the x direction), and z is normal to this plane. The associated electric field is:

$$\mathbf{E}_i = \left(-\sin\phi\hat{\mathbf{x}} + \cos\phi\hat{\mathbf{y}}\right)e^{j(x\sin\theta\cos\phi + y\sin\theta\sin\phi + z\cos\theta)} \tag{97}$$

The incident magnetic field can then be found as:

$$\mathbf{H}_i = \frac{\mathbf{k}\times\mathbf{E}}{\eta}$$
$$\mathbf{H}_i = \frac{1}{\eta}\left(\cos\theta\cos\phi\hat{\mathbf{x}} + \cos\theta\sin\phi\hat{\mathbf{y}} + \sin\theta\hat{\mathbf{z}}\right)e^{j(x\sin\theta\cos\phi + y\sin\theta\sin\phi + z\cos\theta)} \tag{98}$$

The tangential magnetic field oriented along the length of the aperture on the plane of the FSS is simply the x and y components of (98) evaluated at $z = 0$:

$$\mathbf{H}_t^i = \frac{1}{\eta}\left(\cos\theta\cos\phi\hat{\mathbf{x}} + \cos\theta\sin\phi\hat{\mathbf{y}}\right)e^{jk(x\cos\phi\sin\theta + y\sin\phi\sin\theta)} \tag{99}$$

Note that the magnitude of the incident field is dependent on the two spherical angles defining the incident direction, but it is constant across the spatial extent of the FSS. The incident phase, on the other hand, is a function of both the spherical angles of incidence and the spatial location on the plane of the FSS. The phase of (99) is specifically defined such that a point of zero phase is achieved at the origin, which is placed at the bottom left corner of the unit cell in Fig. 37.

The lattice input current (23) must be recalculated for any unique pair of values of θ and ϕ. For this calculation, the half-sinusoid equivalent magnetic current assumption under normal plane wave incidence must be modified as follows:

$$\mathbf{M}_0 = \frac{\cos\phi}{W}\sin\left(\frac{\pi\left(x - n_x D_x\right)}{L}\right)e^{jk(x\sin\theta\cos\phi + y\sin\theta\sin\phi)} \tag{100}$$

This magnetic current accounts for the phase gradient of the field along the plane of the FSS in the spatial domain, as well as a polarization effect (the $\cos\phi$ factor). Note that the sinusoidal envelope of the current is shifted by multiples of the x-directed unit cell size D_x (in integer increments based on the discrete spatial variable n_x). This allows the input current to be determined at multiple values of n_x and n_y such that a sufficiently-size DFT (86) can be computed.

With $\mathbf{H}_t^i$ and $\mathbf{M}_0$ defined in (99) and (100), respectively, the integral (23) can be written more explicitly as:

$$I\left[n_x, n_y\right] = \int_{n_x D_x}^{n_x D_x + L} \int_{n_y D_y}^{n_y D_y + W} \left[\begin{array}{l} \dfrac{\cos^2 \phi \cos\theta}{\eta W} \times \\ \sin\left(\dfrac{\pi\left(x - n_x D_x\right)}{L}\right) e^{jk\left(\begin{smallmatrix} x\sin\theta\cos\phi + \\ y\sin\theta\sin\phi \end{smallmatrix}\right)} \end{array} \right] dydx \qquad (101)$$

Note that this spatial domain current is, as expected, a function of the discrete spatial variables n_x and n_y, with respect to which the DFT $\tilde{I}\left[k_x, k_y\right]$ can be calculated and used in (87).

The actual process of using a DFT with a finite number of terms requires a few clarifying details. Assuming a DFT of size $M_x \times M_y$, M_x and M_y both odd, a "reference" port at is defined at $\left[n_x, n_y\right] = \left[\left(M_x - 1\right)/2 + 1, \left(M_y - 1\right)/2 + 1\right]$. The DFT is computed using the spatial domain points $n_x \in \left\{1, 2, ..., M_x\right\}$ and $n_y \in \left\{1, 2, ..., M_y\right\}$. The reference port sits at the center of this finite two-dimensional spatial domain.

As has already been mentioned, when the spectral domain voltage (87) is computed using this $M_x \times M_y$ DFT and then transformed back into the spatial domain, the resulting voltage distribution only approximates the true solution of an infinite lattice. Specifically, the voltages are less accurate near the edges of the finite domain, whereas the voltage at the center of the domain (i.e. at the reference port) is more accurate. As the DFT size increases, the solution at the reference port converges towards the true solution of the infinite case.

To illustrate this, Fig. 54 shows an example of the voltage solution for a rectangular aperture FSS with angles of incidence $\theta = 10°$ and $\phi = 40°$. For this computation, the FSS is assigned dimensions of $L = 10$ mm, $D_x = 12$ mm, $D_y = 4$ mm, and $W = 0.5$ mm. A 61×61-point DFT is employed. The normalized magnitude of the spatial domain voltage is plotted as a two-dimensional surface. The reference port lies at the center of the surface.

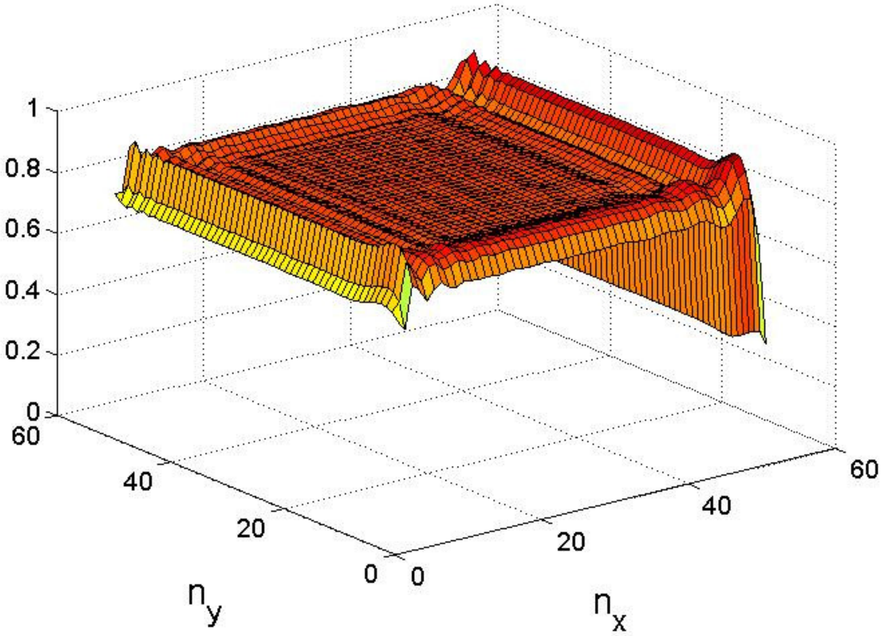

Fig. 54. Spatial distribution of normalized DFT voltage solution. The case under consideration is a rectangular aperture FSS under oblique plane wave incidence. This solution using a finite transform converges to the true infinite case near the center of the surface.

In theory, under oblique incidence, the magnitude of the port voltages should all be identical, and the surface should be completely flat since the incident field has equal magnitude everywhere. Only the phase of the solution should vary from port to port. In Fig. 6, the solution is almost completely flat near the center, but oscillations appear near the edges. These oscillations are errors introduced by the finite DFT approximation. For a sufficiently sized DFT, the solution near the reference aperture accurately approximates the ideal infinite solution. The necessary DFT size depends on both the FSS geometry under consideration and the angles of incidence. However, a formal study of the specific requirements for the DFT size will not be attempted as part of this work.

The application of the lattice model to rectangular aperture FSSs under oblique incidence is demonstrated by a few representative calculations in Fig 55. The FSS under consideration is identical to that used for Fig. 54. The transmission for several different angles of incidence is calculated using both the lattice model and simulation. Clearly, the lattice model achieves good agreement with the full-wave simulations.

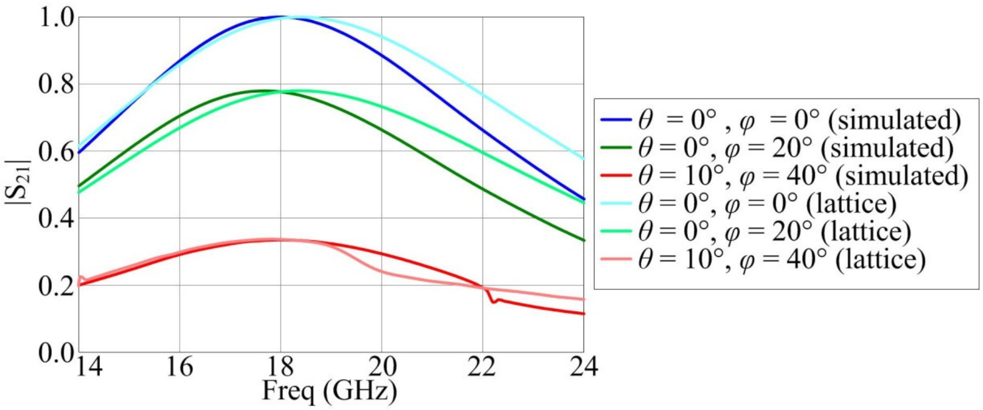

Fig 55. Rectangular aperture FSS under oblique plane wave incidence.

CHAPTER VIII

COMBINED ANALYSIS OF FSS AND ANTENNAS

Beyond the various categories of FSS topologies explored in Chapter VI, including multi-element and multilayer designs, the lattice model theory can also be extended to include the case of an FSS illuminated by an antenna or antenna array radiating in the presence of the FSS. The analysis of such a scenario is of significant practical interest, since a large segment of FSS applications involve the simultaneous deployment of FSSs and antennas. As discussed in Chapter I, these applications may involve, among many possibilities, simple antenna-radome combinations or more integrated structures where an FSS overlays a planar antenna as a superstrate.

In such designs combining antennas and FSSs, the question of mutual electromagnetic interaction between the antenna and FSS is very important [59]. A variety of studies have been undertaken to quantify this interaction (e.g. [60], [61]). However, in practice, the antenna and FSS are often designed independently using separate techniques. As long as the mutual interaction between the two is limited, this approach can work.

As an example, an antenna may be designed assuming normal radiation conditions into free space; simultaneously, an FSS may be designed for a particular filter response assuming it is surrounded by free space. Then, the FSS may be placed in proximity to the antenna in order to window the bandwidth of EM energy that is radiated. Conceptually, this is a straightforward concept, and as long as the FSS is not placed too close to the antenna, it may work well: the radiation pattern and impedance properties of the antenna may not be adversely affected, and the FSS filter response may also not be modified significantly. However, the dimensional requirements of a particular application may force the FSS to be close enough to the antenna that the impedance match or radiation pattern may be compromised. In other scenarios, it may be desirable to make the combined antenna/FSS structure as compact as possible (e.g. the antenna and FSS may be integrated into a single planar, multilayered structure). In these cases, it may be crucial to design the system as a whole. The analytical complexity of this situation, of course, is much higher than a simple antenna design or FSS design by themselves. For instance, the computational expense of analyzing a combined antenna/FSS structure using commercial simulation software may be significantly higher than for either of the structures by themselves.

The lattice model provides a viable candidate as a systematic and canonical methodology for analyzing antennas and FSSs simultaneously. This is because an antenna or antenna array can be directly incorporated into the lattice itself. Conceptually, the incorporation of antennas into the lattice is accomplished by treating the antenna or array structure as additional ports in the multiport network. More specifically, the antennas are added as additional layers in a multilayer FSS lattice.

This chapter begins with a brief overview of some examples of the combined analysis of FSSs and antennas from literature. Then, the lattice model theory is developed for an antenna array radiating through a single layer FSS. The specific case of a rectangular waveguide array (i.e. apertures in a ground plane fed by waveguide) radiating through a rectangular aperture FSS is chosen to illustrate the theory. Two examples are provided, one using single-element FSS, and the other using a dual-element FSS. Next, the theory is extended to the case of solitary antennas radiating through an infinite FSS. Several possible approaches to solving this problem are provided.

Previous Attempts to Combine FSS and Antenna Analysis

Antenna design and FSS design, by themselves, are well-developed fields of knowledge. However, the design of integrated antenna-FSS structures with non-trivial electromagnetic interaction between the components is, relatively speaking, a much-less-explored topic. This section provides a brief set of examples of combined antenna-FSS analysis.

An antenna that is frequency-windowed by a closely placed FSS can simply be analyzed by full-wave simulation after both components have first been designed separately. The simulation may be computationally expensive, but it can determine whether placing the FSS close to the antenna achieves the desired frequency filtering effect. In [6], a standard horn antenna is windowed by a cross-dipole FSS placed across its radiation aperture; the goal is to reduce the radar cross section (RCS) of the horn. The results – which reasonably achieve the stated goal – are studied by simulating the whole structure in three dimensions using commercial numerical software.

A number of more rigorous analytical approaches to integrating antenna and FSS analysis have been proposed. In [60], a solitary open-ended waveguide antenna radiating through a square patch FSS is studied using the plane wave spectrum (PWS) technique. In this method, the electric field is decomposed into a spectrum of multiple plane waves incident from various angles. The method is used to obtain the radiation pattern of the antenna through the FSS. The PWS was previously used to study finite FSSs. Another method, the multimode equivalent network (MEN) approach, has been used to study FSSs integrated with waveguide arrays [62]. In this approach, the fields are separated into "accessible" and "non-accessible" Floquet modes, which leads to a multimode admittance matrix to describe both the FSS and the array. The modes of both structures are matched to enforce the appropriate boundary conditions. Other mode-matching strategies have been devised as well. A "mode matching-finite element" method has been used to study both electromagnetically thick FSS designs [63] and large finite arrays [64]; in [65], this technique was applied to an integrated antenna-FSS where the individual structures have noncommensurate periodicities.

Clearly, analytical and numerical tools already exist to study antenna-FSS interactions. However, some of the unique features and benefits of the lattice model for FSS analysis – such as its circuit domain handling of non-uniform incidence – can also be realized in the antenna-FSS formulation. In the succeeding chapter, polynomial modeling and optimization of FSSs through the lattice model is also applied to the antenna-FSS case. For these reasons, extending the lattice model to include antennas is a worthwhile endeavor; the remainder of the chapter focuses on developing this theory as a viable tool for antenna-FSS design.

Conceptual FSS-Antenna Lattice Model

The basic strategy to incorporate antenna elements into the lattice model is to treat them as additional ports in the multiport network. These antenna ports are coupled to the FSS ports using mutual admittances, just like the FSS elements themselves are coupled together. If there are multiple antennas (an array), then coupling also exists between the antenna ports. In general, the antenna ports are added to the lattice in the form of an additional layer(s) in a multilayer structure, since, physically speaking, an antenna does not lie on the same plane as the FSS itself. Thus, the antenna-FSS problem is inherently a multilayer problem and uses a version of the theory developed in Chapter VI.

Once a multilayer lattice is constructed with both FSS and antenna ports, the structure is excited at the antenna ports, and the resulting transmission through the FSS is analyzed. Thus, in this scenario, the structure is treated like a transmitting device. Alternatively, the structure could be excited by an incoming plane wave, and the resulting voltages produced at the antenna ports could be analyzed; this would represent a receiving device. This may be desirable if, for instance, the receiving characteristics of the antenna(s) under oblique incidence are desired. However, it is typically easier to define the excitations at the antenna ports, if possible. These antenna ports are treated just like the ports encountered in traditional antenna design; they are fed by some kind of transmission line or waveguide structure. This is in contrast to the pure FSS analysis of Chapters IV-VI, where the lattice ports are excited by an incident plane wave in free space.

In the case of an antenna array, the antenna ports, in general, may not have the same excitations. This situation is analogous to the non-uniform FSS incidence discussed in Chapter VII. A phased array, in particular, has a well-defined linear phase gradient along the spatial extent of the array, much like the oblique plane wave incidence case for FSSs. For these cases of non-uniform excitation, the 2D DFT formulation of the FSS lattice model is extended to the antenna-FSS lattice.

Waveguide Array Radiating Through a Single Layer FSS

A simple example of antenna-FSS combination that is readily incorporated into the lattice model theory thus far developed is shown in Fig. 56. It depicts, in (b), an infinite array of rectangular waveguide apertures radiating through a single-layer aperture-type FSS. The waveguides are open-ended and open onto an infinite PEC ground plane. Conceptually, this structure is very similar to the case of a dual-layer FSS, shown in (a). The first FSS layer (on the left) of (a) is simply replaced by an array of waveguides in (b). Rather than being excited by an incident plane wave, the structure is excited by guided propagating waves in the waveguides.

The analogy between the array-FSS and the two-layer FSS is important in terms of establishing the lattice structure for the former. In Fig. 56 (c), the EM domain aperture problem for two apertures on different layers is revisited (from Chapter VI, Fig. 46). This problem is compared to Fig. 56 (d), which shows the analogous problem involving a single waveguide on the array layer radiating through a single aperture on the FSS layer. Note that both problem (c) and problem (d) can be divided into three regions.

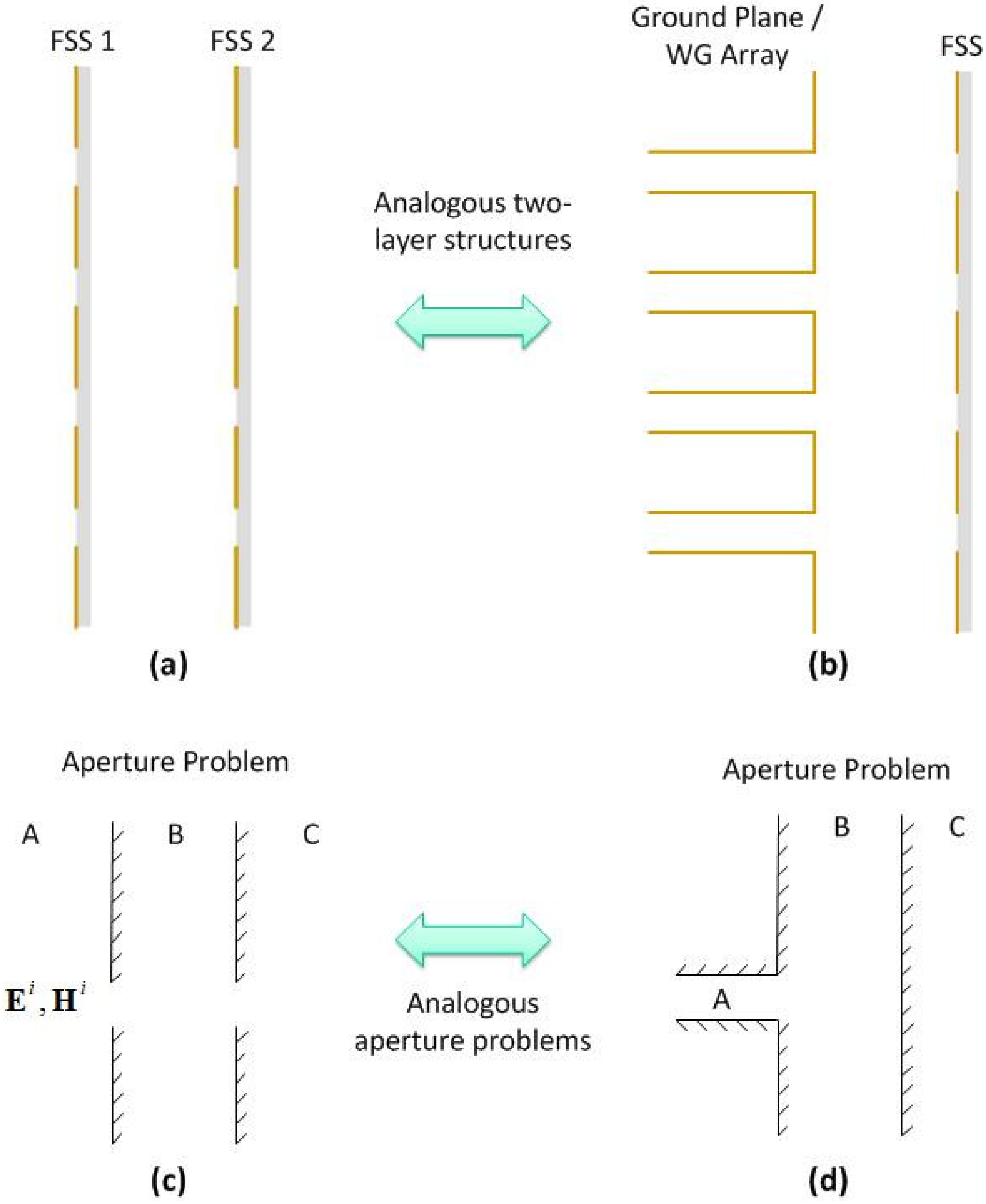

Fig. 56. Analogy of a waveguide array-FSS to a dual-layer FSS problem. (a) Two layer FSS. (b) Array of rectangular waveguides radiating through a single-layer FSS. (c) Aperture problem encountered for dual-layer FSS. (d) Aperture problem encountered for ground plane-backed waveguide radiating through an aperture.

After applying the equivalence principle, the problems in regions B and C are the same for (c) and (d). Only the problem in region A differs. For (c), the equivalent problem is solved in a halfspace, whereas for (d), the problem is solved inside a waveguide.

Uniform Array Excitation

Based on the analogy illustrated in Fig. 56, the lattice model analysis for the waveguide array-FSS proceeds in a similar fashion to that of the dual-layer FSS developed in Chapter VI. The lattice structure looks almost the same as that depicted in Fig. 49; only the admittance terms in region A differ. To see how the overall lattice structure changes, it is instructive to look at the underlying aperture problems in the EM domain of analysis.

EM Domain Aperture Problems

The aperture problem in Fig. 56 (d) can be represented by the equivalent network shown in Fig. 57. This network is almost identical to the network studied in Chapter VI, Fig. 46. In fact, the two-port network of region B and the one-port network of region C are the same and will not be elaborated on here. In region A, the halfspace self admittance $2Y_s^{hs}$ is replaced by a waveguide admittance $2Y_{wg}$ (recall that the factors of two account for the image of the magnetic current due to the ground plane). This waveguide admittance is calculated as:

$$Y_{wg} = \left\langle \mathbf{M}_{wg}, \mathbf{H}_{wg}\left(\mathbf{M}_{wg}\right)\right\rangle \tag{102}$$

Here, $\mathbf{M}_{wg}$ is the equivalent magnetic current covering the waveguide aperture, and $\mathbf{H}_{wg}\left(\mathbf{M}_{wg}\right)$ is the magnetic field on the aperture produced by $\mathbf{M}_{wg}$. The inner product is a surface integral over the aperture. Note, then, that this computation is essentially the same as that for the halfspace self admittance. However, the fields are computed inside the waveguide subject to its boundary conditions, rather than being computed in free space. The details of this waveguide admittance calculation are provided in Appendix A.

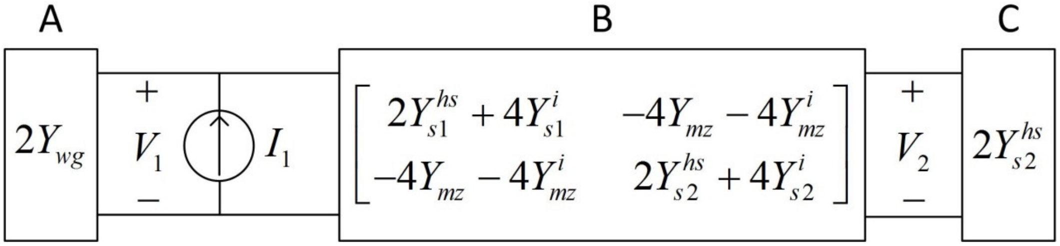

Fig. 57. Equivalent network of waveguide-aperture dual-layer problem.

A similar equivalent network can be constructed for the problem of two waveguide apertures in the first layer and no FSS apertures in the second layer. Fig. 57 (a) shows the physical layout of the problem, and the corresponding network is given in (b). Again, the region A admittances are now waveguide admittances Y_{wg}. Note that no mutual coupling exists between the waveguides in region A, since they are electromagnetically isolated. Region B is identical to that of the analogous problem developed in Fig. 48 of Chapter VI.

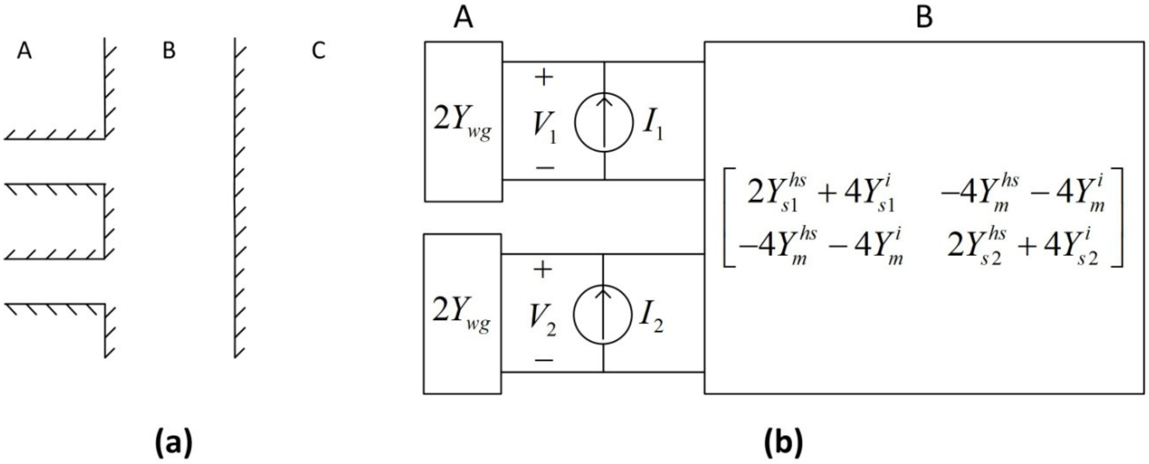

Fig. 58. Equivalent network of dual-waveguide dual-layer problem.

The equivalent networks in Fig. 57 and Fig. 58 (b) form the building blocks of the array-FSS lattice. Again, the overall lattice resembles the two-layer lattice shown in Fig. 49, except that region A is modified. Specifically, there is no mutual admittances in region A, and the halfspace self admittances are replaced by the waveguide admittances.

Collapsed Finite Network under Uniform Excitation

Just as the case of uniform plane wave incidence was considered first in Chapter VI for simplicity, the case of uniform array excitation is considered first here. This means that each rectangular waveguide antenna is fed with the same excitation, equal in both magnitude and phase. By symmetry, this dictates that the fields excited on all waveguide apertures are the same; likewise, the fields on all FSS apertures are identical. Under this assumption, the infinite lattice can be collapsed down into an equivalent finite network, as was done in the pure FSS analysis. Fig 59 shows this collapsed two-port network. It is similar in structure to the collapsed two-port network of the dual-layer FSS in Fig. 50, except that the admittance in region A is no longer an infinite summation; rather, it has been replaced by the waveguide admittance term. There are still four infinite summation terms that must be evaluated: Y^{Σ_1}, which accounts for the waveguide aperture self admittance and mutual admittances in Region B (with image effects); Y^{Σ_2}, which accounts for the inter-layer coupling between the waveguide aperture and the FSS aperture (again with image effects); Y^{Σ_3}, which is the same collection of admittance terms as Y^{Σ_1}, but with respect to the FSS aperture rather than to the waveguide aperture; and Y^{Σ_4}, which is the region C self and mutual admittances of the FSS aperture. Note that Y^{Σ_1} and Y^{Σ_3} are assumed to be dissimilar, since, in general, the FSS aperture is expected to be a different size than the waveguide aperture.

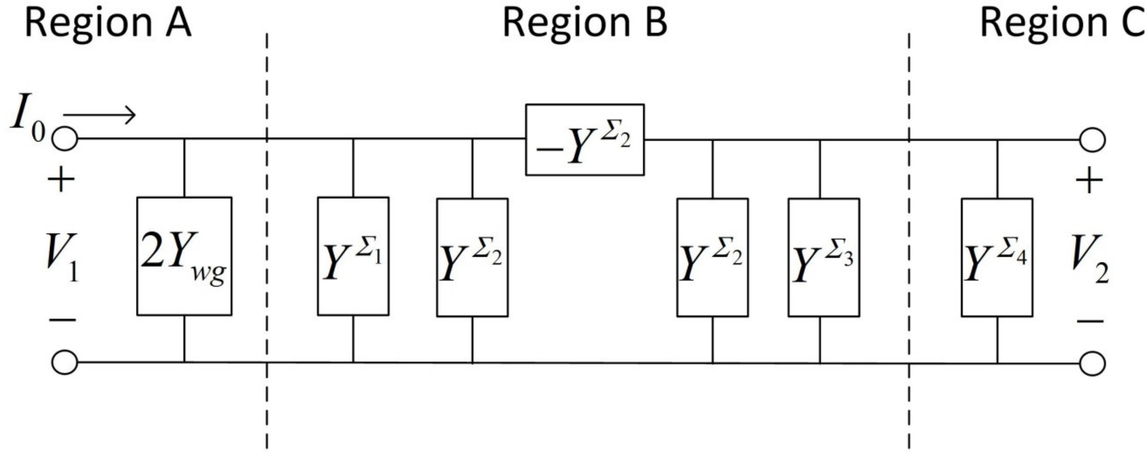

Fig 59. Collapsed lattice of waveguide array-FSS with uniform array excitation.

Lattice Input Current

It is also necessary to calculate the input current to the antenna ports; this current differs from those originally calculated for the pure FSS analysis in Chapter V, since the excitation is a propagating waveguide mode rather than an incident plane wave in free space. The current in this case is given by:

$$I = \left\langle \mathbf{M}_{wg}, \mathbf{H}_{t,wg}^{imp} \right\rangle \tag{103}$$

Here, $\mathbf{H}_{t,wg}^{imp}$ is the tangential magnetic field impressed on the waveguide aperture by an incident waveguide excitation. To define this impressed field, a number of assumptions must be made. First, the excitation is assumed to be a propagating wave in the TE_{10} mode of the waveguide (the fundamental mode of a rectangular waveguide) traveling towards the aperture. Also, the magnitude of the mode is normalized following the convention of [53]; this results in the following impressed magnetic current:

$$\mathbf{H}_{t,wg}^{imp} = 2\sqrt{2}Y_{10}^{TE} \sin\left(\frac{\pi\left(x - x_1\right)}{L_{wg}}\right)\hat{\mathbf{x}} \tag{104}$$

Here, L_{wg} is the length of the waveguide aperture and $x_1 = -\left(D_x - L_{wg}\right)/2$ (the origin of the coordinate system here is placed at the corner of the waveguide aperture, with the length of the aperture extending in the positive x direction). Y_{10}^{TE} is the waveguide admittance of the TE_{10} mode; this can be found in any standard microwave engineering book (e.g. [35]):

$$Y_{10}^{TE} = \frac{1}{\eta}\sqrt{1 - \frac{1}{\mu\varepsilon}\left(\frac{1}{2fL_{wg}}\right)^2} \tag{105}$$

The magnetic field (104) can now be used in (103) to compute the correct input current to the lattice:

$$I = \sqrt{2} Y_{10}^{TE} L_{wg} \cos\left(\frac{\pi x_1}{L_{wg}} \right) \tag{106}$$

Now, the terms of the collapsed lattice network in Fig 59 are fully defined, and the case of uniform array excitation can be solved.

Array Performance

In order to evaluate an array-FSS design, a variety of performance metrics may be desired: impedance match, radiation pattern, etc. It is beyond the scope of this paper to consider the calculation of all such metrics; for the purposes of this work, the analysis is restricted to determining the impedance match of the waveguide array. For quantities such as the radiation pattern, it is sufficient to point out here that in the underlying aperture problems of the EM domain, the radiated fields are readily obtainable (see [54], which shows how such fields are calculated using Harrington's original network formulation of an aperture problem). It only remains to make a sufficient mathematical connection between the EM and circuit domains to translate this radiated field analysis to the full lattice structure. Since the lattice admittances, voltages, and currents are all based off underlying EM problems, there is no reason why the lattice model cannot, in principle, be used to derive any normal array calculations that may be desired.

The impedance match of the array-FSS structure is reported in this work in terms of the voltage standing wave ratio (VSWR). This common antenna parameter is defined in terms of the reflection coefficient Γ at the antenna port:

$$VSWR = \frac{1-|\Gamma|}{1+|\Gamma|} \tag{107}$$

The reflection coefficient, in turn, is defined by:

$$\Gamma = \frac{Z_{ap} - Z_{10}^{TE}}{Z_{ap} + Z_{10}^{TE}} \tag{108}$$

Here, $Y_{10}^{TE} = 1/Z_{10}^{TE}$ is the waveguide admittance of the TE$_{10}$ mode, and $Y_{ap} = 1/Z_{ap}$ is the aperture admittance. This latter term, from [66], is given by:

$$Y_{ap} = \frac{2P_t^*}{|V_{ap}|^2} \tag{109}$$

Here, V_{ap} is the waveguide aperture voltage, which corresponds to V_1 of Fig 59. P_t is the power transmitted from the antenna – in this case, the power transmitted per unit cell in the array. It is equal to the power dissipated in region C of the collapsed lattice network:

$$P_t = \frac{1}{2} V_2 \left(Y^{\Sigma_4}\right)^* V_2^* \tag{110}$$

The VSWR calculated with (107)-(110) is used to determine the impedance bandwidth of the array – that is, the operating frequency band over which an acceptable impedance match is achieved. Specifically, from a microwave network standpoint, an impedance match is desired between the waveguide admittance (105) and the antenna (array) input impedance – which, in this case, is the waveguide aperture admittance

(109). A perfect impedance match results in 100% power transmission from the waveguide to free space region beyond the FSS. In practice, it is typical to define the operating bandwidth as the frequency band where $VSWR < 2$. In this region, the impedance match ensures that roughly 90% of the incident power is radiated.

Windowing by Single-Element Rectangular Aperture FSS

In order to demonstrate the implementation of the lattice theory above that has been modified to an array-FSS structure, an example is given here using a rectangular aperture FSS. Fig. 60 shows the unit cell geometry of such a design; the first layer contains the waveguide array, whereas the second layer contains the FSS array. The waveguide has dimensions $L_{wg} \times W_{wg}$, the FSS has dimensions $L \times W$, and the unit cells on both layers have dimensions $D_x \times D_y$. The area between the two layers is assumed to be free space. The purpose of this design is to achieve single-band frequency windowing of the waveguide array – that is, to restrict the radiation to the relatively narrow operating band of the FSS.

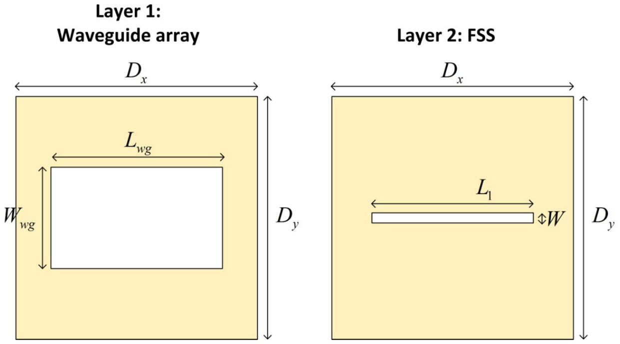

Fig. 60. Unit cell geometry of single-band rectangular waveguide array-FSS.

The lattice model is used to compute the VSWR performance of this design over the frequency range 12-20 GHz. The dimensions are assigned values of $L_{wg} = 13\text{ mm}$, $W_{wg} = 6.5\text{ mm}$, $D_x = 16\text{ mm}$, $D_y = 10\text{ mm}$, and $W = 0.5\text{ mm}$. The distance between the layers is fixed at $z = 5\text{ mm}$, while the length of the FSS aperture L is varied from 8 mm to 11 mm in increments of 1 mm. Fig. 61 shows the performance of the array for these different aperture lengths. Specifically, the VSWR is provided as a function of frequency.

For comparison, the array-FSS designs are also simulated in [16]. Fig. 62 shows the geometry of the simulated model. The simulation is performed over one unit cell – that is, one FSS unit cell and one waveguide antenna. The waveguide portion has PEC boundary conditions and is fed by a standard waveport, while the FSS portion is assigned periodic Floquet boundary conditions and excited by a Floquet port. The simulated results are superimposed on top of the lattice model results in Fig. 61. In general, good agreement is achieved between the lattice model and corresponding simulations. The VSWR minimum – in other words, the nominal operating frequency of the array – is shifted between about 14 and 18 GHz for the various aperture lengths. The impedance match is slightly better for the longer aperture lengths, but all of the designs achieve some kind of appreciable 2:1 VSWR bandwidth. Clearly, with the unit cell size, waveguide size, and layer separation distance fixed, the designs cannot be ideally matched using the aperture length alone; additional degrees of dimensional freedom would have to be introduced.

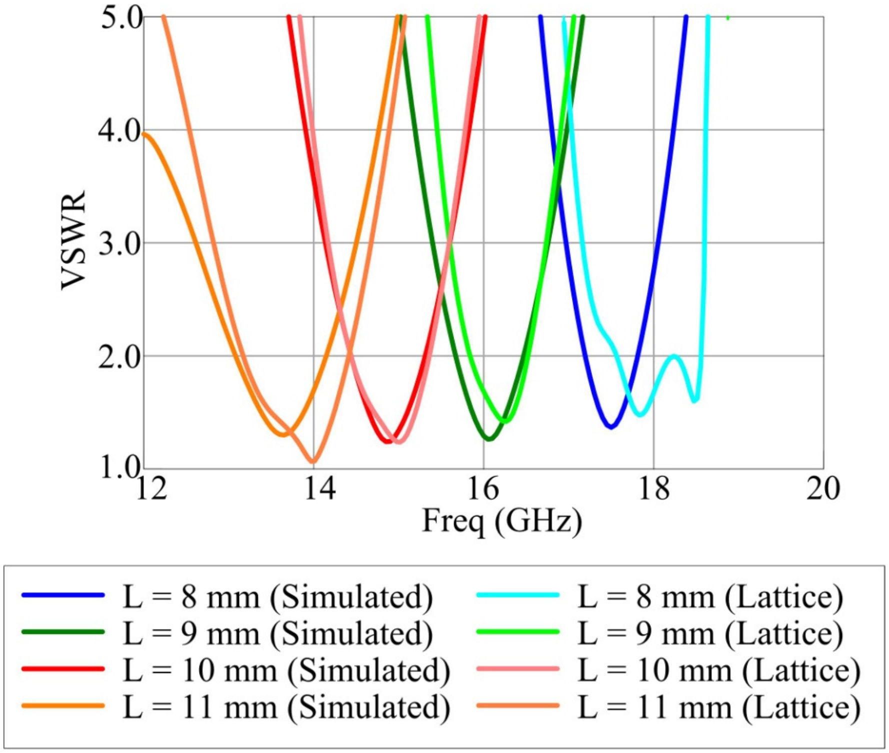

Fig. 61. Performance of a waveguide array / rectangular aperture FSS.

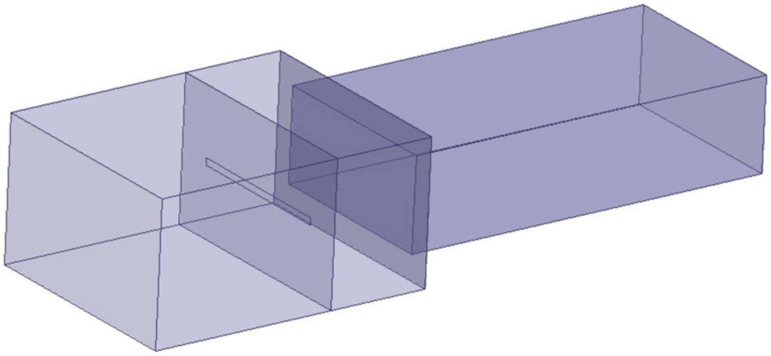

Fig. 62. HFSS simulation of a waveguide array / rectangular aperture FSS.

Windowing by Dual-element Rectangular Aperture FSS

The lattice model is now used to compute the performance of a slightly more complex array-FSS structure: a dual-aperture, single-layer FSS windowing a waveguide array. The geometry of this design, which achieves dual-band frequency windowing, is shown in Fig. 63. The waveguide layer of this design is identical to that of Fig. 60. The second layer (FSS layer), however, now has two apertures with differing lengths L_1 and L_2. Also, the positioning of the apertures within the unit cell is given more freedom: each aperture is located at arbitrary distances in the x direction (x_1 and x_2, respectively) and y direction (y_1 and y_2, respectively), as measured from the bottom left corner of the unit cell. This arbitrary positioning provides the option of using additional degrees of freedom to tune the impedance match of the two operating bands of the structure.

The lattice model for such a structure can be obtained by combining the ideas of a multi-element and multilayer lattice from Chapter VI. Specifically, a two-layer problem is formulated to account for the waveguide layer and the FSS layer (just like for the design of Fig. 60); however, the FSS layer is treated as a multi-element layer, with two ports per unit cell. The details of constructing this lattice will not be elaborated on here; the final lattice, collapsed down into a finite network due to the symmetry of uniform waveguide excitation, will have three network ports corresponding to the one waveguide aperture and two FSS apertures per unit cell.

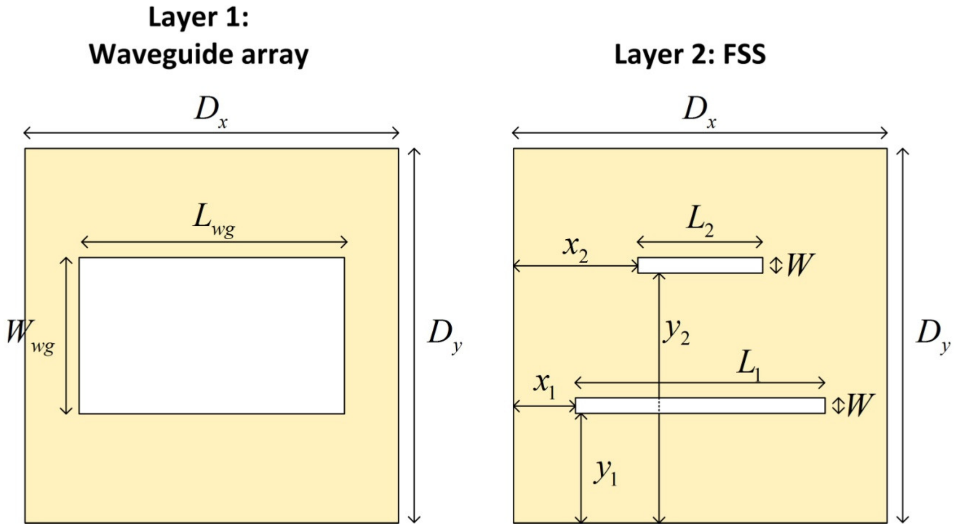

Fig. 63. Unit cell geometry of a waveguide array / dual-aperture FSS.

The dual-band array-waveguide is assigned specific dimensions and analyzed using the lattice model for the frequency range 12-20 GHz. The performance, along with the geometric dimensions, are shown in Fig. 64. As expected, two operating frequency bands are achieved – one near 13 GHz and the other near 17 GHz. The bandwidth of the lower frequency band is considerably smaller. Also provided in the figure is the simulated performance of the structure. Generally good agreement is achieved between the lattice model and simulation, although the VSWR minimums are somewhat shifted in frequency. This is particularly noticeable in the case of the lower operating band; the frequency shift is exaggerated by the smaller bandwidth. Nonetheless, the results demonstrate the utility of the model for analyzing an ideal infinite array-FSS.

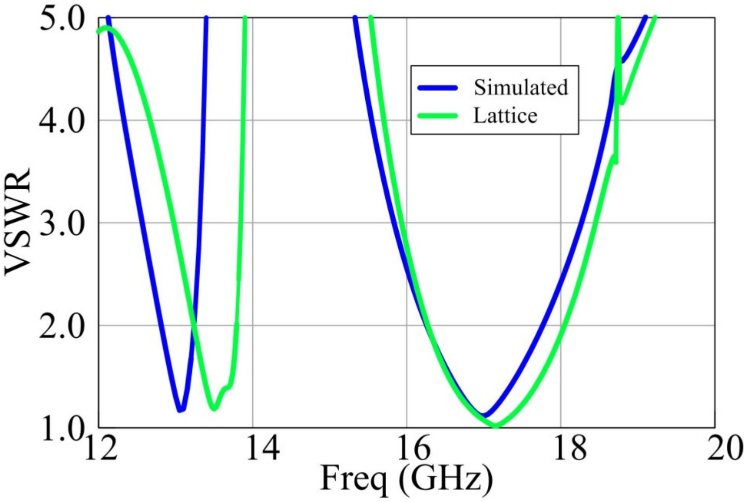

$L_1 = 11$ mm $\quad L_{WG} = 13$ mm $\quad x_1 = 2.5$ mm
$L_2 = 9$ mm $\quad W_{WG} = 6.5$ mm $\quad y_1 = 2$ mm
$W = 0.5$ mm $\quad D_x = 16$ mm $\quad x_2 = 3.5$ mm
$z = 5$ mm $\quad D_y = 10$ mm $\quad y_2 = 7.5$ mm

Fig. 64. Performance of windowed dual-band waveguide array-FSS.

Non-Uniform Array Excitation

In practical arrays, the array elements are not necessarily excited with equal magnitude or phase. This is particularly true in the case of phased array systems, in which the input currents to the array elements are assigned a phase gradient in order to scan the main beam of the array pattern in different directions. It is important that the lattice model be able to handle such situations.

Changing the magnitude and phase of the input currents to the antenna ports of the lattice network is analogous to the case of non-uniform incidence studied in Chapter VII for pure FSS analysis problem. In particular, the 2D DFT formulation of the lattice model developed there can be applied with equal success to the problem of non-uniform array excitation.

The application of the DFT version of the lattice model to antenna-FSS structures is considered here using the example of the single layer, single-element FSS windowing a waveguide aperture (i.e. the lattice constructed using the equivalent networks of Fig. 57 and Fig. 58). This lattice can be described mathematically using system of two finite difference equations:

$$\begin{gathered}\left(2Y_{s1}+2Y_{wg}+4Y_{s1}^{i}+\sum_{n}\left(2Y_{m1,n}4Y_{m1,n}^{i}\right)-4\sum_{n}\left(Y_{mz,n}+Y_{mz,n}^{i}\right)\right)V_{1}\left[n_{x},n_{y}\right]-\\ \left(\sum_{n}\left(2Y_{m1,n}4Y_{m1,n}^{i}\right)\right)\left(V_{1}\left[n_{x},n_{y}\right]-V_{1}\left[n_{x}+a_{n},n_{x}+b_{n}\right]\right)+\\ \left(4\sum_{n}\left(Y_{mz,n}+Y_{mz,n}^{i}\right)\right)\left(V_{1}\left[n_{x},n_{y}\right]-V_{2}\left[n_{x}+a_{n},n_{y}+b_{n}\right]\right)=I\left[n_{x},n_{y}\right]\end{gathered} \tag{111}$$

$$\begin{gathered}\left(4Y_{s2}+4Y_{s2}^{i}+\sum_{n}\left(4Y_{m2,n}4Y_{m2,n}^{i}\right)-4\sum_{n}\left(Y_{mz,n}+Y_{mz,n}^{i}\right)\right)V_{2}\left[n_{x},n_{y}\right]-\\ \left(\sum_{n}\left(2Y_{m2,n}4Y_{m2,n}^{i}\right)\right)\left(V_{2}\left[n_{x},n_{y}\right]-V_{2}\left[n_{x}+a_{n},n_{x}+b_{n}\right]\right)+\\ \left(4\sum_{n}\left(Y_{mz,n}+Y_{mz,n}^{i}\right)\right)\left(V_{2}\left[n_{x},n_{y}\right]-V_{1}\left[n_{x}+a_{n},n_{y}+b_{n}\right]\right)=0\end{gathered} \tag{112}$$

Here, Y_{wg} is the waveguide admittance, and $V_1\left[n_x,n_y\right]$ and $V_2\left[n_x,n_y\right]$ are the voltages on the waveguide and FSS apertures, respectively. Y_{s1} and Y_{s2} hare the halfspace self admittances of waveguide apertures and FSS apertures, respectively, while Y_{s1}^i and Y_{s2}^i are the corresponding “self image” terms (which are infinite summations themselves). $Y_{m1,n}$ and $Y_{m2,n}$ are the mutual admittances between waveguide apertures and between

FSS apertures, respectively, while $Y^i_{m1,n}$ and $Y^i_{m2,n}$ are the corresponding infinite "mutual image" terms; the index n orders the collection of such mutual admittances. $Y_{mz,n}$ are the collection of inter-layer mutual admittances between waveguide and FSS apertures, also indexed by n; these admittances have corresponding infinite image terms $Y^i_{mz,n}$. The system of equations can be simplified as follows:

$$\begin{aligned}&\left(2Y_{s1}+2Y_{wg}+4Y^i_{s1}\right)V_1\left[n_x,n_y\right]+\\&\sum_n\left(2Y_{m1,n}+4Y^i_{m1,n}\right)V_1\left[n_x+a_n,n_x+b_n\right]-\\&4\sum_n\left(Y_{mz,n}+Y^i_{mz,n}\right)V_2\left[n_x+a_n,n_y+b_n\right]=I\left[n_x,n_y\right]\end{aligned}\tag{113}$$

$$\begin{aligned}&\left(4Y_{s2}+4Y^i_{s2}\right)V_2\left[n_x,n_y\right]+\\&4\sum_n\left(Y_{m2,n}+Y^i_{m2,n}\right)V_2\left[n_x+a_n,n_x+b_n\right]-\\&4\sum_n\left(Y_{mz,n}+Y^i_{mz,n}\right)V_1\left[n_x+a_n,n_y+b_n\right]=0\end{aligned}\tag{114}$$

Next, the 2D DFT is applied to both (113) and (114):

$$\begin{aligned}&\left(2Y_{s1}+2Y_{wg}+4Y^i_{s1}\right)\tilde{V}_1\left[k_x,k_y\right]+\\&\tilde{V}_1\left[k_x,k_y\right]\sum_n\left(2Y_{m1,n}4Y^i_{m1,n}\right)e^{-j2\pi\left[(k_x-1)a_n/N_x+(k_y-1)b_n/N_y\right]}-\\&\tilde{V}_2\left[k_x,k_y\right]\sum_n 4\left(Y_{mz,n}+Y^i_{mz,n}\right)e^{-j2\pi\left[(k_x-1)a_n/N_x+(k_y-1)b_n/N_y\right]}=\tilde{I}\left[k_x,k_y\right]\end{aligned}\tag{115}$$

$$\begin{aligned}&\left(4Y_{s2}+4Y^i_{s2}\right)\tilde{V}_2\left[k_x,k_y\right]+\\&\tilde{V}_2\left[k_x,k_y\right]\sum_n 4\left(Y_{m2,n}+Y^i_{m2,n}\right)e^{-j2\pi\left[(k_x-1)a_n/N+(k_y-1)b_n/M\right]}-\\&\tilde{V}_1\left[k_x,k_y\right]\sum_n 4\left(Y_{mz,n}+Y^i_{mz,n}\right)e^{-j2\pi\left[(k_x-1)a_n/N_x+(k_y-1)b_n/M_y\right]}=0\end{aligned}\tag{116}$$

The following sums of admittance terms in (115)-(116) are defined:

$$S_1 = 2Y_{s1} + 2Y_{wg} + 4Y_{s1}^i \tag{117}$$

$$S_2 = \sum_n \left(2Y_{m1,n} 4Y_{m1,n}^i\right) e^{-j2\pi\left[(k_x-1)a_n/N_x + \left(k_y-1\right)b_n/N_y\right]} \tag{118}$$

$$S_3 = 4\sum_n \left(Y_{mz,n} + Y_{mz,n}^i\right) e^{-j2\pi\left[(k_x-1)a_n/N_x + \left(k_y-1\right)b_n/N_y\right]} \tag{119}$$

$$S_4 = 4Y_{s2} + 4Y_{s2}^i \tag{120}$$

$$S_5 = 4\sum_n \left(Y_{m2,n} + Y_{m2,n}^i\right) e^{-j2\pi\left[(k_x-1)a_n/N + \left(k_y-1\right)b_n/M\right]} \tag{121}$$

Note that (118), (119), and (121) are infinite summations in the spectral domain that can be estimated using a finite number of terms through the 2D Shanks transformation. Using (117)-(121), (115)-(116) can be rewritten as::

$$\left(S_1 + S_2\right)\tilde{V}_1\left[k_x, k_y\right] - S_3\tilde{V}_2\left[k_x, k_y\right] = \tilde{I}\left[k_x, k_y\right] \tag{122}$$

$$\left(S_4 + S_5\right)\tilde{V}_2\left[k_x, k_y\right] - S_3\tilde{V}_1\left[k_x, k_y\right] = 0 \tag{123}$$

The solution to the system of equations (122)-(123) for the unknown spectral domain voltages can be written in matrix form:

$$\begin{bmatrix} \tilde{V}_1 \\ \tilde{V}_2 \end{bmatrix} = \begin{bmatrix} S_1 + S_2 & -S_3 \\ -S_3 & S_4 + S_5 \end{bmatrix}^{-1} \begin{bmatrix} \tilde{I} \\ 0 \end{bmatrix} \tag{124}$$

The spectral domain voltages, of course, can be duly converted into the spatial domain using the inverse 2D DFT.

The lattice voltages obtained through the DFT formulation above can be used to determine any number of performance metrics for the array-FSS structure. The details of these calculations depend on the specific formulation of any given problem and will not be elaborated on here.

Solitary Waveguide Radiating Through a Single Layer FSS

When the waveguide array from the previous section is replaced by a solitary radiating waveguide (i.e. a single antenna), the problem immediately becomes more complicated. The structure can no longer be treated directly as a two layer lattice described by a system of two difference equations. This is because one of the two layers (the antenna layer) is now finite. Furthermore, no assumptions can be made about the symmetry of the lattice solution, since the FSS is no longer uniformly excited by the single antenna source. This means that the lattice can in no way be collapsed into an equivalent finite network.

Instead, the structure is now described mathematically by a single two-dimensional difference equation, which accounts for the infinite FSS array, and a system of algebraic equations, which account for the coupling between the solitary antenna and the FSS. In principle, there are an infinite number of such algebraic equations – one for each coupling π-network between the antenna and an FSS lattice port. However, for computational reasons, only a finite number of such algebraic equations can be considered. This limitation is directly analogous to the restriction of a finite number of coupling levels depicted in Fig. 30 for the original basic lattice circuit domain analysis in Chapter IV.

There are a number of different strategies for mathematically solving the lattice problem described above. Two formulations will be considered here. The first, which will be called the "direct formulation", involves solving the difference equations and algebraic equations separately. The strategy is to use N impulse responses of the FSS lattice (governed by a general solution to the difference equation) to construct a system of N algebraic equations that can be solved directly. The second method, which will be called the "alternative formulation", involves modifying the lattice structure by adding additional admittance elements. The goal is to turn the problem back into a two-layer infinite lattice that has essentially the same solution at the lattice ports as the original problem. These two methods are briefly outlined below.

Direct Formulation

In the direct formulation, the FSS array is initially treated as a single-layer lattice problem. The waveguide antenna is removed, and the coupling admittances between the FSS and antenna are ignored and replaced with arbitrary unknown input currents exciting the FSS layer. In other words, a single-layer lattice problem under non-uniform incidence is assumed - a problem that has already been solved in Chapter VII. However, the FSS is still assumed to exist in the presence of the second ground plane (where the waveguide antenna would otherwise be), so the formulation must be somewhat altered.

The difference equation describing this modified one-layer problem is essentially the same as that for a single layer FSS in free space (as developed in Chapter IV), except for the addition of some image terms due to the presence of the second ground plane:

$$\begin{gathered}\left(4Y_s+4Y_s^i+4\sum_n\left(Y_{m,n}+Y_{m,n}^i\right)\right)V\left[n_x,n_y\right]- \\ 4\sum_n\left(Y_{m,n}+Y_{m,n}^i\right)\left(V\left[n_x,n_y\right]-V\left[n_x+a_n,n_y+b_n\right]\right)=I\left[n_x,n_y\right]\end{gathered}\qquad(125)$$

Here, $V\left[n_x,n_y\right]$ is the FSS port voltages, Y_s is the FSS self admittance, $Y_{m,n}$ are the FSS mutual admittances, and Y_s^i and $Y_{m,n}^i$ are the self and mutual infinite image terms, respectively. The difference equation can be simplified as follows:

$$\left(4Y_s+4Y_s^i\right)V\left[n_x,n_y\right]+4\sum_n\left(Y_{m,n}+Y_{m,n}^i\right)V\left[n_x+a_n,n_y+b_n\right]=I\left[n_x,n_y\right]\qquad(126)$$

Note that an arbitrary input current distribution $I\left[n_x,n_y\right]$ is assumed.

To proceed, a finite set of input currents with index k are defined as follows:

$$I_k\left[n_x,n_y\right]=I_k\delta\left[n_x-a_k,n_y-b_k\right]\qquad(127)$$

Here, $\delta\left[n_x,n_y\right]$ is a two-dimensional Kronecker delta function:

$$\delta\left[n_x,n_y\right]=\left\{\begin{matrix}1 & n_x=n_y=0\\ 0 & \text{otherwise}\end{matrix}\right\}\qquad(128)$$

Each of the input currents (127) effectively excites a single port of the lattice network, located at $\left[n_x,n_y\right]=\left[a_k,b_k\right]$, with a current of unknown complex amplitude I_k. The corresponding spectral domain expression for these currents is:

$$\tilde{I}_k\left[k_x,k_y\right]=I_k e^{-j2\pi\left[(k_x-1)a_k/N_x+\left(k_y-1\right)b_k/N_y\right]}\qquad(129)$$

The DFT of the difference equation (126) is computed assuming the input (127) and solved for the spectral domain voltage associated with each current excitation:

$$\tilde{V}_k\left[k_x,k_y\right]=\frac{I_m e^{-j2\pi\left[\left(k_x-1\right)a_k/N_x+\left(k_y-1\right)b_k/N_y\right]}}{4Y_s+4Y_s^i+4\sum_n\left(Y_{m,n}+Y_{m,n}^i\right)e^{-j2\pi\left[\left(k_x-1\right)a_n/N_x+\left(k_y-1\right)b_n/N_y\right]}} \tag{130}$$

This spectral domain voltage solution can be considered an "impulse response" of the FSS lattice - that is, the voltages appearing on the lattice when a single port is excited.

The next step in the analysis is to define a set of spectral domain functions $\tilde{f}_k\left[k_x,k_y\right]$ that correspond to the currents $I_k\left[n_x,n_y\right]$:

$$\tilde{f}_k\left[k_x,k_y\right]=\frac{e^{-j2\pi\left[\left(k_x-1\right)a_k/N_x+\left(k_y-1\right)b_k/N_y\right]}}{4Y^s+4Y^{s,i}+4\sum_n\left(Y_{m,n}+Y_{m,n}^i\right)e^{-j2\pi\left[\left(k_x-1\right)a_n/N_x+\left(k_y-1\right)b_n/N_y\right]}} \tag{131}$$

The functions $\tilde{f}_k\left[k_x,k_y\right]$ share the same index k as the currents $I_k\left[n_x,n_y\right]$. Note that (131) can be computed without knowledge of the magnitude of the specific current excitation; only the location of the impulse current need be known. The spatial domain version of these functions, $f_k\left[n_x,n_y\right]$, can be obtained through the 2D inverse DFT. Then, the following relations hold:

$$\tilde{V}_k\left[k_x,k_y\right]=I_k\tilde{f}_k\left[k_x,k_y\right] \tag{132}$$

$$V_k\left[n_x,n_y\right]=I_k f_k\left[n_x,n_y\right] \tag{133}$$

These equations demonstrate that the spectral domain voltage due to an impulse current at one of the FSS ports is known to within an unknown constant I_k (since $f_k\left[n_x,n_y\right]$ can be calculated). The total voltage due to all of the ports being excited simultaneously with arbitrary amplitude and phase can be found by superposition of all of these solutions:

$$V\left[n_x,n_y\right]=\sum_{\alpha}V_{\alpha}\left[n_x,n_y\right] \tag{134}$$

The reason for dividing the solution up into impulse responses and then using superposition will become clear in the next stage of the analysis.

Now, a finite set of algebraic equations must be defined that relate the waveguide antenna port to all of the FSS ports for which coupling is assumed to exist. Specifically, each of these equations is obtained by writing a node voltage relationship at a port in the network. One equation is obtained by looking at the antenna port, while the remaining equations are obtained by looking at each port in the FSS to which the antenna is coupled. The algebraic node voltage equation at the antenna port can be written as:

$$\begin{gathered}\left(2Y_{sa}+2Y_{wg}+4Y_{sa}^{i}+\sum_{n}\left(-4Y_{mz,n}-4Y_{mz,n}^{i}\right)\right)V_a+\\ \sum_{n}\left(-4Y_{mz,n}-4Y_{mz,n}^{i}\right)\left(V_a-V\left[a_n,b_n\right]\right)=I_{in}\end{gathered} \tag{135}$$

Here, V_a is the voltage of the antenna port, Y_{sa} is the half space self admittance of the waveguide aperture, Y_{wg} is the waveguide admittance, $Y_{mz,n}$ are the inter-layer mutual admittances between the waveguide aperture and FSS apertures (with associated image term $Y_{mz,n}^{i}$), and I_{in} is the input current to the waveguide port and represents the antenna excitation. Equation (135) can be simplified to:

$$\left(2Y_{sa}+2Y_{wg}+4Y_{sa}^{i}\right)V_a+\sum_{n}\left(4Y_{mz,n}+4Y_{mz,n}^{i}\right)V\left[a_n,b_n\right]=I_{in} \tag{136}$$

Using the superposition (134), along with (133), (136) can be written as:

$$\left(2Y_{sa}+2Y_{wg}+4Y_{sa}^{i}\right)V_a+\sum_{n}\sum_{\alpha}\left(4Y_{mz,n}+4Y_{mz,n}^{i}\right)I_{\alpha}f_{\alpha}\left[a_n,b_n\right]=I_{in} \tag{137}$$

A similar node voltage equation can be written at each port in the FSS lattice for which coupling exists to the antenna. The equation at the p^{th} port in the lattice is given by:

$$\begin{aligned}
&\left(4Y_s + 4Y_s^i + 4\sum_n \left(Y_{m,n} + Y_{m,n}^i\right) + \left(-4Y_{mz,p} - 4Y_{mz,p}^i\right)\right) V\left[a_p, b_p\right] + \\
&4\sum_n \left(Y_{m,n} + Y_{m,n}^i\right)\left(V\left[a_p, b_p\right] - V\left[a_p + a_n, b_p + b_n\right]\right) + \\
&\left(4Y_{mz,p} + 4Y_{mz,p}^i\right)\left(V\left[a_p, b_p\right] - V_a\right) = 0
\end{aligned} \tag{138}$$

Note that the one-dimensional index p accounts for ports in both dimensions of the two-dimensional FSS array. Simplification yields:

$$\begin{aligned}
&\left(4Y_s + 4Y_s^i\right) V\left[a_p, b_p\right] + 4\sum_n \left(Y_{m,n} + Y_{m,n}^i\right) V\left[a_p + a_n, b_p + b_n\right] \\
&-\left(4Y_{mz,p} + 4Y_{mz,p}^i\right) V_a = 0
\end{aligned} \tag{139}$$

Now, using the superposition (134), (139) can be written as:

$$\begin{aligned}
&\left(4Y_s + 4Y_s^i\right)\left(\sum_\alpha V_\alpha\left[a_p, b_p\right]\right) + 4\sum_n \left[\left(Y_{m,n} + Y_{m,n}^i\right)\left(\sum_\alpha V_\alpha\left[a_p + a_n, b_p + b_n\right]\right)\right] \\
&-\left(4Y_{mz,p} + 4Y_{mz,p}^i\right) V_a = 0
\end{aligned} \tag{140}$$

Furthermore, employing (133) gives:

$$\begin{aligned}
&\left(4Y_s + 4Y_s^i\right)\left(\sum_\alpha I_\alpha f_\alpha\left[a_p, b_p\right]\right) + \\
&4\sum_n \left[\left(Y_{m,n} + Y_{m,n}^i\right)\left(\sum_\alpha I_\alpha f_\alpha\left[a_p + a_n, b_p + b_n\right]\right)\right] \\
&-\left(4Y_{mz,p} + 4Y_{mz,p}^i\right) V_a = 0
\end{aligned} \tag{141}$$

The set of M equations (141) (indexed by the integer p), along with the equation at the antenna port (136), form a system of $M+1$ equations with $M+1$ unknowns.

Specifically, these unknowns comprise the M unknown current amplitudes I_α and the single unknown antenna port voltage V_a. It is convenient to reorganize (141) as follows:

$$4\sum_{\alpha}\left\{\begin{array}{l}\left(Y_s+Y_s^i\right)f_\alpha\left[a_p,b_p\right]+\\ \sum_n\left(Y_{m,n}+Y_{m,n}^i\right)f_\alpha\left[a_p+a_n,b_p+b_n\right]\end{array}\right\}I_\alpha-\left(4Y_{mz,p}+4Y_{mz,p}^i\right)V_a=0 \tag{142}$$

The system of $M+1$ equations defined by (137) and (142) can now be compiled together into matrix form:

$$\begin{bmatrix} F_0 & F_1 & F_2 & \cdots & F_M \\ F_0^1 & F_1^1 & F_2^1 & \cdots & F_M^1 \\ F_0^2 & F_1^2 & F_2^2 & \cdots & F_M^2 \\ \vdots & \vdots & \vdots & \ddots & \vdots \\ F_0^M & F_2^M & F_2^M & \cdots & F_M^M \end{bmatrix}\begin{bmatrix} V_a \\ I_1 \\ I_2 \\ \vdots \\ I_M \end{bmatrix}=\begin{bmatrix} I_{in} \\ 0 \\ 0 \\ \vdots \\ 0 \end{bmatrix} \tag{143}$$

$$F_0=2Y_{sa}+2Y_{wg}+4Y_{sa}^i \tag{144}$$

$$F_k=\sum_n\left(4Y_{mz,n}+4Y_{mz,n}^i\right)f_k\left[a_n,b_n\right] \tag{145}$$

$$F_0^p=-4\left(Y_{mz,p}+Y_{mz,p}^i\right) \tag{146}$$

$$F_k^p=4\sum_k\left\{\begin{array}{l}\left(Y_s+Y_s^i\right)f_k\left[a_p,b_p\right]+\\ \sum_n\left(Y_{m,n}+Y_{m,n}^i\right)f_k\left[a_p+a_n,b_p+b_n\right]\end{array}\right\} \tag{147}$$

Once (143) is solved, the antenna port voltage V_a is known, and the FSS port voltages $V\left[n_x,n_y\right]$ can be recovered from the currents I_m using (133). Thus, all port voltages in the antenna-FSS lattice structure are known given an input current I_{in} to the solitary antenna port.

Alternative Formulation

The alternative strategy to solve the solitary antenna-FSS problem is to treat the antenna mathematically as if it were actually an array. The lattice admittances are then modified so as to make the port voltages for all the antennas in the array – except for the original solitary antenna - tend towards zero. In other words, the existence of these other antennas in an infinite array are assumed at first, but through proper modifications of the lattice admittances, they appear as short circuits. Electromagnetically, then, they look like the original PEC ground plane. The modifications to the lattice also ensure that the coupling between ports on the FSS array and these "dummy" ports of the antenna array tend towards zero, such that no energy is coupled through the short circuits to ground.

The analysis begins by introducing an additional "dummy layer" to the circuit lattice that resides between the FSS and antenna layers. Fig. 65 illustrates this dummy layer by considering the coupling between a single antenna array port and a single FSS array port. The dummy layer has its own set of ports and associated voltages $V_3\left[n_x, n_y\right]$. The reason for doing this is to allow an additional series admittance $Y_0\left[n_x, n_y\right]$ to be introduced to the coupling network between the original two layers. Specifically, for each pair of FSS port and antenna port, the additional voltage node $V_3\left[n_x, n_y\right]$ separates the physical admittance $4Y_{mz,n} + 4Y^i_{mz,n}$ from $Y_0\left[n_x, n_y\right]$, which are connected in series. The admittance $4Y_{mz,n} + 4Y^i_{mz,n}$ lies between the FSS layer and the dummy layer, whereas the $Y_0\left[n_x, n_y\right]$ lies between the antenna layer and the dummy layer. The new admittance

$Y_0\left[n_x,n_y\right]$ is defined such that it is equal to a very large number (ideally infinite, or a short circuit) for any FSS port coupled to the actual solitary antenna port; it is equal to zero (an open circuit) for all FSS ports coupled to dummy ports of the antenna array. Thus, this term ensures that no energy is coupled from the FSS to the dummy ports of the antenna array. Mathematically:

$$Y_0\left[n_x,n_y\right]=\left\{\begin{matrix} 0 & n_x\neq 0,n_y\neq 0 \\ A_\infty & n_x=n_y=0 \end{matrix}\right\} \tag{148}$$

The constant A_∞ is a large positive number that, ideally, tends towards infinity; in practice, it only needs to be sufficiently large for numeric computations. Note that the solitary antenna is assumed to occur at $n_x=n_y=0$. In addition to $Y_0\left[n_x,n_y\right]$, a second artificial admittance $Y_\infty\left[n_x,n_y\right]$ is introduced that is added in parallel to the self admittance of each antenna port. It is defined as:

$$Y_\infty\left[n_x,n_y\right]=\left\{\begin{matrix} A_\infty & n_x\neq 0,n_y\neq 0 \\ 0 & n_x=n_y=0 \end{matrix}\right\} \tag{149}$$

Note that this admittance is zero at the port of the actual solitary antenna, but "infinite" at all of the other dummy ports in the antenna array. This causes these other ports to effectively be short circuited.

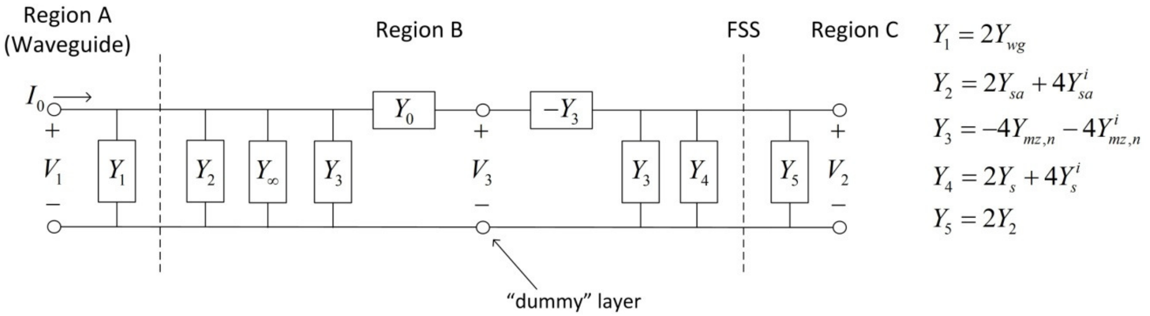

Fig. 65. Modified lattice for alternate formulation of solitary antenna problem.

Analysis of this modified three-layer scenario proceeds by writing a system of three difference equations for the lattice. The first two equations in this system are analogous to (113)-(114) that were used for the waveguide array radiating through a single layer FSS. However, the mutual admittance between ports on the antenna array layer are assumed to be zero (i.e. no coupling between the antennas of the array). This, along with the additional admittances (148) and (149), modifies (113) to become:

$$\begin{gathered}\left(2Y_{sa} + 2Y_{wg} + 4Y_{sa}^i - 4\sum_n \left(Y_{1,n}^{mz} + Y_{1,n}^{mz,i}\right)\right) V_1\left[n_x, n_y\right] + \\ Y_\infty\left[n_x, n_y\right] V_1\left[n_x, n_y\right] + Y_0\left[n_x, n_y\right]\left(V_1\left[n_x, n_y\right] - V_3\left[n_x, n_y\right]\right) = I\left[n_x, n_y\right]\end{gathered} \tag{150}$$

Here, $V_1\left[n_x, n_y\right]$ is the voltage distribution on the antenna array ports (i.e. the actual solitary antenna and all "dummy" antennas).

The second difference equation, written with respect to the dummy layer of the lattice, is:

$$\begin{gathered}Y_0\left[n_x, n_y\right]\left(V_3\left[n_x, n_y\right] - V_1\left[n_x, n_y\right]\right) + \\ 4\sum_n \left(Y_{mz,n} + Y_{mz,n}^i\right)\left(V_3\left[n_x, n_y\right] - V_2\left[n_x + a_n, n_y + b_n\right]\right) = 0\end{gathered} \tag{151}$$

The spatial domain quantity $V_2\left[n_x,n_y\right]$ represents the FSS port voltages. Note that the dummy ports are essentially "floating" nodes in the sense that they have no direct connection to ground; the only have couple to the ports of the FSS and antenna layers.

The final difference equation is written with respect to the FSS ports:

$$\begin{aligned}&\left(4Y_s+4Y_s^i\right)V_2\left[n_x,n_y\right]+\\&4\sum_n\left(Y_{m,n}+Y_{m,n}^i\right)\left(V_2\left[n_x+a_n,n_y+b_n\right]\right)-\\&4\sum_n\left(Y_{mz,n}+Y_{mz,n}^i\right)\left(V_3\left[n_x+a_n,n_y+b_n\right]\right)=0\end{aligned} \tag{152}$$

The system of difference equations (150), (151)-(152) must again be handled in the spectral domain. Computing the 2D DFT of these yields:

$$\begin{aligned}&\left(2Y_{sa}+2Y_{wg}+4Y_{sa}^i-4\sum_n\left(Y_{1,n}^{mz}+Y_{1,n}^{mz,i}\right)\right)\tilde{V}_1\left[k_x,k_y\right]+\\&\tilde{Y}_\infty\left[k_x,k_y\right]\otimes\tilde{V}_1\left[k_x,k_y\right]+\tilde{Y}_0\left[k_x,k_y\right]\otimes\left(\tilde{V}_1\left[k_x,k_y\right]-\tilde{V}_3\left[k_x,k_y\right]\right)=\tilde{I}\left[k_x,k_y\right]\end{aligned} \tag{153}$$

$$\begin{aligned}&\tilde{Y}_0\left[k_x,k_y\right]\otimes\left(\tilde{V}_3\left[k_x,k_y\right]-\tilde{V}_1\left[k_x,k_y\right]\right)+4\tilde{V}_3\left[k_x,k_y\right]\sum_n\left(Y_{mz,n}+Y_{mz,n}^i\right)-\\&4\tilde{V}_2\left[k_x,k_y\right]\sum_n\left(Y_{mz,n}+Y_{mz,n}^i\right)e^{-j2\pi\left[\left(k_x-1\right)a_n/N_x+\left(k_y-1\right)b_n/N_y\right]}=0\end{aligned} \tag{154}$$

$$\begin{aligned}&\left(4Y_s+4Y_s^i+4\sum_n\left(Y_{m,n}+Y_{m,n}^i\right)e^{-j2\pi\left[\left(k_x-1\right)a_n/N_x+\left(k_y-1\right)b_n/N_y\right]}\right)\tilde{V}_2\left[k_x,k_y\right]-\\&4\tilde{V}_3\left[k_x,k_y\right]\sum_n\left(Y_{mz,n}+Y_{mz,n}^i\right)e^{-j2\pi\left[\left(k_x-1\right)a_n/N_x+\left(k_y-1\right)b_n/N_y\right]}=0\end{aligned} \tag{155}$$

Note that the multiplication of $Y_\infty\left[n_x,n_y\right]$ or $Y_0\left[n_x,n_y\right]$ with any of the lattice voltages in the spatial domain becomes a circular convolution operation ($\otimes$) in the spectral domain. Circular convolution of two discrete two-dimensional functions is defined as follows:

$$f\left[k_x,k_y\right]\otimes g\left[k_x,k_y\right]=\sum_{i=1}^{N_x}\sum_{j=1}^{N_y}\begin{pmatrix} f\left[\left\langle k_x-i\right\rangle_{N_x},\left\langle k_y-j\right\rangle_{N_y}\right]\times \\ g\left[\left\langle k_x-i\right\rangle_{N_x},\left\langle k_y-j\right\rangle_{N_y}\right] \end{pmatrix} \tag{156}$$

The next step is to define the following admittance summations using terms from (153)-(155):

$$S_1=2Y_{sa}+2Y_{sa}+4Y_{sa}^i-4\sum_n\left(Y_{mz,n}+Y_{mz,n}^i\right) \tag{157}$$

$$S_2=4\sum_n\left(Y_{mz,n}+Y_{mz,n}^i\right)e^{-j2\pi\left[(k_x-1)a_n/N_x+\left(k_y-1\right)b_n/N_y\right]} \tag{158}$$

$$S_3=4\sum_n\left(Y_{mz,n}+Y_{mz,n}^i\right) \tag{159}$$

$$S_4=4Y_s+4Y_s^i+4\sum_n\left(Y_{m,n}+Y_{m,n}^i\right)e^{-j2\pi\left[(k_x-1)a_n/N_x+\left(k_y-1\right)b_n/N_y\right]} \tag{160}$$

$$S_5=4\sum_n\left(Y_{mz,n}+Y_{mz,n}^i\right)e^{-j2\pi\left[(k_x-1)a_n/N_x+\left(k_y-1\right)b_n/N_y\right]} \tag{161}$$

Then (153)-(155) can be written as:

$$\begin{aligned} &S_1\tilde{V}_1\left[k_x,k_y\right]+\tilde{V}_1\left[k_x,k_y\right]\otimes\left(\tilde{Y}_\infty\left[k_x,k_y\right]+\tilde{Y}_0\left[k_x,k_y\right]\right)- \\ &\tilde{V}_3\left[k_x,k_y\right]\otimes\tilde{Y}_0\left[k_x,k_y\right]=\tilde{I}\left[k_x,k_y\right] \end{aligned} \tag{162}$$

$$\tilde{Y}_0\left[k_x,k_y\right]\otimes\left(\tilde{V}_3\left[k_x,k_y\right]-\tilde{V}_1\left[k_x,k_y\right]\right)+\tilde{V}_3\left[k_x,k_y\right]S_3-\tilde{V}_2\left[k_x,k_y\right]S_2=0 \tag{163}$$

$$S_4\tilde{V}_2\left[k_x,k_y\right]-S_2\tilde{V}_3\left[k_x,k_y\right]=0 \tag{164}$$

The alternative formulation of the solitary antenna-FSS structure allows the entire lattice to be defined by five infinite admittance summations (157)-(161) that depend on the geometric dimensions of the FSS and waveguide. The additional spectral domain admittances, $\tilde{Y}_\infty\left[k_x,k_y\right]$ and $\tilde{Y}_0\left[k_x,k_y\right]$, remain constant over any dimensional design space.

The only complication that (162)-(164) present is that they are not simple algebraic equations which can be solved for the spectral domain voltages (as was done previously for all other spectral domain analyses thus far). The convolution operator, in particular, prevents this. The equations must be solved numerically rather than in closed form. To do this, two sets of integers are defined to represent each discrete point in the spectral domain:

$$\begin{aligned} p &= 1,2,\ldots,N_x \\ q &= 1,2,\ldots,N_y \end{aligned} \tag{165}$$

Using these integers as indexes, three sets of $N_x \times N_y$ unknown port voltages are defined: one set for the FSS ports, one set for the antenna array ports, and one set for the dummy layer ports. These sets, in particular, are:

$$\begin{aligned} \tilde{V}_1^{pq} &= \tilde{V}_1\left[p,q\right] \\ \tilde{V}_2^{pq} &= \tilde{V}_2\left[p,q\right] \\ \tilde{V}_3^{pq} &= \tilde{V}_3\left[p,q\right] \end{aligned} \tag{166}$$

There are also corresponding sets of spectral domain admittances; specifically:

$$\begin{aligned} S_2^{pq} &= S_2\left[p,q\right] \\ S_4^{pq} &= S_4\left[p,q\right] \\ S_5^{pq} &= S_5\left[p,q\right] \end{aligned} \tag{167}$$

Next, (162) is evaluated at $\left[k_x,k_y\right]=\left[p,q\right]$ and rewritten using (166) and the definition of the two-dimensional discrete circular convolution:

$$S_1\tilde{V}_1^{pq} + \left\{ \sum_{i=1}^{N_x}\sum_{j=1}^{N_y} \tilde{V}_1^{ij} \begin{pmatrix} \tilde{Y}_\infty\left[\langle p-i\rangle_{N_x},\langle q-j\rangle_{N_y}\right]\times \\ \tilde{Y}_0\left[\langle p-i\rangle_{N_x},\langle q-j\rangle_{N_y}\right] \end{pmatrix} \right\} - \left\{ \sum_{i=1}^{N_x}\sum_{j=1}^{N_y} \tilde{V}_3^{ij}\tilde{Y}_0\left[\langle p-i\rangle_{N_x},\langle q-j\rangle_{N_y}\right] \right\} = \tilde{I}[p,q] \tag{168}$$

This defines a set of $N_x \times N_y$ equations, each stemming from the evaluation of (162) at a single point in the spectral domain. In a similar fashion, (163)-(164) can be evaluated at each point in the spectral domain to yield two additional sets of $N_x \times N_y$ equations:

$$\left\{ \sum_{i=1}^{N_x}\sum_{j=1}^{N_y} \left(\tilde{V}_3^{ij} - \tilde{V}_1^{ij}\right)\tilde{Y}_0\left[\langle p-i\rangle_{N_x},\langle q-j\rangle_{N_y}\right] \right\} + \tilde{V}_3^{pq}S_3 - \tilde{V}_2^{pq}S_2^{pq} = 0 \tag{169}$$

$$S_4^{pq}\tilde{V}_2^{pq} - S_2^{pq}\tilde{V}_3^{pq} = 0 \tag{170}$$

Together, (168)-(170) form a system of $3 \times N_x \times N_y$ equations with unknowns $\tilde{V}_1^{pq}$, $\tilde{V}_2^{pq}$, and $\tilde{V}_3^{pq}$. This system can be written in block matrix form as follows:

$$\begin{bmatrix} A_{11} & A_{12} & A_{13} \\ A_{21} & A_{22} & A_{23} \\ A_{31} & A_{32} & A_{33} \end{bmatrix} \begin{bmatrix} \tilde{\mathbf{V}}_1 \\ \tilde{\mathbf{V}}_2 \\ \tilde{\mathbf{V}}_3 \end{bmatrix} = \begin{bmatrix} \tilde{\mathbf{I}} \\ \mathbf{0} \\ \mathbf{0} \end{bmatrix} \tag{171}$$

Here, $\mathbf{0}$ represents a column vector of zeros with $N_x \times N_y$ elements. $\mathbf{I}$ is a column vector of the current excitation on the right-hand side of (168). Specifically:

$$\tilde{\mathbf{I}} = \left[\tilde{I}[p_1,q_1] \quad \tilde{I}[p_2,q_2] \quad \cdots \quad \tilde{I}[p_N,q_N] \right]^T \tag{172}$$

The column vectors $\tilde{\mathbf{V}}_i$ represent the unknown spectral domain voltage values $\tilde{V}_i^{pq}$:

$$\tilde{\mathbf{V}}_i = \left[\tilde{V}_i[p_1,q_1] \quad \tilde{V}_i[p_2,q_2] \quad \cdots \quad \tilde{V}_i[p_N,q_N] \right]^T \tag{173}$$

The relevant blocks of the matrix (A_{11}, A_{12}, etc.) can be ascertained by inspection of (168)-(170); they are not listed here explicitly for the sake of brevity. Solving the matrix system (171) by inversion yields the spectral domain voltage vectors (173). These one-dimensional vectors can be duly rearranged into two-dimensional form ($\tilde{V}_1\left[k_x,k_y\right]$, $\tilde{V}_2\left[k_x,k_y\right]$, and $\tilde{V}_3\left[k_x,k_y\right]$) and then transformed back into the spatial domain.

The alternative formulation outlined above, along with the direct formulation from the preceding section, are meant to provide a mathematical groundwork for future investigation. The combination of a finite antenna array (or solitary antenna) with an infinite FSS poses many mathematical challenges, and the above techniques are merely suggested approaches to this problem. Further development of the lattice model may lead to better formulations. As such, computational examples for these problems are beyond the scope of the present work and will not be pursued here.

CHAPTER IX

FSS SYNTHESIS USING THE LATTICE MODEL

The lattice model techniques described in the preceding chapters - along with more traditional techniques, including full-wave Floquet theory on one end of the spectrum and circuit models on the other end - all aim to solve the analysis problem: determining FSS performance based on a given physical structure with a fixed geometry. For practical engineering design purposes, these techniques have to be combined with an engineer's intuition and experience to achieve specified performance criteria for a particular application. This often results in a trial-and-error design methodology, where parametric variations of the same design are successively analyzed and evaluated until a suitable solution is converged upon. However, the final solution may not be "optimal" in any quantifiable sense; rather, it may simply be an "acceptable" solution that happens to achieve good enough performance.

The inverse problem - calculating the necessary FSS dimensions in order to achieve a specified set of performance criteria - is, in general, much more difficult. The task typically involves searching a pre-determined design space - which defines the allowable geometric dimensions of the FSS - to find the one design that best meets the desired performance. The difficulty in systematically synthesizing a design to perform in a particular way is a familiarly difficult problem in almost any discipline of engineering or applied mathematics, so it may often be neglected if intuition and ad-hoc design approaches give acceptable results. Nonetheless, it is of significant interest to develop systematic and efficient methods whereby FSS designs can be synthesized. Such methods, of course, will never fully replace intuition in the design process, but they can certainly allow the design of more complex FSS geometries which may be difficult to handle with intuition alone.

This chapter explores how the lattice model provides a novel methodology for FSS synthesis. In particular, the model provides a unique opportunity to approximate FSS performance as a function of geometric dimensions. The lattice admittances, as formulated in the preceding chapters, tend to be well-behaved functions of the geometric dimensions and can be represented quite accurately using multidimensional polynomials. Thus, the FSS performance over an entire geometric design space can be represented as a circuit domain problem with polynomial-based admittances. As will be shown, this in turn allows simple optimization schemes to be devised to synthesize FSS dimensions to achieve various performance goals.

The chapter is organized as follows. First, a brief overview is given of current FSS synthesis techniques found in the literature. Then, the basis for FSS optimization through the lattice model is established: polynomial representation of the lattice admittances. The motivation and details behind the polynomial modeling is discussed, and examples are provided to demonstrate the accuracy of the approximations involved. Finally, the polynomial modeling is applied to the specific task of constrained FSS optimization problems. To do this, the optimization strategy is first summarized in general; then, a series of optimization examples are provided. Some of the examples are fabricated and measured to compare with the optimization theory and simulation.

Typical FSS Synthesis Procedures

In practice, the inverse problem of FSS synthesis is most commonly solved through iterative techniques that optimize an objective function (or multiple objective functions) subject to a number of formal mathematical constraints. These techniques are commonly referred to as simply "optimization". At the same time, "optimization" is also sometimes loosely used in the literature to refer to the ad-hoc process by which an engineer changes the parameters of a design through intuition until a suitable solution is found (a process mentioned in the chapter introduction above). This latter use of the term is perhaps a poor choice of wording for such an informal procedure; accordingly, it must be stressed that in this work, "optimization" will only be used in the former sense: a formal process for synthesis comprising a well-formulated iterative routine that analyzes the problem repeatedly under varying parameters until an "optimal" solution is achieved in a specifically designated design space. Depending on how the optimization is formulated, the optimal solution may be a global optimum, where the solution is guaranteed to meet the specified criteria better than any other solution in the design space; a local optimum, where the solution is only optimal in a localized region of the design space, but where it may be difficult to distinguish mathematically if other local optimums are, in fact, "better" solutions; or finally, a multi-objective or Pareto optimum, where multiple objectives are desired and trade-offs must be made in a Pareto sense.

By far the most popular algorithms used for FSS optimization in recent years are those based on particle swarm optimization (PSO) and the genetic algorithm (GA). PSO (e.g. [67], [24]) attempts to find a solution within a defined search space by iteratively testing a collection ("swarm") of candidate solutions ("particles") in that space. The quality of a candidate solution is defined by some pre-determined measure, and the direction and "velocity" of the particles in the search space are adjusted at each iteration until the swarm converges on a suitable solution. The PSO is conceptually intended to mimic to the social behavior of swarms of bees, flocks of birds, or schools of fish. In GA (e.g. [68], [69]), a collection of candidate solutions are iteratively "mutated" and tested for "genetic fitness" (i.e. how well the solution conforms to the desired performance) until a suitable solution is found. The GA is conceptually based on the idea of biological natural selection.

PSO and GA have been applied to a wide variety of traditional FSS geometries to determine the appropriate dimensions. Additionally, a completely different class of optimized FSS designs is those that have been variously named "binary", "pixelated", etc. The idea behind these designs is illustrated in Fig. 66 [70]. Essentially, an FSS unit cell is divided into a large number of small squares (sometimes called pixels). Each pixel can either be filled with metallization or left vacant. Thus, a large number of arbitrary metallization patterns are possible, with more pixels resulting in more complex design possibilities. In (a), the pixels are metalized so as to achieve a classic Jerusalem cross geometry. In (b), however, a GA is applied that optimizes the metallization pattern to achieve some desired performance. The resulting pattern, though symmetric, is not particularly intuitive in terms of how it operates, nor does it conform to some readily-identifiable shape such as a cross dipole, patch, etc. It does, however, achieve the desired performance. Many examples of such designs are available in literature (e.g.

[71], [69]). A related idea is to optimize a fractal metallization pattern [72], which will not be elaborated on here.

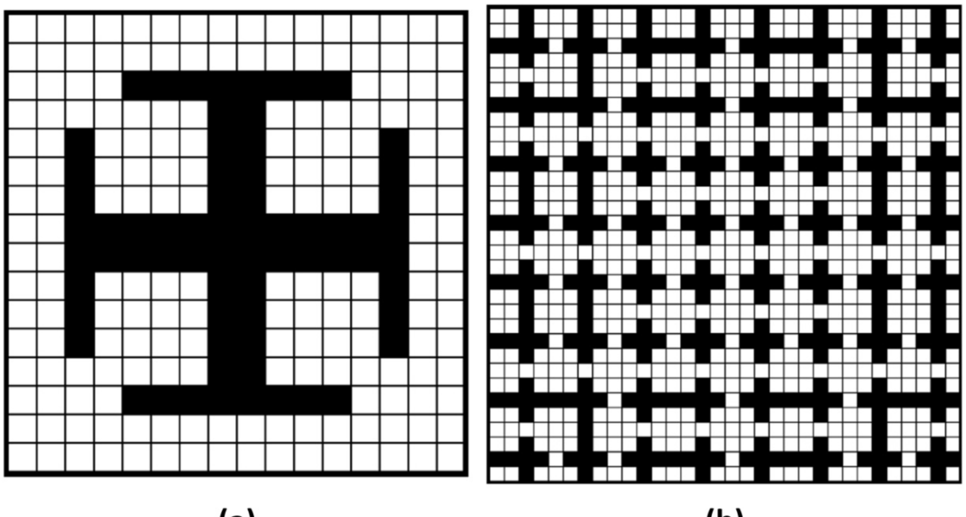

Fig. 66. "Pixelated" FSS unit cells for the purpose of optimization. (a) Jerusalem cross FSS formed using the pixels. (b) Optimized design with arbitrary metallization pattern.

The optimization strategies discussed above - including PSO and GA, among others - can yield excellent results in terms of meeting the desired performance criteria of a particular application. In many cases, these results would largely not be obtainable in any realistic sense by a human designer operating on intuition, so the methods absolutely have much merit. Furthermore, a whole class of arbitrarily-shaped FSS unit cell topologies can be obtained through optimization - namely, those based on pixelated or fractal designs - that would otherwise not exist. The biggest and most common difficulty encountered by these optimization techniques, however, is the computational resources required. These techniques are all iterative, and the methods employed require full-wave solutions at each iteration. In many cases, the full-wave solutions are obtained through commercial simulation software, which, although convenient, are not as efficient as numerical routines specifically customized to a certain problem. The result is that the optimization process may easily take hours or days to complete, even with impressive computational hardware available. The results of one optimization routine are not guaranteed to give the sought-after results, either. Thus, it would obviously be desirable to develop optimization schemes that somehow limit the full-wave computational cost inherently involved in these procedures.

Polynomial Representation of Admittances

The lattice representation of a FSS provides a unique opportunity to approximate its performance over a wide variation in dimensional parameters. Understanding the changes in FSS behavior as the geometrical dimensions are varied over a feasible design space is of significant practical interest, of course, since it allows a designer to quickly locate what dimensions from the design space may provide the best solution to a given performance goal. As an FSS geometry becomes more complex and additional degrees of dimensional freedom are present, it may become increasingly more difficult to successfully apply intuition to solve this problem, as the relationships between multiple dimensions changing simultaneously become increasingly complex.

The specific advantaged afforded by the lattice model is that the infinite admittance summations encountered in the model can be readily approximated by low-order polynomial functions of the dimensional parameters. The behavior of the FSS over a particular geometrical design space can thus be abstracted into a circuit domain model with polynomial admittances. Once the lattice admittances from the EM domain of the model are appropriately fitted to a polynomial function, the FSS can be studied exclusively in the circuit domain, with significantly reduced computational effort. In particular, this can allow a simplified and computationally tractable optimization routine to be performed in the circuit domain that can synthesize FSS dimensions to meet specified performance criteria. This circuit domain optimization should, in principle, be much less computationally expensive than any full-wave optimization routines that are commonly employed.

Motivation

The motivation for this proposed approach comes from the observation that as dimensional parameters of the FSS are varied over a reasonably small range, the self and mutual admittance terms of the lattice experience smooth and gradual variations. The variations of the admittances are such that they can be reasonably fitted to a polynomial function of the dimensional parameters. As an extension to this idea, the infinite sums of admittances necessitated by the model under - whether spatial domain sums under uniform plane wave incidence or spectral domain sums under non-uniform incidence - can also reasonably be expected to behave as polynomials, since a sum of polynomials of like order yields another polynomial of the same order.

The suitability of the lattice admittances to polynomial approximation is best illustrated by example. Fig. 67 shows two such examples of the behavior of lattice admittances as a function of dimensional parameters. The FSS geometries under consideration are the single- and dual-aperture FSSs of Fig. 39 and Fig. 43 (a), respectively. In Fig. 67 (a), the real part of the admittance sum Y^{Σ} is plotted as a function of the dimensions L and $D = D_x = D_y$ (W remains constant). In (b), the imaginary part of the admittance sum Y^{Σ_3} is plotted as a function of L_1 and h (L_2, D_x, D_y, and W are kept constant). It is clear that in both cases, the infinite admittance series is a smoothly varying function of the relevant dimensions.

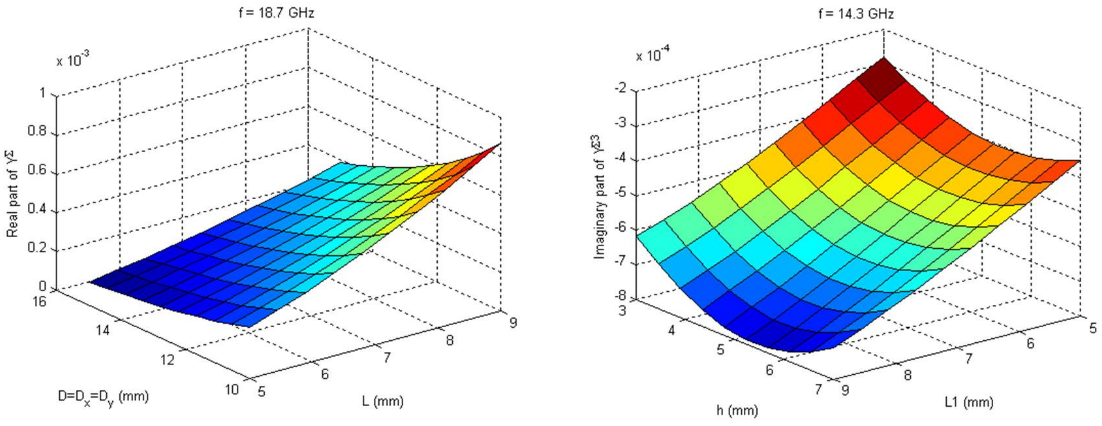

(a) **(b)**

Fig. 67. Variation of infinite lattice admittance series. (a) Single rectangular aperture FSS and (b) dual rectangular aperture FSS.

These observations on the behavior exhibited in Fig. 67 suggest that the behavior of the lattice admittances across the whole dimensional space can be accounted for by calculating the values at a relatively few number of points throughout the space and then applying a polynomial regression to those known points. This would allow the admittance at any arbitrary point in the dimensional space to be calculated quickly without applying the full numerical approach. This idea can easily be extended to include any number of arbitrary dimensions. For example, if all six dimensions of the dual aperture design of Fig. 43 (a) were varied independently and simultaneously, the variation of the lattice admittances could be represented as a six-dimensional polynomial.

It must be stressed that the well-behaved nature of the admittances in Fig. 67 for rectangular aperture designs is, at this point, a purely empirical observation. Examples of the admittance behavior for all of the various FSS topologies considered in this work will not be provided here; it will simply be asserted that similar behavior has, in fact, been observed, to a reasonable empirical extent, in all such designs. Furthermore, in the succeeding sections of this chapter, examples of successful optimization through polynomial modeling will be provided that indirectly support this claim. The goal of this work is to demonstrate the utility of the polynomial approximation with respect to optimization, rather than to formally prove that the approximation is globally applicable. It is not unreasonable, however, to assume that such behavior would also be exhibited by other resonant geometries besides rectangular apertures, although no such claim can be made here in any rigorous sense. Such behavior would be necessary, of course, in order for this feature of the lattice model to be widely applicable to various FSS topologies. A formal study of this claim is beyond the scope of the current work and will not be pursued here.

Implementation

The concept of multidimensional polynomial regression suggested above is relatively straightforward. It simply involves representing any admittance in the lattice as a polynomial function of several different geometric variables by calculating the appropriate polynomial coefficients that best fit an observed set of already-known admittances. Although such regression is a fairly routine and well-known process from a mathematical standpoint, a formal statement of the idea as applicable to the lattice model will briefly be given here.

Consider an infinite lattice admittance term Y and a vector $\mathbf{x} \in \mathbb{R}^N$ of N FSS dimensions, $\mathbf{x} = [x_1, x_2, \ldots, x_N]$. The function of interest is $Y(\mathbf{x})$ - the admittance sum as a function of the dimensions. The allowable values of $\mathbf{x}$ - that is, the physical design space of the FSS - should in most cases by sufficiently defined by a convex polytope in $\mathbb{R}^N$. The proposed concept postulates that the admittance Y can be readily approximated as the following multidimensional polynomial [73]:

$$Y(\mathbf{x}) \cong P(\mathbf{x}) = \sum_{j=1}^{M} c_j \left(\prod_{i=1}^{N} x_i^{q_{ij}} \right) \tag{174}$$

Here, c_j are a set of scalar coefficients to be determined by regression, and the integer exponents q_{ij} are subject to:

$$\sum_{i=1}^{N} q_{ij} \leq R \quad \forall j \tag{175}$$

R is the chosen polynomial order. Also, the number of terms M in the summation (174) (and hence the number of unknown coefficients c_j) is given by $M = (N+R)!/(N!R!)$.

To find the coefficients c_j via regression, a number of admittances from the design space must first be calculated directly. These admittances may be calculated at random points $\mathbf{x}_n$ in the design space or at equally spaced points. These "known" admittance values are then used to compute the regression. The details of the regression procedure, which consist of fairly routine linear algebra operations, are omitted here for brevity; it is sufficient to point out that the number of admittance points used in the regression must be at least as great as the number of coefficients c_j to be determined.

Example: Dual Rectangular Aperture FSS

The concept of a polynomial circuit model is applied here to a specific example in order to demonstrate the potential accuracy of a polynomial approximation of the lattice admittances. The dual rectangular aperture geometry of Fig. 43 (a) is chosen for this purpose. Specifically, a design is studied with fixed dimensions $D_x = D_y = 20$ mm and $W = 1\text{ mm}$. The remaining dimensions are assumed to vary over the following design space:

$$\begin{array}{l} 9\text{ mm} \le L_1 \le 13\text{ mm} \\ 13\text{ mm} \le L_2 \le 19\text{ mm} \\ 2\text{ mm} \le h \le 12\text{ mm} \end{array} \qquad (176)$$

Three-dimensional polynomial models are computed in terms of these three dimensions for the three lattice admittances Y^{Σ_1}, Y^{Σ_2}, and Y^{Σ_3} of Fig. 42 (b). To obtain the polynomials, a number of points from the design space are chosen, and polynomial regression is performed. This procedure is done at both 9 GHz and 11 GHz using both second- and third-order polynomials. Second-order models are computed using 20, 30, 50, and 100 points from the design space, and third-order models are computed using 30, 50, and 100 points. The points are chosen randomly from the three-dimensional design space using a pseudo-random number generator in [58].

Table 1 and Table 2 report the mean relative error between the polynomial models and the actual admittance values over the extent of the three-dimensional design space for second- and third-order polynomials, respectively. The relative error is expressed separately for the real (e_r) and imaginary (e_i) parts of the admittance and is computed as follows. After performing the regression using the randomly chosen points, the design space is gridded into $5^3 = 125$ regularly spaced points; the exact admittance is calculated at each of these points and compared to the value obtained using the derived polynomial expression. For each gridded point $\mathbf{x}_n$ in the space, the relative error for the real part of the admittance is calculated as:

$$e_r = \frac{\left|\operatorname{Re}\left\{Y\left(\mathbf{x}_n\right)\right\} - \operatorname{Re}\left\{P\left(\mathbf{x}_n\right)\right\}\right|}{\left|\frac{1}{125}\sum_{i=1}^{125}\operatorname{Re}\left\{Y\left(\mathbf{x}_i\right)\right\}\right|} \tag{177}$$

The error for the imaginary part of the admittance is analogous. Note that the relative error here is defined as the ratio of the absolute error (between the actual and polynomial-based admittances) to the absolute value of the arithmetic average of all admittances in the gridded space. This somewhat unorthodox definition ensures that the relative error is not biased towards large values near zero crossings of the admittance Y. Furthermore, this ensures that the relative error at each point in the gridded space is calculated relative to the same average admittance value (the denominator).

		9 GHz		11 GHz	
Number of Points	Model Term	% Error (Real)	% Error (Imag)	% Error (Real)	% Error (Imag)
20	Y^{Σ_1}	0.00166	1.13561	0.00597	2.64134
	Y^{Σ_2}	0.00315	3.81328	0.01008	3.58427
	Y^{Σ_3}	0.00125	7.55397	0.00674	7.27468
30	Y^{Σ_1}	0.00140	1.26054	0.00498	2.87238
	Y^{Σ_2}	0.00247	3.87629	0.00730	3.67216
	Y^{Σ_3}	0.00116	8.42598	0.00774	7.89474
50	Y^{Σ_1}	0.00136	1.20504	0.00514	2.66733
	Y^{Σ_2}	0.00239	3.92406	0.00903	3.58124
	Y^{Σ_3}	0.00113	7.92015	0.00661	7.27999
100	Y^{Σ_1}	0.00135	1.06147	0.00530	2.39292
	Y^{Σ_2}	0.00223	3.37716	0.00733	3.08833
	Y^{Σ_3}	0.00097	6.96519	0.00637	6.49852

Table 1. Second-order polynomial admittances.

Based on Table 1 and Table 2, it is clear that the real part of all three admittance terms are highly accurate for both the second-order and third-order polynomials, regardless of how many or how few points are used for the regression. The imaginary part of the admittance, however, exhibits much more significant error in some cases. In fact, the second-order polynomials seem to be somewhat less capable of correctly capturing the admittance behavior, as the relative error is at least 1% or greater for every case at 9 GHz and 2% or greater for every case at 11 GHz. A noticeable improvement in the imaginary error is achieved by the third-order polynomials, although the error is still much higher than for the real part of the admittance. Finally, for all cases considered, the polynomial models do not seem to improve noticeably through the use of more points for the regression. This suggests that at a certain point, adding additional points to the regression may be an exercise in diminishing returns, in terms of accuracy; it may be advantageous to limit the number of admittances to close to the minimum required number.

		9 GHz		11 GHz	
Number of Points	Model Term	% Error (Real)	% Error (Imag)	% Error (Real)	% Error (Imag)
30	Y^{Σ_1}	0.00136	0.29617	0.00591	0.38391
	Y^{Σ_2}	0.00131	0.93272	0.00458	0.53724
	Y^{Σ_3}	0.00027	1.97991	0.00714	1.06401
50	Y^{Σ_1}	0.00153	0.23451	0.00661	0.29458
	Y^{Σ_2}	0.00105	0.74258	0.00985	0.42839
	Y^{Σ_3}	0.00024	1.56487	0.00595	0.81434
100	Y^{Σ_1}	0.00101	0.18742	0.00485	0.27072
	Y^{Σ_2}	0.00123	0.61273	0.00600	0.36068
	Y^{Σ_3}	0.00020	1.24174	0.00489	0.74288

Table 2. Third-order polynomial admittances.

The polynomial circuit model for the dual rectangular aperture FSS given above is simply a representative calculation and is by no means meant to be an exhaustive study of polynomial modeling via the lattice model. Several important considerations - including the number of points necessary for an accurate regression model and the best polynomial order to choose - are complex enough to warrant an extensive study in and of themselves. Such a study is beyond the scope of this work. Nonetheless, the example provides ample evidence that polynomial modeling is a feasible and potentially useful tool achieved afforded by the lattice model. In the following sections, this feature of the model will be applied for the purpose of FSS optimization.

Optimization using Polynomial Model

Typical FSS optimization can be broken down into two general steps. First, a multidimensional optimization space is defined over which an optimized solution is desired. Then, some form of nonlinear constrained optimization routine is performed. As discussed before, this will often take the form of PSO or GA, where each iteration involves numerical full-wave computations. This kind of two-step approach is illustrated at the top of Fig. 68.

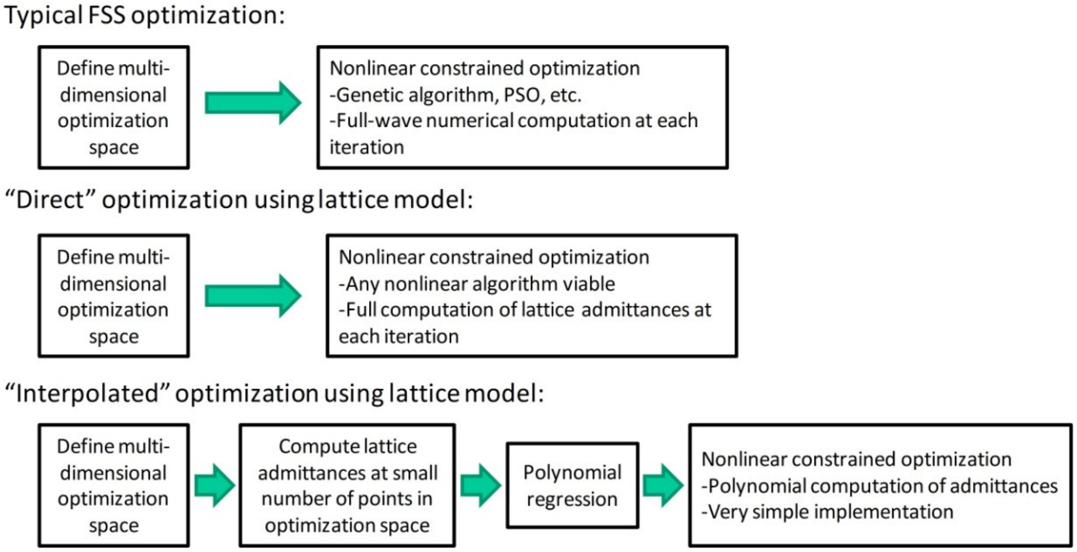

Fig. 68. Summary of potential optimization procedures for FSS.

It is possible to directly mimic this typical optimization approach using the lattice model. Specifically, the full-wave computations at each iteration are replaced by the appropriate lattice model computations. The optimization algorithm itself may remain the same. This method, referred to in Fig. 68 as "direct" optimization using the lattice model, may or may not provide any benefit over the typical process (although it does represent a novel formulation of the problem by employing the lattice theory). The computational benefit (if any) will depend on the specific formulation of the lattice model used and the specific formulation of any other full-wave computation used in alternative schemes. The direct lattice model optimization procedure will not be studied here.

Based on the polynomial representation of admittances introduced above, a second optimization scheme using the lattice model can be implemented. This is referred to in Fig. 68 as "interpolated" optimization. Specifically, after defining the optimization space for the problem, a relatively small number of points from that space are chosen, and the lattice admittances for those points are computed using the normal methodology (i.e. through the EM domain of the lattice model). Next, multidimensional regression is applied to acquire a complete polynomial model of the FSS admittances over the entire optimization space. Then, this polynomial model is used directly in an optimization algorithm.

The interpolated optimization scheme has several potential benefits. First, the optimization algorithm itself can be performed very quickly and efficiently, since it mostly involves simple computations in the polynomial-based circuit domain of the lattice. Thus, complex and custom optimization algorithms are not necessarily needed. In fact, generic nonlinear optimization programs, like those available in [58], can be readily employed. Nonetheless, algorithms such as PSO and GA can still, in principle, be used with this method if desired. These algorithms will complete in much less time than in typical optimization procedures, again due to the circuit domain versus full wave calculations. The interpolated optimization method lends itself, however, to simpler optimization schemes.

A second benefit of the interpolated optimization scheme stems from the fact that calculating the lattice admittances is the most time-consuming task computationally in the lattice model. The only direct admittance computations take place in the second step of the process in Fig. 68, before the polynomial regression is performed. Unlike the direct optimization scheme, no additional lattice computations are necessary during the iterative optimization process. Thus, the whole procedure is "front-loaded" with a known number of admittance computations. The number of these computations necessary for an accurate regression may very well be considerably less than the number of iterative admittance computations necessary under the direct optimization. Likewise, compared to traditional FSS optimization, the computational cost of computing the admittances for regression may be considerably lower than the iterative full-wave computations typically employed.

A third benefit to the interpolated optimization is that once the polynomial model is obtained, any number of fast optimizations can be run using that model. In other words, if the objective function or constraints of the optimization need to be modified, it is easy to do so and quickly obtain a new solution with the new objectives or constraints. There are an endless number of potential ways (i.e. different objective functions and different constraints) that an optimization problem could be formulated for an FSS, so the flexibility of being able to quickly implement such modifications would be a welcome feature in any practical design process.

Optimization Examples

In order to demonstrate the utility of the interpolated optimization scheme via the lattice model, a number of FSS designs comprising rectangular apertures will be optimized here. For further validation, a selected number of these designs are fabricated and measured in order to compare their performance to that predicted by the lattice model and simulation. Specifically, the following pure FSS designs will be synthesized: a single-layer, single-aperture design; a single-layer, dual aperture design; a dual-layer, dual-aperture design; and a dual-layer, triple-aperture design. Then, a few reconfigurable FSSs comprising varactor-tuned slots (like those in Chapter VI) are optimized. Finally, the method is extended to the antenna-FSS structures of Chapter VIII. Specifically, several designs with waveguide arrays and single-layer FSS windowing are optimized.

For each example, a simple optimization problem is formulated. The problems are straightforward enough that they can be readily computed in [58] using a generic function that is meant to solve nonlinear constrained optimization problems. This optimization function, per the documentation, is a gradient-based method that employs an interior point algorithm. The interior point method is a well-known class of algorithms commonly encountered in optimization problems. The details of the specific algorithm will not be elaborated on here. In a sense, the benefit of using a generic optimizing function to successfully design an FSS, without having to worry about the details of the optimization itself or to code a custom algorithm, is one of the primary goals of the interpolated optimization scheme with the lattice model. It allows a designer to focus more on properly formulating the optimization problem itself, rather than spending effort explicitly coding an optimization algorithm.

The optimization problems here all have single objectives; in principle, though, the procedures could be extended to multi-objective cases involving notions of Pareto optimality. Also, the problems are given a number of constraints in the form of linear inequalities and nonlinear inequalities. These inequalities define the geometric limitations of the problem and ensure the performance of the FSS stay within specified bounds. Strict equality constraints are not considered here, but could easily be implemented with little modification.

Standard FSS Examples

Single-Layer, Single-Aperture

A simple synthesis example is to take the single rectangular aperture geometry of Fig. 37 and optimize the dimensions to achieve a transmission peak at a single chosen frequency. Assume that the aperture width W is fixed and that the unit cell size is square such that $D = D_x = D_y$. The goal is to tune the dimension D and the aperture length L to maximize the transmission at a target frequency f_0.

To achieve this goal, a two-dimensional optimization vector $\mathbf{x}$ is defined:

$$\mathbf{x} = \begin{bmatrix} L & D \end{bmatrix}^T \tag{178}$$

A constrained minimization problem can be formulated that optimizes an objective function $T\left(\mathbf{x}, f_0\right)$ over the allowed design space of the dimensional variables $\mathbf{x}$:

$$\begin{array}{ll} \text{min} & -T\left(\mathbf{x}, f_0\right) \\ \text{s.t.} & f\left(\mathbf{x}\right) \le 0 \\ & A\mathbf{x} \le \mathbf{b} \\ & \mathbf{x}_l \le \mathbf{x} \le \mathbf{x}_u \end{array} \tag{179}$$

Here, the function $T\left(\mathbf{x}, f\right)$ is the transmissivity of the FSS as a function of the frequency and the dimensional variables $\mathbf{x}$. Note that the negative of the transmissivity is minimized – or, equivalently, the transmissivity is maximized. In this case, the optimization occurs at the single target frequency $f = f_0$; the rest of the frequency range of the FSS is ignored. The transmissivity can be written more explicitly as:

$$T(\mathbf{x}) = \frac{P_t}{P_{in}} = \frac{I_0^2\left(\mathbf{x}\right)}{2P_{in}Y^{\Sigma}\left(\mathbf{x}\right)} \tag{180}$$

Here, the current $I_0\left(\mathbf{x}\right)$ and the admittance $Y^{\Sigma}\left(\mathbf{x}\right)$ correspond to the input current and admittance, respectively, of the one-port network of Fig. 33.

The three constraints of (179) are identified by "s.t.", which stands for "subject to". The first constraint, $f\left(\mathbf{x}\right) \le 0$, is a nonlinear inequality constraint:

$$f\left(\mathbf{x}\right) = 0.95 - T\left(\mathbf{x}, f_0\right) \tag{181}$$

This ensures that the resulting transmission at the target frequency is sufficiently high, in this case $T \geq 0.95$ (i.e. 95% transmission). The second constraint, $A\mathbf{x} \leq \mathbf{b}$, is a linear equality constraint in matrix form:

$$A = \begin{bmatrix} 1 & -0.9 \\ 0 & -1 \end{bmatrix} \quad b = \begin{bmatrix} 0 \\ -2W \end{bmatrix} \tag{182}$$

This constraint ensures that the optimized dimensions are physically feasible. Specifically, (182) can be used to expand $A\mathbf{x} \leq \mathbf{b}$ into the following relations:

$$\begin{aligned} L &\leq 0.9D \\ D &\geq 2W \end{aligned} \tag{183}$$

These relations dictate that the aperture length is smaller than the unit cell size and that the unit cell size is at least twice as large as the aperture width. The third and final constraint, $\mathbf{x}_l \leq \mathbf{x} \leq \mathbf{x}_u$, is another set of inequality constraints that defines the allowable design space of the geometric variables. In other words, this is the optimization space of the problem. The vectors $\mathbf{x}_l$ and $\mathbf{x}_u$ define the lower and upper limits, respectively, of the variables contained in $\mathbf{x}$.

To implement this specific optimization problem, the aperture width is fixed at $W = 1\ \text{mm}$, and the remaining two dimensions are optimized in the following design space:

$$\begin{aligned} \mathbf{x}_l &= \left[12\ \text{mm} \quad 20\ \text{mm}\right]^T \\ \mathbf{x}_u &= \left[15\ \text{mm} \quad 28\ \text{mm}\right]^T \end{aligned} \tag{184}$$

The target frequency is set at $f_0 = 10\ \text{GHz}$, in the middle of the X-band. The polynomial regression is performed using 20 points from the two-dimensional design space. The resulting dimensions from the interpolated optimization procedure are:

$$\mathbf{x} = \begin{bmatrix} 13.26\ \text{mm} & 26.5\ \text{mm} \end{bmatrix}^T \tag{185}$$

The performance of the FSS with the optimized dimensions (185) is calculated using both the lattice model and simulation in [16]. The results are shown in Fig. 69. As desired, the lattice model (blue curve) achieves a transmission at 10 GHz, indicating a successful optimization. The simulated transmission peak (green curve) is shifted slightly down in frequency; this shift can be attributed to inaccuracies due to approximations in the lattice model itself: the single-mode sinusoidal current approximation, calculation of the infinite admittances series using a finite number of terms, etc. The discrepancy is not a result of the optimization procedure itself.

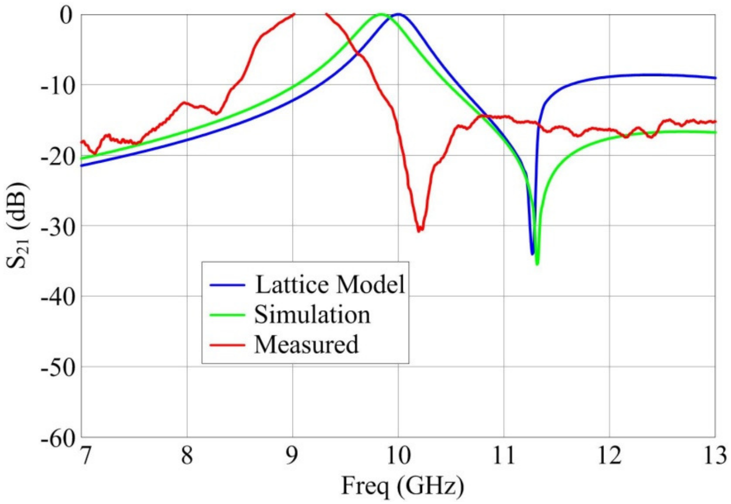

Fig. 69. Optimized single-layer, single-aperture FSS.

As further validation of this particular FSS design, a physical sample was fabricated. Ideally, the FSS comprises an infinitely thin, aperture-perforated PEC ground plane with no dielectric support. This ideal scenario, of course, is not physically achievable, so it was approximated by fabricating on a very thin (2 mil) liquid crystal polymer substrate. The substrate has thin copper cladding on both sides, and the apertures were cut into it on one side through a chemical wet etching process; the cladding on the second side was completely removed. This extremely thin substrate was also mechanically non-rigid, so the FSS also had to be sandwiched between two layers of structural foam for support. Fig. 70 shows a picture of the fabricated sample with one of the two foam layers removed, exposing the FSS inside. The fabricated FSS was measured using a simple ad-hoc free space fixture in which the sample was placed between two X-band horn antennas which were connected to the two ports of a vector network analyzer. The fixture was calibrated using the gated-reflect-line method of [74], and the transmission magnitude ($|S_{21}|$) was measured between the horns.

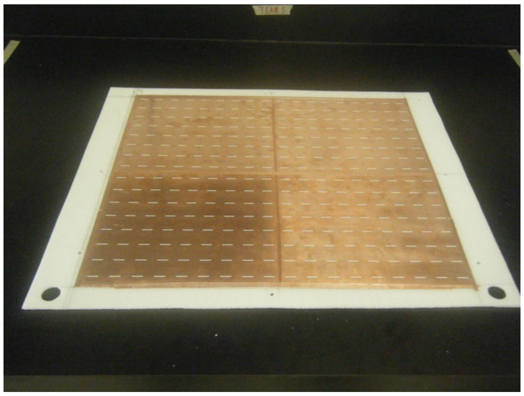

Fig. 70. Fabricated X-band single rectangular aperture FSS.

The combination of the thin dielectric layer, along with the foam layers and a ground plane of finite thickness, was shown through simulation to have a non-trivial lowering effect on the resonant frequency of the FSS, compared to that of an infinitely thin ground plane. This effect is borne out in the measured results, which are shown in Fig. 69 by the red curve. The overall transmission envelope is similar to that of the lattice model and simulated results, but it is shifted down in frequency by almost 1 GHz. Although the measurement does not exactly correspond to the predicted performance, the deviation is reasonably explained by the less-than-ideal fabrication method. However, this result does show the importance, in the case of a real design scenario, of making the lattice model formulation depict as accurately as possible the actual structure to be fabricated; otherwise, the purpose of the optimization procedure is somewhat voided if the specified performance goals are not met.

Single-Layer, Dual-Aperture FSS

A somewhat more complicated optimization than that of the preceding section can be explored by considering the dual rectangular aperture design of Fig. 42 (a). For this geometry, it may be of interest to optimize the dimensions to achieve dual transmission peaks at two different target frequencies. To this end, a constrained optimization problem can be defined as follows:

$$\begin{aligned} \text{min} \quad & \max\left\{-T\left(\mathbf{x}, f_1\right), -T\left(\mathbf{x}, f_2\right)\right\} \\ \text{s.t.} \quad & \mathbf{f}\left(\mathbf{x}\right) \leq 0 \\ & A\mathbf{x} \leq \mathbf{b} \\ & \mathbf{x}_l \leq \mathbf{x} \leq \mathbf{x}_u \end{aligned} \tag{186}$$

Here, the optimization variable $\mathbf{x}$ is a five-dimensional vector of dimensions:

$$\mathbf{x} = \left[L_1 \quad L_2 \quad D_x \quad D_y \quad h\right]^T \tag{187}$$

Only the width of the apertures W is assumed to be fixed. The objective function to be minimized is defined as the maximum value of $-T\left(\mathbf{x}, f\right)$ evaluated at both target frequencies. This type of formulation is usually referred to as a minimax optimization problem. In (186), it forces the lowest transmission value between the two target frequencies to be as high as possible.

The inequality constraint $\mathbf{f}\left(\mathbf{x}\right) \leq 0$ is defined more specifically by:

$$\mathbf{f}\left(\mathbf{x}\right) = \begin{bmatrix} 0.95 - T\left(\mathbf{x}, f_1\right) \\ 0.95 - T_2\left(\mathbf{x}, f_2\right) \\ T\left(\mathbf{x}, f_3\right) - 0.05 \end{bmatrix} \tag{188}$$

This ensures that both transmission peaks achieve 95% or more power transmission. Also, a third frequency f_3 is introduced here; it is located somewhere between the dual transmission peaks, in a region where the transmission should be minimal. The third constraint of (188) requires less than 5% power transmission at this third frequency. The linear inequality constraint $A\mathbf{x} \leq \mathbf{b}$ – which, as in (179), ensures that the FSS dimensions are physically realizable – is defined by:

$$A = \begin{bmatrix} 0 & 0 & 0 & -0.9 & 1 \\ 1 & 0 & -0.9 & 0 & 0 \\ 0 & 1 & -0.9 & 0 & 0 \end{bmatrix} \quad b = \begin{bmatrix} -2W \\ 0 \\ 0 \end{bmatrix} \tag{189}$$

More specifically, this implies:

$$\begin{aligned} &0.9D_y \geq h + 2W \\ &L_1 \leq 0.9D_x \\ &L_2 \leq 0.9D_x \end{aligned} \tag{190}$$

Finally, the linear constraints $\mathbf{x}_l \leq \mathbf{x} \leq \mathbf{x}_u$, as in (179), define the upper and lower bounds of the geometric variables in the allowable five-dimensional design space. In a general n -dimensional optimization problem, the upper and lower bounds $\mathbf{x}_l \leq \mathbf{x} \leq \mathbf{x}_u$ ($\mathbf{x} \in \mathbb{R}^n$) define a set S_1, which is an orthotope in $\mathbb{R}^n$ representing the geometric design space. The corresponding linear inequality constraints of the form $A\mathbf{x} \leq \mathbf{b}$ further refine the allowable dimensions within the design space to a closed convex polytope S_2, where $S_2 \subset S_1$.

To demonstrate the optimization problem (186), the two target frequencies are set at $f_1 = 9$ GHz and $f_2 = 11.3$ GHz, both in the X-band. The third stopband frequency is set at $f_3 = 10$ GHz, and the aperture widths are fixed at $W = 1$ mm. The lattice admittances are assigned polynomial models by using 200 points from the five-dimensional optimization space in the regression procedure. The dimensions resulting from the optimization are:

$$\mathbf{x} = \begin{bmatrix} 11.55 \text{ mm} & 15.56 \text{ mm} & 24.35 \text{ mm} & 23.7 \text{ mm} & 16.57 \text{ mm} \end{bmatrix}^T \tag{191}$$

The performance of the FSS with these dimensions is shown in Fig. 71. Good agreement between the lattice model and simulation is observed, and the target transmission frequencies are successfully achieved. This FSS was also fabricated for comparison, and the measured results are included in the figure. The fabrication, shown in Fig. 72, was carried out in the same fashion as the single aperture FSS of Fig. 70, so the same kinds of inaccuracies were present due to the presence of a 2 mil dielectric substrate and 2 mm layers of structural supporting foam. Nevertheless, the measured results correspond quite well to the simulated results; the lower measured transmission band has a noticeable downward frequency shift, but the upper transmission band lines up quite well with the simulation.

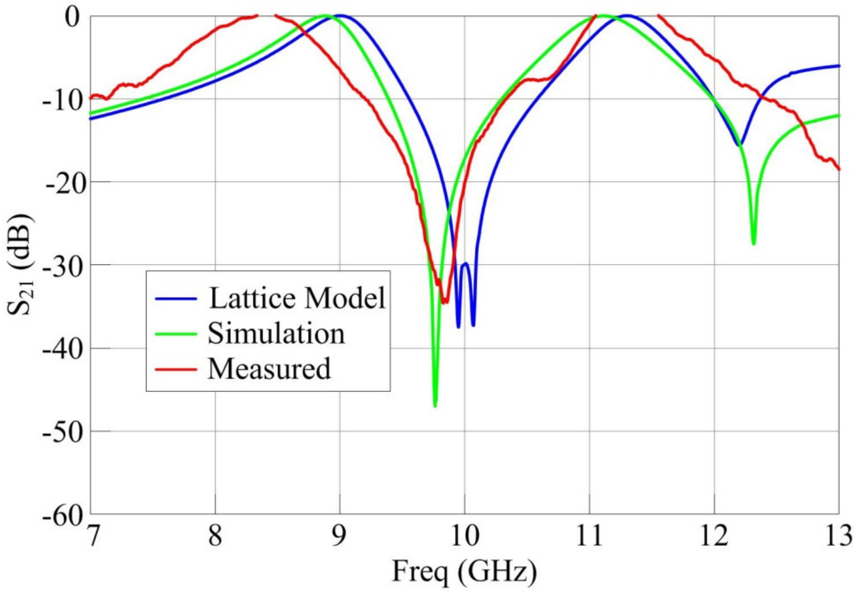

Fig. 71. Performance of optimized dual-aperture, single-layer FSS.

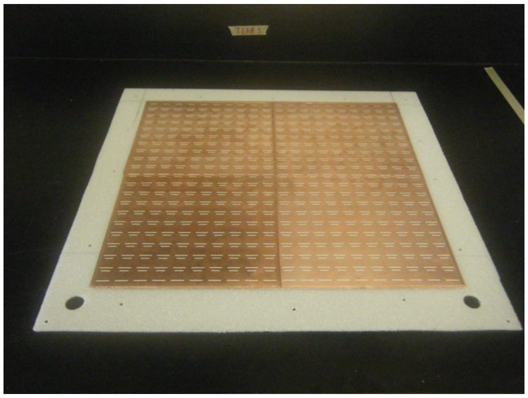

Fig. 72. Fabricated X-band dual rectangular aperture FSS.

Dual-Layer, Dual-Aperture FSS

A somewhat more complex FSS topology is shown in Fig. 73. It comprises a two-layer FSS with two apertures per unit cell on each layer. The goal of this geometry is to achieve a dual-band (dual aperture), second-order (dual layer) filter response over two specified frequency bands. The combination of multiple apertures and multiple layers adds a significant amount of complexity to the coupling relationships between FSS elements. This complexity makes tuning the dimensions of such a design to achieve a reasonable filter response difficult through simple intuition. In this case of an increasingly complex unit cell topology, formulating a formal optimization problem is particularly useful.

For this design, the unit cell size is assumed to be fixed. The two aperture lengths, L_1 and L_2, are varied to achieve second-order passbands over two different frequency bands. In order to achieve a reasonably shaped filter envelope, eight additional degrees of freedom are introduced into the structure by allowing the horizontal and vertical positions of all four apertures (x_n and y_n, respectively, with $n = 1, 2, 3, 4$) to be varied within the unit cell. Also for this example, the separation distance h between the two FSS planes is also assumed to be variable. Altogether, then, the optimization space is an eleven-dimensional vector:

$$\mathbf{x} = \begin{bmatrix} L_1 & L_2 & x_1 & y_1 & x_2 & y_2 & x_3 & y_3 & x_4 & y_4 & h \end{bmatrix}^T \tag{192}$$

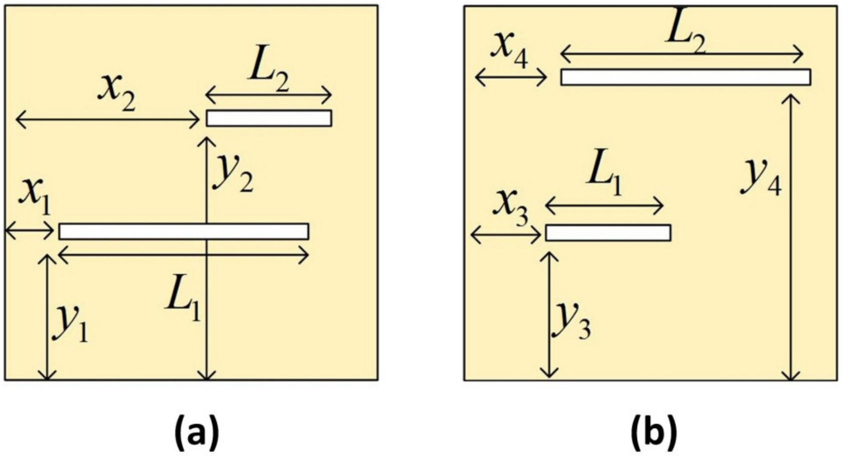

Fig. 73. Geometry of dual-aperture, dual-layer FSS. (a) First layer and (b) second layer.

A simple way to formulate the optimization for this design is as a minimax problem (similar to (186)):

$$\begin{aligned} \text{min} \quad & \max\left\{-T\left(\mathbf{x}, f_1\right), -T\left(\mathbf{x}, f_2\right), -T\left(\mathbf{x}, f_3\right), -T\left(\mathbf{x}, f_4\right)\right\} \\ \text{s.t.} \quad & \mathbf{f}\left(\mathbf{x}\right) \le 0 \\ & A\mathbf{x} \le \mathbf{b} \\ & \mathbf{x}_l \le \mathbf{x} \le \mathbf{x}_u \end{aligned} \tag{193}$$

Here, f_1 and f_2 are assumed to lie within the first passband region, whereas f_3 and f_4 lie within the second passband. The nonlinear inequality constraints are given by:

$$\mathbf{f}(\mathbf{x}) = \begin{bmatrix} 0.95 - T(\mathbf{x}, f_1) \\ 0.95 - T_2(\mathbf{x}, f_2) \\ 0.95 - T_2(\mathbf{x}, f_3) \\ 0.95 - T_2(\mathbf{x}, f_4) \\ T(\mathbf{x}, f_5) - 0.05 \end{bmatrix} \tag{194}$$

As in (188), the passband frequencies are required to have more than 95% transmitted power. The fifth frequency f_5 is assumed to lie within the stopband region between the two passbands; it is required to have less than 5% power transmission. The geometric linear inequality constraints are given by:

$$A = \begin{bmatrix} 1 & 0 & 1 & 0 & 0 & 0 & 0 & 0 & 0 & 0 & 0 \\ 0 & 1 & 0 & 0 & 1 & 0 & 0 & 0 & 0 & 0 & 0 \\ 0 & 1 & 0 & 0 & 0 & 0 & 1 & 0 & 0 & 0 & 0 \\ 1 & 0 & 0 & 0 & 0 & 0 & 0 & 0 & 1 & 0 & 0 \end{bmatrix} \qquad b = \begin{bmatrix} D_x - 1\text{ mm} \\ D_x - 1\text{ mm} \\ D_x - 1\text{ mm} \\ D_x - 1\text{ mm} \end{bmatrix} \tag{195}$$

$$\begin{aligned} L_1 + x_1 &\le D_x - 1\text{ mm} \\ L_2 + x_2 &\le D_x - 1\text{ mm} \\ L_2 + x_3 &\le D_x - 1\text{ mm} \\ L_1 + x_4 &\le D_x - 1\text{ mm} \end{aligned} \tag{196}$$

For illustration, the optimization problem (193) is solved for an FSS operating in the frequency range 6-14 GHz. The goal is to achieve passbands centered over 8 and 12 GHz. The passband frequencies for optimization are defined as $f_1 = 7.5\text{ GHz}$, $f_2 = 8.5\text{ GHz}$, $f_3 = 11.5\text{ GHz}$, and $f_4 = 12.5\text{ GHz}$. The stopband frequency is $f_5 = 10\text{ GHz}$. The unit cell size is fixed at $D_x = 22\text{ mm}$ and $D_y = 20\text{ mm}$, and the aperture widths are fixed at $W = 1$ mm. Table 3 lists the upper and lower bounds on the eleven variable dimensions, as well as the final values computed through optimization. For the optimization, 1000 random points are chosen from the 11-dimensional design space in order to compute the polynomial regression for the lattice admittances.

Dimension	Lower Limit (mm)	Upper Limit (mm)	Optimized Value (mm)
L_1	10	15	11.5
L_2	15	20	19.1
x_1	1	11	5.2
y_1	1	8	1
x_2	1	6	1.1
y_2	11	18	17.1
x_3	1	6	1.7
y_3	1	8	8
x_4	1	11	8.8
y_4	11	18	14.6
h	2	10	7

Table 3. Optimization dimensions for a dual-aperture, dual-layer FSS.

Fig. 74 shows the filter behavior of the optimized FSS, computed using both the lattice model and simulation over the frequency range 6-14 GHz. Clearly, two second-order passbands are achieved, centered over 8 GHz and 12 GHz, and the correspondence between the lattice model and simulation is very good. This design is a very good example of how the interpolated optimization scheme can simplify FSS optimization. Using traditional full-wave optimization approaches, the solution to such an 11-dimensional problem may require a prohibitive amount of time. With the circuit domain optimization of the interpolated lattice method, however, the optimization is much more tractable.

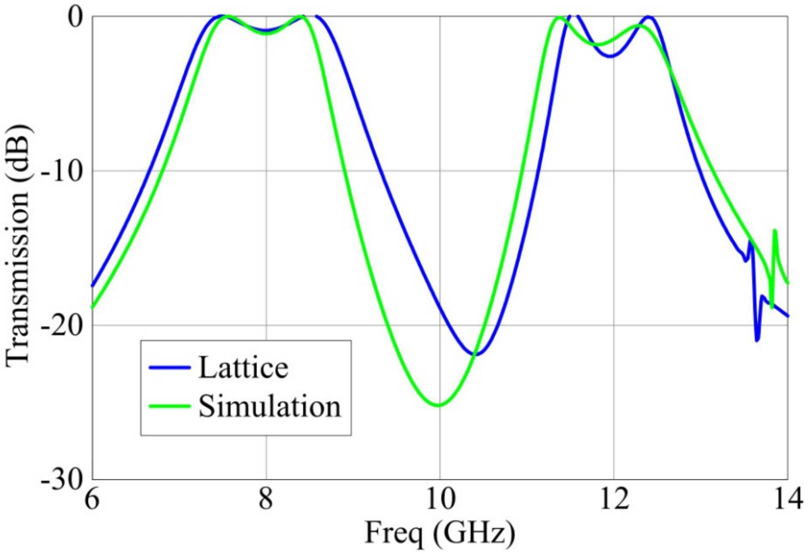

Fig. 74. Performance of dual-aperture, dual-layer FSS. The FSS achieves dual second-order passbands centered at 8 and 12 GHz.

Dual-Layer, Triple-Aperture FSS

Although it provides an instructive example of FSS synthesis through the lattice model, the design of Table 3 cannot be readily fabricated into a physical structure because the two ideal ground planes are separated by a vacuum with no structural support. It is desirable to demonstrate such a dual-layer, multi-aperture FSS experimentally, so a second design is synthesized that can be more easily fabricated on a duroid substrate. The apertures are cut out of the metallization layers on either side of the substrate. The duroid region between the ground planes has a dielectric constant of $\varepsilon_r = 2.2$ and a thickness of 62 mil.

The performance goal of this second modified design is somewhat more ambitious than the dual passbands of Fig. 74 centered at 8 and 12 GHz: the two passbands are now to be located in the Ku and Ka bands, respectively. Specifically, for the first passband, $f_1 = 13\text{ GHz}$ and $f_2 = 17\text{ GHz}$, and for the second passband, $f_3 = 29\text{ GHz}$, and $f_4 = 33\text{ GHz}$. Due to the relatively large separation between these two operating bands, the necessary aperture lengths are also quite different in size. In particular, the smaller aperture will be less than half the length of the larger aperture. For this reason, a modified unit cell geometry, shown in Fig. 75, is proposed that incorporates two smaller apertures and one larger aperture. Thus, the FSS is effectively now a triple-aperture, dual-layer design. For simplicity, only the variable dimensions are shown in the figure. Note, however, that only two aperture lengths are assumed such that $L_1 = L_4$ and $L_2 = L_3 = L_5 = L_6$. Also, in order to somewhat reduce the dimensionality of the optimization space, the horizontal positions x_n are assumed to be fixed; specifically:

$$\begin{aligned}
x_1 &= \left(D_x - L_1\right)/2 \\
x_2 &= D_x/4 - L_2/2 \\
x_3 &= 3D_x/4 - L_3/2 \\
x_4 &= \left(D_x - L_4\right)/2 \\
x_5 &= \left(D_x/4 - L_5\right)/2 \\
x_6 &= 3D_x/4 - L_6/2
\end{aligned} \tag{197}$$

Further note that since the size of the substrate for this modified design is now fixed, the dimension h is removed from the optimization space. The overall result of these changes to the unit cell design is that the optimization space (192) is modified to the following 8-dimensional vector:

$$\mathbf{x} = \begin{bmatrix} L_1 & L_2 & y_1 & y_2 & y_3 & y_4 & y_5 & y_6 \end{bmatrix}^T \tag{198}$$

Also, in this case, the linear inequality constraints are unnecessary (due to the x_n horizontal positions being fixed) and are thus removed from the problem. The nonlinear inequality constraints are the same as in (194), with the stopband frequency f_5 set at 25 GHz.

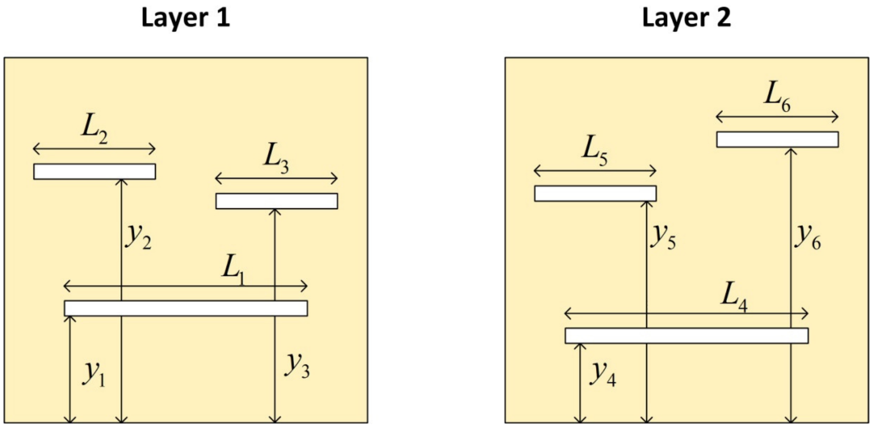

Fig. 75. Unit cell geometry of dual-layer, triple-aperture FSS.

The optimized dimensions of the dual-layer, triple-aperture FSS are given in Table 4. The upper and lower limits of the optimization space for each variable are also provided. The performance of the optimized design is plotted in Fig. 76 using both the lattice model and simulation in [16]. The lattice model results clearly achieve the stated goals of the optimization, resulting in passbands in the Ku and Ka bands. The agreement with simulation is very good in the Ku band; however, some notable disagreement between the curves occurs in the Ka band. This observation is readily explainable, though, since a single-mode half-sinusoid field distribution is assumed over all apertures in the FSS at all frequencies. The large disparity in frequency between the two passbands, however, dictates that within the higher Ka passband, the longer apertures in the FSS will experience higher-order modes beyond the simple half-sinusoid. This can be verified by looking at the simulated field distributions at these frequencies. Thus, in this case, it is expected that the lattice model will have inaccuracies for this particular FSS in the Ka band. A more accurate approach would incorporate one or more of the ideas discussed for multiple-mode formulations in Chapter V. In any case, even the simple single-mode approximation yields lattice model results that are close to simulation.

Dimension	Lower Limit (mm)	Upper Limit (mm)	Optimized Value (mm)
$L_1 = L_4$	7	11	10.44
$L_2 = L_3 = L_5 = L_6$	2.5	6.5	4.02
y_1	1	11	4.50
y_2	1	8	2.21
y_3	1	6	1.98
y_4	11	18	4.50
y_5	1	6	2.15
y_6	1	8	1.22

Table 4. Optimized dimensions for a dual-layer, triple-aperture FSS.

The design was fabricated by milling out the apertures on either side of a Rogers 5880 duroid sheet. A 15 mil end-mill bit was used for all of the apertures. The number of unit cells was limited by the working range of the milling machine. The fabricated design is shown in Fig. 77.

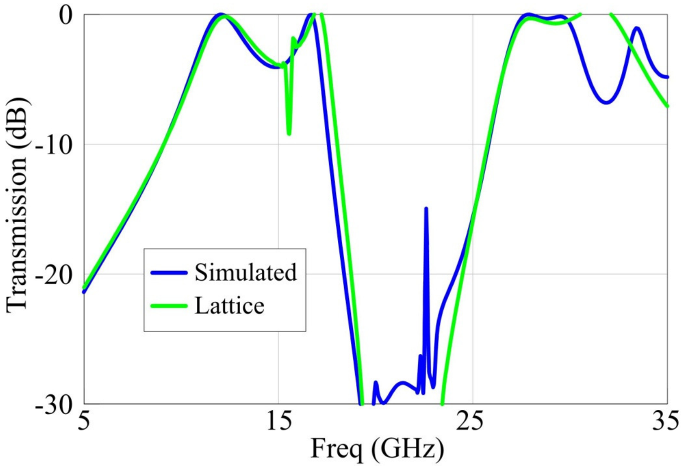

Fig. 76. Performance of dual-layer, triple-aperture FSS.

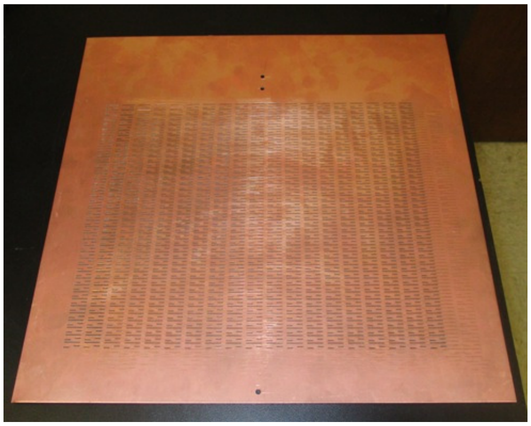

Fig. 77. Fabricated dual-layer, triple-aperture FSS.

Reconfigurable Designs

The lattice model can also be potentially useful for the purpose of synthesizing reconfigurable designs. Two simple examples involving varactor-tuned rectangular aperture FSSs - similar to those analyzed in Chapter VI - are explored here for illustration.

X-band Varactor-Tuned FSS

In the first example, a single rectangular aperture FSS tuned by a varactor is optimized to achieve frequency agility across the entire X-band (8-12 GHz). The geometry is identical to that in Chapter VI, Fig. 52. The dimensions $D_x = 15 \text{ mm}$ and $W = 0.25 \text{ mm}$ are fixed. Also, the varactor is assumed to have a fixed lower capacitance value of $C = C_0 = 0.1 \text{ pF}$; the capacitance is to be varied to values greater than this. The goal is to find the dimensions L and D_y, along with the upper capacitive limit $C = C_1$ of the varactor, such that the transmission peak of the FSS reconfigures between 8 GHz $\left(C = C_1\right)$ and 12 GHz $\left(C = C_0\right)$.

The optimization problem formulated to achieve this goal is the following minimax problem:

$$\begin{aligned} \text{min} \quad & g\left(\mathbf{x}\right) \\ \text{s.t.} \quad & \mathbf{f}\left(\mathbf{x}\right) \leq 0 \\ & \mathbf{x}_l \leq \mathbf{x} \leq \mathbf{x}_u \end{aligned} \qquad (199)$$

Here, the optimization vector is:

$$\mathbf{x} = \begin{bmatrix} L & D_y & C_1 \end{bmatrix}^T \tag{200}$$

Note that the unknown upper capacitance value C_1 is treated as an additional dimension in the multidimensional optimization space. This perhaps requires a brief justification. From the discussion of the varactor-tuned rectangular aperture in Chapter VI, the admittance Y_c associated with the varactor capacitance C is simply added to the self admittances of the lattice. Y_c itself is a linear function of C, $Y_c = j\omega C$ (or, by extension, a polynomial function). Since the admittances themselves (without Y_c) are polynomial functions of the geometric dimensions, it follows that the addition of Y_c simply adds another "dimension" to the polynomial in the form of the capacitance C.

The objective function of (199) is the maximum transmission value between that at $f_1 = 12$ GHz and $f_2 = 8$ GHz:

$$g(\mathbf{x}) = g\left(\begin{bmatrix} L & D_y & C_1 \end{bmatrix}^T\right) = \max \begin{Bmatrix} -T\left(\begin{bmatrix} L & D_y & C_0 \end{bmatrix}^T, f_1\right) \\ -T\left(\begin{bmatrix} L & D_y & C_1 \end{bmatrix}^T, f_2\right) \end{Bmatrix} \tag{201}$$

Note that the transmission at f_1 depends on the fixed lower capacitance C_0, whereas the transmission at f_2 depends on the unknown upper capacitance C_1 (both transmission values depend on L and D_y). The nonlinear inequality constraints, which are not specified explicitly here, ensure that the transmission at both frequencies is above 95%.

The optimization is performed using the following upper and lower bounds for the optimization space:

$$\begin{aligned}\mathbf{x}_l &= \left[8\ \text{mm} \quad 4\ \text{mm} \quad 0.1\ \text{pF}\right]^T \\ \mathbf{x}_u &= \left[14.5\ \text{mm} \quad 10\ \text{mm} \quad 0.4\ \text{pF}\right]^T\end{aligned} \tag{202}$$

The yields an aperture length of $L = 9\ \text{mm}$, a unit cell width of $D_y = 7\ \text{mm}$, and an upper capacitance value of $C_1 = 0.3178\ \text{pF}$. The lattice model and simulated performance of the FSS with these parameters is shown in Fig. 78. In the figure, "state 1" refers to the condition where $C = C_0$ and the passband is at 12 GHz, while "state 2" refers to the condition where $C = C_1$ and the passband is at 8 GHz. Clearly, the design achieves the desired frequency reconfiguration across the X-band. Although the frequencies between 8 and 12 GHz were not considered explicitly, it is reasonable to assume that tuning to any frequency within the X-band can be achieved with a capacitance value $C_0 \le C \le C_1$. This could be verified with more computations, but such results are omitted here for brevity.

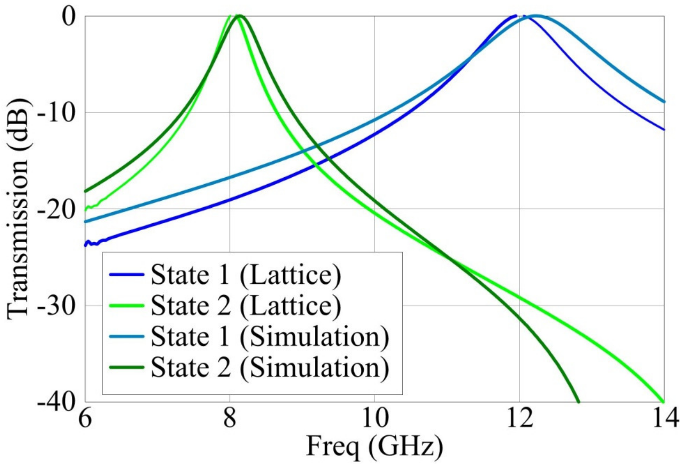

Fig. 78. Performance of optimized varactor-tunable X-band FSS.

Single-Band / Dual-Band Reconfiguration

In the second reconfigurable example, a dual rectangular aperture FSS, with both apertures tuned independently by varactors, is optimized such that it operates in two states: in one state, it behaves as a single-band filter with a transmission peak at 10 GHz; in the second state, it behaves as a dual-band filter with transmission peaks at 9 and 11 GHz. The geometry for such a design is shown in Fig. 79. Note that each of the two apertures has its own independent varactor.

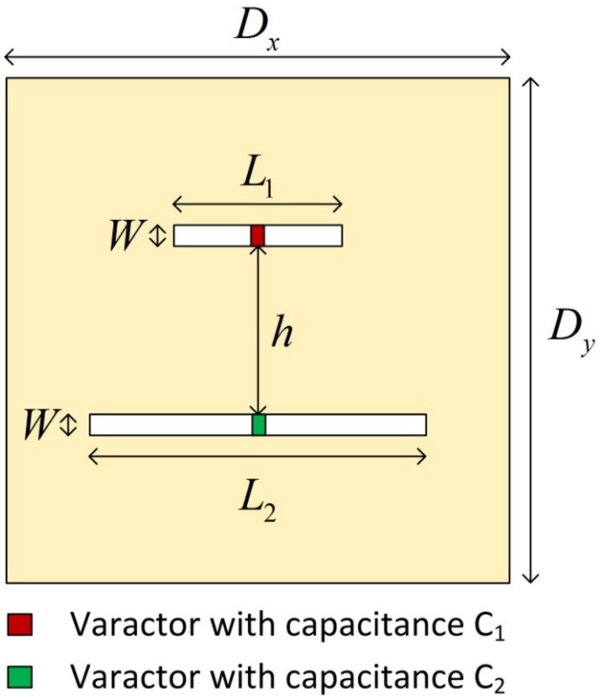

Fig. 79. Geometry of a varactor-tuned, dual rectangular aperture FSS.

For this example, the unit cell dimensions are fixed at $D_x = D_y = 15\text{ mm}$, and the aperture widths are fixed at $W = 0.25\text{ mm}$. The apertures in this case are assumed to be the same length, $L = L_1 = L_2$; however, L is variable and subject to the optimization procedure. This choice of identical physical lengths dictates that for single-band operation, the two varactors must also have the same capacitance; for dual-band operation, the capacitances will be different. The separation distance between apertures h is also variable. Three capacitances are defined: $C_1 = C_a$ is the lowest capacitance and corresponds to the passband at 11 GHz in dual-band operation; $C_2 = C_b$ is the highest capacitance and corresponds to the passband at 9 GHz in dual-band operation; and $C_1 = C_2 = C_c$ corresponds to the 10 GHz passband in single-band operation. The lowest capacitance C_a is assumed to be fixed at $0.1\,\mathrm{pF}$, while the other two capacitances are variable with some capacitance greater than this.

The optimization problem for this scenario is formulated as follows:

$$\begin{array}{ll} \min & \mathrm{g}(\mathbf{x}) \\ \text{s.t.} & \mathbf{f}(\mathbf{x}) \le 0 \\ & \mathbf{x}_l \le \mathbf{x} \le \mathbf{x}_u \end{array} \tag{203}$$

$$\mathbf{x} = \begin{bmatrix} L & h & C_b & C_c \end{bmatrix}^T \tag{204}$$

$$g(\mathbf{x}) = \max \begin{Bmatrix} -T(L, h, C_a, C_b, f_1) \\ -T(L, h, C_a, C_b, f_2) \\ -T(L, h, C_c, C_c, f_3) \end{Bmatrix} \tag{205}$$

The optimization vector (204) is four-dimensional, with two dimensions corresponding to the two unknown capacitances. The objective function (205) is again in minimax format; three transmission peaks are maximized simultaneously, corresponding to the one passband in single-band operation and the two passbands in dual-band operation.

The three frequencies in (205) are $f_1 = 9$ GHz, $f_2 = 11$ GHz, and $f_3 = 10$ GHz. The nonlinear and linear inequality constraints will not be elaborated on here.

Fig. 80 shows the performance of the optimized design. The final parameters are $L = 9.44$ mm, $h = 8.33$ mm, $C_b = 0.1887$ pF, and $C_c = 0.1483$ pF. Both the single- and dual-band states of operation are shown, and each state successfully achieves the target frequencies. In principle, the capacitances of this design could be varied in many more ways to achieve other states of operation. In particular, the capacitances could be kept equal but shifted away from the initial value C_c to tune the single-band passband up or down. The two passbands of the dual-band state could also be independently tuned up or down by changing C_a and C_b; however, it is not guaranteed that full transmission will necessarily be achieved at both bands for any arbitrary combination of capacitances. Only the passbands at the optimized capacitance values are guaranteed to achieve full transmission.

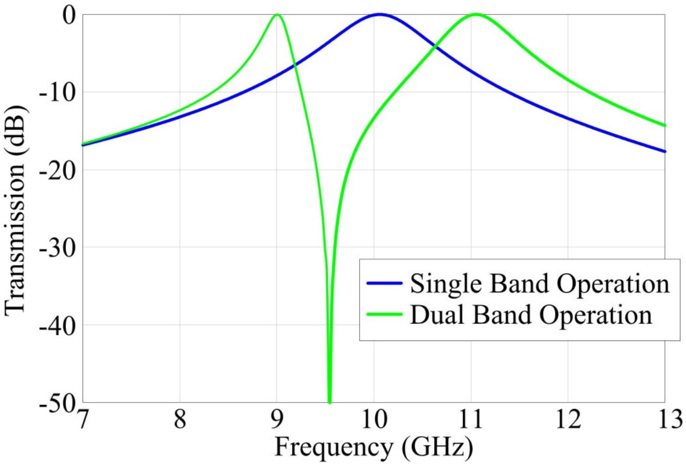

Fig. 80. Performance of single-band / dual-band reconfigurable FSS.

Combined Antenna/FSS Designs

The lattice model optimization can also be applied to the combined antenna-FSS structures studied in Chapter VIII. The procedure is similar to that outlined above for the pure FSS designs; thus, some of the details will be omitted here. Two designs are considered that involve a single-layer FSS windowing a waveguide aperture antenna array. The FSSs are single- and dual-band respectively.

Single-Band Windowed Waveguide Array

The first antenna-FSS optimization example is performed on the structure shown in Chapter VIII, Fig. 60: a single-band, single-layer rectangular aperture FSS windowing a rectangular waveguide array. The goal is to achieve a VSWR minimum (i.e. impedance match) at a specified target frequency f_0.

$$\begin{array}{ll} \min & f(\mathbf{x}, f_0) = \text{VSWR of array} \\ \text{s.t.} & f\left(\mathbf{x}, f_0\right) \leq 1.2 \\ & A\mathbf{x} \leq \mathbf{b} \\ & \mathbf{x}_l \leq \mathbf{x} \leq \mathbf{x}_u \end{array} \tag{206}$$

Note that unlike the objective functions of the pure FSS optimization problems, the objective function here calculates the VSWR. The nonlinear inequality constraint $f\left(\mathbf{x}, f_0\right) \leq 1.2$ ensures that the VSWR is below a certain threshold.

To illustrate this optimization problem in use, the structure is assigned several fixed dimensions: $W = 0.5$ mm, $L_{WG} = 13$ mm, $W_{WG} = 6.5$ mm, $D_x = 16$ mm, and $D_y = 10$ mm. The FSS aperture length L and the separation distance z between the waveguide array and the FSS are assumed to be variable in a two-dimensional optimization space ($\mathbf{x}=\begin{bmatrix}L & z\end{bmatrix}^T$). The space between the FSS and waveguide array is assumed to be free space. The target frequency is $f_0 = 16\ \text{GHz}$. After optimization, these variable dimensions are determined as $L = 9.356\ \text{mm}$ and $z = 13\ \text{mm}$. The performance of the design with these parameters is shown in Fig. 81. Good agreement is achieved between the lattice model and simulation, and the VSWR minimums of both curves are close to the target frequency, as desired.

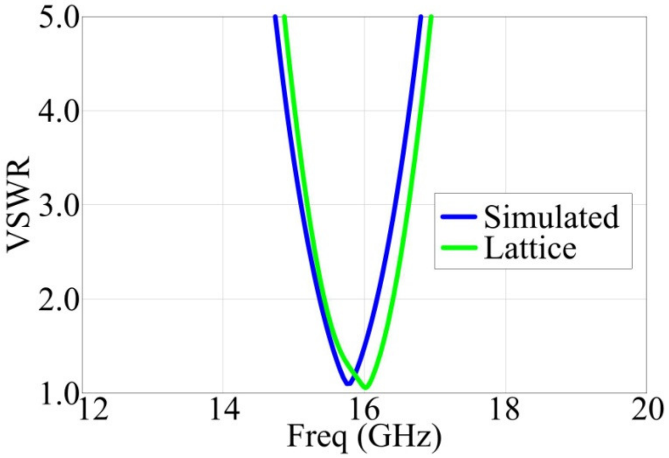

Fig. 81. Performance of an optimized waveguide array-FSS.

Dual-Band Windowed Waveguide Array

The second array-FSS optimization example to be considered is the same as that in the previous section, except that the single-band FSS is replaced by a dual-band FSS. The unit cell geometry of this structure is summarized in Fig. 82. The optimization goal is to achieve VSWR minimums at two target frequencies, $f_1 = 14\ \text{GHz}$ and

$f_2 = 17\text{ GHz}$. The optimization problem (206) for the single-band design must be modified slightly into a minimax format:

$$\begin{aligned} \text{min} \quad & \max\left\{ f\left(\mathbf{x}, f_1\right), f\left(\mathbf{x}, f_2\right) \right\} \\ \text{s.t.} \quad & f\left(\mathbf{x}, f_1\right) \leq 1.2 \\ & f\left(\mathbf{x}, f_2\right) \leq 1.2 \\ & A\mathbf{x} \leq \mathbf{b} \\ & \mathbf{x}_l \leq \mathbf{x} \leq \mathbf{x}_u \end{aligned} \tag{207}$$

$$\mathbf{x} = \begin{bmatrix} L_1 & L_2 & x_1 & y_1 & x_2 & y_2 & z \end{bmatrix}^T \tag{208}$$

As before, the function f calculates the VSWR. The minimax formulation, much like that for the dual-aperture FSS in (186), simultaneously minimizes the VSWR at both target frequencies. The optimization space in this case is 7-dimensional, with both aperture lengths (L_1 and L_2), the aperture horizontal and vertical positions (x_1, y_1, x_2, and y_2), and the separation distance between the FSS and waveguide array (z) all assumed to be variable. The unit cell size, waveguide aperture dimensions, and aperture widths are all fixed with the same values used in the example of the preceding section.

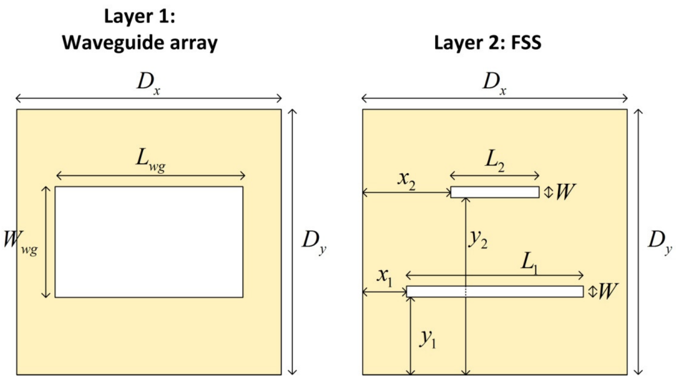

Fig. 82. Geometry of a waveguide array windowed by a dual-aperture FSS.

Fig. 83 shows the performance of the optimized dual-band windowed waveguide array. The optimized dimensions are summarized as follows:

$$\mathbf{x} = \begin{bmatrix} 8.1\text{ mm} & 10\text{ mm} & 1.3\text{ mm} & 1\text{ mm} & 4\text{ mm} & 8.8\text{ mm} & 3.1\text{ mm} \end{bmatrix}^T \qquad (209)$$

As desired, dual-band windowing is achieved, and each operating band has an appreciable 2:1VSWR bandwidth close to the desired target frequencies. The lattice model results, however, seem to contain some inaccuracies as compared to the simulation. These may be the result of poor convergence of some of the lattice admittances, since the behavior of the lattice model curve is somewhat erratic at certain frequencies; however, this potential issue is just one of many possibilities. Since the goal here is simply to obtain a working design and demonstrate an optimization procedure, investigation of these inaccuracies will not be pursued in detail here.

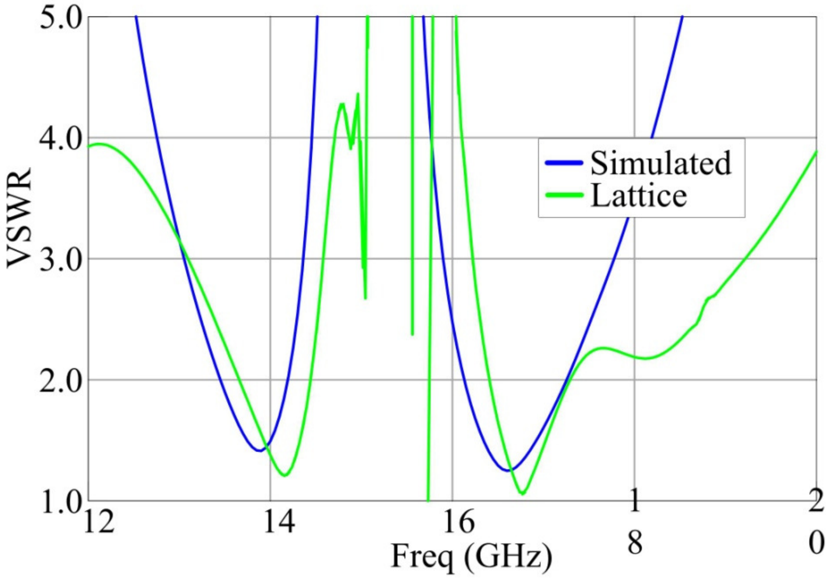

Fig. 83. Performance of a waveguide array windowed by a dual-aperture FSS.

CHAPTER X

CONCLUSION

This work provides a systematic overview - as well as the mathematical foundation - for a novel analytical approach to designing frequency selective surfaces. The approach involves a lattice-based, multiport network representation of FSSs in the circuit domain that nonetheless retains strong connections to the underlying electromagnetic behavior of the individual elements comprising an FSS. In this sense, the "lattice model" serves as a unique compromise between typical full-wave numerical Floquet analyses and simplified aggregated circuit models. It retains much of the accuracy of full-wave techniques, yet also provide many conveniences through its scalar, circuit domain formulation.

The lattice model is canonical in the sense that it can be applied to wide variety of FSS topologies not considered explicitly in this paper. Although the specific computational examples provided in this work only involve rectangular aperture resonant elements, the formulation of the circuit domain analysis is very general, and the EM domain analysis can be reformulated for other resonant geometries. As demonstrated in Chapter VI, the model can also handle arbitrary multi-element and multilayer topologies. Chapter VIII showed how it can be further extend to analyze integrated structures combining FSSs with antennas or antenna arrays. This is a significant area of potential utility for the lattice model, as the design of such structures have received relatively small consideration in literature (compared to pure FSS design or pure antenna design).

Besides simply incorporating beneficial characteristics of both full-wave techniques and circuit models, the lattice model offers a number of unique features with significant practical utility. First, the separation of the analysis into the circuit and EM domains allows different cases of non-uniform incidence on the same FSS structure to be handled fairly efficiently. As shown in Chapter VII, different incident field patterns can be handled entirely in the circuit domain using the same lattice admittance values as are calculated for uniform normal plane wave incidence. This allows, for example, different angles of plane wave incidence to be quickly calculated in the circuit domain without re-performing expensive admittance computations. Second, as discussed in Chapter IX, the lattice model allows FSS performance to be approximated through polynomial regression over a multidimensional design space. Specifically, the admittances comprising the lattice behave in a polynomial fashion for changing geometric dimensions. This approximation, in turn, makes possible a wide variety of simple constrained optimization problems for the purpose of FSS synthesis.

The FSS lattice theory developed herein had to be developed in a manner that was general enough to demonstrate both the canonical nature of the model and the various features of the model that make it unique and of practical interest. As such, it was difficult to fully explore all facets of the model within the limited scope of this work. In order to make the model more practical, a variety of detailed investigations and lines of inquiry must be undertaken in future work. As already mentioned, it would be of significant interest to apply the model to FSS geometries not composed of rectangular aperture unit cells. Limiting the examples in this work to the rectangular aperture simplified the task of providing a general overview, but the model needs to be shown to be equally valid for other geometries. As an extension of this idea, application of the model to more general FSS topologies that combine multi-element and multilayer features will go a long way to more thoroughly demonstrating its broad utility.

Several other computational issues that arise from the lattice model need to be addressed as well. A number of approximations are made in the model, and the effects of these approximations deserve a much more thorough treatment. These include the infinite summations of admittances encountered in the circuit domain (which are currently handled through the Shanks transformation), as well as the use of a finite-sized DFT to calculate cases of non-uniform incidence that are inherently aperiodic. In the former issue, the effect of the number of levels of coupling admittances needs to be better understood so as to find the correct balance between computational efficiency and accuracy. Also, issues with convergence of the Shanks transformation in specific cases need to be identified and understood, and perhaps other approaches to infinite series estimation could be applied to the model. In the latter issue, a more systematic way of determining the size of the DFT necessary to achieve a particular level of accuracy would be beneficial.

The entire interpolated optimization procedure discussed in Chapter IX, which involves the multidimensional polynomial modeling of the lattice admittances, should also be explored in more depth. In particular, the quality of polynomial models for various FSS topologies needs to be better understood. The number of “known” admittance terms that are needed to yield an accurate polynomial regression is an important factor that has significant bearing on the computational cost of the method. It must also be determined if any cases exist in which the assumption of a good polynomial fit may break down. Furthermore, identifying alternative representations of the admittances - for example, by using splines - could be useful in avoiding some deficiencies in the polynomial approach. In short, the polynomial modeling of admittances, in and of itself, is an area that could benefit from extensive empirical and theoretical investigation. Beyond these considerations, the interpolated optimization scheme needs to simply be applied to more variety FSS structures, and the results compared to designs obtained through more traditional optimization procedures. Also, the complexity of the constrained optimization formulations, which were deliberately simplified for this work, could very easily be expanded in future work to match the complexity seen elsewhere.

In summary, the content of this dissertation provides the basic mathematical tools necessary to perform FSS analysis and synthesis problems via the newly introduced lattice method. A fair amount of examples have been provided on how to apply the theory to actual FSS and antenna-FSS designs. Although the utility of the model still remains largely unexplored in practical applications, this work provides the foundation on which further investigations can be built.

REFERENCES

[1] B. A. Munk, *Frequency Selective Surfaces: Theory and Design*. New York, NY: John Wiley & Sons, Inc., 2000.

[2] A. E. Farahat and K. F. A. Hussein, "Spatial Filters for Linearly Polarized Antennas Using Free Standing Frequency Selective Surfaces," *Progress in Electromagnetics Research,* vol. 2, pp. 167-188, 2008.

[3] T. Cwik, R. Mittra, K. Lang, and T. Wu, "Frequency selective screens," *Antennas and Propagation Society Newsletter, IEEE,* vol. 29, pp. 5-10, 1987.

[4] L. Kyung-Won, J. Yi-Ru, Y. Jong-Gwan, and H. Ic-Pyo, "Prediction of FSS radome performane using simple design equation," in *Antennas and Propagation (EUCAP), 2012 6th European Conference on*, 2012, pp. 1124-1126.

[5] Z. Hang, S. Qu, L. Baoqin, J. Wang, H. Ma, X. Zhuo*, et al.*, "Filter-Antenna Consisting of Conical FSS Radome and Monopole Antenna," *Antennas and Propagation, IEEE Transactions on,* vol. 60, pp. 3040-3045, 2012.

[6] Z. Jun and X. Xiaowen, "Study of the effect of a finite FSS radome on a horn antenna," in *Microwave Technology & Computational Electromagnetics (ICMTCE), 2011 IEEE International Conference on*, 2011, pp. 74-76.

[7] F. Bayatpur and K. Sarabandi, "Miniaturized FSS and Patch Antenna Array Coupling for Angle-Independent, High-Order Spatial Filtering," *Microwave and Wireless Components Letters, IEEE,* vol. 20, pp. 79-81, 2010.

[8] A. Pirhadi, H. Bahrami, and J. Nasri, "Wideband High Directive Aperture Coupled Microstrip Antenna Design by Using a FSS Superstrate Layer," *Antennas and Propagation, IEEE Transactions on,* vol. 60, pp. 2101-2106, 2012.

[9] R. Dickie, R. Cahill, H. S. Gamble, V. F. Fusco, A. G. Schuchinsky, and N. Grant, "Spatial demultiplexing in the submillimeter wave band using multilayer free-standing frequency selective surfaces," *Antennas and Propagation, IEEE Transactions on,* vol. 53, pp. 1904-1911, 2005.

[10] C. Chao-Chun, "Transmission through a Conducting Screen Perforated Periodically with Apertures," *Microwave Theory and Techniques, IEEE Transactions on,* vol. 18, pp. 627-632, 1970.

[11] L. FernandezrMartinez, E. Garcia, D. de Castro-Galan, and D. Segovia-Vargas, "Equivalent Circuit Model Proposal Applied to Frequency Selective Surfaces," in *Applied Electromagnetics and Communications, 2005. ICECom 2005. 18th International Conference on*, 2005, pp. 1-4.

[12] R. Dubrovka, J. Vazquez, C. Parini, and D. Moore, "Equivalent circuit method for analysis and synthesis of frequency selective surfaces," *Microwaves, Antennas and Propagation, IEE Proceedings,* vol. 153, pp. 213-220, 2006.

[13] Y. Xiayuan, B. Ming, and M. Jungang, "Equivalent Circuit Method for Analyzing Frequency Selective Surface With Ring Patch in Oblique Angles of Incidence," *Antennas and Wireless Propagation Letters, IEEE,* vol. 10, pp. 820-823, 2011.

[14] S. Komeylian and F. Hojjat-Kashani, "Intense scrutiny in cross-dipole Frequency Selective Surface," in *Antenna Technology (iWAT), 2012 IEEE International Workshop on*, 2012, pp. 221-224.

[15] D. Pozar, *Microwave Engineering*, 3rd ed. Hoboken, NJ: John Wiley & Sons, Inc., 2005.

[16] "High Frequency Structural Simulator," 15th ed. Pittsburgh, PA: ANSYS, Inc., 2012.

[17] K. Delihacioglu, "Frequency Selective Surfaces With Multiple-Strip Group Elements," *Antennas and Wireless Propagation Letters, IEEE,* vol. 11, pp. 1370-1373, 2012.

[18] D. Cure, T. Weller, and F. Miranda, "A comparison between Jerusalem Cross and Square Patch Frequency Selective Surfaces for low profile antenna applications," in *Electromagnetics in Advanced Applications (ICEAA), 2011 International Conference on*, 2011, pp. 1019-1022.

[19] R. Mittra, R. C. Hall, and T. Chich-Hsing, "Spectral-domain analysis of circular patch frequency selective surfaces," *Antennas and Propagation, IEEE Transactions on,* vol. 32, pp. 533-536, 1984.

[20] L. Bin, B. Ming, M. Hui, Z. Haibo, and M. Jungang, "Four-band frequency selective surface with circular ring patch elements," in *Microwave and Millimeter Wave Technology (ICMMT), 2012 International Conference on*, 2012, pp. 1-4.

[21] W. Te-Kao, "Four-band frequency selective surface with double-square-loop patch elements," *Antennas and Propagation, IEEE Transactions on,* vol. 42, pp. 1659-1663, 1994.

[22] C. Hsing-Yi, T. Yu, H. Kuo-Lun, and C. Hsi-Tseng, "Bandwidth enhancement using dual-band frequency selective surface with Jerusalem cross elements for 2.4/5.8 GHz WLAN antennas," in *Wireless Information Technology and Systems (ICWITS), 2010 IEEE International Conference on*, 2010, pp. 1-4.

[23] D. S. Lockyer, J. C. Vardaxoglou, and R. A. Simpkin, "Complementary frequency selective surfaces," *Microwaves, Antennas and Propagation, IEE Proceedings,* vol. 147, pp. 501-507, 2000.

[24] A. L. Gutierrez, M. Lanza, I. Barriuso, L. Valle, M. Domingo, J. R. Perez*, et al.*, "Multilayer FSS Optimizer based on PSO and CG-FFT," in *Antennas and Propagation (APSURSI), 2011 IEEE International Symposium on*, 2011, pp. 2661-2664.

[25] D. Lockyer, R. Seager, and J. C. Vardaxoglou, "Reconfigurable FSS using multilayer conducting and slotted array structures," in *Advances in Electromagnetic Screens, Radomes and Materials (Digest No.: 1996/270), IEE Colloquium on*, 1996, pp. 6/1-6/6.

[26] T. Zhang, H. H. Ouslimani, Y. Letestu, A. Le Bayon, and L. R. Darvil, "A low profile multilayer seventh order band-pass frequency selective surface (FSS) for millimeter-wave application," in *Wireless and Microwave Technology Conference (WAMICON), 2012 IEEE 13th Annual*, 2012, pp. 1-4.

[27] J. A. Reed, "Frequency Selective Surfaces with Multiple Periodic Elements," Doctor of Philosophy, Univeristy of Texas at Dallas, 1997.

[28] L. Mingyun, H. Minjie, and W. Zhe, "Design of multi-band frequency selective surfaces using multi-periodicity combined elements," *Systems Engineering and Electronics, Journal of,* vol. 20, pp. 675-680, 2009.

[29] A. Ghasemi, N. Ghahvehchian, A. Mallahzadeh, and S. Sheikholvaezin, "A reconfigurable printed monopole antenna for MIMO application," in *Antennas and Propagation (EUCAP), 2012 6th European Conference on*, 2012, pp. 1-4.

[30] L. Boccia, I. Russo, G. Amendola, and G. Di Massa, "Varactor tuned frequency selective surface for beam steering applications," in *Antennas and Propagation Society International Symposium (APSURSI), 2010 IEEE*, 2010, pp. 1-4.

[31] G. I. Kiani, T. S. Bird, and K. Y. Chan, "MEMS enabled frequency selective surface for 60 GHz applications," in *Antennas and Propagation (APSURSI), 2011 IEEE International Symposium on*, 2011, pp. 2268-2269.

[32] S. N. Azemi, K. Ghorbani, and W. S. T. Rowe, "A Reconfigurable FSS Using a Spring Resonator Element," *Antennas and Wireless Propagation Letters, IEEE,* vol. 12, pp. 781-784, 2013.

[33] R. A. Shelby, D. R. Smith, and S. Schultz, "Experimental Verification of a Negative Index of Refraction," *Science,* vol. 292, pp. 77-79, April 6, 2001 2001.

[34] F. Bayatpur, "Metamaterial-Inspired Frequency-Selective Surfaces," Doctor of Philosophy, Electrical Engineering, University of Michigan, 2009.

[35] C. A. Balanis, *Advanced Engineering Electromagnetics*, 2nd ed. Hoboken, NJ: John Wiley & Sons, 2012.

[36] D. F. Sievenpiper, "High-Impedance Electromagnetic Surfaces," Doctor of Philosophy, Electrical Engineering, University of California, Los Angeles, 1999.

[37] P. Kuchment, *Floquet Theory for Partial Differential Equations*. Basel, Switzerland: Birkhauser Verlag, 1993.

[38] W. Zhuang, Z. H. Fan, D. Z. Ding, and R. S. Chen, "An Efficient Technique for Analysis of Frequency Selective Surface in Spectral Domain with RWG Basis Functions," in *Art of Miniaturizing RF and Microwave Passive Components, 2008. IMWS 2008. IEEE MTT-S International Microwave Workshop Series on*, 2008, pp. 224-226.

[39] "CST Microwave Studio," Farmingham, MA: Computer Simulation Technology AG, 2014.

[40] R. J. Langley and E. A. Parker, "Equivalent circuit model for arrays of square loops," *Electronics Letters,* vol. 18, pp. 294-296, 1982.

[41] R. J. Langley and A. J. Drinkwater, "Improved empirical model for the Jerusalem cross," *Microwaves, Optics and Antennas, IEE Proceedings H,* vol. 129, pp. 1-6, 1982.

[42] R. J. Langley and E. A. Parker, "Double-square frequency-selective surfaces and their equivalent circuit," *Electronics Letters,* vol. 19, pp. 675-677, 1983.

[43] T. Koleck, H. Diez, and J. C. Bolomey, "Techniques for analysing finite frequency selective surfaces," in *Antennas and Propagation, Tenth International Conference on (Conf. Publ. No. 436)*, 1997, pp. 161-165 vol.1.

[44] E. B. Tchikaya, H. Aubert, and N. J. G. Fonseca, "Modeling of a finite-size thick metallic waveguide FSS under oblique plane wave incidence using Scale Changing Technique," in *Antennas and Propagation Society International Symposium (APSURSI), 2010 IEEE*, 2010, pp. 1-4.

[45] B. A. Munk, D. S. Janning, J. B. Pryor, and R. J. Marhefka, "Scattering from surface waves on finite FSS," *Antennas and Propagation, IEEE Transactions on,* vol. 49, pp. 1782-1793, 2001.

[46] A. J. Guttmann, "Lattice Green's functions in all dimensions," *Journal of Physics A: Mathematical and Theoretical,* vol. 43, 2010.

[47] J. Cserti, "Application of the Lattice Green's Function for Calculating the Resistance of an Infinite Network of Resistors," *American Journal of Physics,* vol. 68, p. 896, 2000.

[48] S. Hollos. (2005, August 5). *A Lattice Green's Function Introduction* [Online]. Available: http:/ http://www.exstrom.com/lgf/lgfint.pdf.

[49] R. C. McOwen, *Partial Differential Equations: Methods and Applications*, 2nd ed. New Jersey: Prentice Hall, 2003.

[50] Y. T. Lo and S. W. Lee, *Antenna Handbook*. New York, NY: Champman & Hall, 1993.

[51] N. C. Albertsen, G. Jacobsen, and S. B. Sorensen, "Nonlinear transformations for accelerating the convergence of M-dimensional series," *Mathematics of Computation,* vol. 41, pp. 623-634, 1983.

[52] S. Singh and R. Singh, "On the use of Shank's transform to accelerate the summation of slowly converging series," *Microwave Theory and Techniques, IEEE Transactions on,* vol. 39, pp. 608-610, 1991.

[53] I. C. Jan, R. F. Harrington, and J. R. Mautz, "Aperture admittance of a rectangular aperture and its use," *Antennas and Propagation, IEEE Transactions on,* vol. 39, pp. 423-425, 1991.

[54] R. F. Harrington and J. R. Mautz, "A generalized network formulation for aperture problems," *Antennas and Propagation, IEEE Transactions on,* vol. 24, pp. 870-873, 1976.

[55] W. C. Gibson, *The Method of Moments in Electromagnetics, Second Edition*: Taylor & Francis, 2014.

[56] P. Pyong, "Mutual admittance between slots on a plane," in *Antennas and Propagation Society International Symposium, 1984*, 1984, pp. 393-396.

[57] C. A. Valagiannopoulos and N. K. Uzunoglu, "Green's function of a parallel plate waveguide with multiple abrupt changes of interwall distances," *Radio Science,* vol. 44, p. RS5001, 2009.

[58] "MATLAB Release 2012a." Natick, MA: The MathWorks, Inc., 2012.

[59] R. Mittra, "A look at some challenging problems in computational electromagnetics," *Antennas and Propagation Magazine, IEEE,* vol. 46, pp. 18-32, 2004.

[60] V. V. S. Prakash and R. Mittra, "Analysis of interaction between microwave antennas and frequency selective surface (FSS) radomes," in *Antennas and Propagation Society International Symposium, 2003. IEEE*, 2003, pp. 404-407 vol.4.

[61] R. Mittra and L. Dongwoon, "Analysis of a frequency selective surface (FSS) radome located in closed proximity of a phased array antenna," in *Antennas and Propagation Society International Symposium, 2001. IEEE*, 2001, pp. 370-373 vol.4.

[62] S. Monni, N. L. Juan, A. Neto, and G. Gerini, "A closely spaced waveguide phased array integrated with a frequency selective surface. Modeling and design," in *Antennas and Propagation Society International Symposium, 2003. IEEE*, 2003, pp. 829-832 vol.2.

[63] A. Monorchio, P. Grassi, and G. Manara, "A hybrid mode-matching finite-elements approach to the analysis of thick dichroic screens with arbitrarily shaped apertures," *Antennas and Wireless Propagation Letters, IEEE,* vol. 1, pp. 120-123, 2002.

[64] A. Pellegrini, A. Monorchio, and G. Manara, "Analysis of Finite Large Phased Arrays of Waveguides by the Mode Matching/Finite Element and a Spectral

Decomposition Approach," in *Electromagnetics in Advanced Applications, 2007. ICEAA 2007. International Conference on*, 2007, pp. 587-590.

[65] A. Pellegrini, A. Monorchio, and R. Mittra, "Analysis of a waveguide array/frequency selective surface composite with dissimilar periodicities," in *Antennas and Propagation Society International Symposium, 2009. APSURSI '09. IEEE*, 2009, pp. 1-4.

[66] J. R. T. Compton, "The aperture admittance of a rectangular waveguide radiating into a lossy half-space," NASA1963.

[67] P. H. da F Silva, R. M. S. Cruz, and A. G. D'Assuncao, "Blending PSO and ANN for Optimal Design of FSS Filters With Koch Island Patch Elements," *Magnetics, IEEE Transactions on,* vol. 46, pp. 3010-3013, 2010.

[68] E. A. Parker, A. D. Chuprin, J. C. Batchelor, and S. B. Savia, "GA optimisation of crossed dipole FSS array geometry," *Electronics Letters,* vol. 37, pp. 996-997, 2001.

[69] M. Ohira, H. Deguchi, M. Tsuji, and H. Shigesawa, "Optimized Multiband Single-layer Frequency Selective Surface and Its Experimental Verification," in *Microwave Conference, 2002. 32nd European*, 2002, pp. 1-4.

[70] L. Ling, D. H. Werner, J. A. Bossard, and T. S. Mayer, "A model-based parameter estimation technique for wide-band interpolation of periodic moment method impedance matrices with application to genetic algorithm optimization of frequency selective surfaces," *Antennas and Propagation, IEEE Transactions on,* vol. 54, pp. 908-924, 2006.

[71] A. L. Gutierrez, J. R. Perez, and J. Basterrechea, "Binary particle swarm optimization of FSS using a CG-FFT modelling," in *Antennas and Propagation, 2009. EuCAP 2009. 3rd European Conference on*, 2009, pp. 45-49.

[72] A. Anuradha, A. Patnaik, S. N. Sinha, and J. R. Mosig, "Design of customized fractal FSS," in *Antennas and Propagation Society International Symposium (APSURSI), 2012 IEEE*, 2012, pp. 1-2.

[73] M.-H. Tsai and M.-M. Zen, "Criterion-robust optimal designs for model discrimination and parameter estimation: multivariate polynomial regression case," *Statistica Sinica,* vol. 14, pp. 591-601, 2004.

[74] P. G. Bartley and S. B. Begley, "Improved Free-Space S-Parameter Calibration," in *Instrumentation and Measurement Technology Conference, 2005. IMTC 2005. Proceedings of the IEEE*, 2005, pp. 372-375.

APPENDIX A

RECTANGULAR APERTURE LATTICE ADMITTANCES

In this appendix, the calculation of the self and mutual admittance terms of the lattice model is detailed for rectangular aperture resonant elements of length L and width W. First, the inner product formulations of the self admittance (21) and mutual admittance (26) are expanded in terms of the equivalent magnetic currents covering the apertures. The resulting integral expressions are valid for any arbitrary magnetic current, or, equivalently any arbitrary aperture geometry. Then, these expressions are specialized to the case of rectangular apertures; in this case, the magnetic currents are assumed to be sinusoidal, per (44) and Fig. 38. The computation of the integral expressions is briefly outlined.

Self Admittance

The half-space self admittance (21), as defined by Harrington's formulation of a single isolated aperture problem [54], is given by:

$$Y_s^{hs} = -\left\langle \mathbf{M}_0, \mathbf{H}\left(\mathbf{M}_0\right)\right\rangle \tag{210}$$

$\mathbf{M}_0$ is the equivalent magnetic current on the aperture and is assumed to span the entire aperture area; $\mathbf{H}\left(\mathbf{M}_0\right)$ is the magnetic field produced by this magnetic current. Expanding the inner product into its full surface integral form yields:

$$Y_{s1}^{hs} = -\iint_A \mathbf{M}_0 \cdot \mathbf{H}\left(\mathbf{M}_0\right) dydx \tag{211}$$

Note that the limits of the integration are defined by the area $0 \le x \le L,\ 0 \le \mathrm{y} \le \mathrm{W}$.

The magnetic field $\mathbf{H}(\mathbf{M}_0)$ can be expanded in terms of the electric vector potential due to the magnetic current, $\mathbf{F}(\mathbf{M}_0)$, and the magnetic scalar potential due to the magnetic current, $\phi_m(\mathbf{M}_0)$:

$$\begin{aligned} Y_s^{hs} &= \iint_A \mathbf{M}_0 \cdot \left(j\omega \mathbf{F}(\mathbf{M}_0) + \nabla \phi_m(\mathbf{M}_0) \right) dydx \\ Y_s^{hs} &= \iint_A \left\{ j\omega \mathbf{M}_0 \cdot \mathbf{F}(\mathbf{M}_0) + \mathbf{M}_0 \cdot \nabla \phi_m(\mathbf{M}_0) \right\} dydx \end{aligned} \tag{212}$$

Note that ω is the angular frequency. This expression can be rewritten using a vector identity:

$$\begin{aligned} Y_s^{hs} &= \iint_A \left\{ j\omega \mathbf{M}_0 \cdot \mathbf{F}(\mathbf{M}_0) - \phi_m(\mathbf{M}_0) \nabla \cdot \mathbf{M}_0 \right\} dydx \\ Y_s^{hs} &= j\omega \iint_A \left\{ \mathbf{M}_0(x,y) \cdot \mathbf{F}(\mathbf{M}_0) - \frac{\nabla \cdot \mathbf{M}_0(x,y)}{j\omega} \phi_m(\mathbf{M}_0) \right\} dydx \end{aligned} \tag{213}$$

The electric vector potential and magnetic scalar potential themselves are given by their standard electromagnetic definitions:

$$\mathbf{F}(\mathbf{M}_0) = \frac{\varepsilon}{4\pi} \iint_{A'} 2\mathbf{M}_0(x',y') \frac{e^{-jkr}}{r} dy'dx' = \frac{\varepsilon}{2\pi} \iint_{A'} \mathbf{M}_0(x',y') \frac{e^{-jkr}}{r} dy'dx' \tag{214}$$

$$\begin{aligned} \phi_m(\mathbf{M}_0) = \frac{1}{4\pi\mu} \iint_{A'} \frac{\nabla \cdot 2\mathbf{M}_0(x',y')}{-j\omega} \frac{e^{-jkr}}{r} dy'dx' = \\ \frac{-1}{j2\pi\mu\omega} \iint_{A'} \nabla \cdot \mathbf{M}_0(x',y') \frac{e^{-jkr}}{r} dy'dx' \end{aligned} \tag{215}$$

Here, ε and μ are the electromagnetic permittivity and permeability, respectively. The integrals are again over the area of the aperture; however, the variables of integration are different from the integral (211) and are distinguished by the prime notation. Note that the factor of two in (214)-(215) accounts for the presence of the ground plane in the aperture problem. The distance r is given by:

$$r=\sqrt{\left(x-x'\right)^2+\left(y-y'\right)^2} \tag{216}$$

Substitution of the potentials (214)-(215) into admittance expression (213) yields:

$$\begin{gathered}
Y_s^{hs}=j\omega\iint_A\left\{\begin{array}{l}\mathbf{M}_0\left(x,y\right)\cdot\dfrac{\varepsilon}{2\pi}\displaystyle\iint_{A'}\mathbf{M}_0\left(x',y'\right)\dfrac{e^{-jkr}}{r}dy'dx'\\ -\dfrac{\nabla\cdot\mathbf{M}_0\left(x,y\right)}{2\pi\mu\omega^2}\displaystyle\iint_{A'}\nabla\cdot\mathbf{M}_0\left(x',y'\right)\dfrac{e^{-jkr}}{r}dy'dx'\end{array}\right\}dydx\\
Y_s^{hs}=j\omega\iint_A\left\{\begin{array}{l}\dfrac{\varepsilon}{2\pi}\displaystyle\iint_{A'}\mathbf{M}_0\left(x,y\right)\cdot\mathbf{M}_0\left(x',y'\right)\dfrac{e^{-jkr}}{r}dy'dx'-\\ \dfrac{1}{2\pi\mu\omega^2}\displaystyle\iint_{A'}\left(\nabla\cdot\mathbf{M}_0\left(x,y\right)\right)\left(\nabla\cdot\mathbf{M}_0\left(x',y'\right)\right)\dfrac{e^{-jkr}}{r}dy'dx'\end{array}\right\}dydx
\end{gathered} \tag{217}$$

Equation (217) constitutes a general expression for the self admittance given a full-domain, a-priori magnetic current $\mathbf{M}_0$. Note that it essentially amounts to a four-fold integral. Depending on the geometry, the computational details of the integrals will vary.

Mutual Admittance

The half-space mutual admittance, taken from (26), is given by:

$$Y_m^{hs}=-\left\langle\mathbf{M}_{0,1},\mathbf{H}_1\left(\mathbf{M}_{0,2}\right)\right\rangle \tag{218}$$

Here, $\mathbf{M}_{0,1}$ is the magnetic current on the first aperture, $\mathbf{M}_{0,2}$ is the magnetic current on the second aperture, and $\mathbf{H}_1\left(\mathbf{M}_{0,2}\right)$ is the magnetic field on the first aperture due to the magnetic current on the second aperture. The inner product is understood to be a surface integral over the area of the first aperture. The same steps employed for the self admittance can be used here to expand the mutual admittance into a four-fold integral expression. The details are analogous and will not be repeated here; the resulting expression is:

$$Y_m^{hs} = j\omega \iint_{A_1} \left\{ \iint_{A_2'} \left[\begin{array}{l} \frac{\varepsilon}{2\pi} \mathbf{M}_{0,1}(x,y) \cdot \mathbf{M}_{0,2}(x',y') - \\ \frac{1}{2\pi\mu\omega^2} \left(\nabla \cdot \mathbf{M}_{0,1}(x,y)\right)\left(\nabla \cdot \mathbf{M}_{0,2}(x',y')\right) \end{array} \right] \frac{e^{-jkr}}{r} dy' dx' \right\} dy dx \quad (219)$$

Specialization to Rectangular Apertures

The FSS examples in this work comprise rectangular aperture unit cells. The expressions (217) and (219) for the self and mutual admittances, respectively, can be specialized to the case of rectangular apertures. There are many possible methods to perform the specific calculations. These methods will differ in how they compute the integrals in the admittance expression, which cannot be integrated analytically without approximations. Also, singularities in the free space Green's function must be dealt with in some cases. Tradeoffs in accuracy and computational efficiency are an important consideration, especially since the admittance calculations are the most computationally expensive part of the lattice model.

Self Admittance

The self admittance is calculated through an analytical evaluation of the four-fold integral (217) using polynomial approximations for the terms in the integrand.

Specifically, the equivalent magnetic current is represented as a sum of piecewise linear functions, and the numerator of the free space Green's function is approximated using a Taylor series. The integrals are evaluated analytically in order to deal with singularities in the Green's function; at singular points, limits can be computed using the analytical expressions (which would not be possible using a numerical evaluation of the integrals).

From (44), the magnetic current is assumed to be a half sinusoid. The relevant terms from (217) are:

$$\mathbf{M}_0\left(x,y\right)=\frac{1}{W}\sin\left(\frac{\pi x}{L}\right) \tag{220}$$

$$\mathbf{M}_0\left(x',y'\right)=\frac{1}{W}\sin\left(\frac{\pi x'}{L}\right) \tag{221}$$

The divergences of these terms are also necessary:

$$\nabla\mathbf{M}_0\left(x,y\right)=\frac{\pi}{WL}\cos\left(\frac{\pi x}{L}\right) \tag{222}$$

$$\nabla\mathbf{M}_0\left(x',y'\right)=\frac{\pi}{WL}\cos\left(\frac{\pi x'}{L}\right) \tag{223}$$

In order to make the integral analytically tractable, the aperture is discretized along its length (in the x or x' direction), and the sinusoidal functions of (220)-(223) are approximated as a sum of piecewise linear functions as follows:

$$\mathbf{M}_0\left(x,y\right)\cong\mathbf{A}\left(x\right)=\sum_{i=1}^{N}\mathbf{A}_i\left(x\right)=\sum_{i=1}^{N}W_i\left(x\right)\left(c_i^1x+c_i^2\right)\hat{\mathbf{x}} \tag{224}$$

$$\mathbf{M}_0\left(x',y'\right)\cong\mathbf{A}\left(x'\right)=\sum_{i=1}^{N}\mathbf{A}_i\left(x'\right)=\sum_{i=1}^{N}W_i\left(x'\right)\left(c_i^1x'+c_i^2\right)\hat{\mathbf{x}} \tag{225}$$

$$\nabla \mathbf{M}_0 \left(x,y \right) \cong B\left(x \right) = c_i^1 W_i \left(x \right) \tag{226}$$

$$\nabla \mathbf{M}_0 \left(x',y' \right) \cong B\left(x \right) = c_i^3 W_i \left(x \right) \tag{227}$$

Here, the aperture is divided into N equal segments, and $W_i\left(x\right)$ is a rectangular window function:

$$W_i\left(x\right) = \begin{cases} 1 & \dfrac{\left(i-1\right)L}{N} \le x \le \dfrac{iL}{N} \\ 0 & \text{otherwise} \end{cases} \tag{228}$$

The coefficients c_i^1, c_i^2, c_i^3 and c_i^4 in (224)-(227) are given by:

$$c_1^i = c_3^i = \frac{\dfrac{1}{W}\sin\left(\dfrac{\pi i L}{LN}\right) - \dfrac{1}{W}\sin\left(\dfrac{\pi\left(i-1\right)L}{LN}\right)}{\dfrac{iL}{N} - \dfrac{\left(i-1\right)L}{N}} = \frac{N}{WL}\left(\sin\left(\frac{\pi i}{N}\right) - \sin\left(\frac{\pi\left(i-1\right)}{N}\right)\right) \tag{229}$$

$$c_2^i = c_4^i = \frac{1}{W}\sin\left(\frac{\pi\left(i-1\right)L}{LN}\right) - \frac{c_1^i\left(i-1\right)L}{N} \tag{230}$$

The complex exponential (numerator) of the free space Green's function is also approximated; it is expanded in a Taylor series (third-order):

$$e^{-jkr} \cong e^{-jkr_0}\left[1 - jk\left(r-r_0\right) - \frac{k^2}{2}\left(r-r_0\right)^2 + \frac{jk^3}{6}\left(r-r_0\right)^3\right] = e^{-jkr_0}P\left(r\right) \tag{231}$$

This expansion is computed at the point $r = r_0$; for now, r_0 is left unspecified. With the complex exponential approximated as such, and the magnetic current given by (224)-(225), the admittance can be written as:

$$Y_s^{hs} = j\omega e^{-jkr_0} \sum_{i=1}^{N} \iint_{A} \left\{ \iint_{A'} \left[\begin{array}{l} \frac{\varepsilon}{2\pi} \mathbf{A}_i\left(x\right) \cdot \mathbf{A}_i\left(x'\right) - \\ \frac{1}{2\pi\mu\omega^2} B\left(x\right) B\left(x\right) \end{array} \right] \frac{P\left(r\right)}{r} dy'dx' \right\} dydx \tag{232}$$

Note that due to linearity, the summation of the piecewise linear functions from (224)-(225) can be pulled outside of the four-fold integral.

The analytical evaluation of the four-fold integral proceeds by considering the numerator of the integrand, designated $N_i\left(x, x', y, y'\right)$:

$$N_i\left(x, x', y, y'\right) = \left(\frac{\varepsilon}{2\pi} \mathbf{A}_i\left(x\right) \cdot \mathbf{A}_i\left(x'\right) - \frac{1}{2\pi\mu\omega^2} B\left(x\right) B\left(x\right) \right) P\left(r\right) \tag{233}$$

The numerator, which comprises all polynomial terms, can be expanded and reorganized algebraically into a single polynomial with the following general form:

$$N_i\left(x, x', y, y'\right) = \sum_j c_{i,j} x^{\alpha_j} x'^{\beta_j} r^{\gamma_j} \tag{234}$$

Here, $c_{i,j}$ are coefficients of a sum of monomials involving a power of x, a power of y, and a power of r. The denominator of the integrand is simply r, so the entire integrand, designated $f_{i,j}\left(x, x', y, y'\right)$ can be written as:

$$f_i\left(x, x', y, y'\right) = \sum_j f_{i,j}\left(x, x', y, y'\right) = \sum_j c_{i,j} x^{\alpha_j} x'^{\beta_j} r^{\gamma_j - 1} \tag{235}$$

To be clear, the index i here refers to the summation over the piecewise linear functions (i.e. the approximation to the sinusoidal magnetic current), whereas the index j is tied to the summation over the monomials.

The full set of monomials and their coefficients in (235) are not listed in detail here for brevity; they can be obtained from routine algebraic operations. The indefinite four-fold integral can be evaluated separately for each of these monomials using a commercial analytical software package. The indefinite integral of the individual monomials are of the following form (using the definition of r in (216):

$$\begin{aligned} F_{i,j}\left(x,x',y,y'\right) &= \int\int\int\int f_{i,j}\left(x,x',y,y'\right) dxdydx'dy' = \\ &\int\int\int\int c_{i,j} x^{\alpha_j} x'^{\beta_j} \left(\left(x-x'\right)^2+\left(y-y'\right)^2\right)^{\left(\gamma_j-1\right)/2} dxdydx'dy' \end{aligned} \qquad (236)$$

The specific results of these integrals are no listed in detail here, as some of them are quite cumbersome algebraically.

Once the indefinite integrals (236) are known, the associated definite integrals, which employ the integration limits of (232), are evaluated using the following general formula, which is an extension of the fundamental theorem of calculus to the four-fold case:

$$\begin{aligned} &\int_{x'_1}^{x'_2}\int_{y'_1}^{y'_2}\int_{x_1}^{x_2}\int_{y_1}^{y_2} f_{i,j}\left(x,x',y,y'\right) dxdydx'dy' = \\ &F_{i,j}\left(x_1,x'_1,y_1,y'_1\right)+F_{i,j}\left(x_2,x'_1,y_1,y'_1\right)+F_{i,j}\left(x_1,x'_1,y_2,y'_1\right)+F_{i,j}\left(x_2,x'_1,y_2,y'_1\right)+ \\ &F_{i,j}\left(x_1,x'_2,y_1,y'_1\right)+F_{i,j}\left(x_2,x'_2,y_1,y'_1\right)+F_{i,j}\left(x_1,x'_2,y_2,y'_1\right)+F_{i,j}\left(x_2,x'_2,y_2,y'_1\right)+ \\ &F_{i,j}\left(x_1,x'_1,y_1,y'_2\right)+F_{i,j}\left(x_2,x'_1,y_1,y'_2\right)+F_{i,j}\left(x_1,x'_1,y_2,y'_2\right)+F_{i,j}\left(x_2,x'_1,y_2,y'_2\right)+ \\ &F_{i,j}\left(x_1,x'_2,y_1,y'_2\right)+F_{i,j}\left(x_2,x'_2,y_1,y'_2\right)+F_{i,j}\left(x_1,x'_2,y_2,y'_2\right)+F_{i,j}\left(x_2,x'_2,y_2,y'_2\right)+ \end{aligned}$$

(237)

As long as $x \neq x'$ and $y \neq y'$, the terms $F_{i,j}\left(x,x',y,y'\right)$ can be computed directly. However, if either or both of these conditions are not met, $F_{i,j}\left(x,x',y,y'\right)$ may be singular. In these cases, an analytical limit as $x \to x'$ or $y \to y'$ can be computed. To summarize:

$$F_{i,j}\left(x,x',y,y'\right)=\begin{cases} F_{i,j}\left(x,x',y,y'\right) & x\neq x', y\neq y' \\ \lim\limits_{x\to x'} F_{i,j}\left(x,x',y,y'\right) & x=x', y\neq y' \\ \lim\limits_{y\to y'} F_{i,j}\left(x,x',y,y'\right) & x\neq x', y=y' \\ \lim\limits_{y\to y'}\left(\lim\limits_{x\to x'} F_{i,j}\left(x,x',y,y'\right)\right) & x=x', y=y' \end{cases} \tag{238}$$

These limits may be obtained using a commercial analytical package. For brevity, they are not explicitly listed here.

In summary, the self admittance (217) is computed using the following formula that makes use of analytical integration and approximations to the terms in the integrand:

$$Y_s^{hs} = j\omega e^{-jkr_0}\sum_{i=1}^{N}\sum_{j}\left[\int_{x_1'}^{x_2'}\int_{y_1'}^{y_2'}\int_{x_1}^{x_2}\int_{y_1}^{y_2} f_{i,j}\left(x,x',y,y'\right)dxdydx'dy'\right] \tag{239}$$

The four-fold definite integral within the brackets is computed from the analytically-derived terms $F_{i,j}\left(x,x',y,y'\right)$ using (237). Computationally, this is done for each value of i and j. Then, the results of these integrals are summed, first over j (the various monomials in the polynomial approximation of the original integrand), and then over i (the piecewise linear approximations to the magnetic currents).

Mutual Admittance

The mutual admittance computation (219) does not suffer from singularities like the self admittance (assuming the two apertures under consideration are spatially distinct and do not overlap). It is more convenient to perform a simple numerical integral approximation in the sense of a Riemann sum. This approach requires less analytical manipulation and is actually less expensive computationally, since it does not involve large algebraic expressions resulting from the four-fold analytical integrals (236).

The specific numerical approach is as follows. First, the integration space over the area of the aperture (both A and A') is discretized into a regular four-dimensional grid. This yields a set of points $(i\Delta x, j\Delta y, i'\Delta x', j'\Delta y')$, where i, j, i', and j' are integers, and Δx, Δy, $\Delta x'$, and $\Delta y'$ are the space between points in the x, y, x', and y' directions, respectively. Also, the magnetic currents of (219) are approximated as piecewise linear functions, as was done for the self admittance calculation; the form of these currents is analogous to (224)-(225). The total admittance, then, can be computed as:

$$Y_m^{hs} = \sum_{i,j,i',j'} \left[\begin{pmatrix} \frac{\varepsilon}{2\pi} \mathbf{M}_{0,1}(i\Delta x, j\Delta y) \cdot \mathbf{M}_{0,2}(i'\Delta x', j'\Delta y') - \\ \frac{1}{2\pi\mu\omega^2} \left(\nabla \cdot \mathbf{M}_{0,1}(i\Delta x, j\Delta y)\right)\left(\nabla \cdot \mathbf{M}_{0,2}(i'\Delta x', j'\Delta y')\right) \end{pmatrix} \frac{e^{-jkr}}{r} \right] \quad (240)$$

In summary, the admittance is calculating by discretizing the four-fold integration space, computing the integrand at each point in the discretized space, and adding the results of these computations in a four-fold summation.

APPENDIX B

SIMULATION OF VARACTOR-TUNED FSS

The simulation of varactor-tuned rectangular aperture FSSs using commercial simulation software poses a number of difficulties in terms of producing results that corroborate with the corresponding reconfigurable lattice model formulation presented in Chapter VI. The specific treatment of the varactor elements in the simulation is the primary consideration in question. Different commercial programs have different methodologies for integrating a varactor model into the basic FSS simulation.

When working in [16] – the program used for the majority of the simulations in this work – varactors can be added to the simulation using a small, two-dimensional surface placed across the width of the rectangular aperture; this surface is subsequently assigned a lumped impedance boundary that corresponds to the desired varactor capacitance. Ideally, this surface is added to the center of the aperture (where the varactor would be physically located) and given the same dimensions as the physical varactor. However, this method inherently changes the field distribution on the aperture; specifically, the distribution is no longer a half-sinusoid. Although this may more accurately depict what physically happens to the field distribution in the presence of a finite-sized varactor, it does not correspond directly to the lattice model formulation of the varactor-tuned aperture in Chapter VI, which assumes the same aperture field distribution as for a standard rectangular aperture (the aperture is simply loaded by a perfect capacitive impedance without changing the field distribution). Since the purpose of the reconfigurable lattice formulation in this work is purely illustrative in nature (to show the potential application of the model to reconfigurable designs), this simulation option is not considered an ideal way to validate the lattice theory.

For the purposes of this work, [39] was found to provide a method for incorporating varactors that was more suitable to direct comparison with the lattice model. In this program, “lumped ports” can be added to a simulation by defining two points in the three-dimensional design space; these points comprise the positive and negative terminals of an additional ideal microwave network port in the model (besides the standard wave ports used to excite plane wave propagation). This additional port can be assigned any arbitrary characteristic impedance. It does not affect the field distribution of the simulation, so the results are identical to a simulation without the port. However, it adds an additional dimension to the simulated S-parameters; for example, a standard two-port FSS simulation with one additional lumped port yields three-port S-parameters. The additional port can be loaded with various lumped impedances in post-processing in order to simulate the effect of actual lumped elements on the structure.

In the first section of this appendix, the simulation method using [39] is applied to the varactor-tuned, single rectangular aperture design of Fig. 52. Post processing of the three-port S-parameters is performed in [58] in order to load the simulated design with various varactor capacitances. In the second section, this method is extended to the dual-aperture varactor design of Fig. 79, this time using four-port simulated S-parameters.

Three-port model for varactor-tuned single-element FSS

For a varactor-tuned single rectangular aperture, a third port (lumped port) is added to the simulation in [39]. The three-port S-parameters are simulated, exported, and post-processed in [58]. The three-port S-parameters from the simulation can be summarized in matrix form:

$$S = \begin{bmatrix} S_{11} & S_{12} & S_{13} \\ S_{21} & S_{22} & S_{23} \\ S_{31} & S_{32} & S_{33} \end{bmatrix} \tag{241}$$

From standard microwave network theory, the three-port S-parameters have a corresponding set of Z-parameters, which relate the port voltages to the port currents:

$$\begin{aligned} \mathbf{V} &= Z\mathbf{I} \\ Z &= \begin{bmatrix} Z_{11} & Z_{12} & Z_{13} \\ Z_{21} & Z_{22} & Z_{23} \\ Z_{31} & Z_{32} & Z_{33} \end{bmatrix} \\ \mathbf{V} &= \begin{bmatrix} V_1 & V_2 & V_3 \end{bmatrix}^T \\ \mathbf{I} &= \begin{bmatrix} I_1 & I_2 & I_3 \end{bmatrix}^T \end{aligned} \tag{242}$$

Here, $\mathbf{V}$ is a vector of the port voltages, $\mathbf{I}$ is a vector of the port currents, and Z is the impedance matrix. The characteristic impedance associated with the ports is assumed to be $Z_0 = 377\ \Omega$ (free space); this establishes the relationship between S and Z.

It is assumed that the lumped port of the FSS – in this case, port 1 of the network – is terminated in the capacitance of the varactor. This capacitive impedance associated with the varactor is defined as Z_c; if the capacitance is C, then $Z_c = 1/j\omega C$. By terminating port 1 with this impedance, the network effectively becomes a two-port network. The FSS performance can then be ascertained from the equivalent two-port network (in the sense illustrated by Fig. 2 in Chapter II). Fig. 84 illustrates this effective reduction in the number of network ports. In (a), the three-port network is terminated with the capacitive varactor impedance; in (b), an equivalent two-port network is proposed that achieves the same port voltages and currents as the three port network. Specifically, $V_2 = \tilde{V}_1$, $I_2 = \tilde{I}_1$, $V_3 = \tilde{V}_2$, and $I_3 = \tilde{I}_2$. The network parameters of the equivalent two-port network are defined through an impedance matrix $\tilde{Z}$:

$$\begin{aligned} &\tilde{\mathbf{V}} = \tilde{Z}\tilde{\mathbf{I}} \\ &\tilde{Z} = \begin{bmatrix} \tilde{Z}_{11} & \tilde{Z}_{12} \\ \tilde{Z}_{21} & \tilde{Z}_{22} \end{bmatrix} \\ &\tilde{V} = \begin{bmatrix} \tilde{V}_1 & \tilde{V}_2 \end{bmatrix}^T \\ &\tilde{I} = \begin{bmatrix} \tilde{I}_1 & \tilde{I}_2 \end{bmatrix}^T \end{aligned} \tag{243}$$

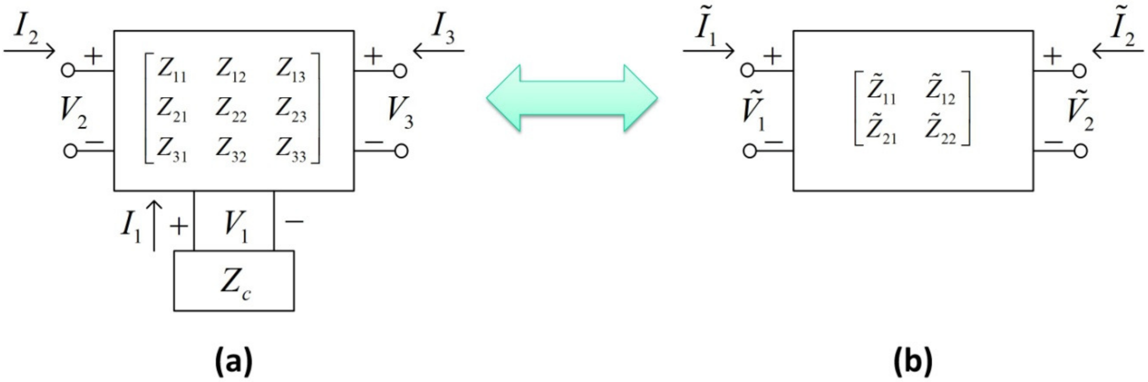

Fig. 84. Conversion of terminated three-port network to two-port network.

The two-port impedance parameters $\tilde{Z}$ can be computed directly from the three-port impedance parameters Z, which are known from the simulation. To do this, the following relation, employing Ohm's law at port 1 of Fig. 84 (a), is needed:

$$I_1 = -\frac{V_1}{Z_c} \tag{244}$$

Note that this relation is dictated by the chosen varactor capacitance. Next, by definition, the terms of $\tilde{Z}$ can be found via:

$$\tilde{Z}_{ij} = \left.\frac{\tilde{V}_i}{\tilde{I}_j}\right]_{\tilde{I}_k = 0, k \neq j} \tag{245}$$

In words, if the input currents at all ports except port j are set to zero, the impedance at port i can be measured as V_i/I_j. Thus, the terms $\tilde{Z}_{11}$ and $\tilde{Z}_{21}$ can be found by setting the input current at port 3 to zero ($I_3 = 0$). With this assumption and the relation (244), (242) can be used to write a system of three equations:

$$\begin{aligned} I_2 Z_{12} - V_1 - \frac{V_1 Z_{11}}{Z_c} &= 0 \\ I_2 Z_{22} - V_2 - \frac{V_1 Z_{21}}{Z_c} &= 0 \\ I_2 Z_{32} - V_3 - \frac{V_1 Z_{31}}{Z_c} &= 0 \end{aligned} \tag{246}$$

This system can be solved for the three unknowns V_2, V_3, and I_2. Appropriate substitution of these solutions into (245) yields:

$$\tilde{Z}_{11} = Z_{22} - \frac{Z_{12} Z_{21}}{Z_{11} + Z_c} \tag{247}$$

$$\tilde{Z}_{12} = Z_{23} - \frac{Z_{13}Z_{21}}{Z_{11} + Z_c} \tag{248}$$

Similarly, the terms $\tilde{Z}_{21}$ and $\tilde{Z}_{22}$ can be found by setting the input current at port 2 to zero ($I_2 = 0$). This yields another system of three equations:

$$\begin{aligned} I_3 Z_{13} - V_1 - \frac{V_1 Z_{11}}{Z_c} &= 0 \\ I_3 Z_{23} - V_2 - \frac{V_1 Z_{21}}{Z_c} &= 0 \\ I_3 Z_{33} - V_3 - \frac{V_1 Z_{31}}{Z_c} &= 0 \end{aligned} \tag{249}$$

Solving for the unknowns V_2, V_3, I_3 and employing the results in (245) yields:

$$\tilde{Z}_{21} = Z_{32} - \frac{Z_{12}Z_{31}}{Z_{11} + Z_c} \tag{250}$$

$$\tilde{Z}_{22} = Z_{33} - \frac{Z_{13}Z_{31}}{Z_{11} + Z_c} \tag{251}$$

The two-port impedance parameters (247), (248), (250), and (251) can be duly converted into S-parameters in order to obtain the performance of the varactor-tuned FSS for a particular value of Z_c.

Four-port model for varactor-tuned dual aperture FSS

In Chapter IX, the varactor-tuned FSS idea is extended to a dual aperture topology with independently tuned varactors. For simulation purposes in [39], this design is assigned two (rather than one) lumped ports. The resulting simulated S-parameters are four-port (rather than three-port). During post-processing in [58], the two lumped ports are terminated with capacitive impedances Z_{c1} and Z_{c2}, which correspond to the two varactors. Thus, in order to obtain the FSS performance parameters, an equivalent two-port network must be formulated from the four-port network. Fig. 85 summarizes the problem.

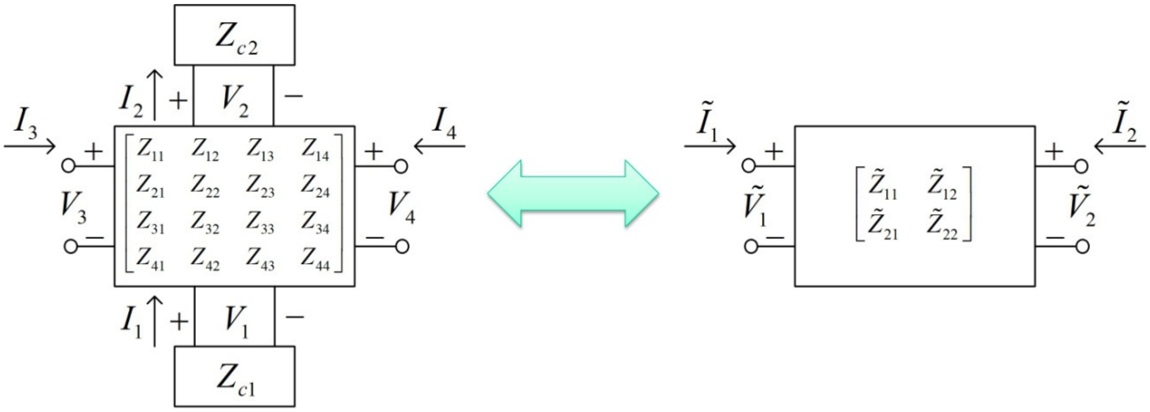

(a) **(b)**

Fig. 85. Conversion of terminated four-port network to two-port network.

The process of converting the terminated four-port impedance parameters Z to equivalent two-port impedance parameters $\tilde{Z}$ is analogous to the process used for the three-port to two-port conversion in the previous section. The algebraic details are somewhat more involved for the four-port case and will not be elaborated on here, but the results can be summarized as follows:

$$\tilde{Z}_{11} = \frac{\begin{pmatrix} \left(Z_{23}Z_{32} - Z_{22}Z_{33} - Z_{33}Z_{c2}\right)Z_{11} + Z_{12}Z_{21}Z_{33} - Z_{12}Z_{23}Z_{31} - Z_{13}Z_{21}Z_{32} + \\ Z_{13}Z_{22}Z_{31} + Z_{13}Z_{31}Z_{c2} - Z_{22}Z_{33}Z_{c1} + Z_{23}Z_{32}Z_{c1} - Z_{33}Z_{c1}Z_{c2} \end{pmatrix}}{\left(-Z_{22} - Z_{c2}\right)Z_{11} + Z_{12}Z_{21} - Z_{22}Z_{c1} - Z_{c1}Z_{c2}} \qquad (252)$$

$$\tilde{Z}_{12} = \frac{\begin{pmatrix} \left(Z_{24}Z_{32} - Z_{22}Z_{34} - Z_{34}Z_{c2}\right)Z_{11} + Z_{12}Z_{21}Z_{34} - Z_{12}Z_{24}Z_{31} - Z_{14}Z_{21}Z_{32} + \\ Z_{14}Z_{22}Z_{31} + Z_{14}Z_{31}Z_{c2} - Z_{22}Z_{34}Z_{c1} + Z_{24}Z_{32}Z_{c1} - Z_{34}Z_{c1}Z_{c2} \end{pmatrix}}{\left(-Z_{22} - Z_{c2}\right)Z_{11} + Z_{12}Z_{21} - Z_{22}Z_{c1} - Z_{c1}Z_{c2}} \quad (253)$$

$$\tilde{Z}_{21} = \frac{\begin{pmatrix} \left(Z_{23}Z_{42} - Z_{22}Z_{43} - Z_{43}Z_{c2}\right)Z_{11} + Z_{12}Z_{21}Z_{43} - Z_{12}Z_{23}Z_{41} - Z_{13}Z_{21}Z_{42} + \\ Z_{13}Z_{22}Z_{41} + Z_{13}Z_{41}Z_{c2} - Z_{22}Z_{43}Z_{c1} + Z_{23}Z_{42}Z_{c1} - Z_{43}Z_{c1}Z_{c2} \end{pmatrix}}{\left(-Z_{22} - Z_{c2}\right)Z_{11} + Z_{12}Z_{21} - Z_{22}Z_{c1} - Z_{c1}Z_{c2}} \quad (254)$$

$$\tilde{Z}_{22} = \frac{\begin{pmatrix} \left(Z_{24}Z_{42} - Z_{22}Z_{44} - Z_{44}Z_{c2}\right)Z_{11} + Z_{12}Z_{21}Z_{44} - Z_{12}Z_{24}Z_{41} - Z_{14}Z_{21}Z_{42} + \\ Z_{14}Z_{22}Z_{41} + Z_{14}Z_{41}Z_{c2} - Z_{22}Z_{44}Z_{c1} + Z_{24}Z_{42}Z_{c1} - Z_{44}Z_{c1}Z_{c2} \end{pmatrix}}{\left(-Z_{22} - Z_{c2}\right)Z_{11} + Z_{12}Z_{21} - Z_{22}Z_{c1} - Z_{c1}Z_{c2}} \quad (255)$$

Again, the FSS performance can be obtained by converting these impedance parameters to S-parameters.